

Mapping and modelling the spatial variation in strain accumulation along the North Anatolian Fault

Ekbal Hussain

Submitted in accordance with the requirements for the degree of
Doctor of Philosophy

The University of Leeds
School of Earth and Environment

June 2016

The candidate confirms that the work submitted is his own, except where work which has formed part of jointly authored publications has been included. The contribution of the candidate and the other authors to this work has been explicitly indicated below. The candidate confirms that appropriate credit has been given within the thesis where reference has been made to the work of others.

The work in Chapter 2 of the thesis has appeared in the following publication:

Hussain, E., T.J. Wright, R.J. Walters, D.P.S. Bekaert, G. Houseman and A.J. Hooper (2016), *Geodetic observations of postseismic creep in the decade after the 1999 Izmit earthquake, Turkey: Implications for a shallow slip deficit*, Journal of Geophysical Research, doi:10.1002/2015JB012737.

The ideas and methodologies in this paper were developed with the co-authors. I expanded on these ideas and further developed the methods. I performed the data processing and analysis, and wrote the manuscript, which was improved by suggestions and comments from the co-authors.

The work in Chapter 3 of the thesis has been accepted for publication pending major revisions under the following publication:

Hussain, E., A.J. Hooper, T.J. Wright, R.J. Walters and D.P.S. Bekaert (2016), *Intra-seismic strain accumulation across the central North Anatolian Fault from iteratively unwrapped InSAR measurements*, Journal of Geophysical Research, doi:10.1002/2015JB012737.

The idea for the new iterative unwrapping algorithm presented in this paper initially originated from Andrew Hooper. I expanded on this and further developed the method, and wrote and tested the algorithm. Andrew Hooper implemented my algorithm into the existing Stanford Method for Persistent Scatterers (StaMPS) program. I performed the data processing and analysis, and wrote the manuscript, which was improved by suggestions and comments from the co-authors.

The work in Chapter 4 of the thesis is a manuscript about to be submitted:

Hussain, E., T.J. Wright, R.J. Walters, D.P.S. Bekaert, and R. Lloyd (in prep), *Strong lower crust required by strain observations spanning an entire earthquake cycle*

The ideas in this paper initially originated from Tim Wright. I expanded on these further, developed the methods and processed all the data. I used Tim Wright's code to produce forward calculations of the velocity profiles for different viscosities, which I then used to determine the strain rate variation with time. I performed all the analysis, and wrote the draft, which was improved by suggestions and comments from the co-authors.

This copy has been supplied on the understanding that it is copyright material and that no quotation from the thesis may be published without proper acknowledgement

Copyright © **2016** The University of Leeds and **Ekbal Hussain**
The right of **Ekbal Hussain** to be identified as Author of this work has been asserted
by him in accordance with the Copyright, Designs and Patents Act 1988.

Acknowledgements

The 4 years spent on my PhD has been an enlightening experience and I am proud of all I have accomplished. But the journey was the cumulative sum of many moments shared with friends, colleagues and complete strangers (who later became friends). I have many many people to thank and I am sure I will miss some in this acknowledgement, for that I sincerely apologise!

First and foremost, my sincerest gratitude go to my supervisors Tim Wright and Greg Houseman. I thank you for sharing your wealth of knowledge and experience with me over the past 4 years. In particular Tim, who prodded me back on track when I started to verge off course but allowed me to indulge my passion for science communication and international development, and who ended up reading all of my thesis in the end. It's been a pleasure working with you.

Thanks to David Bekaert who was one of the first people I met in Leeds and who has since become one of my best friends. You have been sorely missed this past year. Thanks for your patience with the many interruptions and questions I had about InSAR processing and coding in Matlab. Thanks are due to Karsten Spaans who took over your role of 'question answerer' this past year.

Richard Rigby deserves the equivalent of a Nobel Prize for IT and computing support! Without him my PhD would have fallen apart many moons ago and I would still be trying to figure out how to connect to the internet ...

Richard Walters has been a solid source of useful information and helpful feedback over the years, as has Andy Hooper, who has helped enormously with some of the technical work on InSAR and statistics. Many thanks for your encouragement and helpful discussions while writing my papers.

I have had the pleasure of meeting lots of new people through the various national and international events I've attending throughout the PhD. I've enjoyed many engaging and helpful discussions at the numerous COMET meetings throughout the years. Thanks to all involved.

My PhD has been generously supported by NERC through the FaultLab project. I have also had financial support from the European Commission, the European Geoscience Union, Leeds for Life and the Climate and Geohazard Services. Thanks for the monies!

Thanks to the Cake Man. Your weekly supply of delicious cakes made Mondays actually something I looked forward to!

To my office mates and PhD friends, old and new, you've been a great bunch and we've had some great experiences. Special mentions to Daniela, Edine, Jo, Karsten, Anna and Dave. Good luck with everything you do. Always remember the wise advice of Douglas Adams: Don't panic, and always have your towel with you!

To my house mates at Oatland Close. Thanks for all the happy memories. It's been a wonderful experience sharing the last 4 years with you.

Thank you to Betty Meulen. Your friendship means a lot to me and I am so sorry I've been neglecting you. I hope to make it up to you soon! Thanks to Tabby for brightening my day with a lovely message each time I sent off a finance request. It's the little things that make a difference.

To all the wonderful people in the School of Earth and Environment, you have made my time in Leeds a fantastic experience. Thank you all! Special mentions to Katie Livesey and Pre Carbo for allowing me to indulge my love for global development and science outreach.

Emma Caton, you alone have seen how progressively grey (and sparse ...) my hair has become over the past few years. I owe you an enormous debt of gratitude for sticking with me throughout the ups and downs of the PhD, as well as joining me on some adventures abroad. Thank you for everything!

And last but by no means least, I owe a lifetime of gratitude to my parents who, despite never going to university themselves, encouraged me to pursue my education as far as I could. My PhD is dedicated to you.

Abstract

Since 1900, earthquakes worldwide have been responsible for over 2 million fatalities and caused nearly \$2 trillion of economic damage. Accurate assessment of earthquake hazard is therefore critical for nations in seismically active regions. For a complete understanding of seismic hazard, the temporal pattern of strain accumulation, which will eventually be released in earthquakes, needs to be understood. But earthquakes typically occur every few hundred to few thousand years on any individual fault, and our observations of deformation usually only cover time periods of a decade or less. For this reason, our knowledge of the temporal variation in strain accumulation rate is limited to insights gleaned from kinematic models of the earthquake cycle that use measurements of present-day strain to infer the behaviour on long time scales. Previous studies have attempted to address this issue by combining data from multiple faults with geological estimates of long-term strain rates. In this thesis I propose a different approach, which is to observe deformation at multiple stages of the earthquake cycle for a single fault with segments that have failed at different times.

In the last century the North Anatolian Fault (NAF) in Turkey has accommodated 12 large earthquakes ($M_w > 6.5$) with a dominant westward progression in seismicity. If we assume that each of these fault segments are at a different stage of the earthquake cycle then this provides a unique opportunity to study the variation in along-strike surface deformation, which can be equated to variation of deformation in time.

In this thesis I use Interferometric Synthetic Aperture Radar (InSAR) and Global Navigation Satellite System (GNSS) observations to examine the spatial distribution of strain along the NAF. InSAR is an attractive technique to study surface displacements at a much higher spatial resolution (providing a measurement every 30 m) compared to established GNSS measurements, with station separations between 10 km to 100 km in Turkey. I specifically address a key technical challenge that limits the wide uptake of InSAR: phase unwrapping, the process of recovering continuous phase values from phase data that are measured modulo 2π radians. I develop a new unwrapping procedure for small baseline InSAR measurements that iteratively unwraps InSAR phase. For each iteration, this method identifies pixels unwrapped correctly in the previous iteration and applies a high cost to changing the phase difference between these pixels in the next iteration. In this way, the iterative unwrapping method uses the error-free pixels as a

guide to unwrap the regions that contained unwrapping errors in previous iterations.

I combine measurements of InSAR line-of-sight displacements with published GNSS velocities to show that an ~ 80 km section of the NAF that ruptured in the 1999 Izmit earthquake (Mw 7.4) is creeping at a steady rate of ~ 5 mm/yr with a maximum rate of 11 ± 2 mm/yr near the city of Izmit within the observation period 2002-2010. I show that in terms of the moment budget and seismic hazard the effect of the shallow, aseismic slip in the past decade is small compared to that from plate loading. Projecting the shallow creep displacement rates late into the earthquake cycle does not produce enough slip to account for the 2-3 m shallow coseismic slip deficit observed in the Izmit earthquake. Therefore, distributed inelastic deformation in the uppermost few kilometers of the crust or slip transients during the interseismic period are likely to be important mechanisms for generating the shallow slip deficit.

I used similar techniques to confirm that a ~ 130 km section of the central NAF near the town of Ismetpasa, is also undergoing aseismic creep at a steady rate of 8 ± 2 mm/yr. Using simple elastic dislocation models to fit fault perpendicular velocities I show that there is an eastward decreasing fault slip rate in this region from ~ 32 mm/yr to ~ 21 mm/yr over a distance of about 200 km. The cause of this decrease remains unclear, but it could be due to postseismic effects from the 1999 Izmit and Düzce earthquakes and/or long-term influence from the 1943 (Mw 7.4) and 1944 (Mw 7.5) earthquakes.

Finally, I combine line-of-sight displacements from 23 InSAR tracks to produce the first high resolution horizontal velocity field for the entire continental expression of the NAF (~ 1000 km). I show that the strain rate does not vary significantly along the fault, and since each segment of the NAF is at a different stage of the earthquake cycle, the strain rate is invariant with respect to the time since the last earthquake. This observation is inconsistent with viscoelastic coupling models of the earthquake cycle, which predict a decreasing strain rate with time after an earthquake. My observations imply that strain accumulation reaches a steady-state fairly rapidly after an earthquake ($< 7-10$ years) after which strain is localised on a narrow shear zone centred on the fault and does not vary with time. A time-invariant strain rate is consistent with a strong lower crust in the region away from the fault with a viscosity $\geq 10^{20}$ Pas.

My results imply that short term snapshots of the present-day strain accumulation (as long as it is after the postseismic period) are representative of the entire earthquake cycle, and therefore geodetic estimates of the strain rate can be used to estimate the total strain accumulation since the last earthquake on a fault, and be used as a proxy for future seismic hazard assessment.

The techniques I developed to explore the spatial and temporal pattern of aseismic fault creep and long-term strain accumulation along the NAF are general and can be applied to all strike-slip faults globally. The archived ERS-1/2 and Envisat satellite data are an extremely valuable resource that can and should be used to extend InSAR time series measurements back to the early 1990s. Together with the new Sentinel-1 data

sets, this provides an unprecedented opportunity to explore tectonic deformation over several decades and on continental scales. Despite the availability of numerous correction techniques (in this thesis I use global weather models to calculate the atmospheric contribution), atmospheric delays remain the major challenge to exploiting Sentinel-1 data for global strain mapping, the mitigation of these delays are an important goal for the InSAR community.

Contents

List of Figures	xiii
List of Tables	xvii
Nomenclature	xix
1 Introduction	1
1.1 Earthquake cycle deformation	2
1.1.1 Coseismic deformation	3
1.1.2 Postseismic deformation	3
1.1.3 Interseismic deformation	6
1.2 Modelling the earthquake cycle	10
1.3 Aseismic fault creep	13
1.4 The shallow slip deficit	14
1.5 The North Anatolian Fault	16
1.5.1 Seismicity	17
1.5.2 Fault slip rates and locking depths	18
1.6 Interferometric Synthetic Aperture Radar (InSAR)	20
1.6.1 Decorrelation noise	22
1.6.2 Atmospheric noise	23
1.6.3 Phase unwrapping	25
1.7 Aims and objectives	26
1.8 Thesis roadmap	28
2 Postseismic creep in the decade after the 1999 Izmit earthquake	39
Abstract	40
2.1 Introduction	40
2.2 InSAR processing and applied corrections	42
2.2.1 Atmospheric delay corrections	44
2.2.2 InSAR Line of sight velocity field in a GPS reference frame	44
2.3 Along strike variation in fault creep rate	46
2.4 InSAR velocity decomposition	50

2.4.1	Adapazari basin subsidence	52
2.5	Modelling profile velocities	53
2.6	Fault creep time series	57
2.7	Discussion	59
2.7.1	Fault creep and elastic modelling	59
2.7.2	Time series	64
2.7.3	Moment release	65
2.7.4	Implications for the shallow slip deficit	66
2.8	Conclusion	68
3	Interseismic strain across the central North Anatolian Fault	77
	Abstract	78
3.1	Introduction	78
3.2	InSAR processing	80
3.3	Iterative phase unwrapping	82
3.3.1	Method description	82
3.3.2	Testing the iterative unwrapping procedure	84
3.4	Interseismic velocity field across the central NAF	85
3.5	Modelling profile velocities	90
3.6	Fault creep along the central NAF	94
3.7	Discussion	96
3.7.1	Iterative unwrapping benefits and limitations	96
3.7.2	Interseismic slip rates	97
3.7.3	Fault creep	99
3.8	Conclusion	101
4	Time-invariant strain accumulation and a strong lower crust	111
	Abstract	112
4.1	Introduction	112
4.2	Surface deformation from InSAR	113
4.3	Variation in strain accumulation along the NAF	114
4.4	Discussion and Conclusions	118
4.5	Methods	120
5	Discussion and Conclusions	127
5.1	Summary of results and implications	127
5.1.1	Chapter 2	127
5.1.2	Chapter 3	128
5.1.3	Chapter 4	129
5.2	Locking depth and slip rate variation with time	130
5.3	Detecting fault creep	132

5.3.1	Use high temporal resolution InSAR measurements	132
5.3.2	Correct for long wavelength signals	133
5.3.3	Network inversion filters	134
5.3.4	Creepmeter measurements	136
5.4	Evolution of scale	136
5.5	Towards a global strain map	137
5.6	Future work	141
5.6.1	Disaster response	141
5.6.2	Atmospheric corrections	141
5.6.3	Rheology of the crust from fault creep measurements	142
5.6.4	Detecting hidden faults	142
5.7	Concluding remarks	143
A	Appendix for the Introduction chapter	149
B	Supplementary material for Chapter 2	159
C	Supplementary material for Chapter 3	165
D	Supplementary material for Chapter 4	171
E	Appendix of the backmaterial	181

List of Figures

1.1	The elastic rebound theory	2
1.2	InSAR coseismic slip for 1992 Landers earthquake	4
1.3	Global compilation of rheological interpretations of postseismic geodetic data	7
1.4	The elastic dislocation model for strain accumulation	8
1.5	Fault parallel velocity and strain rates from the screw dislocation model	9
1.6	Postseismic vs interseismic velocity	11
1.7	Predicted velocity profiles using the viscoelastic coupling model	12
1.8	The shallow slip deficit in several large strike-slip earthquakes	15
1.9	Deep afterslip after the 1999 Izmit earthquake	16
1.10	Earthquake progression along the NAF	17
1.11	Historical earthquake sequences along the NAF	19
1.12	Published slip rate estimates along the NAF	19
1.13	Published locking depth estimates along the NAF	20
1.14	Phase simulation for distributed and persistent scatterer pixels	22
1.15	ERA-I atmospheric correction example	24
1.16	Schematic of the phase unwrapping problem	25
1.17	GNSS velocity field over Turkey	27
2.1	The 1999 magnitude 7.4 Izmit and magnitude 7.2 Düzce earthquake surface ruptures	41
2.2	Baseline vs time plots	43
2.3	The average Line of Sight (LOS) velocities for the tracks used in this study	45
2.4	Close-up of the creep signal at Izmit	47
2.5	Fault creep rate decomposed into the east-west and vertical components	49
2.6	LOS InSAR velocities decomposed into the east-west and vertical components	51
2.7	A profile of east-west velocities at location B-B'	53
2.8	A schematic of our elastic model	54
2.9	Projected east-west velocities along the profiles	56
2.10	Profile B-B'	57

2.11	The sampled marginal probability distributions of the model parameters	58
2.12	A time series of relative displacement	60
2.13	The sampled marginal probability distributions of the model parameters	61
2.14	Projected east-west velocities along the profiles B-B' and C-C'	63
2.15	A zoom-in of the region around the fault south of the city of Izmit	67
3.1	The central section of the North Anatolian Fault	79
3.2	A simple interferometric loop consisting of 3 acquisitions	83
3.3	Total percentage of pixels in the small baseline network	85
3.4	Changes in the percentage of error-free pixels per iteration	86
3.5	Evolution of the number of error-free pixels per iteration	87
3.6	Descending and ascending line-of-sight velocities with each track	88
3.7	LOS InSAR velocities decomposed into the fault parallel and vertical components of motion	89
3.8	Profiles through the fault parallel velocities along three lines	92
3.9	Marginal probability distributions for profile A-A', B-B' and C-C'	93
3.10	The variation in LOS fault creep rate along the central NAF	95
3.11	Eastward decreasing fault slip rate	98
3.12	Fault parallel velocities along profile D-D'	99
3.13	Slip rate and creep rate compared with coseismic slip	100
4.1	The LOS and decomposed east-west velocities used in this study	115
4.2	A selection of profiles used to estimate the fault slip rate and locking depth	116
4.3	The variation in strain rate along the NAF	117
4.4	The temporal evolution of strain rate for the NAF	119
5.1	Seismicity in Turkey	129
5.2	Locking depth and slip rate variation with time	131
5.3	Transient slip on the Ismetpasa section of the NAF	133
5.4	Fault creep versus interseismic deformation	134
5.5	Automatic detection of fault creep	135
5.6	Creepmeter measurements at Ismetpasa	137
5.7	Scaling up InSAR studies	138
5.8	The Sentinel-1 satellite	139
5.9	Sentinel-1 and Envisat velocity field over Turkey	140
B.1	Four examples of interferograms before any atmospheric corrections	160
B.2	The reduction in variance after applying the ERA-I weather model correction	161
B.3	An example of a short 10 km profile of line-of-sight velocities	162
B.4	Uncertainty maps for the E-W velocity and the vertical velocity	162

B.5	The sampled marginal probability distributions of the model parameters for profiles A-A' and C-C'	163
C.1	Baseline vs time plots for each of the tracks used in our study	166
C.2	The reduction in standard deviation for our descending tracks after applying the ERA-I weather model correction	167
C.3	The reduction in standard deviation for our ascending tracks after applying the ERA-I weather model correction.	167
C.4	The north component of the GNSS velocities interpolated to every InSAR grid location.	168
C.5	Fault parallel and vertical velocity uncertainties	169
D1	Baseline vs time plots for each of the descending tracks	172
D2	Baseline vs time plots for each of the ascending tracks	173
D3	Normalised histograms of the horizontal velocity differences between overlapping InSAR tracks	174
D4	Interpolated GNSS north component velocities	175
D5	The decomposed vertical component of the InSAR LOS velocities	175
D6	Slip rate estimates using a fixed locking depth	176
D7	Profiles of GNSS fault parallel velocities	176
D8	Fault parallel velocity profiles with our MAP model solution	177
D8	continued	178
D8	continued	179

List of Tables

1.1	The most recent earthquake sequence along the NAF	18
2.1	Data coverage from each Envisat track used in this study	42
2.2	Regions used to determine the noise covariance function	47
3.1	Data coverage for each Envisat track used in this study	80
3.2	The centre of the 50 km by 50 km region used to estimate the noise covariance function parameters.	82
4.1	Data coverage for each Envisat track used in this study.	113
4.2	θ_{rot} values used for the rotation correction.	122
A.1	Compilation of published slip rate estimates for the North Anatolian Fault	150
A.2	Compilation of published locking depth estimates for the North Anatolian Fault	154
E.1	Compilation of slip rate and locking depth estimates for large strike-slip faults with the time since the last large earthquake ($M_w > 6$)	182

Nomenclature

List of acronyms

CalTech	California Institute of Technology
COMET	Centre for the Observation and Modelling of Earthquakes, Volcanoes and Tectonics
DEM	Digital Elevation Model
DORIS	Delft Object-oriented Radar Interferometric Software
Envisat	Environmental satellite
ERS	European Remote-sensing Satellite
ESA	European Space Agency
GMT	Generic Mapping Tools
GNSS	Global Navigation Satellite System
GPS	Global Positioning System
InSAR	Interferometric Synthetic Aperture Radar
JPL	Jet Propulsion Laboratory
LOS	Line Of Sight
MAP	Maximum A posteriori Probability
MCMC	Marcov Chain Monte Carlo
NAF	North Anatolian Fault
NERC	Natural Environment Research Council
PS	Persistent Scatterer
ROLPAC	Repeat Orbit Interferometry PACkage

SAR	Synthetic Aperture Radar
SRTM	Shuttle Radar Topography Mission (DEM)
StaMPS	Stanford Method of Persistent Scatter
TRAIN	Toolbox for Reducing Atmospheric InSAR Noise

List of symbols

α	Satellite flight azimuth	[°]
λ	Characteristic length for noise covariance	[km]
ϕ	Radar phase	[rad]
σ	Normal stress	[Pa]
θ	Incidence angle	[°]
θ_{rot}	Rotation correction for fault parallel velocities	[mm/yr/km]
$a - b$	Rate-and-state friction parameters	[-]
B_{perp}	Perpendicular baseline	[m]
C	Fault creep rate	[mm/yr]
d_1	Locking depth	[km]
d_2	Maximum creep depth	[km]
d_c	Critical slip distance	[m]
D_E, D_N, D_U	East, North, Up components of motion	[mm/yr]
k	Stiffness	[Pa/m]
M_w	Moment Magnitude	[-]
S	Fault slip rate	[mm/yr]
t_c	Characteristic decay time for transient afterslip	[years]
v_{EW}	East-west component of velocity	[mm/yr]
v_{max}	Depth-averaged maximum afterslip velocity	[mm/yr]
v_{par}	Fault parallel component of velocity	[mm/yr]
v_p	Pre-seismic fault creep rate	[mm/yr]
x	Distance	[km]

Chapter 1

Introduction

“Data! Data! Data!” he cried
impatiently. “I can’t make
bricks without clay.”

SHERLOCK HOLMES

The catalogue of earthquake disasters since the year 2000 now contains 7 individual events that have each resulted in the loss of 10,000 lives or more (USGS). Five of these occurred in the continental interiors, often in regions where the hazard was underestimated and the strain accumulation poorly understood. For a complete understanding of seismic hazard the temporal pattern of strain accumulation during the entire earthquake cycle needs to be understood. This includes the centuries to millennia of slow strain accumulation during the interseismic period, which is released in a coseismic event, and the days to years of postseismic readjustments following an earthquake.

This thesis will focus on the use of Interferometric Synthetic Aperture Radar (InSAR) to measure strain accumulation at various stages of the earthquake cycle. Our understanding of surface deformation during the earthquake cycle is limited by the fact that high quality geodetic measurements exist only for a small fraction of the long time interval (centuries to millennia) between earthquakes on a single fault segment (*Meade et al., 2013*). In this thesis I propose to address this problem by investigating the variation in surface deformation along the North Anatolian Fault (NAF) in Turkey. Thanks to a consistent set of propagating earthquakes over 70 years (*Barka, 1996*) and geodetic observations before the 1999 Izmit earthquake, the NAF offers a unique opportunity to measure strain accumulation at various stages of the ~ 250 year earthquake cycle on the fault.

InSAR offers the potential to measure surface deformation at a much higher spatial resolution compared to the established Global Navigation Satellite System (GNSS) network in Turkey (e.g. *Reilinger et al., 2006, Aktuğ et al., 2013*). However, such large scale InSAR analysis requires the development of more robust processing procedures and careful consideration of noise terms. When combined with GNSS, InSAR enables

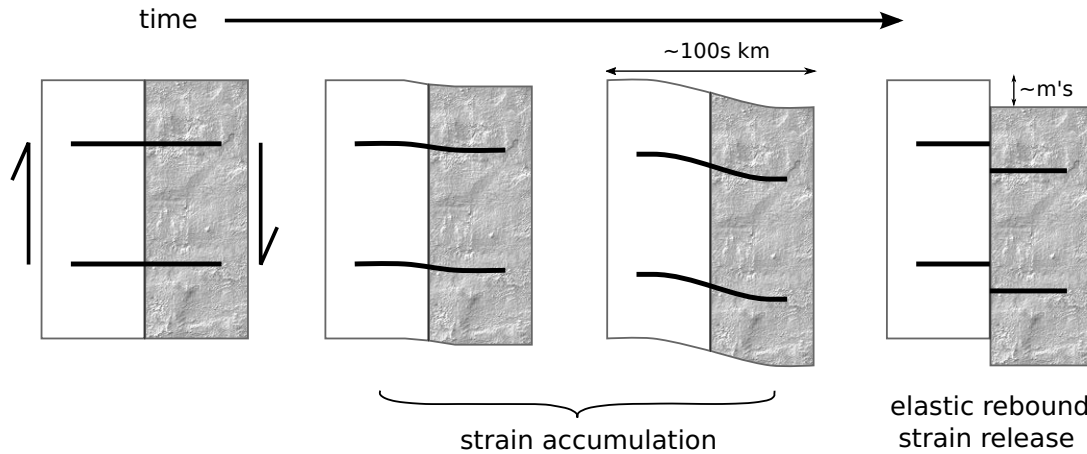


Figure 1.1: The elastic rebound theory for earthquakes in which elastic strain accumulates in the upper crust over a long period of time and is released instantly in an earthquake.

detailed investigations of the 3-dimensional velocity field not only to understand long-term strain accumulation but also to detect transient deformation, arising from fault creep and postseismic deformation.

In this chapter I will provide background information on the key observations and processes during the earthquake cycle, as well as an overview of the North Anatolian Fault. I will give a brief summary of the InSAR procedure and discuss some of the key challenges using this technique. I end with my aims and objectives along with a roadmap for the thesis.

1.1 Earthquake cycle deformation

Harry Fielding Reid developed the earthquake cycle model to explain the pattern of ground deformation from the 1906 San Francisco earthquake (*Reid, 1910*). From examining the ground displacements before and after the earthquake he first proposed the idea of an ‘elastic rebound’ of previously-stored elastic stresses during a coseismic event.

In Reid’s model, far-field tectonic displacements slowly build up stresses and accumulate elastic strain on faults over long periods of time. This is released instantly during an earthquake once a critical limit is reached. We now know that the life cycle of an earthquake is not purely limited to the energy release during an earthquake (coseismic), and the centuries to millennia of slow strain accumulation before (interseismic), but also includes the days to years of stress redistribution after an earthquake (postseismic) (*Thatcher, 1993*).

1.1.1 Coseismic deformation

The coseismic phase of the elastic rebound model is the instantaneous release of accumulated strain from the interseismic period. This occurs when the stresses built up over the interseismic period can no longer be supported by friction on the fault. The release of accumulated strain causes permanent displacements of the ground either side of the fault rupture (Figure 1.1). The seismic waves produced by medium-large sized earthquakes can be measured using the network of seismometer instruments deployed around the world and analysed to study the source parameters of the earthquake. Originally this was the principle method used to understand the role of earthquake deformation and the links with large scale tectonics (e.g. *McKenzie, 1972, Jackson and McKenzie, 1984*). However, with the advent of a satellite radar interferometry technique known as Interferometric Synthetic Aperture radar (InSAR) (Section 1.6) - high resolution maps of surface displacements can now be routinely made over most major continental earthquake ruptures. The first map of coseismic ground surface displacements using InSAR was made by *Massonnet et al. (1993)* for the 1992 Landers earthquake in California (Figure 1.2).

For moderate to large continental earthquakes ($M_w > \sim 6$), geodetic observations can also be used to determine earthquake source geometries and slip distributions (*Wright et al., 2013*). These source models have several advantages over models derived from seismological methods. Firstly, they provide very accurate information on the exact location of the fault, particularly if the earthquake is shallow. Secondly, the source models do not suffer to the same degree from the fault plane ambiguity inherent in many seismic methods (*Biggs et al., 2006*). Finally, the distribution of slip on the fault plane can be determined more reliably using geodetic observations, particularly from InSAR, than using seismic observations (e.g. *Funning et al., 2007*).

1.1.2 Postseismic deformation

The postseismic phase of the earthquake cycle is the period of accelerated transient deformation after the coseismic phase. Postseismic deformation rates are at a maximum immediately after the coseismic event and decay to the background interseismic rates. The timescale of this decay may vary from hours to decades depending on the dominant process involved.

The earliest evidence of postseismic deformation came from studies of the 1906 San Francisco earthquake. *Thatcher (1975)* used data from post-earthquake triangulation surveys to first show that postseismic strain rates were a factor of 4 higher than long term strain rates.

While the distribution of coseismic fault slip provides valuable information about the mechanics of the earthquake process on the main fault zone, postseismic deformation provides clues about the mechanical behavior of the region surrounding the coseismic

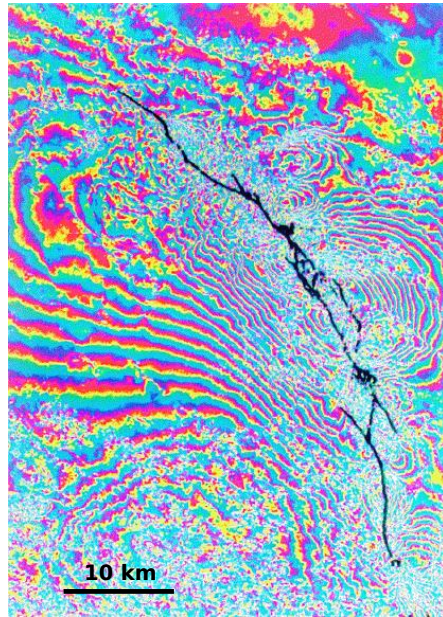


Figure 1.2: The first InSAR map of coseismic surface displacements for the 1992 Landers earthquake in California. Figure after *Massonnet et al. (1993)*.

fault and in deeper parts of the earthquake generation zone (e.g. *Thatcher, 1983, Tse and Rice, 1986, Scholz, 1988*).

Several mechanisms are often invoked to explain the surface observations from transient postseismic deformation: poroelastic rebound, afterslip and viscoelastic relaxation.

Poroelastic rebound

Poroelastic deformation results from the flow of pore-fluid in response to coseismic stress induced pore-pressure changes (*Nikolaevskii et al., 1970, Peltzer et al., 1998*).

The best example of poroelastic rebound occurred in the first few months following two moderate sized earthquakes (Mw 6.5) in June 2000 in Iceland. *Jonsson et al. (2003)* combined geodetic observations of surface deformation with independent observations from geothermal wells to show that the water level rose in wells that were in regions around the fault that contracted during the earthquakes, and dropped in wells that were in regions that dilated. In the 3 months following the earthquake water flowed from the high pore-pressure regions, i.e. the region that contracted in the earthquakes, to regions of low pore-fluid pressure, i.e. regions that dilated in the earthquakes. This flow of water resulted in surface deformation with a spatial pattern identical to that predicted from models of poroelastic deformation.

Poroelastic rebound has also been invoked to explain transient surface deformation following the 1992 Landers earthquake (*Peltzer et al., 1998, Fialko, 2004*), but appear to be a relatively insignificant mechanism for most earthquakes (*Wright et al., 2013*).

Afterslip

Afterslip is a general term referring to continued slip on parts of a fault after an earthquake. Afterslip was first observed after the 1966 Parkfield earthquake on the San Andreas Fault (*Smith and Wyss, 1968*) and has since been measured following several other large earthquakes (e.g. *Savage and Church, 1974, Ryder et al., 2007, Barbot et al., 2008*).

Marone et al. (1991) showed that afterslip can be explained as a manifestation of rate-state variable friction behaviour within fault zones. Earthquakes occur on parts of the fault plane where the dynamic coefficient of friction is lower than the static friction, while afterslip is thought to occur where the dynamic coefficient of friction is higher than the static friction, meaning stable slip can occur as a result of stress changes due to the coseismic rupture (*Scholz, 2002*).

Inversions of surface displacements following large earthquakes reveal that afterslip often occurs on parts of the fault that did not fail in the earthquake, with slip usually localised to the region below the main slip patch. For example, *Bürgmann et al. (2002b)* showed that in the 87 days following the Mw 7.4 Izmit earthquake the earthquake, the afterslip rate decayed from a rate of 2 m/yr to 1.2 m/yr. In Chapter 2 I show that shallow fault creep, which also initiated after the earthquake, can also be explained using a rate-and-state dependent afterslip model.

Viscoelastic relaxation

The rheology of the upper crust appears well described by linear elastic relations between stress and strain (a Hooke solid) at stresses lower than those required to induce brittle fracture or frictional sliding of faults. Due to the increased temperatures and pressures in the lower crust and below, deformation involves both elastic (at short timescales) and viscous behaviour.

Therefore, another way in which the Earth adjusts during the postseismic period is through viscous flow of the lower crust and upper mantle. This flow is controlled by grain-scale mechanisms within crystals, such as dislocation and diffusion creep (e.g. *Bürgmann and Dresen, 2008*).

The key parameter that controls the rate and spatial pattern of surface deformation due to deep viscoelastic relaxation is the viscosity (η), which is a function of stress (σ) and strain rate ($\dot{\epsilon}$):

$$\eta \propto \frac{\sigma}{\dot{\epsilon}} \quad (1.1)$$

The viscosity is a measure of the strength of the lower crust and upper mantle. Originally, surface uplift measurements caused by the viscoelastic response of the mantle due to rapid unloading of ice sheets since the last glacial maximum, a process called post-glacial rebound, were used to determine the viscosity of the mantle (e.g. *Peltier,*

1976). The first demonstration of viscoelastic relaxation following an earthquake was by *Nur and Mavko (1974)*, who showed that the postseismic deformation following the large 1946 Nankaido earthquake could be explained using a simple viscoelastic model with a mantle viscosity of 5×10^{18} Pa s.

Despite these three distinctly different mechanisms it is often difficult to determine which is responsible for transient postseismic deformation following a large earthquake. Vigorous debate persists because the models can be parametrised to produce similar patterns of surface deformation for a two-dimensional infinitely long strike-slip rupture. For this reason, it is possible that prejudices of authors can bias results.

More often than not, multiple relaxation processes occur after a major earthquake. Some studies have explained transient postseismic deformation by invoking a combination of poroelastic rebound and crustal afterslip (e.g. *Fialko, 2004, Peltzer et al., 1996*), or poroelastic rebound and viscoelastic relaxation in the lower crust (e.g. *Masterlark and Wang, 2002*); while *Freed et al. (2006)* showed that surface observations following the 2002 Mw 7.9 Denali earthquake in Alaska could only be explained by invoking deep viscoelastic relaxation and shallow afterslip. In a 2013 review of the literature, *Wright et al. (2013)* found 49 studies of postseismic deformation with many employing a combination of processes to describe the surface observations from geodetic data (Figure 1.3). Of the 20 individual earthquakes/sequences considered, they found that 16 had viscoelastic relaxation, 3 had poroelastic rebound, and 16 had shallow or deep afterslip inferred by at least one study. Therefore, a broad conclusion is that viscoelastic relaxation in the lower crust and/or upper mantle with transient afterslip is to be expected after most large earthquakes.

1.1.3 Interseismic deformation

Reid's simple earthquake model describes the slow build up of strain over a long period of time, which is eventually released in an earthquake. This slow strain accumulation is known as the interseismic phase of the earthquake cycle, and is usually thought of as steady-state deformation associated with the far-field motion of the tectonic plates.

The interseismic strain rates are small compared to the total strain release in the coseismic period. Typically, interseismic displacement rates are of the order 1 to 10s mm/yr over a region covering tens to one hundred kilometres. This gives strain rates of the order of $10^{-6} - 10^{-8}$ yr⁻¹. Therefore, studies of the interseismic period require a long time series of measurements to accurately filter the deformation signal from the various noise sources.

The first estimate of interseismic deformation were from triangulation surveys after the 1906 San Francisco earthquake (*Reid, 1910*). However, most modern estimates are from GNSS measurements (e.g. *Straub et al., 1997, Hubert-Ferrari et al., 2000*,

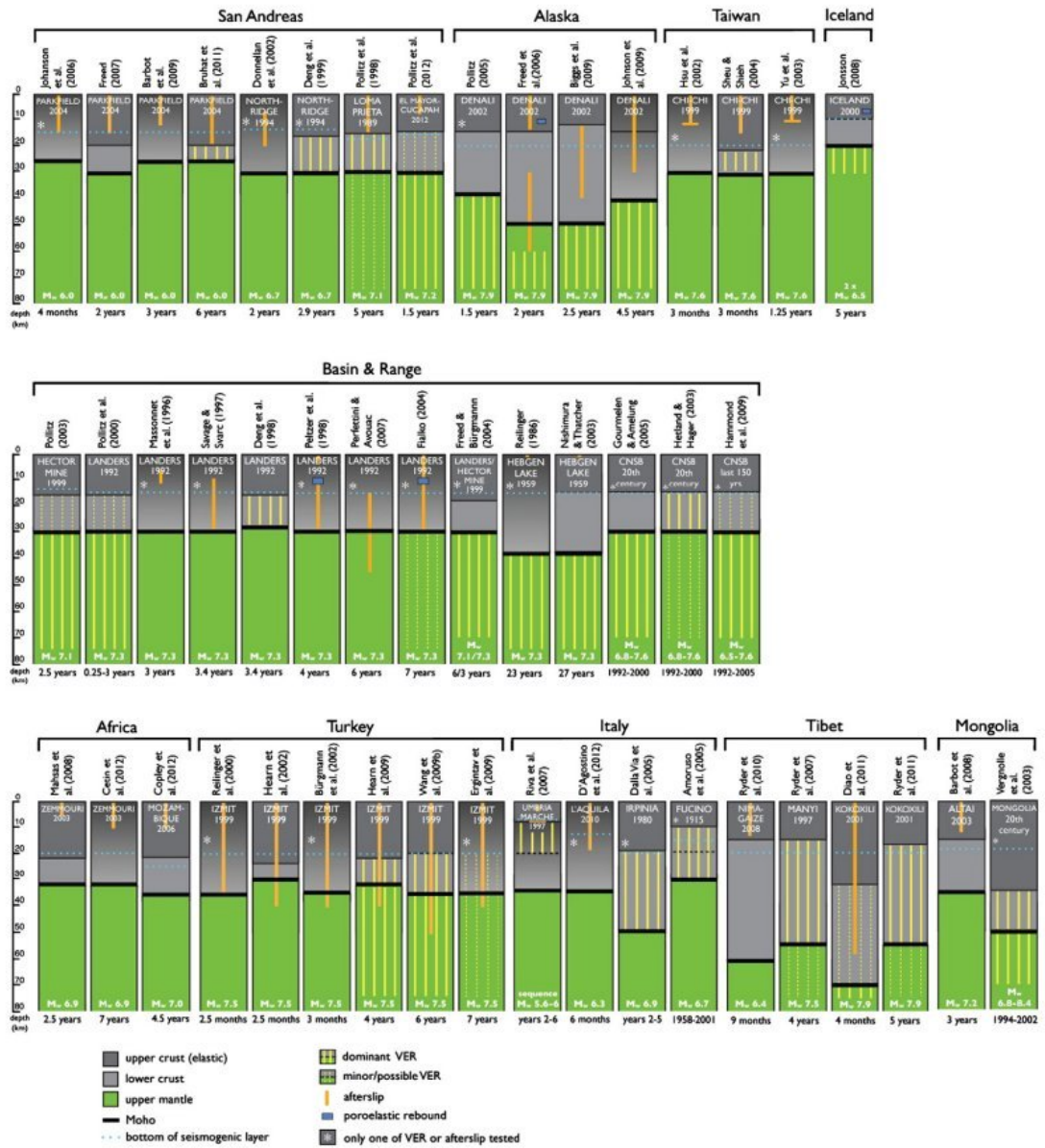


Figure 1.3: Global compilation of rheological interpretations of postseismic geodetic data. VER = viscoelastic relaxation. Each column represents a single case study, either for an individual earthquake or a group of earthquakes. Figure from *Wright et al. (2013)*.

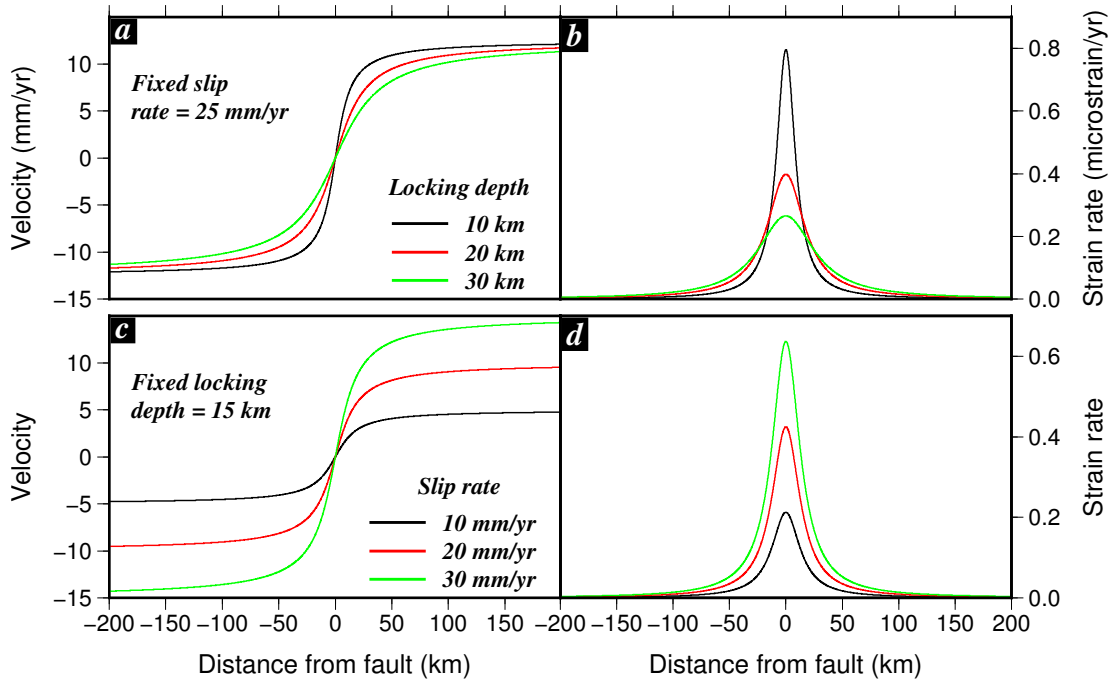


Figure 1.5: Forward calculations of fault perpendicular velocity and strain rate using the simple screw dislocation model (*Savage and Burford, 1973*). (a) and (b) are the results for a fixed slip rate while (c) and (d) are for a fixed locking depth.

not possible to distinguish between slip on a narrow fault and slip in a shear zone that is π times thicker than the locking depth (*Moore, 1999*). For example, the observed surface deformation across the eastern end of the North Anatolian Fault in Turkey, is consistent with slip on a single deep fault plane (*Wright et al., 2001a*), although a shear zone narrower than 75 km cannot be discounted. *Savage and Prescott (1978)* compared a completely elastic model with a viscoelastic model and found that the resulting surface velocity field is similar for both models if the lower crustal viscosity is high ($\geq 10^{20} \text{Pas}$).

As a result, the simplicity of the 2-parameter elastic dislocation model has meant it remains a popular choice for inverting geodetically measured surface velocities in order to calculate the strain accumulation rate across strike-slip faults (*Wright et al., 2013*). Although it is not a realistic representation of the physical processes that occur in a fault zone, it is a convenient way of abstracting the two real measurements that can be obtained from geodetic observables at locked strike-slip faults:

1. The integrated strain rate across the fault, which is equivalent to the slip rate (S) for a fixed locking depth (d)
2. The width of the straining zone, which is related to the locking depth

Differentiating Equation 1.2 gives the strain rate ($\dot{\epsilon}$):

$$\dot{\epsilon} = \frac{dS}{\pi(d^2 + x^2)} \quad (1.3)$$

At the fault trace ($x = 0$), Equation 1.3 reduces to:

$$\dot{\epsilon} = \frac{S}{\pi d} \quad (1.4)$$

Therefore, for a fixed locking depth, the strain rate is equivalent to the slip rate on the fault. Figure 1.5 shows forward calculations of the variation in fault perpendicular velocity for different values of slip rate and locking depth, and the corresponding strain rates. It is clear that for a constant slip rate, an increase in the locking depth results in a broader deformation zone; while for a fixed locking depth, an increase in the slip rate results in larger strain rates at the fault.

1.2 Modelling the earthquake cycle

Post-earthquake GNSS and InSAR measurements of surface displacements made at high temporal and spatial resolutions have enabled detailed studies of postseismic deformation after major earthquakes (e.g. *Peltzer et al., 1996*, *Kenner and Segall, 2000*, *Bürgmann et al., 2002b*, *Ergintav et al., 2009*). Many authors have attempted to estimate the viscosity structure of the crust and upper mantle from geodetic observations of postseismic deformation (e.g. *Hearn et al., 2002*, *Pollitz, 2005*, *Hetland and Hager, 2006*, *Vaghri and Hearn, 2012*). However, it has been difficult to reconcile the viscosity structure inferred from postseismic displacements with that inferred from interseismic displacements.

A self-consistent understanding of earthquake-related viscous relaxation requires a viscosity structure that can explain the observed geodetic deformation at all stages of the earthquake cycle (Figure 1.6). The key observations that models need to explain are:

1. Rapid postseismic transients following an earthquake
2. Focused strain on the fault late in the earthquake cycle

Simple geodynamic models of the entire earthquake cycle, often called viscoelastic coupling models, consist of a constant-viscosity layer beneath an elastic lid. Coseismic slip is usually imposed in these models at a fixed repeat interval. The models suggest that the observed surface deformation is a function of time since the last earthquake (e.g. *Savage and Prescott, 1978*, *Thatcher, 1983*, *Savage, 2000*).

Figure 1.7 shows the predicted velocity profiles calculated for three different lower crustal viscosities. For a weak lower crust (e.g. $\sim 10^{18}$ Pa s), it is possible to produce

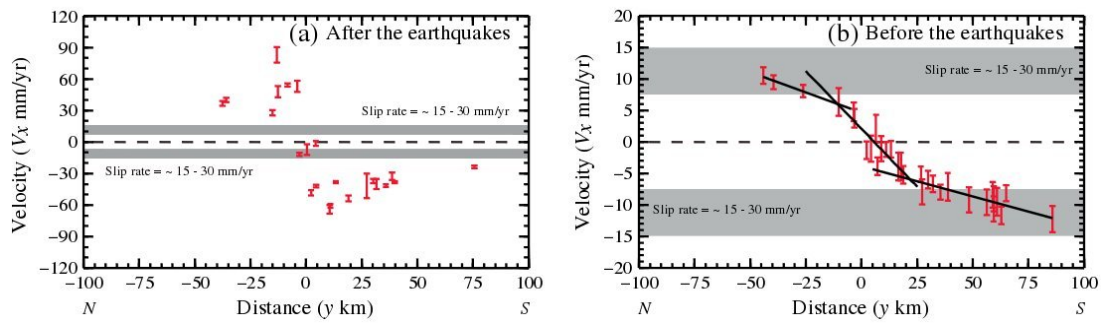


Figure 1.6: (a) Measurements of postseismic velocities after the Izmit earthquake show rapid transients around the fault rupture while long-term interseismic velocities (b) show focused strain around the fault. Figure from [Yamasaki et al. \(2014\)](#).

rapid postseismic deformation that decays with time, while a strong lower crust (e.g. $\sim 10^{20}$ Pa s) can produce focused strain on the fault late in the earthquake cycle. However, a single lower crustal viscosity cannot explain both observations.

The observational data have led to the development of a new generation of earthquake cycle models that are able to predict focused interseismic deformation as well as rapid postseismic transients (e.g. [Hetland and Hager, 2006](#), [Johnson et al., 2007](#), [Takeuchi and Fialko, 2012](#), [Yamasaki and Houseman, 2012](#)). These studies vary in the viscosity structures used to set up the model. For example, [Johnson et al. \(2007\)](#) employ a layered structure assuming the behaviour of each layer is governed by a constant viscosity (Maxwell), while [Takeuchi and Fialko \(2012\)](#) use non-Newtonian viscosity and [Hearn et al. \(2009\)](#) use a Burger's body model with two time-dependent viscosities. [Yamasaki et al. \(2014\)](#) used a viscoelastic model consisting of a low viscosity region immediately beneath the seismogenic fault embedded in a high viscosity medium to fit both the long term interseismic velocities and the postseismic transients after the Izmit earthquake.

Other models of the earthquake cycle consist of rate-and-state dependent frictional behaviour in fault zones, where strain accumulates on locked asperities due to aseismic creep in the surrounding regions. An earthquake occurs when the stresses exceed the frictional resistance on the asperities (e.g. [Marone, 1998](#), [Scholz, 1998](#)). These frictional relations have been used to develop 3-D dynamic models of the earthquake cycle that are able to reproduce a realistic earthquake sequence of irregular moment magnitude (e.g. [Lapusta and Liu, 2009](#), [Barbot et al., 2012](#)).

In order to be able to distinguish between many of the models described above, more observations of surface deformation are needed at different times during the interseismic period. However, owing to the long inter-event time in many large fault zones, typically hundreds to thousands of years, we do not have deformation observations with modern

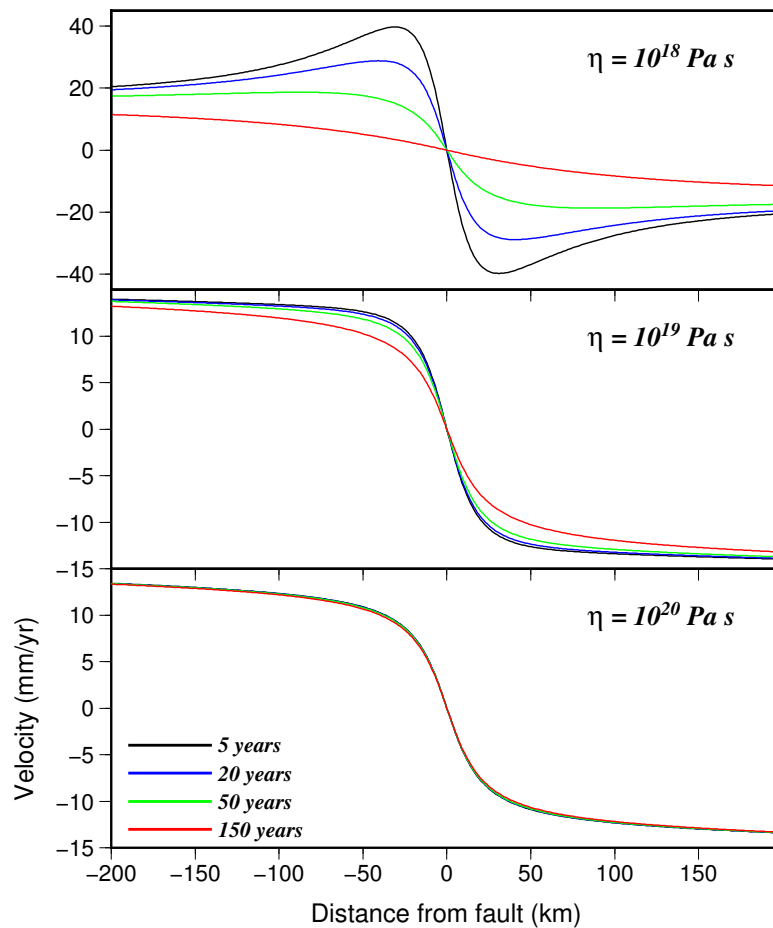


Figure 1.7: Predicted fault perpendicular velocity profiles using the viscoelastic coupling model (*Savage and Prescott, 1978, Savage, 2000*), calculated for three different lower crustal viscosities and at different times after the earthquake. See Chapter 4 for a discussion of the model.

instruments spanning a complete earthquake cycle for any single fault.

Meade et al. (2013) attempted to overcome this problem by comparing long-term geologic slip rates with geodetically derived fault slip rates, which observe only a small fraction (0.001%-0.1%) of the earthquake cycle, for 15 large continental strike-slip faults. They found that geologically and geodetically inferred slip rates agree well, and used this observation to suggest that multiple relaxation timescales, e.g. a Burger's model, are required to reconcile these with rapid postseismic transients. The inherent assumption with this approach is that the crust and continental strike-slip fault zones are the same everywhere. In this thesis I propose a different approach to observe deformation at multiple stages of the earthquake cycle for a single fault that has failed at different times.

In the last century the North Anatolian Fault (NAF) has accommodated 12 large earthquakes ($M_w > 6.5$) with a dominant westward progression in seismicity (Section 1.5, Table 1.1). If we assume that each of these fault segments are at a different stage of the earthquake cycle then this provides a unique opportunity to study the variation in along-strike surface deformation, which can be equated to variation in time. Geodetic observations along the Izmit section of the fault before the 1999 earthquake also provides strain measurements ~ 245 years late in the cycle. The key assumption with this approach is that the earthquake cycle can be investigated by studying the surface deformation along different segments of the same fault, i.e. it assumes the temporal behaviour of each segment along the fault is the same.

A principle aim of this thesis is to investigate the strain accumulation along each of these rupture segments and relate it to changes during the earthquake cycle.

1.3 Aseismic fault creep

Earthquakes are not the only way strain is released on a fault. Aseismic fault creep is also an important mechanism that can influence the size and timing of large earthquakes along partially coupled faults.

While the upper crustal portions of most active faults are locked, storing elastic strain energy for decades to centuries and releasing it almost instantaneously in earthquakes, some faults instead slip steadily at slow rates over various timescales and spatial distributions. This slow movement at a fault is known as aseismic fault creep. If fault creep occurs throughout the seismogenic crust at a rate equal to the tectonic loading then these faults store little to no strain energy and are unlikely to produce significant earthquakes (*Bürgmann et al., 2000*).

However, most faults do not undergo aseismic creep at all depths in the crust at the full tectonic loading rate, implying that not all the accumulated strain energy is being released aseismically. In these cases, parts of the fault are fully or partially locked and can still generate moderate to large earthquakes (e.g. *Avouac, 2015*).

The best documented examples of creeping faults are the central section of the San Andreas Fault ([Maurer and Johnson, 2014](#), [Jolivet et al., 2015](#)), the Longitudinal Valley Fault ([Champenois et al., 2012](#), [Thomas et al., 2014](#)) and the Ismetpasa section of the North Anatolian Fault ([Kaneko et al., 2013](#), [Cetin et al., 2014](#)). Although more creeping faults are being identified with the use of long time series satellite data at high spatial resolution (e.g. [Schmidt et al., 2005](#), [Jolivet et al., 2012](#), [Cakir et al., 2012](#)).

In most models of afterslip or aseismic creep, the creep rate is thought to vary uniformly with time. However studies on the San Andreas Fault using creepmeter measurements have shown that fault creep can have highly variable temporal behaviour ([Nason, 1973](#)). Creep may occur gradually over a long period of time (months to years), or it may occur as episodes of displacements, called “creep events”, which last from a few hours to days and include displacements of a few millimetres or less to a few centimetres ([Wesson, 1988](#)). For example, [Rousset et al. \(2016\)](#) used InSAR analysis of high temporal resolution satellite data acquired between 2013 and 2014 to identify a major burst of aseismic slip spanning 31 days with a maximum slip of 2 cm on the Ismetpasa section of the North Anatolian Fault.

The relationship between the spatial distribution and temporal pattern of aseismic slip, and tectonic loading is important for understanding both the pattern of strain accumulation along a fault and its ability to generate large, damaging earthquakes. In chapter 2 of my thesis I investigate the creeping behaviour of the Izmit section of the North Anatolian Fault (NAF), which was first observed to begin creeping after the 1999 Izmit earthquake ([Cakir et al., 2012](#)). Part of chapter 3 focuses on the spatial pattern of fault creep along the Ismetpasa section of the central NAF. Creeping along this segment of the NAF first was first documented some thirty years ago by [Ambraseys \(1970\)](#), who measured the slow displacement of a wall that crossed the fault near the town of Ismetpasa.

1.4 The shallow slip deficit

Over the past two decades, new information about the near-field deformation pattern due to large earthquakes, largely obtained with the help of InSAR measurements, has enabled investigations into the distribution of coseismic slip on the shallow portions of faults (e.g. [Massonnet et al., 1993](#), [Simons et al., 2002](#), [Lasserre et al., 2005](#)).

In general, coseismic slip distribution studies of many large strike-slip earthquakes reveal that the maximum seismic moment release usually occurs in the middle of the seismogenic layer (at average depths of 4-6 km) with a decay in coseismic slip in the upper (<3-4 km) and lower portions of the brittle crust (>4-6 km) (Figure 1.8) (e.g. [Fialko et al., 2005](#), [Ryder and Bürgmann, 2008](#), [Kaneko and Fialko, 2011](#), [Dolan and Haravitch, 2014](#)).

A gradual decay in coseismic slip in the lower portions of the seismogenic crust

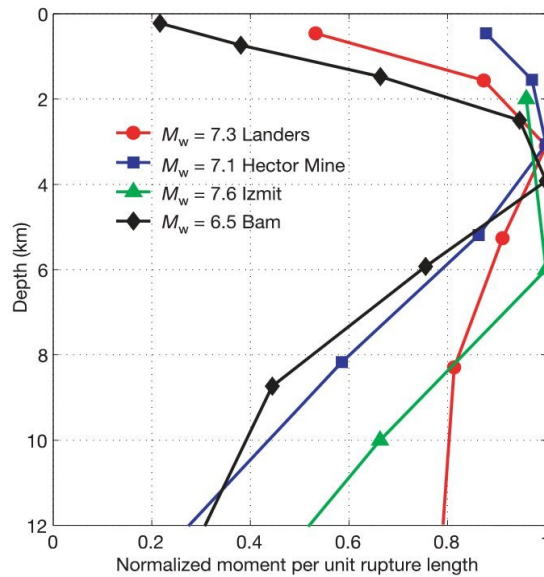


Figure 1.8: The shallow slip deficit in several large strike-slip earthquakes. Figure from *Fialko et al. (2005)*.

is probably compensated by postseismic and interseismic strain accumulation and is reasonably well understood (e.g. *Thatcher, 1983, Tse and Rice, 1986, Savage and Swarc, 1997*). For example, *Bürgmann et al. (2002b)* showed that deep (>10 km) postseismic afterslip after the 1999 Izmit earthquake was highest between and below the regions of maximum coseismic slip and propagated downward to, or even below, the base of the crust. Maximum afterslip rates decayed from greater than 2 m/yr, immediately after the Izmit earthquake to about 1.2 m/yr just prior to the Düzce earthquake. The cumulative deep afterslip in the 87 days after the Izmit earthquake was sufficient to account for the deep slip deficit (Figure 1.9).

The uppermost few kilometres of the crust is known to have mechanical properties that differ from those of the rest of the brittle upper crust. In particular, the shallow layer has a higher density of cracks, pores and voids (*Manning and Ingebritsen, 1999*), and may exhibit velocity-strengthening behaviour (*Marone, 1998*). The latter may explain why the coseismic slip may be impeded in the shallow crust, but it is not clear how the resulting deficit of shallow slip is accommodated throughout the earthquake cycle.

There are two possible explanations for the origin of the shallow slip deficit: the deficit arises due to distributed off-fault deformation in the upper crust, in which case it is not strictly speaking a deficit as such, or the shallow slip deficit is accounted for by aseismic slip on the shallow fault, in which case it could be due to postseismic afterslip or continuous/episodic creep throughout the earthquake cycle.

In Chapter 2 I discuss my results of shallow postseismic fault creep (or afterslip) obtained from high resolution InSAR measurements, and its implications for the shallow

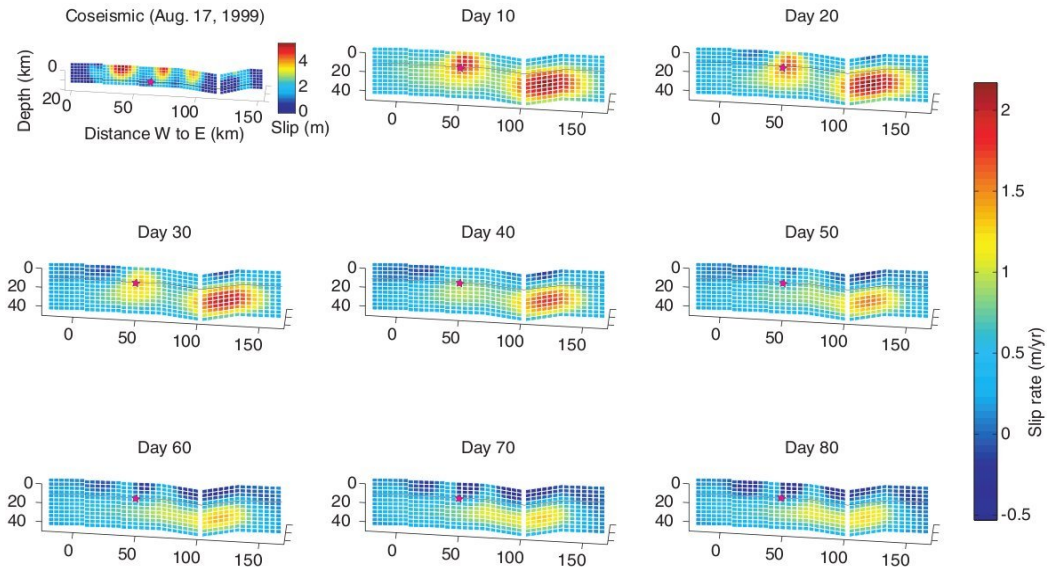


Figure 1.9: Top left panel shows the coseismic slip model (modified from [Reilinger et al. \(2000\)](#)). Remaining panels show snapshots of time-dependent distributed strike-slip rate inverted from the postseismic GNSS measurements in 10-day intervals. Following rapid slip over a large portion of the model fault early on, most slip occurs down-dip of the coseismic rupture. Figure from [Bürgmann et al. \(2002b\)](#).

slip deficit in the region of the Izmit earthquake.

1.5 The North Anatolian Fault

The presence of a band of seismicity across the northern region of Turkey was recognised as early as the mid nineteenth century ([Mallet \(1862\)](#), map D; as cited by [Sengör et al. \(2005\)](#)). But it was Ihsan Ketin ([Ketin, 1948](#)) who observed that the surface breaks of all major earthquakes in the region since 1939 had the characteristics of a right-lateral fault. This was the first documented record of the existence of a large and active strike-slip fault in the world ([Ketin, 1948](#)).

The origin of the NAF has long been considered to be in the Neogene. [Ketin \(1957\)](#) noted that the fault cuts across early Miocene age orogenic deposits implying it was younger than the early Miocene. He used cross cutting relationships to estimate the start of sliding along the NAF to be around 15-20 Ma. [Hubert-Ferrari et al. \(2009\)](#) used ^{40}Ar - ^{39}Ar dating on volcanic deposits that cross the NAF's eastern termination to infer that motion along the fault probably started around 12 Ma ago in an initial phase characterised by a slip rate of about 3 mm/yr and a fault propagation rate of 120 mm/yr during which most of the fault trace developed. The fault slip rate then jumped to around 20 mm/yr over the last 2.5 Ma without a substantial increase in fault length ([Armijo et al., 2002](#)).

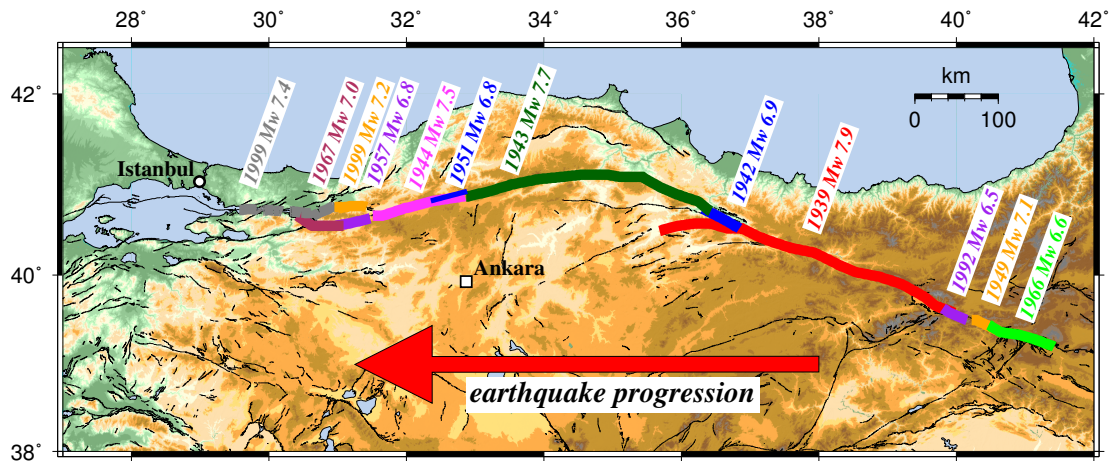


Figure 1.10: Ruptures along the North Anatolian Fault due to large earthquakes ($M_w \geq 6.5$) in the last 80 years. Large earthquakes on the NAF in the last century have followed a general westward trends in seismicity.

1.5.1 Seismicity

Since the 1939 Erzincan earthquake there have been a series of large earthquakes (Table 1.1) that have ruptured over 1000 km of the North Anatolian Fault. These earthquakes have, in general, ruptured progressive westward sections of the fault (*Barka, 1996, Stein et al., 1997*) (Figure 1.10). One of the aims of my thesis is to investigate whether there are spatial correlations in fault slip rate and locking depth with the locations of these past ruptures.

The most recent events along the NAF were the 1999 Izmit ($M_w 7.4$) and 1999 Düzce ($M_w 7.2$) earthquakes that together ruptured ~ 180 km of the western section of the fault. The Izmit earthquake epicentre was located less than 100 km east of Istanbul. In light of the westward progression of previous ruptures along the fault, many authors have raised concerns of the large hazard of a future strong earthquake in the Istanbul region (e.g. *Parsons et al., 2000, Atakan et al., 2002*), where the last major earthquake was in 1894 ($M \sim 7$) (*Ambraseys, 2002*). *Parsons (2004)* used finite-element modelling incorporating a detailed analysis of fault geometry in the Marmara Sea along with stress transfer from the Izmit earthquake, to estimate the 30 year probability of a $M_w \geq 7$ earthquake rupturing beneath the Sea of Marmara to be $\sim 35\text{-}70\%$. This is a significant hazard to the ~ 12 million inhabitants of the greater Istanbul region.

Although clustering of earthquakes in space and time is common (*Dieterich, 1994, Kagan and Jackson, 1991*), and migrating earthquake sequences have occurred elsewhere (*Kasahara, 1981, Mogi, 1985*), none is as spectacular as on the North Anatolian Fault. *Stein et al. (1997)* found that the migrating behaviour can be accurately modelled as a result of Coulomb stress transfer where one earthquake increases the stress on the adjacent fault segment bringing it closer to failure.

The North Anatolian fault has experienced several historical episodes of migrating

Table 1.1: The most recent earthquake sequence along the NAF

Event	Moment magnitude	Fatalities
1939 Erzincan	7.9	32,962
1942 NiksarErbaa	6.9	~3,000
1943 TosyaLadik	7.7	2,824
1944 BoluGerede	7.5	3,959
1949 Karliova	7.1	320
1951 Kursunlu	6.9	50
1957 Abant	6.8	52
1966 Varto	6.6	2,394
1967 Mudurnu Valley	7.1	86
1992 Erzincan	6.5	~550
1999 Izmit	7.4	17,480
1999 Düzce	7.2	894

earthquake sequences (Figure 1.11) (*Stein et al., 1997*). Large earthquakes progressed ~250 km eastwards during 967, 1035, and 1050 AD (*Ambraseys, 1970*). A sequence ruptured perhaps ~700 km of the fault during 1650 to 1668 (*Ambraseys and Finkel, 1995*). It is not yet clear why the NAF exhibits such propensity to progressive failure. *Stein et al. (1997)* suggest that the behaviour is a product of the fault's simple, straight geometry, which makes for efficient transfer of stress and its general isolation from other faults, which minimizes stress transferred between the North Anatolian and competing faults.

1.5.2 Fault slip rates and locking depths

Various attempts have been made at estimating the quaternary slip rate across the NAF. Figure 1.12 shows a compilation of published estimates for the NAF. The horizontal extent of each measurements corresponds to the spatial extent of the data used to make an average estimate of the slip rate. For example, some of the geodetic (red) measurements are an average slip rate for the entire fault. Estimates with no error bars are fixed values. It is clear that there is significant scatter in published slip rates along the fault with the greatest scatter in the western section where the NAF splits into multiple segments. However, most estimates of the fault slip rate fall within 15-32 mm/yr.

One of the first attempts at quantifying the slip rate across the fault was by *Jackson and McKenzie (1988)* who used seismic slip estimates to determine the NAF slip rate to be about 31 mm/yr.

Hubert-Ferrari et al. (2002) conducted a field study of offset features associated with small rivers across the fault and determined a Holocene slip rate of 18 mm/yr which confirms slip rate estimates deduced from ^{14}C dating of offset stream terraces.

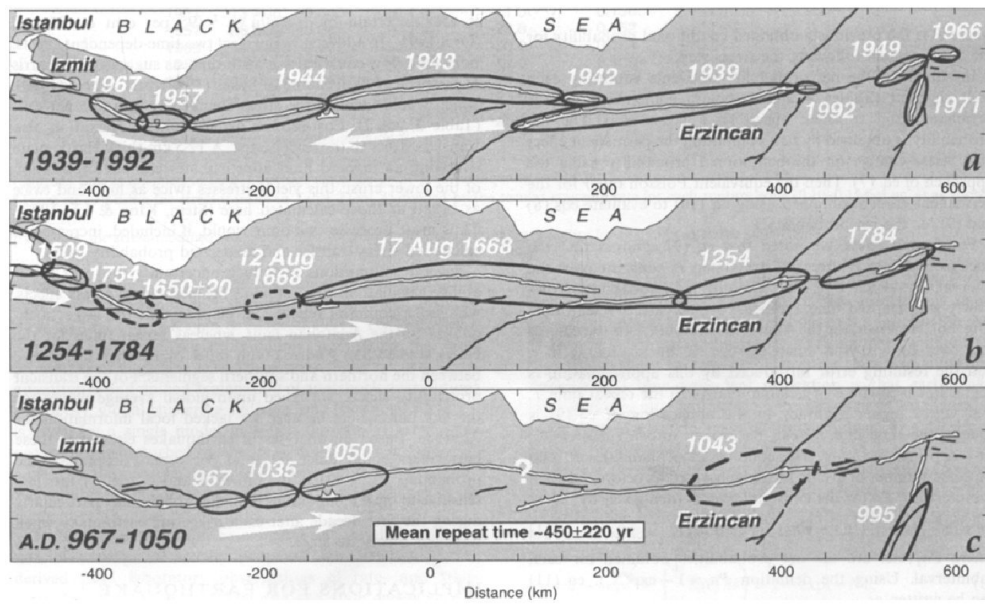


Figure 1.11: Historical earthquake sequences along the NAF. Figure from *Stein et al. (1997)*.

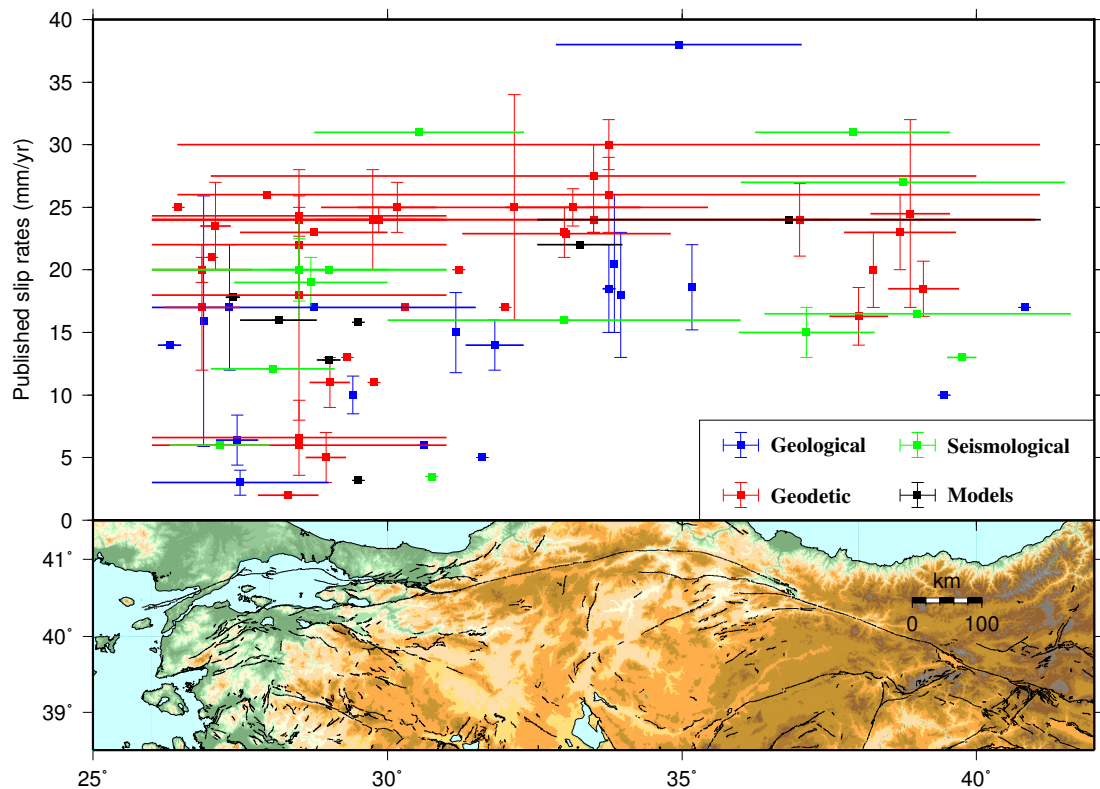


Figure 1.12: Published slip rate estimates along the North Anatolian Fault (data in Table A.1). Geological estimates (blue) are mostly from offset geological features or trench studies while geodetic estimates (red) are generally from inversions of GNSS and/or InSAR data and seismological estimates (green) are from slip vector studies of large earthquakes along the NAF. Black points are estimates from geodynamic or visco-elastic models. The horizontal bar indicates the data extent used to produce each slip rate estimate.

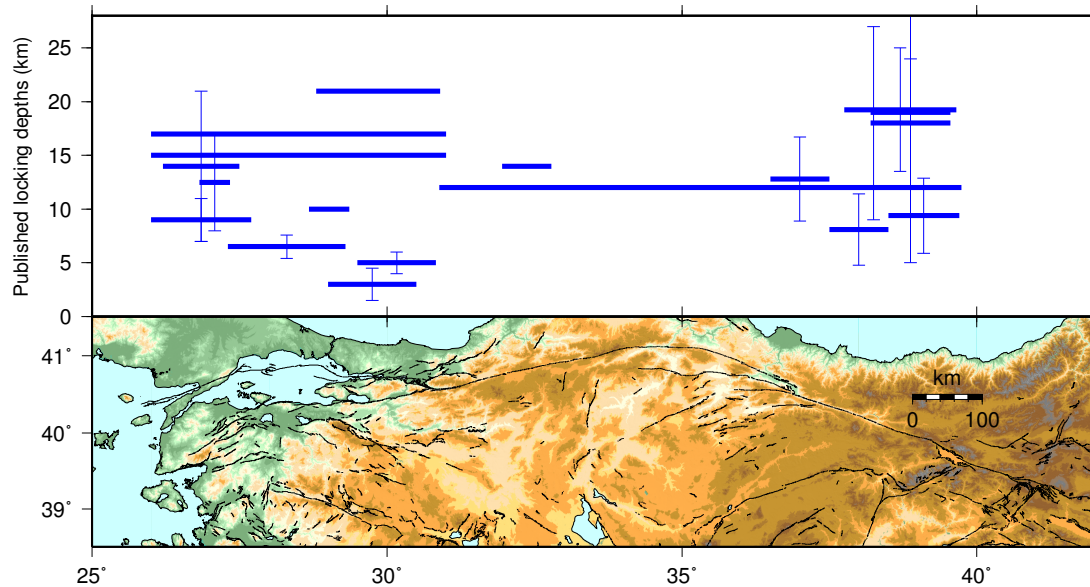


Figure 1.13: Published locking depth estimates along the NAF (data in Table A.2). Most estimates are using geodetic measurements of surface velocities (GNSS and/or InSAR), which are inverted for the locking depth using the screw dislocation model of *Savage and Burford (1973)*.

Kozaci et al. (2007), *Kozaci et al. (2009)* dated offset river terraces using cosmogenic radionuclides yielding a Holocene slip rate of 20.5 ± 5.5 mm/yr for the central part of the NAF.

Most previous estimates of the locking depth are from inversions of geodetic data with estimates ranging between 3 km and 21 km (Figure 1.13).

One of the key aims of my thesis is to make estimates of the variation in fault slip rate and locking depth along the North Anatolian Fault using a consistent dataset and method.

1.6 Interferometric Synthetic Aperture Radar (InSAR)

Before the early 1990s and the onset of space based Synthetic Aperture Radar (SAR) measurements, most investigations of surface velocity fields were made using a sparse network of Global Navigation Satellite System (GNSS) measurements, the most popular being the U.S. based Global Positioning System (GPS). However, even the most dense network of GNSS stations (~ 20 km station spacing in Japan) cannot match the pixel resolution achievable by InSAR, which has a spatial resolution of ~ 30 m (for C-band radar measurements).

For a detailed description of InSAR I refer the reader to *Rosen et al. (2000)*, *Hanssen (2001)*, *Ferretti et al. (2007)*. Below I will only provide a brief summary of the key processing steps and challenges in producing ground displacements maps using this technique.

InSAR refers to the phase difference between two Synthetic Aperture Radar (SAR) acquisitions over the same region, which were acquired at different times. The radar signal, as recorded at the antenna for each acquisition, has two components: the amplitude, a measure of the intensity of the returned radar waves, and the phase. This information is encoded as a series of complex numbers, Z :

$$Z = Ae^{i\phi} \quad (1.5)$$

where A is the amplitude and ϕ the phase component.

In general, the first acquisition is referred to as the master, while the second acquisition is the slave. Prior to InSAR computation, the slave SAR images need to be aligned with that of the master. This is achieved through a two-step coregistration procedure (e.g. [Brown, 1992](#), [Hanssen, 2001](#)). The first step involves a coarse-coregistration where large correlation windows are used to estimate the slave image translation offsets with respect to the master to within a few pixels. This is followed by a fine-coregistration in which the slave is resampled to the master grid using subpixel offset estimation and a polynomial transformation.

To extract the change in phase due to surface displacements the phase contribution from a flat-earth and terrain elevation changes need to be accounted for (e.g. [Hanssen, 2001](#)). The flat-earth refers to the phase signal introduced from a reference global ellipsoid such as WGS84 or a locally best fitting ellipsoid such as Bessel. It is estimated using the precise satellite orbit information and the formulation of the reference surface. Phase changes introduced by changes in viewing geometry between the master and slave are also accounted for by radar-coding a Digital Terrain Model (DEM), e.g. from the Shuttle Radar Topography Mission (SRTM) ([Farr et al., 2007](#)), and combining this with the satellite viewing geometry to calculate the phase signal related to a change in elevation. The interferogram formation step involves a multiplication between the master and the complex conjugate of the slave once these corrections have been made.

Several interferogram processors are available that perform the steps described above, such as ROI-PAC ([Rosen et al., 2004](#)) (now superseded by ISCE ([Gurrola et al., 2010](#))), GAMMA and DORIS ([Kampes et al., 2003](#)). For the InSAR processing in my thesis I employ the DORIS software package.

Several important challenges remain in the widespread uptake of InSAR: (1) decorrelation noise in interferograms, (2) delays caused by changes in atmospheric properties between master and slave acquisition (e.g. [Zebker et al., 1997](#), [Bekaert et al., 2015a](#)), and (3) phase unwrapping.

In the following sections I briefly explain each of these challenges, and the ways in which it is possible to address them.

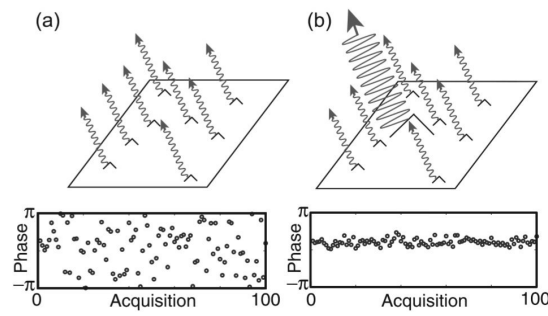


Figure 1.14: Simulation of the phase for (a) a distributed scatterer pixel, and (b) a Persistent Scatterer (PS) pixel. For the PS pixel, a dominant scatterer over time results in a stable phase over time. Figure from *Hooper et al. (2007)*.

1.6.1 Decorrelation noise

Decorrelation noise in radar interferograms is introduced by a change in satellite acquisition geometry and surface scattering properties between the master and slave acquisitions (*Zebker and Villasenor, 1992*). This can be reduced by applying new state-of-the-art InSAR time series methods that are typically split into Persistent Scatterer methods (e.g. *Ferretti et al., 2001, Perissin and Ferretti, 2007, Hooper et al., 2007*) and Small Baseline methods (e.g. *Berardino et al., 2002, Lanari et al., 2004, Biggs et al., 2007, Hooper, 2008*).

These two processing methods rely on the exploitation of resolution elements on the ground with two different end-member scattering properties. The persistent scatterer approach is optimised for resolution cells containing a single point scatterer, whereas small baseline methods are optimised for resolution cells containing a distribution of scatterers (Figure 1.14). Recently, methods have been developed that take advantage of both types of scattering (*Ferretti et al., 2011, Hooper, 2008*). These methods have been used to measure mean velocities and displacement time series due to volcanic deformation, land subsidence and tectonic motion associated with faults.

Throughout my thesis, I apply the Stanford Method for Persistent Scatterers (StaMPS) time series processing software (*Hooper, 2008, Hooper et al., 2012*), which takes advantage of the spatial correlation between pixels and does not impose a temporal deformation model when identifying targets with stable phase characteristics through time. The StaMPS software selects only those pixels that have stable phase noise characteristics in time, and uses this subset to compute velocities and time series.

I employ a combination of the persistent scatterer (PS) and the small baseline processing strategies of StaMPS. The small baseline interferograms for each of the tracks processed for this thesis were chosen to reduce decorrelation noise by minimising the time difference between acquisition dates (the temporal baseline) and the spatial separation of the satellite orbits (the perpendicular baseline).

1.6.2 Atmospheric noise

The spatial and temporal variations in tropospheric humidity, pressure and temperature between the master and slave acquisitions is often the largest source of error in radar interferograms (e.g. *Doin et al.*, 2009, *Walters et al.*, 2013, *Jolivet et al.*, 2014, *Bekaert et al.*, 2015a).

These atmospheric phase delays result from the combined effects of turbulent mixing in the atmosphere and stratification of the lower troposphere (e.g. *Hanssen*, 2001, *Doin et al.*, 2009). Many previous studies have shown that the turbulent atmospheric delay patterns are generally random in space and time, and can be reduced by temporal filtering long time series of Synthetic Aperture Radar (SAR) measurements (e.g. *Ferretti et al.*, 2001, *Berardino et al.*, 2002, *Hooper et al.*, 2007, *Hetland et al.*, 2012). On the other hand, *Doin et al.* (2009) and *Jolivet et al.* (2014) showed that phase delays due to stratified tropospheric conditions, if not accounted for, can result in a long-term bias in estimates of surface deformation, particularly when seasonal oscillations are not well sampled in time.

There are numerous approaches available to reduce the tropospheric noise contribution to radar interferograms. (*Bekaert et al.*, 2015c) showed that the best corrections are achieved when using multi-spectral observations of the troposphere, e.g. from the Medium Resolution Imaging Spectrometer (MERIS) onboard the Envisat satellite or the Moderate Resolution Imaging Spectroradiometer (MODIS) on the Terra and Aqua satellites. However these measurements are limited to periods with cloud free conditions, limiting the data available for the time series calculations (e.g. *Li et al.*, 2009, *Walters et al.*, 2013). Other researchers have used GNSS zenith delay measurements to constrain tropospheric delays (e.g. *Williams et al.*, 1998, *Onn and Zebker*, 2006), which requires a relatively dense network of GNSS stations in order to accurately map the spatial pattern in atmospheric delays. Tropospheric corrections can also be calculated using auxiliary information from global atmospheric models. Based on the reanalysis of global meteorological data, these models provide estimates of atmospheric variables, including temperature, water vapour, partial pressure, and geopotential height of pressure levels, on a regular spatial grid (global or regional) at regular time steps. These variables are then used to compute synthetic delay maps and directly correct for tropospheric delays in interferograms.

For all interferograms produced in my thesis I estimated the phase delay due to the atmosphere using the ERA-Interim global atmospheric model reanalysis product (*Dee et al.*, 2011) obtained from the European Centre for Medium-Range Weather Forecasts (ECMWF). The ERA-Interim product provides atmospheric information at approximately 80 km spatial resolution on 60 vertical levels from the surface up to 0.1 hPa every 12 hours. I interpolate the atmospheric variables to the InSAR pixel locations and SAR acquisition times and estimate the radar delay caused by these atmospheric

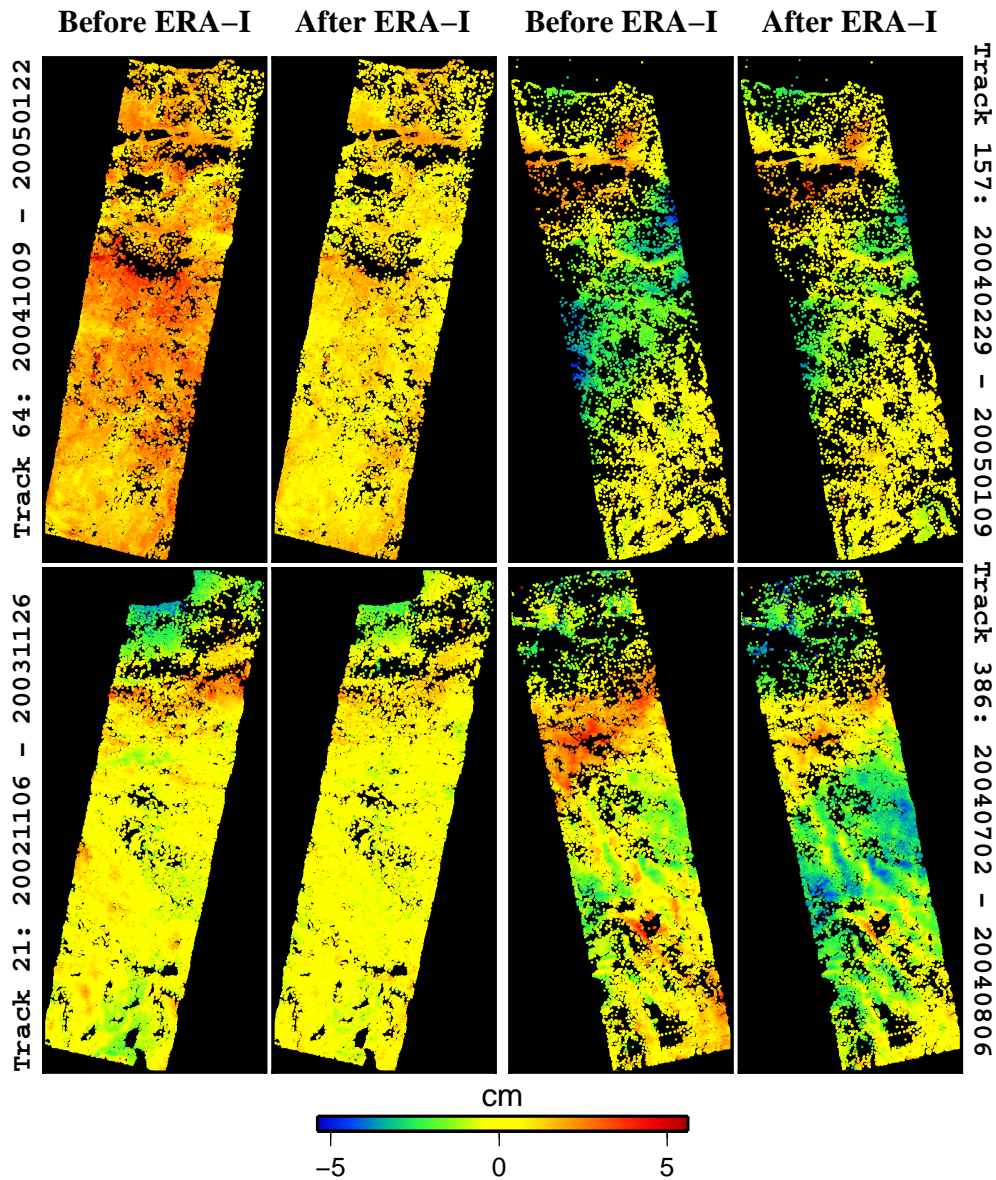


Figure 1.15: Four examples of interferograms before and after the ERA-I atmospheric correction. The source of each interferogram (Envisat track number and date span) is shown in vertical on the side. From a visual inspection it is clear that the application of a ERA-I weather model correction for the troposphere results in a decrease in variance across each interferogram. Figure from [Hussain et al. \(2016\)](#).

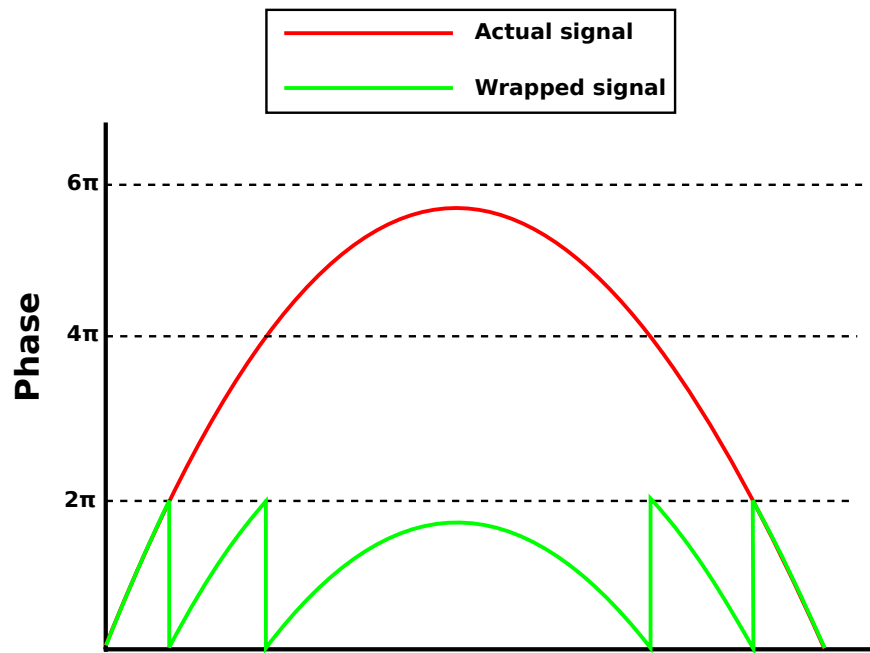


Figure 1.16: A simple schematic of the 1D phase unwrapping problem. The interferometric phase is wrapped modulo 2π (green line). The unwrapping process involves adding arbitrary integer multiples of 2π to the wrapped phase to reproduce the real continuous signal (red line).

conditions and remove this from each interferogram (e.g. Figure 1.15), implementing the correction using the TRAIN (Toolbox for Reducing Atmospheric InSAR Noise) software toolbox for Matlab (*Bekaert et al., 2015c*).

1.6.3 Phase unwrapping

Phase unwrapping is the process of recovering continuous phase values from phase data that are measured modulo 2π radians (wrapped data) (*Ghiglia and Pritt, 1998*) (Figure 1.16). Original 2D phase unwrapping algorithms unwrapped the phase of each individual interferogram in space independently (e.g. *Goldstein et al., 1988*, *Costantini, 1998*, *Zebker and Lu, 1998*). However, a time series of selected interferogram pixels can be considered a 3D data set, the third dimension being that of time. *Hooper and Zebker (2007)* showed that treating the unwrapping problem as one 3D problem as opposed to a series of 2D problems leads to an improvement in the accuracy of the solution in a similar way to which 2D unwrapping provides an improvement over one-dimensional spatial methods.

Fully 3D phase-unwrapping algorithms commonly assume that the phase difference between neighbouring pixels is generally less than half a phase cycle (2π radians) in all dimensions (*Hooper and Zebker, 2007*). However, due to atmospheric delays, InSAR signals are effectively uncorrelated in time over long arcs, violating this assumption. Other unwrapping algorithms require the assumption of a temporal parametric func-

tion, such as a linear phase evolution in time (*Ferretti et al., 2001*), to unwrap the phase signals.

The standard unwrapping algorithm used in the Stanford Method for Persistent Scatterers (StaMPS) software (*Hooper, 2010*) uses the actual phase evolution in time to guide unwrapping in the spatial dimension without assuming a particular temporal evolution model. The phase difference between nearby pixels (double-difference phase) is filtered in time to give an estimate of the unwrapped displacement phase for each satellite acquisition and an estimate of the phase noise. This is used to construct probability density functions for each unwrapped double-difference phase in every interferogram. An efficient algorithm (SNAPHU *Chen and Zebker (2000, 2001)*) then searches for the solution in space that maximises the total joint probability, i.e. minimises the total ‘cost’.

For a connected network of small baseline interferograms, the phase-unwrapping of individual interferograms can be checked for network consistency by summing the phase around closed interferometric loops (*Pepe and Lanari, 2006, Biggs et al., 2007*). In the standard unwrapping approach used in StaMPS, any interferograms identified to have large unwrapping errors are removed from the small baseline network, which can result in loss of information and/or reduction in network redundancy. Note that some other InSAR practitioners (e.g. *Biggs et al., 2007, Wang et al., 2009, Walters et al., 2011*) generally do not drop badly unwrapped interferograms, but attempt to correct unwrapping errors by manually adding integer multiples of 2π to badly unwrapped regions of pixels. However, this is a time consuming process.

In Chapter 3 of my thesis I describe a new iterative unwrapping procedure that I developed during my PhD (*Hussain et al., 2016 in revision*). For each iteration, this method identifies pixels unwrapped correctly in the previous iteration and applies a high cost to changing the phase difference between these pixels in the next iteration. In this way, the iterative unwrapping method uses the error-free pixels as a guide to unwrapping the regions that contained unwrapping errors in previous iterations.

1.7 Aims and objectives

Previous investigations of interseismic deformation along the the North Anatolian Fault have focused on isolated sections of the fault with most studies based on the eastern and western ends of the fault. The spatial distribution of GNSS stations throughout Turkey is variable, but overall the network is good with station separations between ~ 10 km and ~ 100 km (Figure 1.17).

Interferometric Synthetic Aperture Radar (InSAR) can be used to produce measurements of surface displacements at an even higher resolution. Where good coherence is maintained InSAR can provide an observation every ~ 30 m, enabling us to investigate the detailed spatial distribution of surface deformation along the NAF, which is

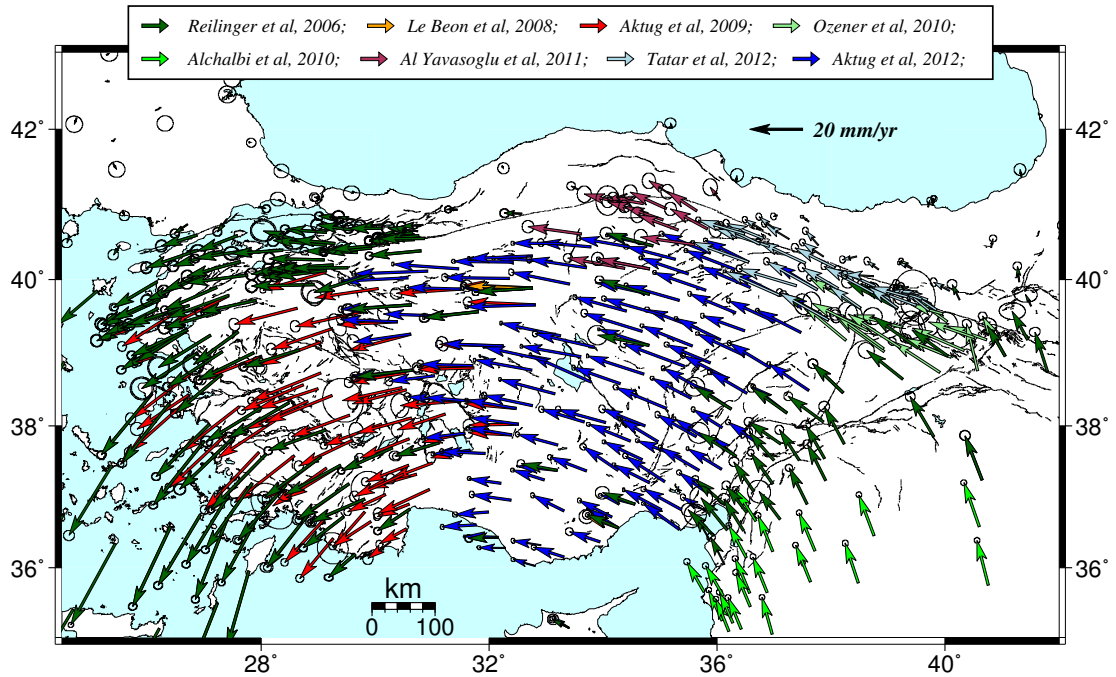


Figure 1.17: The GNSS horizontal velocity field over Turkey in a Eurasia-fixed reference frame. The vectors are colour coded by the original publication the data were gathered from.

not possible with GNSS alone.

The overall aim of my thesis is to produce a high resolution velocity field for the entire continental expression of the NAF, investigate spatial variations in interseismic strain accumulation along the fault and use this to investigate the pattern of strain accumulation during the earthquake cycle. To enable this, my specific objectives are:

1. Develop a more robust method for unwrapping InSAR measurements that can correct spatial unwrapping errors.
2. Investigate postseismic fault creep after the 1999 Izmit earthquake and discuss the implications for the shallow slip deficit.
3. Investigate the fault creep and variation in fault slip rate on the central section of the NAF.
4. Combine all InSAR measurements with published GNSS velocities to produce a 3D velocity field for the NAF and investigate the spatial variation in strain accumulation along the fault.
5. Use my estimates of strain rates with the timing of large earthquakes on the NAF to understand earthquake cycle deformation on major continental transform faults.

1.8 Thesis roadmap

In **Chapter 2**, I investigate the spatial distribution and temporal behaviour of post-seismic fault creep after the 1999 Izmit earthquake (published as [Hussain et al. \(2016\)](#)). The investigation is an improvement on previous work in this region, which only used satellite data from a single look direction. I show that this has biased estimates of fault creep. I also show that a region encompassing the Adapazari basin is subsiding at a steady rate during the observation period. I end this chapter discussing the temporal behaviour of postseismic fault creep and its implications for the shallow coseismic slip deficit after the Izmit earthquake. This chapter supports the 2nd objective set within my thesis.

In **Chapter 3**, I develop a new unwrapping algorithm that iteratively detects and corrects spatial unwrapping errors in our InSAR measurements. I investigate the spatial distribution of fault slip rate along the central section of the NAF, a region of GNSS scarcity (Figure 1.17). Previous work in this region have mainly just focused on the fault creep. I also investigate the spatial distribution of fault creep along this segment of the NAF utilising data from both ascending and descending satellite geometries. This chapter supports the 1st and 3rd objectives set within my thesis. The work in this chapter has been through peer-review as [Hussain et al. \(2016 in revision\)](#).

In **Chapter 4**, I combine all my InSAR measurements to create the first high resolution velocity field of the entire continental expression of the NAF. I combine the line-of-sight velocities with GNSS measurements to calculate the east-west and vertical components of motion and use simple elastic dislocation models to estimate the fault slip rate and locking depth along the fault. I show that the strain rate does not vary significantly with the time since the last earthquake, as predicted by simple viscoelastic earthquake cycle models. I discuss the implications of this observation and end the chapter with a discussion of the spatial variation in slip rate and locking depth along the NAF and its implications for “block-like” motion of central Turkey. The work in this chapter is written as a draft paper and supports the 4th and 5th objectives set within my thesis.

In **Chapter 5**, I summarise the key findings of each of my results chapters and discuss their broader implications. I expand on my locking depth analysis from Chapter 4 to a global dataset and discuss the implications for general earthquake cycle deformation for continental strike-slip faults. I suggest possible methods to automatically detect fault creep on strike-slip faults and discuss some of the opportunities and challenges that might arise with the wealth of data from the European Space Agency’s new Sentinel-1 radar satellite constellation.

References

- Aktuğ, B., E. Parmaksız, M. Kurt, O. Lenk, A. Kılıçoğlu, M. A. Gürdal, and S. Özdemir (2013), Deformation of Central Anatolia: GPS implications, *Journal of Geodynamics*, 67, 78–96. [1](#)
- Ambraseys, N. (2002), The seismic activity of the Marmara Sea region over the last 2000 years, *Bulletin of the Seismological Society of America*, 92(1), 1–18. [1.5.1](#)
- Ambraseys, N. N. (1970), Some characteristic features of the Anatolian fault zone, *Tectonophysics*, 9(2), 143–165. [1.3](#), [1.5.1](#)
- Ambraseys, N. N. N., and C. F. Finkel (1995), *Seismicity of Turkey and Adjacent Areas: A Historical Review, 1500-1800*, MS Eren. [1.5.1](#)
- Armijo, R., B. Meyer, S. Navarro, G. King, and A. Barka (2002), Asymmetric slip partitioning in the Sea of Marmara pull-apart: a clue to propagation processes of the North Anatolian Fault?, *Terra Nova*, 14(2), 80–86. [1.5](#)
- Atakan, K., A. Ojeda, M. Meghraoui, A. A. Barka, M. Erdik, and A. Bodare (2002), Seismic hazard in Istanbul following the 17 August 1999 Izmit and 12 November 1999 Düzce earthquakes, *Bulletin of the Seismological Society of America*, 92(1), 466–482. [1.5.1](#)
- Avouac, J.-P. (2015), From geodetic imaging of seismic and aseismic fault slip to dynamic modeling of the seismic cycle, *Annual Review of Earth and Planetary Sciences*, 43(1), 233–271, doi:[10.1146/annurev-earth-060614-105302](#). [1.3](#)
- Barbot, S., Y. Hamiel, and Y. Fialko (2008), Space geodetic investigation of the coseismic and postseismic deformation due to the 2003 Mw 7.2 Altai earthquake: Implications for the local lithospheric rheology, *Journal of Geophysical Research: Solid Earth*, 113(B3). [1.1.2](#)
- Barbot, S., N. Lapusta, and J.-P. Avouac (2012), Under the hood of the earthquake machine: Toward predictive modeling of the seismic cycle, *Science*, 336(6082), 707–710. [1.2](#)
- Barka, A. (1996), Slip distribution along the North Anatolian Fault associated with the large earthquakes of the period 1939 to 1967, *The Bulletin of the Seismological Society of America*, 86, 1238–1254. [1](#), [1.5.1](#)
- Bekaert, D., R. Walters, T. Wright, A. Hooper, and D. Parker (2015c), Statistical comparison of InSAR tropospheric correction techniques, *Remote Sensing of Environment*, 170, 40–47, doi:[10.1002/2014JB011557](#). [1.6.2](#), [1.6.2](#)
- Bekaert, D. P. S., A. Hooper, and T. J. Wright (2015a), A spatially variable power-law tropospheric correction technique for InSAR data, *Journal of Geophysical Research (Solid Earth)*, 120, 1345–1356, doi:[10.1002/2014JB011558](#). [1.6](#), [1.6.2](#)
- Berardino, P., G. Fornaro, R. Lanari, and E. Sansosti (2002), A new algorithm for surface deformation monitoring based on small baseline differential SAR interferograms, *Geoscience and Remote Sensing, IEEE Transactions on*, 40(11), 2375–2383. [1.6.1](#), [1.6.2](#)

- Biggs, J., E. Bergman, B. Emmerson, G. J. Funning, J. Jackson, B. Parsons, and T. J. Wright (2006), Fault identification for buried strike-slip earthquakes using InSAR: The 1994 and 2004 Al Hoceima, Morocco earthquakes, *Geophysical Journal International*, *166*(3), 1347–1362. [1.1.1](#)
- Biggs, J., T. Wright, Z. Lu, and B. Parsons (2007), Multi-interferogram method for measuring interseismic deformation: Denali Fault, Alaska, *Geophysical Journal International*, *170*(3), 1165–1179, doi:[10.1111/j.1365-246X.2007.03415.x](#). [1.6.1](#), [1.6.3](#)
- Bourne, S., T. Arnadóttir, J. Beavan, D. Darby, P. England, B. Parsons, R. Walcott, and P. Wood (1998), Crustal deformation of the Marlborough fault zone in the South Island of New Zealand: geodetic constraints over the interval 1982–1994, *Journal of Geophysical Research: Solid Earth*, *103*(B12), 30,147–30,165. [1.1.3](#)
- Brown, L. G. (1992), A survey of image registration techniques, *ACM computing surveys (CSUR)*, *24*(4), 325–376. [1.6](#)
- Bürgmann, R., and G. Dresen (2008), Rheology of the lower crust and upper mantle: Evidence from rock mechanics, geodesy, and field observations, *Annual Review of Earth and Planetary Sciences*, *36*(1), 531. [1.1.2](#)
- Bürgmann, R., D. Schmidt, R. M. Nadeau, M. d’Alessio, E. Fielding, D. Manaker, T. V. McEvilly, and M. H. Murray (2000), Earthquake potential along the Northern Hayward Fault, California, *Science*, *289*, 1178–1182, doi:[10.1126/science.289.5482.1178](#). [1.3](#)
- Bürgmann, R., S. Ergintav, P. Segall, E. H. Hearn, S. McClusky, R. E. Reilinger, H. Woith, and J. Zschau (2002b), Time-dependent distributed afterslip on and deep below the Izmit earthquake rupture, *Bulletin of the Seismological Society of America*, *92*(1), 126–137. [1.1.2](#), [1.2](#), [1.4](#), [1.9](#)
- Cakir, Z., S. Ergintav, H. Ozener, U. Dogan, A. M. Akoglu, M. Meghraoui, and R. Reilinger (2012), Onset of aseismic creep on major strike-slip faults, *Geology*, *40*, 1115–1118, doi:[10.1130/G33522.1](#). [1.3](#)
- Cetin, E., Z. Cakir, M. Meghraoui, S. Ergintav, and A. M. Akoglu (2014), Extent and distribution of aseismic slip on the Ismetpasa segment of the North Anatolian Fault (Turkey) from persistent scatterer InSAR, *Geochemistry, Geophysics, Geosystems*, *15*, 2883–2894, doi:[10.1002/2014GC005307](#). [1.3](#)
- Champenois, J., B. Fruneau, E. Pathier, B. Deffontaines, K.-C. Lin, and J.-C. Hu (2012), Monitoring of active tectonic deformations in the Longitudinal Valley (Eastern Taiwan) using persistent scatterer InSAR method with ALOS PALSAR data, *Earth and Planetary Science Letters*, *337*, 144–155, doi:[10.1016/j.epsl.2012.05.025](#). [1.3](#)
- Chen, C. W., and H. A. Zebker (2000), Network approaches to two-dimensional phase unwrapping: Intractability and two new algorithms, *JOSA A*, *17*(3), 401–414. [1.6.3](#)
- Chen, C. W., and H. A. Zebker (2001), Two-dimensional phase unwrapping with use of statistical models for cost functions in nonlinear optimization, *JOSA A*, *18*(2), 338–351. [1.6.3](#)
- Costantini, M. (1998), A novel phase unwrapping method based on network programming, *Geoscience and Remote Sensing, IEEE Transactions on*, *36*(3), 813–821. [1.6.3](#)
- Dee, D. P., S. M. Uppala, A. J. Simmons, P. Berrisford, P. Poli, S. Kobayashi, U. Andrae, M. A. Balmaseda, G. Balsamo, P. Bauer, P. Bechtold, A. C. M. Beljaars, L. van de Berg, J. Bidlot, N. Bormann, C. Delsol, R. Dragani, M. Fuentes, A. J. Geer, L. Haimberger, S. B. Healy, H. Hersbach, E. V. Hólm, L. Isaksen, P. Kállberg, M. Köhler, M. Matricardi, A. P. McNally, B. M. Monge-Sanz, J.-J. Morcrette, B.-K. Park, C. Peubey, P. de Rosnay, C. Tavolato, J.-N. Thépaut, and F. Vitart (2011),

- The ERA-Interim reanalysis: configuration and performance of the data assimilation system, *Quarterly Journal of the Royal Meteorological Society*, 137, 553–597, doi:[10.1002/qj.828](https://doi.org/10.1002/qj.828). 1.6.2
- Dieterich, J. (1994), A constitutive law for rate of earthquake production and its application to earthquake clustering, *Journal of Geophysical Research: Solid Earth*, 99(B2), 2601–2618. 1.5.1
- Doin, M.-P., C. Lasserre, G. Peltzer, O. Cavali, and C. Doubre (2009), Corrections of stratified tropospheric delays in SAR interferometry: Validation with global atmospheric models, *Journal of Applied Geophysics*, 69(1), 35 – 50, doi:<http://dx.doi.org/10.1016/j.jappgeo.2009.03.010>. 1.6.2
- Dolan, J. F., and B. D. Haravitch (2014), How well do surface slip measurements track slip at depth in large strike-slip earthquakes? The importance of fault structural maturity in controlling on-fault slip versus off-fault surface deformation, *Earth and Planetary Science Letters*, 388, 38–47. 1.4
- Ergintav, S., S. McClusky, E. Hearn, R. Reilinger, R. Cakmak, T. Herring, H. Ozener, O. Lenk, and E. Tari (2009), Seven years of postseismic deformation following the 1999, M = 7.4 and M = 7.2, Izmit-Düzce, Turkey earthquake sequence, *Journal of Geophysical Research (Solid Earth)*, 114, B07403, doi:[10.1029/2008JB006021](https://doi.org/10.1029/2008JB006021). 1.2
- Farr, T. G., P. A. Rosen, E. Caro, R. Crippen, R. Duren, S. Hensley, M. Kobrick, M. Paller, E. Rodriguez, L. Roth, D. Seal, S. Shaffer, J. Shimada, J. Umland, M. Werner, M. Oskin, D. Burbank, and D. Alsdorf (2007), The shuttle radar topography mission, *Reviews of Geophysics*, 45, RG2004, doi:[10.1029/2005RG000183](https://doi.org/10.1029/2005RG000183). 1.6
- Ferretti, A., C. Prati, and F. Rocca (2001), Permanent scatterers in SAR interferometry, *Geoscience and Remote Sensing, IEEE Transactions on*, 39(1), 8–20. 1.6.1, 1.6.2, 1.6.3
- Ferretti, A., A. Monti-Guarnieri, C. Prati, and F. Rocca (2007), *InSAR Principles: Guidelines for SAR Interferometry Processing and Interpretation*, ESA TM-19, ESA Publications. 1.6
- Ferretti, A., A. Fumagalli, F. Novali, C. Prati, F. Rocca, and A. Rucci (2011), A new algorithm for processing interferometric data-stacks: SqueeSAR, *Geoscience and Remote Sensing, IEEE Transactions on*, 49(9), 3460–3470. 1.6.1
- Fialko, Y. (2004), Evidence of fluid-filled upper crust from observations of postseismic deformation due to the 1992 Mw7. 3 Landers earthquake, *Journal of Geophysical Research: Solid Earth*, 109(B8). 1.1.2, 1.1.2
- Fialko, Y., D. Sandwell, M. Simons, and P. Rosen (2005), Three-dimensional deformation caused by the Bam, Iran, earthquake and the origin of shallow slip deficit, *Nature*, 435(7040), 295–299. 1.4, 1.8
- Freed, A. M., R. Bürgmann, E. Calais, J. Freymueller, and S. Hreinsdóttir (2006), Implications of deformation following the 2002 Denali, Alaska, earthquake for postseismic relaxation processes and lithospheric rheology, *Journal of Geophysical Research: Solid Earth*, 111(B1). 1.1.2
- Funning, G. J., B. Parsons, and T. J. Wright (2007), Fault slip in the 1997 Manyi, Tibet earthquake from linear elastic modelling of InSAR displacements, *Geophysical Journal International*, 169(3), 988–1008. 1.1.1
- Ghiglia, D. C., and M. D. Pritt (1998), *Two-dimensional phase unwrapping: Theory, algorithms, and software*, vol. 4, Wiley New York. 1.6.3
- Goldstein, R. M., H. A. Zebker, and C. L. Werner (1988), Satellite radar interferometry: Two-dimensional phase unwrapping, *Radio science*, 23(4), 713–720. 1.6.3

- Gurrola, E., P. Rosen, G. Sacco, W. Szeliga, H. Zebker, M. Simons, D. Sandwell, P. Shanker, C. Wortham, and A. Chen (2010), Insar scientific computing environment, in *2010 American Geophysical Union Meeting*. 1.6
- Hanssen, R. F. (2001), *Radar interferometry: Data interpretation and error analysis*, vol. 2, Springer Science & Business Media. 1.6, 1.6, 1.6.2
- Hearn, E., S. McClusky, S. Ergintav, and R. Reilinger (2009), Izmit earthquake post-seismic deformation and dynamics of the North Anatolian Fault Zone, *Journal of Geophysical Research: Solid Earth*, 114(B8). 1.2
- Hearn, E. H., R. Bürgmann, and R. E. Reilinger (2002), Dynamics of Izmit earthquake postseismic deformation and loading of the Düzce earthquake hypocenter, *Bulletin of the Seismological Society of America*, 92(1), 172–193. 1.2
- Hetland, E., and B. Hager (2006), The effects of rheological layering on post-seismic deformation, *Geophysical Journal International*, 166(1), 277–292. 1.2, 1.2
- Hetland, E., P. Musé, M. Simons, Y. Lin, P. Agram, and C. DiCaprio (2012), Multiscale InSAR time series (MInTS) analysis of surface deformation, *Journal of Geophysical Research: Solid Earth*, 117(B2). 1.6.2
- Hooper, A. (2008), A multi-temporal InSAR method incorporating both persistent scatterer and small baseline approaches, *Geophysical Research Letters*, 35, L16302, doi:10.1029/2008GL034654. 1.6.1, 1.6.1
- Hooper, A. (2010), A statistical-cost approach to unwrapping the phase of insar time series, in *Proceeding of International Workshop on ERS SAR Interferometry, Frascati, Italy*, vol. 30. 1.6.3
- Hooper, A., and H. A. Zebker (2007), Phase unwrapping in three dimensions with application to insar time series, *JOSA A*, 24(9), 2737–2747. 1.6.3, 1.6.3
- Hooper, A., P. Segall, and H. Zebker (2007), Persistent scatterer interferometric synthetic aperture radar for crustal deformation analysis, with application to Volcán Alcedo, Galápagos, *Journal of Geophysical Research (Solid Earth)*, 112, B07407, doi:10.1029/2006JB004763. 1.14, 1.6.1, 1.6.2
- Hooper, A., D. Bekaert, K. Spaans, and M. Arıkan (2012), Recent advances in SAR interferometry time series analysis for measuring crustal deformation, *Tectonophysics*, 514, 1–13, doi:10.1016/j.tecto.2011.10.013. 1.6.1
- Hubert-Ferrari, A., A. Barka, E. Jacques, S. S. Nalbant, B. Meyer, R. Armijo, P. Tapponnier, and G. C. P. King (2000), Seismic hazard in the Marmara Sea region following the 17 August 1999 Izmit earthquake, *Nature*, 404, 269–273. 1.1.3
- Hubert-Ferrari, A., R. Armijo, G. King, B. Meyer, and A. Barka (2002), Morphology, displacement, and slip rates along the North Anatolian Fault, Turkey, *Journal of Geophysical Research: Solid Earth (1978–2012)*, 107(B10), ETG–9. 1.5.2
- Hubert-Ferrari, A., G. King, J. Van Der Woerd, I. Villa, E. Altunel, and R. Armijo (2009), Long-term evolution of the North Anatolian Fault: new constraints from its eastern termination, *Geological Society, London, Special Publications*, 311(1), 133–154. 1.5
- Hussain, E., T. J. Wright, R. J. Walters, D. Bekaert, A. Hooper, and G. A. Houseman (2016), Geodetic observations of postseismic creep in the decade after the 1999 izmit earthquake, turkey: Implications for a shallow slip deficit, *Journal of Geophysical Research: Solid Earth*, 121(4), 2980–3001. 1.15, 1.8
- Hussain, E., A. Hooper, T. J. Wright, R. J. Walters, and D. Bekaert (2016 in revision), Interseismic strain accumulation across the central north anatolian fault from iteratively unwrapped insar measurements, *Submitted*. 1.6.3, 1.8

- Jackson, J., and D. McKenzie (1984), Active tectonics of the Alpine/Himalayan belt between western Turkey and Pakistan, *Geophysical Journal*, *77*, 185–264, doi:10.1111/j.1365-246X.1984.tb01931.x. 1.1.1
- Jackson, J., and D. McKenzie (1988), The relationship between plate motions and seismic moment tensors, and the rates of active deformation in the Mediterranean and Middle East, *Geophysical Journal International*, *93*(1), 45–73. 1.5.2
- Johnson, K. M., G. E. Hilley, and R. Bürgmann (2007), Influence of lithosphere viscosity structure on estimates of fault slip rate in the Mojave region of the San Andreas fault system, *Journal of Geophysical Research: Solid Earth*, *112*(B7). 1.2
- Jolivet, R., C. Lasserre, M.-P. Doin, S. Guillaso, G. Peltzer, R. Dailu, J. Sun, Z.-K. Shen, and X. Xu (2012), Shallow creep on the Haiyuan fault (Gansu, China) revealed by SAR interferometry, *Journal of Geophysical Research: Solid Earth*, *117*(B6). 1.3
- Jolivet, R., P. S. Agram, N. Y. Lin, M. Simons, M.-P. Doin, G. Peltzer, and Z. Li (2014), Improving InSAR geodesy using global atmospheric models, *Journal of Geophysical Research: Solid Earth*, *119*(3), 2324–2341. 1.6.2
- Jolivet, R., M. Simons, P. Agram, Z. Duputel, and Z.-K. Shen (2015), Aseismic slip and seismogenic coupling along the central San Andreas Fault, *Geophysical Research Letters*, *42*(2), 297–306. 1.3
- Jonsson, S., P. Segall, R. Pedersen, and G. Björnsson (2003), Post-earthquake ground movements correlated to pore-pressure transients, *Nature*, *424*(6945), 179–183. 1.1.2
- Kagan, Y. Y., and D. D. Jackson (1991), Long-term earthquake clustering, *Geophysical Journal International*, *104*(1), 117–133. 1.5.1
- Kampes, B. M., R. F. Hanssen, and Z. Perski (2003), Radar interferometry with public domain tools, in *FRINGE 2003 Workshop, ESA Special Publication*, vol. 550, p. 10. 1.6
- Kaneko, Y., and Y. Fialko (2011), Shallow slip deficit due to large strike-slip earthquakes in dynamic rupture simulations with elasto-plastic off-fault response, *Geophysical Journal International*, *186*(3), 1389–1403. 1.4
- Kaneko, Y., Y. Fialko, D. T. Sandwell, X. Tong, and M. Furuya (2013), Interseismic deformation and creep along the central section of the North Anatolian Fault (Turkey): InSAR observations and implications for rate-and-state friction properties, *Journal of Geophysical Research (Solid Earth)*, *118*, 316–331, doi:10.1029/2012JB009661. 1.3
- Kasahara, K. (1981), *Earthquake mechanics*, Cambridge university press. 1.5.1
- Kenner, S. J., and P. Segall (2000), Postseismic deformation following the 1906 san francisco earthquake, *Journal of Geophysical Research: Solid Earth*, *105*(B6), 13,195–13,209. 1.2
- Ketin, I. (1948), Über die tektonisch-mechanischen Folgerungen aus den grossen anatolischen Erdbeben des letzten Dezenniums, *Geologische Rundschau*, *36*(1), 77–83. 1.5
- Ketin, I. (1957), Kuzey Anadolu deprem fayi, *ITU Dergisi*, *15*, 49–52. 1.5
- Kozaci, Ö., J. Dolan, R. Finkel, and R. Hartleb (2007), Late Holocene slip rate for the North Anatolian Fault, Turkey, from cosmogenic ³⁶Cl geochronology: Implications for the constancy of fault loading and strain release rates, *Geology*, *35*(10), 867–870. 1.5.2
- Kozaci, Ö., J. F. Dolan, and R. C. Finkel (2009), A late Holocene slip rate for the central North Anatolian fault, at Tahtaköprü, Turkey, from cosmogenic ¹⁰Be geochronology: Implications for fault loading and strain release rates, *Journal of Geophysical Research: Solid Earth (1978–2012)*, *114*(B1). 1.5.2

- Lanari, R., O. Mora, M. Manunta, J. J. Mallorquí, P. Berardino, and E. Sansosti (2004), A small-baseline approach for investigating deformations on full-resolution differential SAR interferograms, *Geoscience and Remote Sensing, IEEE Transactions on*, 42(7), 1377–1386. [1.6.1](#)
- Lapusta, N., and Y. Liu (2009), Three-dimensional boundary integral modeling of spontaneous earthquake sequences and aseismic slip, *Journal of Geophysical Research: Solid Earth*, 114(B9). [1.2](#)
- Lasserre, C., G. Peltzer, F. Crampé, Y. Klinger, J. Van Der Woerd, and P. Tapponnier (2005), Coseismic deformation of the 2001 Mw= 7.8 Kokoxili earthquake in Tibet, measured by synthetic aperture radar interferometry, *Journal of Geophysical Research: Solid Earth*, 110(B12). [1.4](#)
- Li, Z., E. Fielding, P. Cross, and R. Preusker (2009), Advanced InSAR atmospheric correction: MERIS/MODIS combination and stacked water vapour models, *International Journal of Remote Sensing*, 30(13), 3343–3363. [1.6.2](#)
- Mallet, R. (1862), Great Neapolitan earthquake of 1857 – the first principles of observational seismology, *Storia Geofisica Ambiente, Bologna*, 2, 399 and 3 foldout plates. [1.5](#)
- Manning, C., and S. Ingebritsen (1999), Permeability of the continental crust: Implications of geothermal data and metamorphic systems, *Reviews of Geophysics*, 37(1), 127–150. [1.4](#)
- Marone, C. (1998), Laboratory-derived friction laws and their application to seismic faulting, *Annual Review of Earth and Planetary Sciences*, 26(1), 643–696. [1.2](#), [1.4](#)
- Marone, C. J., C. Scholtz, and R. Bilham (1991), On the mechanics of earthquake afterslip, *Journal of Geophysical Research: Solid Earth (1978–2012)*, 96(B5), 8441–8452. [1.1.2](#)
- Massonnet, D., M. Rossi, C. Carmona, F. Adragna, G. Peltzer, K. Feigl, and T. Rabaute (1993), The displacement field of the Landers earthquake mapped by radar interferometry, *Nature*, 364(6433), 138–142. [1.1.1](#), [1.2](#), [1.1.3](#), [1.4](#)
- Masterlark, T., and H. F. Wang (2002), Transient stress-coupling between the 1992 Landers and 1999 Hector Mine, California, earthquakes, *Bulletin of the Seismological Society of America*, 92(4), 1470–1486. [1.1.2](#)
- Maurer, J., and K. Johnson (2014), Fault coupling and potential for earthquakes on the creeping section of the central San Andreas Fault, *Journal of Geophysical Research: Solid Earth*, 119(5), 4414–4428. [1.3](#)
- McKenzie, D. (1972), Active tectonics of the Mediterranean region, *Geophysical Journal International*, 30(2), 109–185. [1.1.1](#)
- Meade, B. J., Y. Klinger, and E. A. Hetland (2013), Inference of multiple earthquake-cycle relaxation timescales from irregular geodetic sampling of interseismic deformation, *Bulletin of the Seismological Society of America*, 103(5), 2824–2835. [1](#), [1.2](#)
- Mogi, K. (1985), Earthquake prediction. [1.5.1](#)
- Moore, M. A. (1999), Crustal deformation in the southern new zealand region, Ph.D. thesis, University of Oxford. [1.1.3](#)
- Nason, R. D. (1973), Fault creep and earthquakes on the San Andreas fault, in *Proceedings of the Conference on Tectonic Problems of the San Andreas Fault System, Stanford Univ. Publ. Geol. Sci*, vol. 13, pp. 275–285. [1.3](#)
- Nikolaevskii, V., K. Basniev, A. Gorbunov, and G. Zotov (1970), Mechanics of saturated porous media (in russian), *Nedra, Moscow*, 335. [1.1.2](#)

- Nur, A., and G. Mavko (1974), Postseismic viscoelastic rebound, *Science*, *183*(4121), 204–206. [1.1.2](#)
- Onn, F., and H. Zebker (2006), Correction for interferometric synthetic aperture radar atmospheric phase artifacts using time series of zenith wet delay observations from a GPS network, *Journal of Geophysical Research: Solid Earth*, *111*(B9). [1.6.2](#)
- Parsons, T. (2004), Recalculated probability of M 7 earthquakes beneath the Sea of Marmara, Turkey, *Journal of Geophysical Research: Solid Earth*, *109*(B5), doi:[10.1029/2003JB002667](#). [1.5.1](#)
- Parsons, T., S. Toda, R. S. Stein, A. Barka, and J. H. Dieterich (2000), Heightened odds of large earthquakes near Istanbul: An interaction-based probability calculation, *Science*, *288*, 661–665, doi:[10.1126/science.288.5466.661](#). [1.5.1](#)
- Peltier, W. (1976), Glacial-isostatic adjustmentii. the inverse problem, *Geophysical Journal International*, *46*(3), 669–705. [1.1.2](#)
- Peltzer, G., P. Rosen, F. Rogez, and K. Hudnut (1996), Postseismic rebound in fault step-overs caused by pore fluid flow, *Science*, *273*(5279), 1202. [1.1.2](#), [1.2](#)
- Peltzer, G., P. Rosen, F. Rogez, and K. Hudnut (1998), Poroelastic rebound along the Landers 1992 earthquake surface rupture, *Journal of Geophysical Research*, *103*(B12), 30,131–30,145. [1.1.2](#)
- Peltzer, G., F. Crampé, S. Hensley, and P. Rosen (2001), Transient strain accumulation and fault interaction in the Eastern California shear zone, *Geology*, *29*(11), 975–978. [1.1.3](#)
- Pepe, A., and R. Lanari (2006), On the extension of the minimum cost flow algorithm for phase unwrapping of multitemporal differential SAR interferograms, *Geoscience and Remote Sensing, IEEE Transactions on*, *44*(9), 2374–2383. [1.6.3](#)
- Perissin, D., and A. Ferretti (2007), Urban-target recognition by means of repeated spaceborne SAR images, *Geoscience and Remote Sensing, IEEE Transactions on*, *45*(12), 4043–4058. [1.6.1](#)
- Pollitz, F. F. (2005), Transient rheology of the upper mantle beneath central alaska inferred from the crustal velocity field following the 2002 Denali earthquake, *Journal of Geophysical Research: Solid Earth*, *110*(B8). [1.2](#)
- Prescott, W. H., and A. Nur (1981), The accommodation of relative motion at depth on the San Andreas fault system in California, *Journal of Geophysical Research: Solid Earth*, *86*(B2), 999–1004. [1.1.3](#)
- Reid, H. F. (1910), *The mechanics of the earthquake*, vol. 2, Carnegie Institution of Washington. [1.1](#), [1.1.3](#)
- Reilinger, R., S. Ergintav, R. Bürgmann, S. McClusky, O. Lenk, A. Barka, O. Gurkan, L. Hearn, K. Feigl, R. Cakmak, et al. (2000), Coseismic and postseismic fault slip for the 17 August 1999, M= 7.5, Izmit, Turkey earthquake, *Science*, *289*(5484), 1519–1524. [1.9](#)
- Reilinger, R., S. McClusky, P. Vernant, S. Lawrence, S. Ergintav, R. Cakmak, H. Ozener, F. Kadirov, I. Guliev, R. Stepanyan, M. Nadariya, G. Hahubia, S. Mahmoud, K. Sakr, A. ArRajehi, D. Paradissis, A. Al-Aydrus, M. Prilepin, T. Guseva, E. Evren, A. Dmitrotsa, S. V. Filikov, F. Gomez, R. Al-Ghazzi, and G. Karam (2006), GPS constraints on continental deformation in the Africa-Arabia-Eurasia continental collision zone and implications for the dynamics of plate interactions, *Journal of Geophysical Research: Solid Earth*, *111*(B5), doi:[10.1029/2005JB004051](#). [1](#), [1.1.3](#)
- Rosen, P. A., S. Hensley, I. R. Joughin, F. K. Li, S. N. Madsen, E. Rodriguez, and R. M. Goldstein (2000), Synthetic aperture radar interferometry, *Proceedings of the IEEE*, *88*(3), 333–382. [1.6](#)

- Rosen, P. A., S. Hensley, G. Peltzer, and M. Simons (2004), Updated repeat orbit interferometry package released, *Eos, Transactions American Geophysical Union*, 85(5), 47–47, doi:[10.1029/2004EO050004](https://doi.org/10.1029/2004EO050004). 1.6
- Rousset, B., R. Jolivet, M. Simons, C. Lassarre, B. Riel, P. Milillo, Z. Cakir, and F. Renard (2016), An aseismic slip transient on the North Anatolian Fault, *Geophysical Research Letters*, p. 4, doi:[10.1002/2016GL068250](https://doi.org/10.1002/2016GL068250). 1.3
- Ryder, I., and R. Bürgmann (2008), Spatial variations in slip deficit on the central San Andreas Fault from InSAR, *Geophysical Journal International*, 175(3), 837–852. 1.4
- Ryder, I., B. Parsons, T. J. Wright, and G. J. Funning (2007), Post-seismic motion following the 1997 Manyi (Tibet) earthquake: InSAR observations and modelling, *Geophysical Journal International*, 169(3), 1009–1027. 1.1.2
- Savage, J. (2000), Viscoelastic-coupling model for the earthquake cycle, *Journal of Geophysical Research*, 105. 1.2, 1.7
- Savage, J., and J. Church (1974), Evidence for postearthquake slip in the Fairview Peak, Dixie Valley, and Rainbow Mountain fault areas of Nevada, *Bulletin of the Seismological Society of America*, 64(3-1), 687–698. 1.1.2
- Savage, J., and W. Prescott (1978), Asthenosphere readjustment and the earthquake cycle, *Journal of Geophysical Research: Solid Earth*, 83(B7), 3369–3376. 1.1.3, 1.2, 1.7
- Savage, J., and J. Svarc (1997), Postseismic deformation associated with the 1992 Mw = 7.3 Landers earthquake, southern California, *Journal of Geophysical Research: Solid Earth*, 102(B4), 7565–7577. 1.4
- Savage, J. C., and R. O. Burford (1973), Geodetic determination of relative plate motion in central California, *Journal of Geophysical Research*, 78, 832–845, doi:[10.1029/JB078i005p00832](https://doi.org/10.1029/JB078i005p00832). 1.4, 1.1.3, 1.5, 1.13
- Schmidt, D. A., R. Bürgmann, R. M. Nadeau, and M. D’Alessio (2005), Distribution of aseismic slip rate on the Hayward fault inferred from seismic and geodetic data, *Journal of Geophysical Research (Solid Earth)*, 110, B08406, doi:[10.1029/2004JB003397](https://doi.org/10.1029/2004JB003397). 1.3
- Scholz, C. (1988), *The critical slip distance for seismic faulting*, Nature Publishing Group. 1.1.2
- Scholz, C. H. (1998), Earthquakes and friction laws, *Nature*, 391(6662), 37–42. 1.2
- Scholz, C. H. (2002), *The mechanics of earthquakes and faulting*, Cambridge university press. 1.1.2
- Sengör, A., O. Tüysüz, C. Imren, M. Sakingç, H. Eyidogan, N. Görür, X. Le Pichon, and C. Rangin (2005), The North Anatolian fault: A new look, *Annu. Rev. Earth Planet. Sci.*, 33, 37–112. 1.5
- Simons, M., Y. Fialko, and L. Rivera (2002), Coseismic deformation from the 1999 Mw 7.1 Hector Mine, California, earthquake as inferred from InSAR and GPS observations, *Bulletin of the Seismological Society of America*, 92(4), 1390–1402. 1.4
- Smith, S. W., and M. Wyss (1968), Displacement on the San Andreas Fault subsequent to the 1966 Parkfield earthquake, *Bulletin of the Seismological Society of America*, 58(6), 1955–1973. 1.1.2
- Stein, R. S., A. A. Barka, and J. H. Dieterich (1997), Progressive failure on the North Anatolian Fault since 1939 by earthquake stress triggering, *Geophysical Journal International*, 128, 594–604, doi:[10.1111/j.1365-246X.1997.tb05321.x](https://doi.org/10.1111/j.1365-246X.1997.tb05321.x). 1.5.1, 1.5.1, 1.11

- Straub, C., H.-G. Kahle, and C. Schindler (1997), GPS and geologic estimates of the tectonic activity in the Marmara Sea region, NW Anatolia, *Journal of Geophysical Research: Solid Earth (1978–2012)*, *102*(B12), 27,587–27,601. [1.1.3](#)
- Takeuchi, C. S., and Y. Fialko (2012), Dynamic models of interseismic deformation and stress transfer from plate motion to continental transform faults, *Journal of Geophysical Research: Solid Earth*, *117*(B5). [1.2](#)
- Thatcher, W. (1975), Strain accumulation and release mechanism of the 1906 San Francisco earthquake, *Journal of Geophysical Research*, *80*(35), 4862–4872. [1.1.2](#)
- Thatcher, W. (1983), Nonlinear strain buildup and the earthquake cycle, *Journal of Geophysical Research*, *88*, 5893–5902. [1.1.2](#), [1.2](#), [1.4](#)
- Thatcher, W. (1993), The earthquake cycle and its role in the long-term deformation of the continental lithosphere, *Annali Di Geofisica*, *36*(2), 13–24. [1.1](#)
- Thomas, M. Y., J.-P. Avouac, J. Champenois, J.-C. Lee, and L.-C. Kuo (2014), Spatiotemporal evolution of seismic and aseismic slip on the Longitudinal Valley Fault, Taiwan, *Journal of Geophysical Research: Solid Earth*, *119*(6), 5114–5139. [1.3](#)
- Tse, S. T., and J. R. Rice (1986), Crustal earthquake instability in relation to the depth variation of frictional slip properties, *Journal of Geophysical Research*, *91*, 9452–9472, doi:[10.1029/JB091iB09p09452](https://doi.org/10.1029/JB091iB09p09452). [1.1.2](#), [1.4](#)
- Vaghri, A., and E. H. Hearn (2012), Can lateral viscosity contrasts explain asymmetric interseismic deformation around strike-slip faults?, *Bulletin of the Seismological Society of America*, *102*(2), 490–503. [1.2](#)
- Walters, R., R. Holley, B. Parsons, and T. Wright (2011), Interseismic strain accumulation across the North Anatolian Fault from Envisat InSAR measurements, *Geophysical research letters*, *38*(5). [1.6.3](#)
- Walters, R. J., J. R. Elliott, Z. Li, and B. Parsons (2013), Rapid strain accumulation on the Ashkabad Fault (Turkmenistan) from atmosphere-corrected InSAR, *Journal of Geophysical Research: Solid Earth*, *118*(7), 3674–3690. [1.6.2](#)
- Wang, H., T. Wright, and J. Biggs (2009), Interseismic slip rate of the northwestern Xianshuihe fault from InSAR data, *Geophysical Research Letters*, *36*(3). [1.6.3](#)
- Weertman, J., and J. R. Weertman (1964), *Elementary Dislocation Theory*, New York: Macmillan. Pub. [1.1.3](#)
- Wesson, R. L. (1988), Dynamics of fault creep, *Journal of Geophysical Research: Solid Earth*, *93*(B8), 8929–8951. [1.3](#)
- Williams, S., Y. Bock, and P. Fang (1998), Integrated satellite interferometry: Tropospheric noise, GPS estimates and implications for interferometric synthetic aperture radar products, *Journal of geophysical research*, *103*(B11), 27,051–27,067. [1.6.2](#)
- Wright, T., B. Parsons, and E. Fielding (2001a), Measurement of interseismic strain accumulation across the North Anatolian Fault by satellite radar interferometry, *Geophysical Research Letters*, *28*(10), 2117–2120. [1.1.3](#), [1.1.3](#)
- Wright, T. J., J. R. Elliott, H. Wang, and I. Ryder (2013), Earthquake cycle deformation and the Moho: Implications for the rheology of continental lithosphere, *Tectonophysics*, *609*, 504–523. [1.1.1](#), [1.1.2](#), [1.1.2](#), [1.3](#), [1.1.3](#)
- Yamasaki, T., and G. A. Houseman (2012), The signature of depth-dependent viscosity structure in post-seismic deformation, *Geophysical Journal International*, *190*(2), 769–784. [1.2](#)

- Yamasaki, T., T. J. Wright, and G. A. Houseman (2014), Weak ductile shear zone beneath a major strike-slip fault: Inferences from earthquake cycle model constrained by geodetic observations of the western North Anatolian Fault Zone, *Journal of Geophysical Research: Solid Earth*, *119*(4), 3678–3699. [1.6](#), [1.2](#)
- Zebker, H. A., and Y. Lu (1998), Phase unwrapping algorithms for radar interferometry: residue-cut, least-squares, and synthesis algorithms, *JOSA A*, *15*(3), 586–598. [1.6.3](#)
- Zebker, H. A., and J. Villasenor (1992), Decorrelation in interferometric radar echoes, *IEEE Transactions on Geoscience and Remote Sensing*, *30*, 950–959, doi:[10.1109/36.175330](#). [1.6.1](#)
- Zebker, H. A., P. A. Rosen, R. M. Goldstein, A. Gabriel, and C. L. Werner (1994), On the derivation of coseismic displacement fields using differential radar interferometry: The Landers earthquake, *Journal of Geophysical Research: Solid Earth (1978–2012)*, *99*(B10), 19,617–19,634. [1.1.3](#)
- Zebker, H. A., P. A. Rosen, and S. Hensley (1997), Atmospheric effects in interferometric synthetic aperture radar surface deformation and topographic maps, *Journal of Geophysical Research: Solid Earth*, *102*(B4), 7547–7563. [1.6](#)

Chapter 2

Geodetic observations of postseismic creep in the decade after the 1999 Izmit earthquake, Turkey: Implications for a shallow slip deficit.

E. Hussain¹, T.J. Wright¹, R.J. Walters², D.P.S. Bekaert¹, A. Hooper¹ and G.A. Houseman¹

¹ COMET, School of Earth and Environment, University of Leeds, UK

² COMET, Department of Earth Sciences, University of Durham, UK

Citation: Hussain, E., T. J. Wright, R. J. Walters, D. Bekaert, A. Hooper, and G. A. Houseman (2016), Geodetic observations of postseismic creep in the decade after the 1999 Izmit earthquake, Turkey: Implications for a shallow slip deficit, *J. Geophys. Res. Solid Earth*, 121, 29803001, doi:10.1002/2015JB012737.

Abstract

The relationship between aseismic slip and tectonic loading is important for understanding both the pattern of strain accumulation along a fault and its ability to generate large earthquakes. We investigate the spatial distribution and temporal evolution of aseismic creep on the western North Anatolian Fault (NAF) using time series analysis of Envisat Interferometric Synthetic Aperture Radar (InSAR) data, covering the full extent of the 1999 Izmit and Duzce earthquake ruptures and spanning 2002-2010. Discontinuities in the line-of-sight velocity across the fault imply that fault creep reaches the Earth's surface at an average fault-parallel rate of ~ 5 mm/yr along an ~ 80 km section of the NAF. By combining InSAR and published GPS velocities, we are able to extract the vertical and east-west components of motion and show that the Adapazari basin is subsiding at a rate of ~ 6 mm/yr. Vertical motions have biased previous estimates of creep in this region. The displacement time series close to the fault is consistent with an afterslip model based on rate-and-state friction, which predicts a rapid deceleration in fault creep rate after the Izmit earthquake to a near steady-state ~ 5 mm/yr after 5 years. Projecting our model 200 years into the future we find that the cumulative displacement of 1-1.3 m is insufficient to account for the shallow coseismic slip deficit observed in previous studies. Distributed off-fault deformation in the shallow crust or transient episodes of faster slip are likely required to release some of the long-term strain during the earthquake cycle.

2.1 Introduction

While the upper crustal portions of most active faults are locked, storing elastic strain energy for decades to centuries and releasing it almost instantaneously in earthquakes, some faults instead slip steadily at slow rates over various time scales and spatial distributions. These steadily slipping (creeping) faults may store little to no strain energy and are unlikely to produce significant earthquakes if aseismic creep occurs throughout the seismogenic crust and the creep rate is equal to the tectonic loading ([Bürgmann et al., 2000](#)).

However, most faults do not undergo aseismic creep at all depths in the crust at the full tectonic loading rate. Examples from the Hayward Fault ([Schmidt et al., 2005](#)), the Longitudinal Valley Fault ([Champenois et al., 2012](#), [Thomas et al., 2014](#)), the central section of the San Andreas Fault ([Maurer and Johnson, 2014](#), [Jolivet et al., 2015](#)) and the Isetpasa section of the North Anatolian Fault ([Kaneko et al., 2013](#), [Cetin et al., 2014](#)) show that aseismic fault slip occurs in the upper crust on some segments of major strike-slip faults at rates that are significantly less than the full tectonic loading rate, implying that not all the accumulated strain energy is being released aseismically. In these cases, parts of the fault are fully or partially locked and can still generate moderate

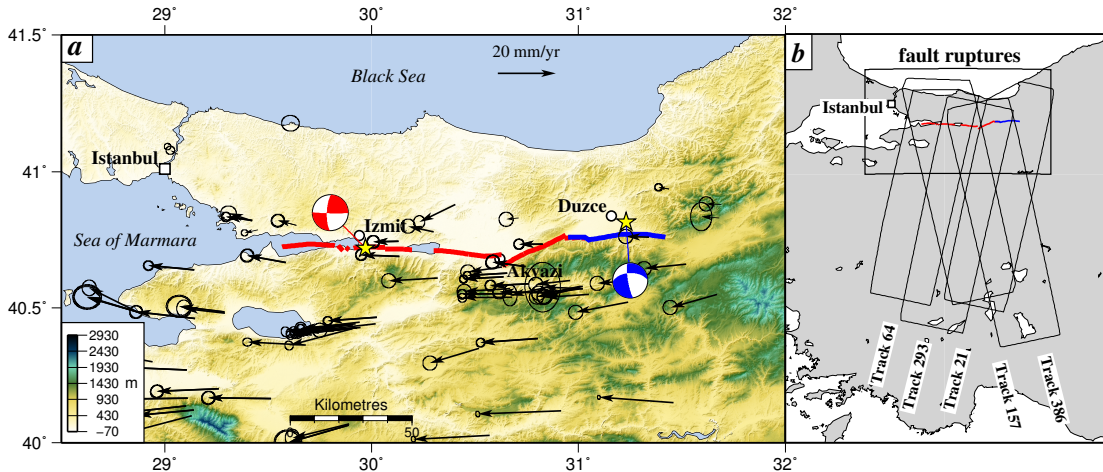


Figure 2.1: (a) The 1999 magnitude 7.4 Izmit and magnitude 7.2 Düzce earthquake surface ruptures. Focal mechanisms are from the Global Centroid Moment Tensor (GCMT) catalogue. The black vectors are the average Eurasia-fixed preseismic GPS velocities obtained from the the Global Strain Rate Model project (*Kreemer et al., 2014*) website (<http://gsm.unavco.org>). (b) The spatial coverage of the Envisat tracks used in this study. The box labelled fault ruptures is the region shown in (a).

to large earthquakes (e.g. *Avouac, 2015*). The spatial and temporal distribution of fault creep rate is therefore important for understanding the pattern of strain accumulation along a fault and its ability to generate large, damaging earthquakes.

The North Anatolian Fault (NAF) is a major continental right-lateral strike-slip fault located in northern Turkey. Together with the East Anatolian Fault, it facilitates the motion of Anatolia away from the Arabia-Asia collision zone towards the Hellenic subduction zone. Since the 1939 Mw 7.9 Erzincan earthquake in eastern Turkey, the NAF has slipped in a sequence of large (Mw >6.7) earthquakes with a dominant westward progression in seismicity (*Barka, 1996, Stein et al., 1997*). This sequence of earthquakes has been interpreted as a result of stress transfer along strike, where one earthquake brings the adjacent segment closer to failure (*Stein et al., 1997, Hubert-Ferrari et al., 2000*). The most recent events were the Mw 7.4 Izmit and Mw 7.2 Düzce earthquakes in 1999. The Izmit earthquake ruptured ~ 140 km of the western section of the North Anatolian Fault on 17 August 1999 (e.g. *Wright et al., 2001b, Barka et al., 2002*) and was followed by the Düzce earthquake on 11 November 1999, which ruptured another ~ 45 km of the fault (e.g. *Akyuz, 2002, Bürgmann et al., 2002b*) (Figure 2.1).

Cakir et al. (2012) were the first to document postseismic fault creep along the Izmit rupture. Using Interferometric Synthetic Aperture Radar (InSAR) analysis of Envisat satellite images from ascending tracks 157 and 386 between 2003-2009, they observed a discontinuity in the InSAR velocities across the section of the rupture between Izmit and Akyazi. Their analysis of ERS satellite images showed no evidence of creep prior to the 1999 earthquakes. The authors concluded that the observed fault creep is postseismic deformation initiated by the 1999 Izmit earthquake.

Table 2.1: Data coverage from each Envisat track used in this study

Track	Geometry	Time span	No. of images	Total ifgs created	Ifgs used
64	Descending	20040103 - 20100327	21	61	27
293	Descending	20040119 - 20101004	19	46	22
21	Descending	20021106 - 20090930	25	76	35
157	Ascending	20030404 - 20080328	19	44	26
386	Ascending	20040229 - 20080727	12	29	17

Using elastic dislocation models, *Cakir et al. (2012)* estimate the aseismic creep rate to reach a maximum of 27 mm/yr and to extend from the surface to a depth of 12 km. This estimated creep rate is comparable to published geodetic slip rates for the NAF at this longitude, which lie between 11-26 mm/yr (*Straub et al., 1997, Hubert-Ferrari et al., 2000, Ayhan et al., 2002, Meade et al., 2002, Le Pichon et al., 2003, Reilinger et al., 2006, Aktug et al., 2009, Ergintav et al., 2009, Ergintav et al., 2014*). If accurate, their estimate suggests that little or no elastic strain is currently accumulating along this section of the NAF.

In this study we measure surface velocities between 2002 and 2010 across the region encompassing the Izmit and Düzce ruptures. We use Envisat ASAR images from three descending and two ascending tracks along with published GPS velocities. Each satellite track roughly covers a 100 km by 400 km area. We use this velocity field to investigate the spatial distribution and temporal evolution of aseismic creep along the Izmit rupture. We use an elastic half-space dislocation model to determine the depth and rate of the creep and examine its temporal behaviour using an afterslip model based on rate-and-state friction (*Ruina, 1983, Rice and Ruina, 1983, Tse and Rice, 1986, Rice, 1993, Segall, 2010*).

2.2 InSAR processing and applied corrections

Our dataset consists of 96 Envisat images from five overlapping tracks acquired in descending (64, 293, 21) and ascending (157, 386) geometries (Figure 2.1b). The images span the period between 2002 and 2010 and fully cover the Izmit and Düzce ruptures. Details of the data processed for each track are given in Table 2.1.

We focus the raw Synthetic Aperture Radar (SAR) image products using the JPL/Caltech ROI-PAC software (*Rosen et al., 2004*) and constructed 229 interferograms using the DORIS software (*Kampes et al., 2003*). The interferograms were chosen to minimise the time difference between acquisition dates (the temporal baseline) and the spatial separation of the satellite orbits (the perpendicular baseline). We correct topographic contributions to the radar phase using the 3 arcsecond SRTM DEM (*Farr et al., 2007*) and account for the known oscillator drift for Envisat according to

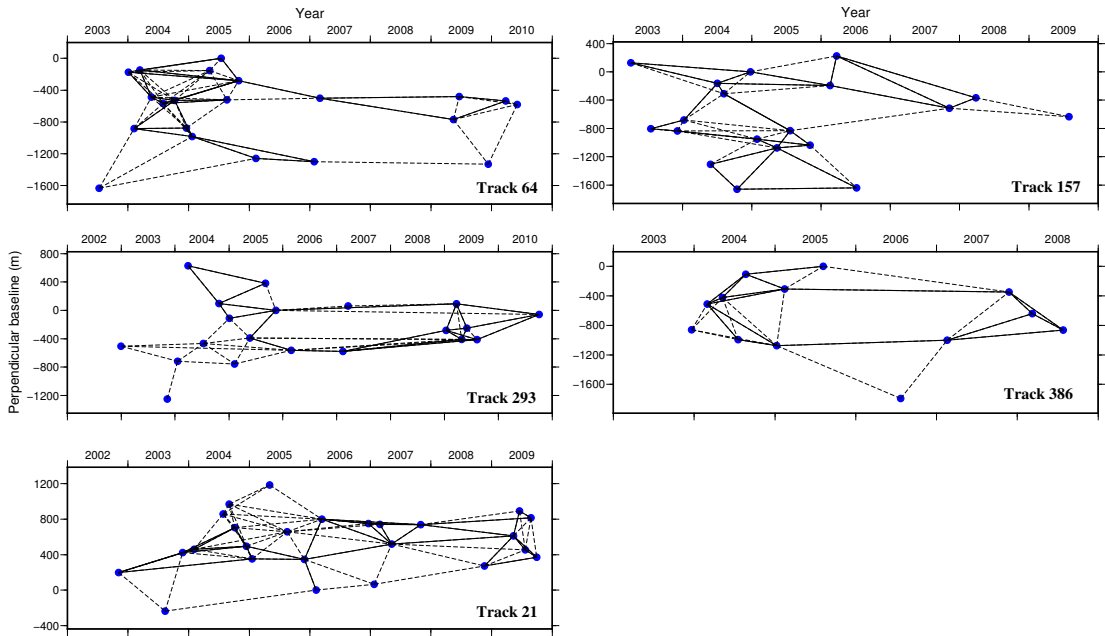


Figure 2.2: Baseline vs time plots for the five tracks used in this study. The dotted connections are the interferograms created for each track. The solid black connections are the interferograms used in the final LOS velocity estimation.

Marinkovic and Larsen (2013).

We remove incoherent pixels and reduce the noise contribution to the deformation signal by applying the StaMPS persistent scatterer small baseline time series InSAR technique (*Hooper, 2008, Hooper et al., 2012*), which takes advantage of the spatial correlation between pixels and does not impose a temporal deformation model when identifying targets with stable phase characteristics through time. The StaMPS software selects only those pixels that have stable phase noise characteristics in time, and uses this subset to compute velocities and time series.

The small baseline network allows for unwrapping error checks by summing the phase around closed interferometric loops (*Biggs et al., 2007*). Interferograms showing obvious unwrapping errors were corrected manually, any others that could not be corrected were removed. In this way we ensure that we have a redundant network of interferograms with minimal unwrapping errors, which enables us to make a more robust estimate of the time-averaged LOS velocity. Figure 2.2 shows that we are left with a good redundant network spanning the time series for each track.

Over the five tracks we use a total of 127 interferograms in the final redundant small baseline networks. The uncertainties on the final velocity for each pixel are calculated using bootstrap resampling and are presented at the 1 sigma level in the following work.

As the InSAR phase delay is a superposition of multiple signals, including tectonic deformation, atmosphere and orbital errors, additional corrections are required. In section 2.2.1 we elaborate on our atmospheric corrections. As InSAR is a relative

measurement, we simultaneously account for orbital errors and any remaining long wavelength signals by combining the InSAR velocities with published GPS velocities in a Eurasia-fixed reference frame (Section 2.2.2).

2.2.1 Atmospheric delay corrections

The spatial and temporal variation in tropospheric humidity, pressure and temperature is often the largest source of error in radar interferograms (e.g. *Doin et al., 2009, Walters et al., 2013, Jolivet et al., 2014, Bekaert et al., 2015a*).

We calculate the estimated phase delay due to the atmosphere for each of our interferograms using the ERA-Interim global atmospheric model reanalysis product (*Dee et al., 2011*) obtained from the European Centre for Medium-Range Weather Forecasts (ECMWF). The ERA-Interim product provides atmospheric information at approximately 80 km spatial resolution on 60 vertical levels from the surface up to 0.1 hPa every 12 hours. We then remove this atmospheric signal from each interferogram, implementing the correction using the TRAIN (Toolbox for Reducing Atmospheric InSAR Noise) software package (*Bekaert et al., 2015c*) after the method of *Doin et al. (2009)* and *Jolivet et al. (2011)*.

On average over the five InSAR tracks, the tropospheric correction reduces the standard deviation of each interferogram by about 6%. Note that, as the standard deviations are mainly reflecting the capability to correct for the long-wavelength tropospheric signal, we removed a ramp from each interferogram prior to the std computation. The average reduction in standard deviation is small, implying that the ERA-Interim weather model is not capturing the full tropospheric variation, which means that there are still some residual atmospheric signals remaining after the ERA-Interim correction (Figure B.1). The average reductions in standard deviation per track are 13% for track 64, 3% for track 293, 8% for track 21, 7% for track 157 and -2% for track 386 (Figure B.2). The weather model correction makes the interferograms for track 386 slightly noisier; this is also our track with the least number of interferograms in the final small baseline network. In total, the standard deviation is reduced in 62% of our interferograms after the ERA-I atmospheric correction.

2.2.2 InSAR Line of sight velocity field in a GPS reference frame

Figure 2.3 shows the calculated average line-of-sight (LOS) velocity through the InSAR time series with the reference for each track shown by the orange star. For all tracks, blue is motion towards the satellite and red is away. Our results are consistent with a right-lateral sense of motion across the fault. The difference between track 293 and track 21 in the overlap region is likely due to residual atmosphere. The higher uncertainties in the overlap region (Figure B.4) reflect this discrepancy.

To obtain a consistent velocity field across the region we transform our InSAR ve-

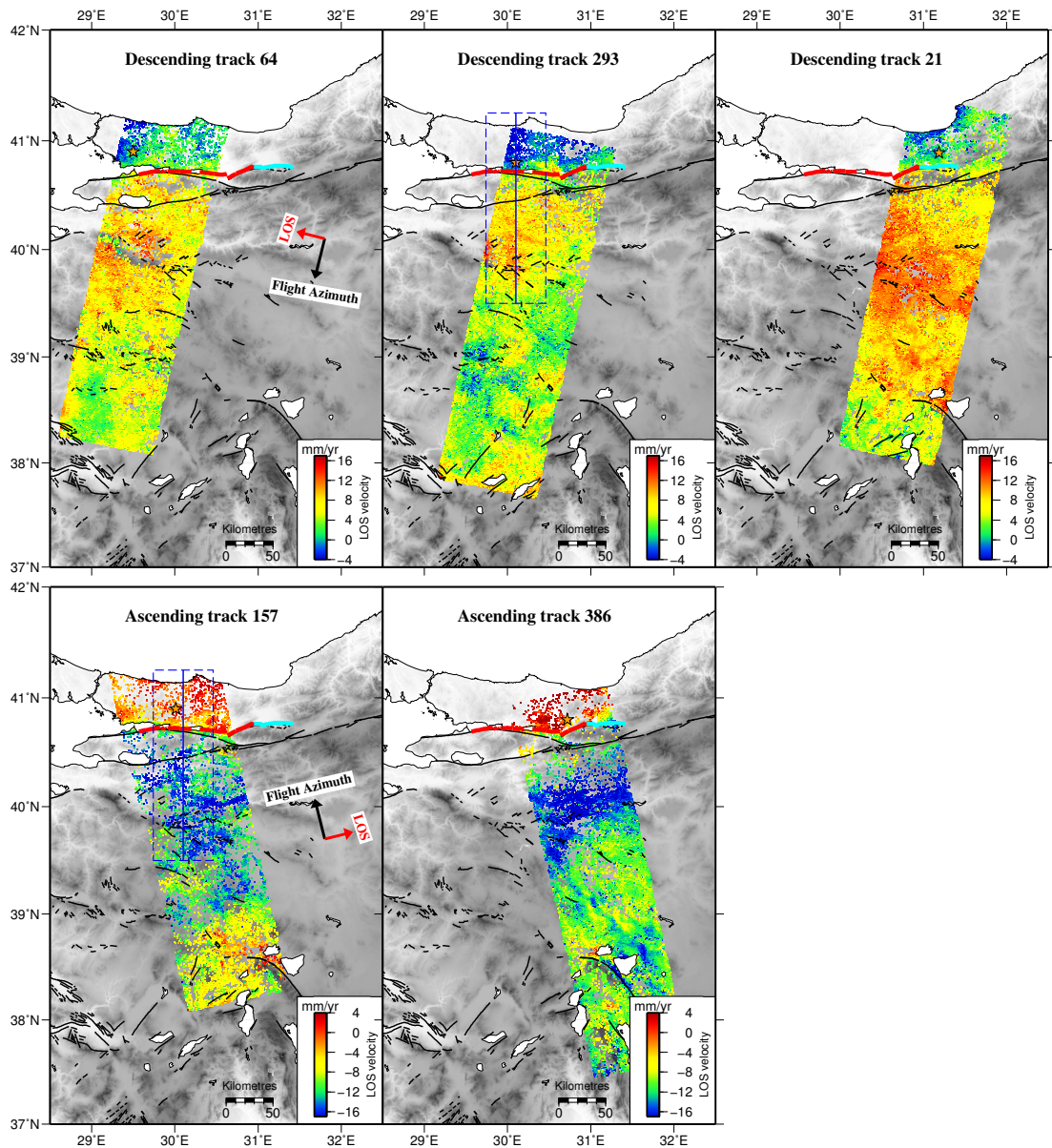


Figure 2.3: The average Line of Sight (LOS) velocities, before adjustment to a Eurasia-fixed reference frame, between the period 2002-2010 for Envisat descending tracks 64, 293, 21 and ascending tracks 157, 386. The orange stars mark the reference location for each track. The bold red and cyan lines are the surface ruptures of the Izmit earthquake and Düzce earthquakes respectively. Thin black lines indicate other mapped faults in the region. The blue lines on tracks 293 and 157 are the locations of the profiles shown in Figure 2.4 with the dashed blue box showing the perpendicular extent of the velocities projected onto the profile line.

locities for each track into a Eurasia-fixed reference frame as defined by the Global Strain Rate Model project (*Kreemer et al., 2014*), from which we download the compilation of input GPS data. The GPS velocities immediately around the Izmit rupture are those published by *Reilinger et al. (2006)*, which were derived from pre-1999 earthquake observations and therefore do not include postseismic or coseismic deformation (*Reilinger et al., 2000, Ergintav et al., 2002*).

We transform the InSAR into the GPS-Eurasia reference frame by first averaging the InSAR velocities that fall in a 1 km radius around every GPS station within the boundaries of the InSAR track. We project the GPS velocities into the local satellite line-of-sight and calculate the difference from the InSAR velocities. We then determine the best-fit plane through the residual velocities using a weighted linear least squares adjustment. We remove this plane from the InSAR velocities to transform the LOS velocities into a Eurasia fixed GPS reference frame.

2.3 Along strike variation in fault creep rate

We observe a discontinuity in the line-of-sight velocities across the fault, seen as a sharp colour contrast in Figure 2.4b. This is most clearly seen in tracks 64, 293 and 157 between 29.9°E and 30.7°E. This discontinuity is superimposed onto a longer wavelength smooth variation in velocity across the fault. Figure 2.4a shows profiles of line-of-sight velocities through tracks 293 and 157. These two components of the deformation are most clearly seen in track 293 where a velocity discontinuity at the fault location is imposed onto a longer wavelength variation across the fault.

We interpret the long wavelength signal to result from the relative motion of Anatolia with respect to Eurasia in the lower crust and upper mantle. The velocity discontinuity is due to shallow fault creep.

We calculate the LOS variance-covariance matrix of the noise for each track by computing the average radial covariance vs. distance (autocorrelation) using the velocities in a 50 km by 50 km region ~ 200 km to the south of the fault. This region is assumed to have no tectonic deformation and contain only atmospheric noise. We fit a covariance function, $C(r)$, of the form

$$C(r) = \sigma^2 e^{-\frac{r}{\lambda}}, \quad (2.1)$$

estimating the variance, σ^2 and the characteristic length λ , which gives the spatial correlation of noise as a function of distance between pixels, r . Our best fit values for each track, and the east-west velocities used in section 2.5, as well as the centre of the region used to calculate the covariance function are shown in Table 2.2.

We estimate the rate of fault creep at various locations along the fault trace for both the Izmit and Düzce ruptures using the LOS velocities from each track. We first make

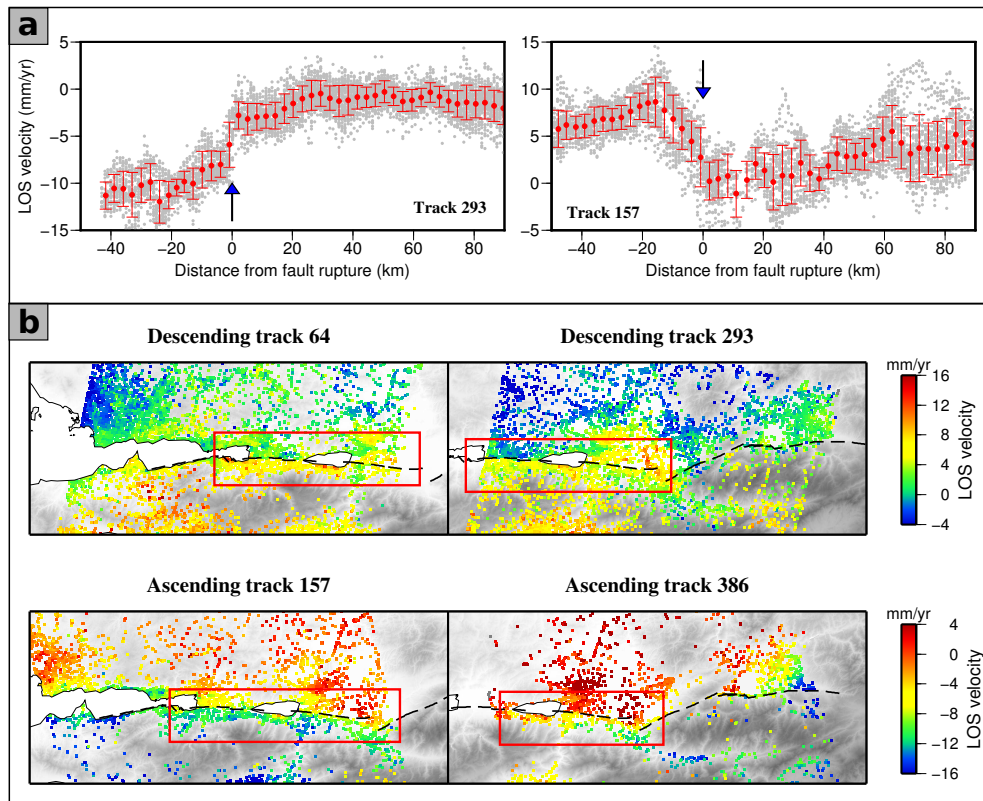


Figure 2.4: (a) Selected north-south profiles of LOS InSAR velocities, here shown for track 293 and 157 at the locations indicated in Figure 2.3. The grey point cloud are velocities within 20 km perpendicular distance from the profile line. The red points are binned averages every 3 km along the profile with the error bars representing the standard deviation of the distribution of points within each bin. The fault location is indicated by the blue arrow. (b) Close-up of the LOS velocities of persistent scatterers in the region around the NAF. The Izmit and Düzce fault ruptures are shown by the dashed black line. The red boxes highlight velocity discontinuities across the fault, here interpreted as aseismic fault creep.

Table 2.2: Regions used to determine the noise covariance function. The centre is the middle of the 50 km by 50 km region used to estimate the covariance function parameters.

Track	Centre (Lon, Lat)	Variance ² (mm/yr) ²	Characteristic Length (km)
64	29.37°E, 39.14°N	2.88	6
293	30.23°E, 39.44°N	2.86	8
21	31.14°E, 40.08°N	2.34	5
157	30.26°E, 39.76°N	4.02	4
386	31.15°E, 39.21°N	5.01	9
E-W velocities	30.20°E, 40.30°N	9.14	20

short profiles of LOS velocity extending 5 km either side of the fault and then project velocities onto this line from within a 2.5 km window either side of the profile. We fit two straight lines through the LOS velocities on either side of the fault and determine the offset at the fault trace (v_{creep}), i.e. the LOS fault creep rate, using the following linear set of equations

$$\begin{bmatrix} v_1^N \\ \vdots \\ v_i^N \\ v_j^S \\ \vdots \\ v_n^S \end{bmatrix} = \begin{bmatrix} x_1^N & 0 & 1 & 0 \\ \vdots & \vdots & \vdots & \vdots \\ x_i^N & 0 & 1 & 0 \\ 0 & x_j^S & 1 & 1 \\ \vdots & \vdots & \vdots & \vdots \\ 0 & x_n^S & 1 & 1 \end{bmatrix} \begin{bmatrix} a_N \\ a_S \\ b_N \\ v_{creep} \end{bmatrix} + \epsilon, \quad (2.2)$$

where $v_{(1:i)}^N$ and $v_{(j:n)}^S$ are the LOS velocities north and south of the fault respectively, $x_{(1:i)}^N$ and $x_{(j:n)}^S$ are the perpendicular distance north and south of the fault respectively, a_N and b_N are respectively the gradient and offset of the best-fit line through the velocities north of the fault, a_S the gradient of the best-fit line through the southern velocities and ϵ represents errors in the model.

We solve these equations and determine the error distribution of each parameter using the percentile bootstrap method ([Efron and Tibshirani, 1986](#)). Unlike the regular bootstrap algorithm, where n random samples are taken from n observation, we select n_1 and n_2 random samples from n_1 and n_2 observations (LOS velocities) north and south of the fault respectively ([Bekaert et al., 2015b](#)), where $n_1 + n_2$ is the total number of observations on both sides of the fault. Each bootstrap simulation provides an estimate for the unknown parameters (a_N , a_S , b_N , v_{creep}). We do this calculation at each location marked with a black circle in [Figure 2.5b](#) for every track.

In most cases the Best Linear Unbiased Estimator (BLUE) value for the fault creep approximates the mean from bootstrap resampling. We use the bootstrap results for our creep estimates because in some cases where the errors on each point are particularly large, the BLUE technique underestimates the uncertainty on the fault creep rate (see [Figure B.3](#)).

Our results ([Figure 2.5a](#)) show that a section of the Izmit rupture extending about 80 km, from the Gulf of Izmit in the west to as far as 30.7° east, has undergone shallow creep during the period 2002-2010, at an average LOS rate of ~ 2.3 mm/yr and ~ 3.3 mm/yr in the descending and ascending tracks respectively. The western extent of the creep is unknown due to the lack of near-fault geodetic data in the gulf.

The LOS fault creep rates east of 30.7°E (beyond 100 km in [Figure 2.5a](#)), covering the eastern end of the Izmit rupture and all of the Düzce rupture, appear to show little to no resolvable creep in the LOS descending geometry. The ascending fault creep rates (from track 386) in this region have large errors due to a sparse pixel coverage resulting

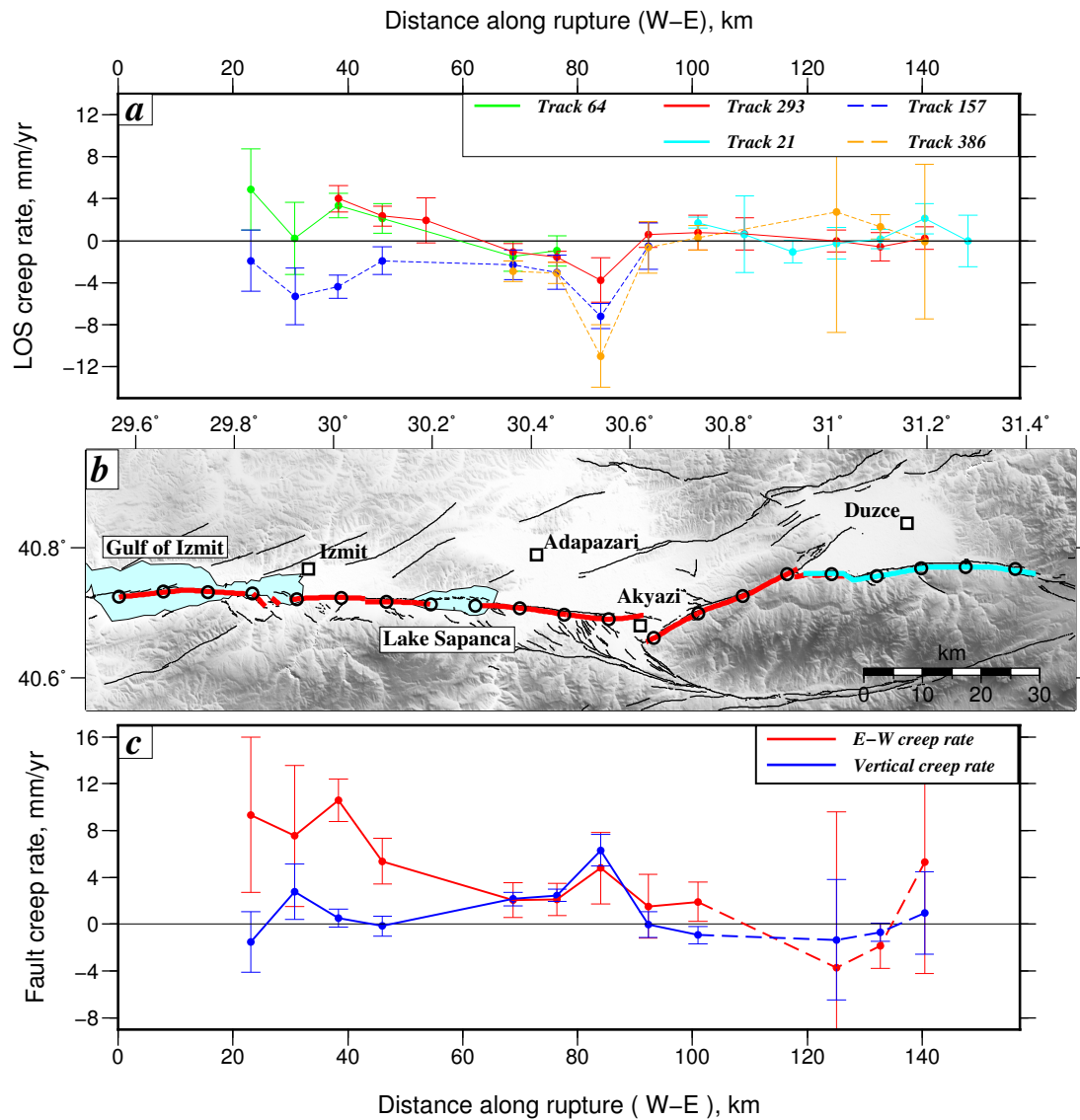


Figure 2.5: (a) The variation in line-of-sight fault creep rate along strike of the Izmit and Düzce ruptures with a map of the ruptures shown in (b). Error bars represent 1σ . The descending creep rates (tracks 64, 293 and 21) are indicated by solid lines and the ascending (tracks 157 and 386) by dashed. The along strike correlation of LOS fault creep rate in the descending and ascending tracks is characteristic of vertical deformation. The Düzce rupture shows little to no surface creep in the LOS. (c) The fault creep rate decomposed into the east-west - approximately fault parallel - and vertical components for locations with both ascending and descending information. Positive creep values in E-W indicate right-lateral motion, while in the vertical this represents subsidence of the north with respect to the south side of the fault. The dashed section implies low confidence due to large uncertainties in fault creep rates from ascending track 386.

from InSAR decorrelation, particularly in the mountains south of the fault.

The difference in sign between the creep rates on ascending and descending tracks (Figure 2.5a) is a result of the two different satellite viewing geometries. Vertical motion manifests as ascending and descending InSAR signals with approximately equal magnitude and the same sign in the LOS while east-west motions, by contrast, result in signals with opposite sign. Therefore, signals that show a positive correlation between ascending and descending tracks (e.g. between 20 km and 100 km distance on Figure 2.5a) are indicative of vertical motion.

The Izmit rupture is oriented east-west with little north-south coseismic deformation in the region adjacent to the fault; the fault plane solution for the earthquake (Figure 2.1) shows pure east-west right-lateral strike-slip motion, and GPS velocities adjacent to the fault are also approximately east-west (Figure 2.1). To simplify our calculations we therefore assume that deformation in the north-south direction is negligible. This allows us to decompose the displacement rates at points where we have both ascending and descending information into east-west (approximately fault-parallel) and vertical rates (Figure 2.5c).

West of 30.7°E , we find an average horizontal fault-parallel creep rate of ~ 5 mm/yr with a maximum horizontal creep rate of 11 ± 2 mm/yr near the city of Izmit. This maximum rate is significantly slower than the estimate of 27 mm/yr between 2003-2009 from *Cakir et al. (2012)*, but is still more than a third of the long term slip rate on the fault. We find this to be due to contamination of the estimated horizontal velocities by vertical motions, which were assumed negligible by *Cakir et al. (2012)* on which we further elaborate in section 2.4.1. In general the fault creep rate decreases along strike towards the east with a small increase near the town of Akyazi. East of 30.7°E , including the Düzce rupture, the rate can be considered to be zero within uncertainty.

2.4 InSAR velocity decomposition

To further investigate the spatial distribution of the apparent vertical motions, we decompose our full InSAR velocity field into east-west and vertical components (Figure 2.6a and 2.6b). We do this first by resampling our InSAR LOS velocities onto a 1 km by 1 km grid encompassing the spatial extent of all our tracks. We use a nearest neighbour resampling technique including only those persistent scatterer pixels with a nearest neighbour within 2 km of the centre of each grid point, and we reference each track to a Eurasia-fixed GPS reference frame, as described in section 2.2.2. For every pixel where information from both ascending and descending geometries are available, we invert for the east-west and vertical components of the velocity using the method described by *Wright et al. (2004)*, taking into account the local incidence angles and assuming there is no north-south motion.

The east-west component of the InSAR velocity (Figure 2.6a) clearly shows fault

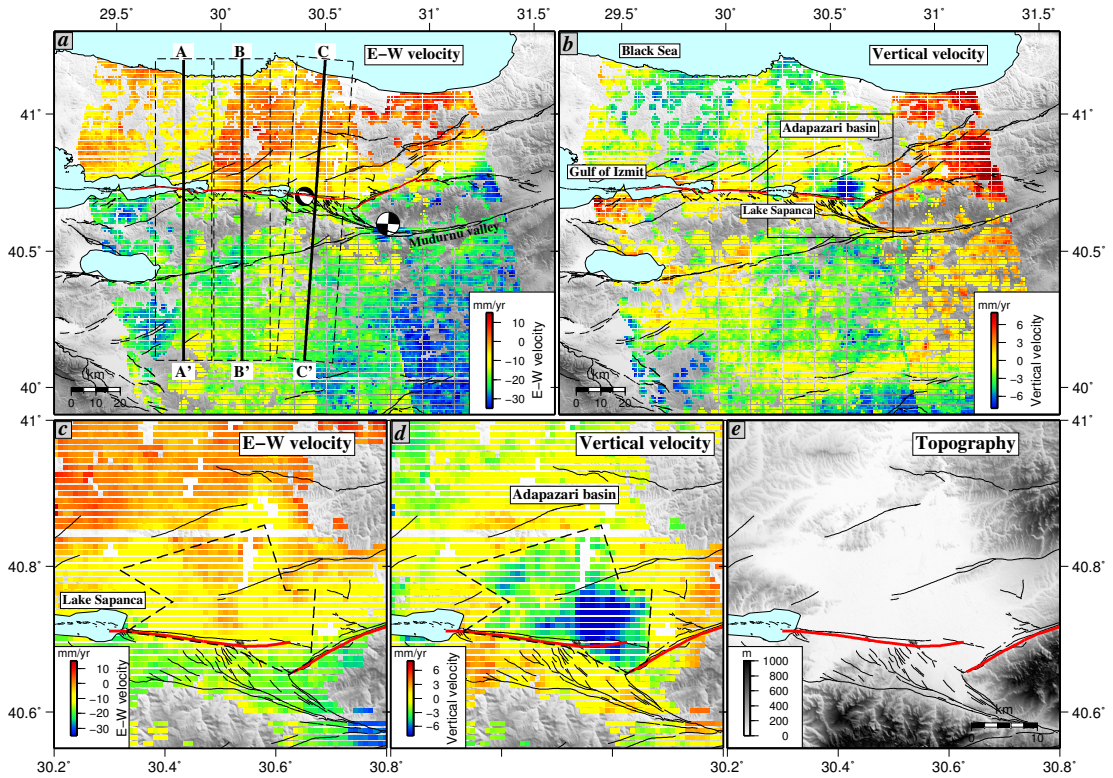


Figure 2.6: LOS InSAR velocities decomposed into the east-west and vertical components (assuming negligible north-south motion). Figure (a) is the east-west component and (b) shows the vertical component where negative values indicate surface subsidence. The 1999 Izmit earthquake surface rupture is indicated by the red line. Fault plane solutions are the 1967 Mw 7 earthquake (strike-slip) and its main aftershock (magnitude 5.5, normal) from *Jackson and McKenzie (1984)*. The lines labelled A-A', B-B' and C-C' are profiles through the velocities shown in Figure 2.8 with the dashed box indicating the projection width. Uncertainty maps for these components are shown in Figure B.4. Figures (c), (d) and (e) are close-ups of the region labelled Adapazari basin in (b). The dotted line is the boundary of the subsiding region highlighted by the negative vertical velocities (blue colours) in (d). The subsiding region roughly correlates with the boundaries of a topographic low that corresponds to the Sakarya River floodplain shown in the topographic map (e).

creep as a velocity discontinuity on the Izmit earthquake rupture continuing east along the fault from the Gulf of Izmit. The velocity discontinuity becomes unclear east of about 30.7°E , implying no shallow creep reaches the Earth surface east of this longitude. The vertical component (Figure 2.6b) shows no clear discontinuities across the fault other than in the Adapazari basin region.

2.4.1 Adapazari basin subsidence

The Adapazari basin is roughly 30 km wide and located around the town of Adapazari to the north of the NAF. It is located in a transtensional region between the Izmit-Adapazari and Mudurnu valley segments of the NAF (*Emre et al., 1998, Ünay et al., 2001*). After detailed analysis of the regional geology, fault pattern, morphology and stress and strain pattern in the region, *Neugebauer (1995)* suggested a pull-apart mechanism for the basin formation. The superficial geology consists of alluvial and fluvial sediments deposited by the the Sakarya River, which flows through the centre of the basin (*Yigitbas et al., 2004, Ulutaş et al., 2011*). The thickness of the alluvium in the mid-section of the basin is estimated to be more than 200 m according to groundwater wells drilled by the State Hydraulic Works (*SHW, 1983, Ulutaş et al., 2011*) and possibly up to 2 km thick determined from a seismic refraction survey across the basin (*Karahan et al., 2001*).

The displacement in the Adapazari basin (Figure 2.6c-e) is seen only in the vertical component, with the basin subsiding at a rate up to 6 mm/yr. The subsidence is bound to the north and west by a region of high topography (Figure 2.6e) and by the NAF to the south. The eastern limit of subsidence correlates with the extent of Holocene sedimentary deposits (*Yigitbas et al., 2004*).

The cause of this subsidence is unclear but there are several possible explanations. The Adapazari basin is a region of high agricultural productivity (*Erinç and Tunçdilek, 1952, Gedikli, 2004, Ikiel et al., 2012*). The two regions of rapid subsidence (the south-east corner and a smaller region in the north-west corner of the basin) are former wetland/swamps, which were drained in the last 30 years (*Bilgin, 1984*). The subsidence could, therefore, be a surface response to this drainage. To first order, the shape of the subsiding region from our InSAR velocities matches the shape of the basin (Figure 2.6d and e), hence the subsidence could also be due to sediment compaction. However, there may also be a tectonic influence on the subsidence in this region; *Neugebauer et al. (1997)* and *Poyraz et al. (2015)* showed that microseismicity fault plane solutions within the basin have significant normal faulting components. Solutions for the 1967 Mw 7 earthquake (strike-slip) and its main aftershock (magnitude 5.5, normal) (*Jackson and McKenzie, 1984*) are also in good agreement with a pull-apart mechanism (Figure 2.6a) for this basin formation.

Cakir et al. (2012)'s estimate of the fault creep rate was derived using a single ascending satellite orbit, in which eastward motion and subsidence both cause motion

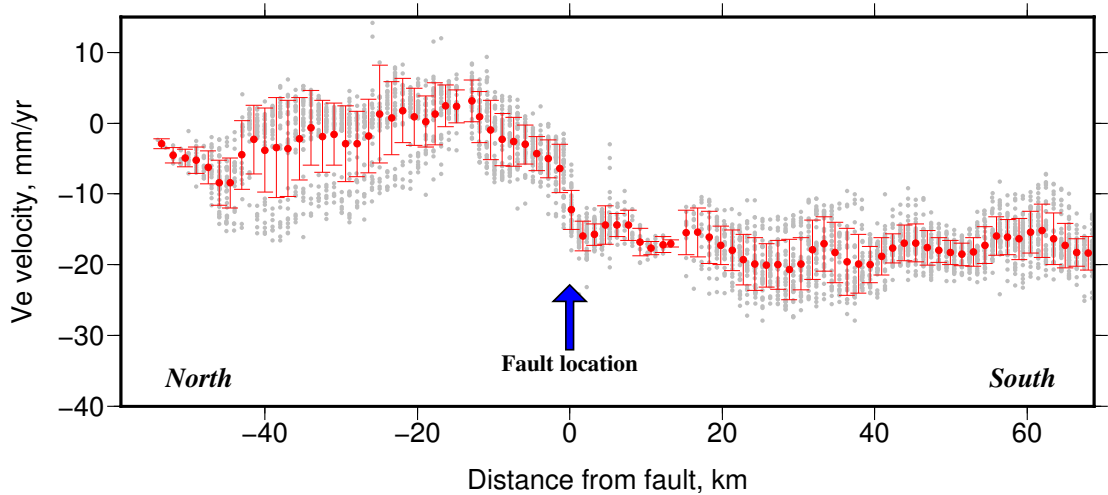


Figure 2.7: A profile of east-west velocities at location B-B' shown in Figure 2.6a with velocities within 15 km perpendicular distance projected onto the line in grey circles. The red points are binned averages every 3 km along the profile with the error bars representing the standard deviation of the distribution of points within each bin. It is clear that there are signals at two characteristic wavelengths in this profile: a long wavelength signal responsible for the far field offsets either side of the fault and a velocity discontinuity at the fault location.

away from the satellite. Their estimate of the fault creep rate is therefore contaminated by subsidence from these vertical signals.

2.5 Modelling profile velocities

A fault-perpendicular profile of east-west velocities (Figure 2.7) confirms that there are two different deformation signals: a long wavelength signal, related to relative interseismic motion of Eurasia and Anatolia at depth, and a velocity discontinuity at the fault, consistent with shallow fault creep. We model the long wavelength signal as a screw dislocation at a depth d_1 in an elastic half-space, equivalent to interseismic slip on a fault plane below locking depth d_1 at rate S (Weertman and Weertman, 1964, Savage and Burford, 1973). For the shallow creep, between the surface and depth d_2 at rate C (Figure 2.8), we use a back-slip approach (Savage, 1983) in which the shallow creep is modelled as the sum of slip on the entire fault plane (Heaviside function, $\mathcal{H}(\mathbf{x})$) plus a screw dislocation in the opposite sense to the plate motion at depth d_2 . We also solve for a possible static offset (a) between the profile and the model. The fault parallel (east-west) velocity, $v_{EW}(x)$ is:

$$v_{EW}(x) = -\frac{S}{\pi} \arctan\left(\frac{\mathbf{x}}{d_1}\right) + C \left[\frac{1}{\pi} \arctan\left(\frac{\mathbf{x}}{d_2}\right) - \mathcal{H}(\mathbf{x}) \right] + a, \quad (2.3)$$

where \mathbf{x} is the perpendicular distance from the fault.

We find best-fit values for each model parameter (S , d_1 , C and d_2) and offset a , using a Bayesian approach, implementing the Goodman and Weare (2010) affine-

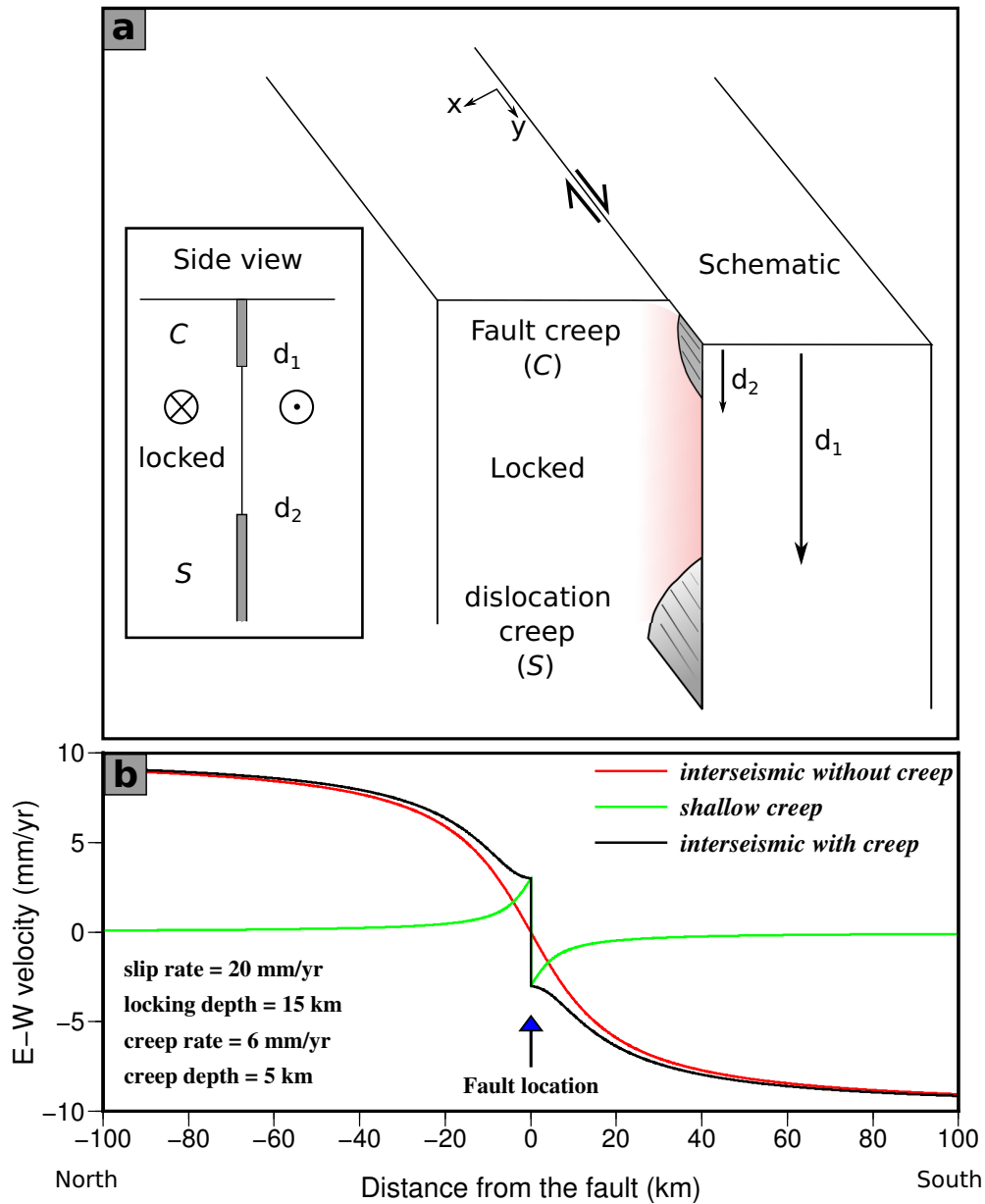


Figure 2.8: (a) A schematic of our elastic model. The locking depth, d_1 , is always greater than or equal to the creep depth, d_2 . (b) A forward calculation using the given parameters to show that our model can produce both the long and short wavelength signals seen in the InSAR profiles.

invariant ensemble Markov Chain Monte Carlo (MCMC) sampler ([Foreman-Mackey et al., 2013](#)). MCMC methods enable us to retrieve the full uncertainties associated with each model parameter. The algorithm ensures that we collect samples to build the desired posterior distribution. The most important benefits of the algorithm from [Goodman and Weare \(2010\)](#) compared to the typically used Metropolis-Hasting algorithm is reduced convergence time and the ability to efficiently explore highly irregular probability distributions. The algorithm consists of running multiple parallel Markov chains, or walkers, where the next iteration for each chain requires randomly selecting another chain from the ensemble and choosing a new position that is a random linear combination of the positions of both walkers. Each individual chain is initiated from a randomly selected point in the parameter space within defined prior constraints.

An important prior constraint in our inversion is that the maximum depth of fault creep, d_2 , must be less than or equal to the interseismic locking depth, d_1 . In addition, our MCMC sampler explores the parameter space constrained by: $-60 < S$ (mm/yr) < 0 , $0 < d_1$ (km) < 40 , $-30 < a$ (mm/yr) < 30 , $0 < C$ (mm/yr) < 15 , $0 < d_2$ (km) < 40 , assuming a uniform prior probability distribution over each range.

Our initial runs assuming a uniform prior probability distribution over the locking depth range (0-40 km) revealed that the data do not constrain the maximum locking depth d_1 . We therefore include an extra prior constraint on the locking depth noting that published values are generally in the range 11-22 km (e.g. [Reilinger et al., 2000](#), [Wright et al., 2001b](#), [Michel and Avouac, 2002](#)), we assume a Gaussian prior constraint for $d_1 = 17$ km with a 1σ value of 5 km.

For our model runs, we use 600 walkers to explore the parameter space over 1,000,000 iterations producing 160,800 independent random samples from which we estimate both the maximum a posteriori (MAP) solution and corresponding parameter uncertainties.

We perform the inversion on three profiles for which velocities from within 15 km perpendicular distance are projected onto the profile lines shown in Figure 2.6a. The results of our MCMC analysis are shown in Figure 2.9. For each profile the black line is the maximum a posteriori probability solution with the 68% and 95% confidence bounds on the model represented by the light and dark grey bands. The MAP solutions are consistent across all three profiles with the fault slip rate, locking depth and creep depth for each profile within ± 1 of the average.

Profile C-C' shows a lower creep rate than profile B-B' (2 mm/yr compared to 5 mm/yr), which is consistent with the creep rates inferred directly from the InSAR velocity discontinuities (Figure 2.5). Although the MAP solutions for maximum fault creep depth are consistent between profiles (6 km, 8km and 7 km), the 95% confidence bounds are very large. Figure 2.10 helps explain the cause behind the large confidence intervals. Changing maximum creep depth between 4 km, 8 km and 12 km, with the other parameters fixed, makes only a small difference to the shape of the profile relative to the estimated uncertainty of the east-west velocities.

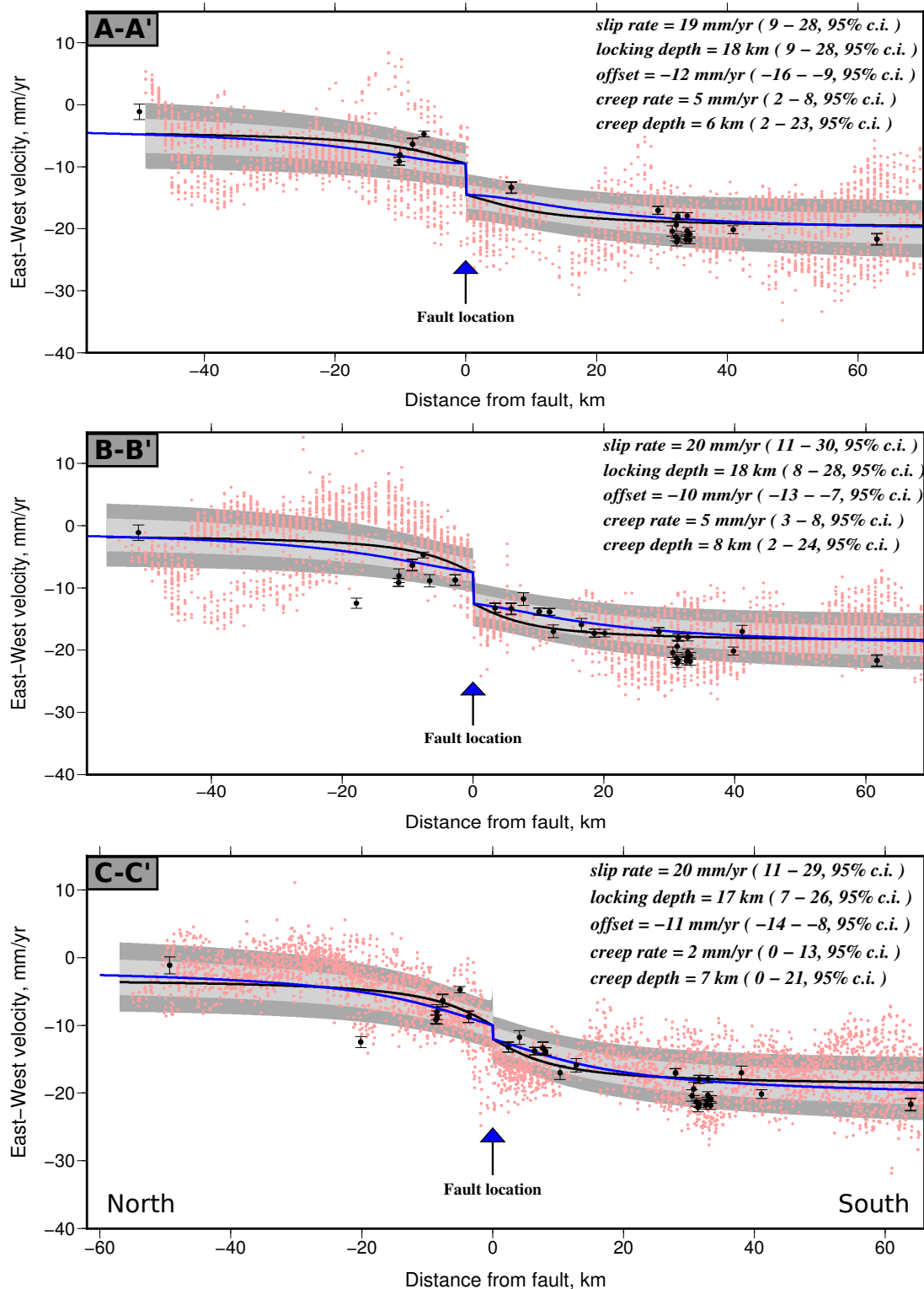


Figure 2.9: Projected east-west velocities along the profiles indicated in Figure 2.6a. The red points are the data point cloud showing velocities within 15 km perpendicular distance from the profile line. The black points are the published GPS velocities. The black line through the velocities is the maximum a posteriori probability (MAP) solution to our model assuming a uniform prior for the locking depth. The blue line (our preferred solution) is the MAP solution assuming a Gaussian prior for the locking depth. See text for details. The dark and light grey shading around the best fit line represent the 95% and 68% confidence bounds on our preferred model. The model parameters values in text are our preferred MAP solution with the 95% confidence range in brackets.

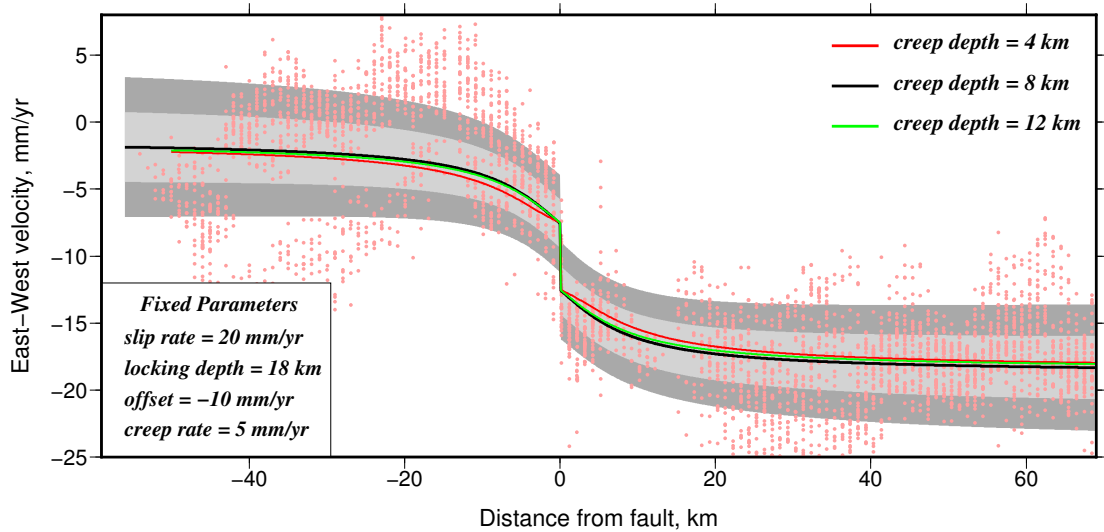


Figure 2.10: Profile B-B' from Figure 2.9 with the bold black line representing the MAP solution with a maximum creep depth of 8 km. The dark and light grey shading around the best fit line represent 2σ and 1σ model uncertainties respectively. We fix the slip rate, locking depth, offset and creep rate to the MAP solution for this profile and plot two other model calculations for creep depths of 4 km and 12 km, shown in red and green respectively. The difference between each model is within the noise level of the velocities and is the principle cause behind the large confidence intervals for the MAP creep depths in Figure 2.9.

Figure 2.11 shows the marginal probability distribution for each model parameter for profile line B-B', which shows the clearest velocity discontinuity at the fault. The distributions for profiles A-A' and C-C' can be found in the supplementary material (Figure B.5), but the following description applies to all three cases.

The sampled distributions for the fault slip rate, the static offset and the fault creep rate are approximately normally distributed. Our distributions reveal that several parameters trade-off with one another. The clearest example is between the fault slip rate and the locking depth.

2.6 Fault creep time series

Theoretical studies and laboratory experiments, in the framework of rate-and-state friction, suggest that the mechanism of fault creep is linked to steady-state velocity-strengthening behaviour (e.g. *Ruina, 1983, Rice and Ruina, 1983*). Rate-and-state models predict that these regions slip stably under tectonic loading, whereas velocity-weakening regions produce stick-slip motion (e.g. *Tse and Rice, 1986, Rice, 1993, Kaneko et al., 2013*).

The relative motion of two points, ~ 3 km either side of the fault west of Lake Sapanca is constrained by a long time series of displacements from GPS (*Cakir et al., 2012*), as well as by InSAR displacements from our tracks (Figure 2.12). We correct these for a static coseismic offset by aligning the projection of the preseismic and

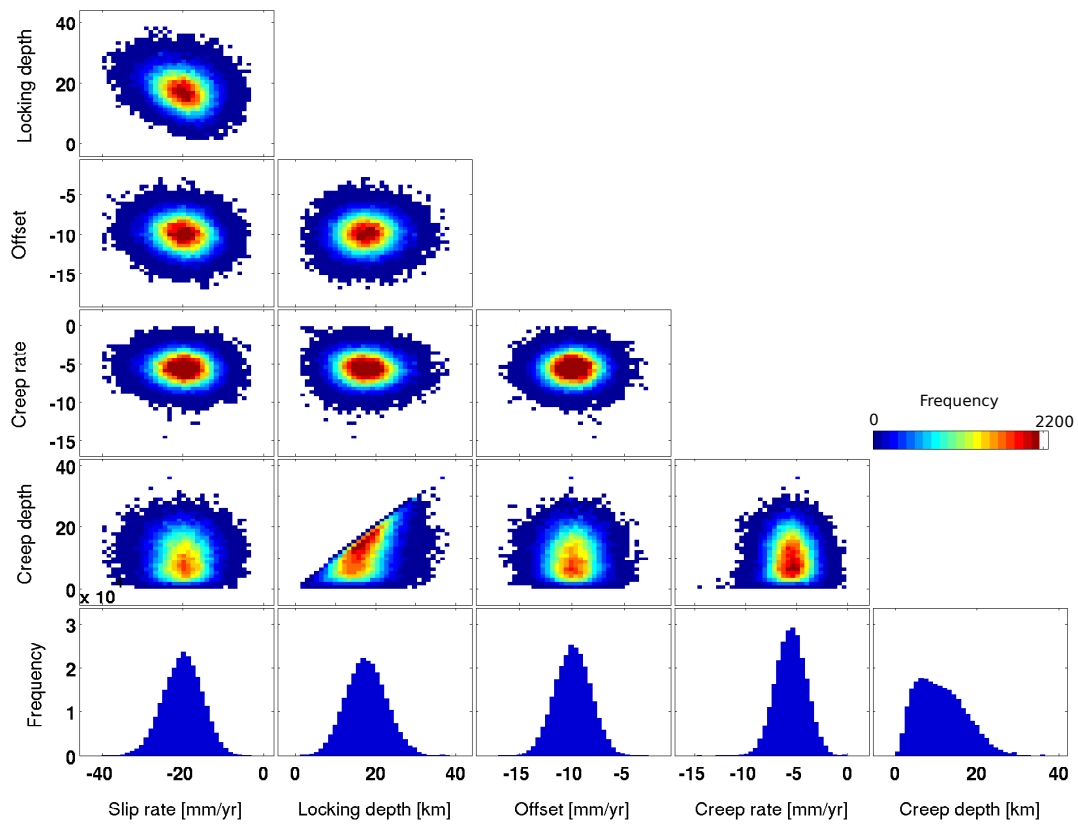


Figure 2.11: The sampled marginal probability distributions of the model parameters assuming a Gaussian prior for the locking depth and a uniform prior for the other parameters. See text for more information.

postseismic displacements to zero at the time of the earthquake. We correct for the small interseismic component due to slip on a vertical dislocation using the model of *Savage and Burford (1973)*'s with a locking depth of 18 km and slip rate of 20 mm/yr (average values from our profiles in Figure 2.9). Any remaining relative displacement between the two stations can be attributed to shallow fault creep.

After this correction, we find that the preseismic fault creep rate (v_p) from the GPS observations is 1 ± 1 mm/yr. The time series shows a period of rapid displacement after the earthquake, which we interpret as afterslip, followed by a slow decay spanning our InSAR data time window.

We model the time evolution of fault creep using a rate-and-state afterslip formulation (*Marone et al., 1991, Scholz, 2002, Segall, 2010*), which approximates the behaviour of the system using a simple spring slider model. We note that the characteristic decay time t_c of transient afterslip depends on both frictional properties as well as the system stiffness k :

$$t_c = \frac{\sigma(a - b)}{kv_p}, \quad (2.4)$$

where σ is the normal stress, a and b are rate-and-state friction parameters and v_p is the preseismic fault creep rate.

Integrating equation (2.4) with a substitution (for details see (*Segall, 2010*)) gives the displacement

$$\delta(t) = \frac{\sigma(a - b)}{k} \ln \left[\frac{v_{max}}{v_p} \left(e^{t/t_c} - 1 \right) + 1 \right], \quad (2.5)$$

where v_{max} is the depth-averaged maximum afterslip velocity.

We use an MCMC approach (as described in section 2.5) to find the model parameters that best fit the data (Figure 2.12c). Our MAP solution gives a maximum afterslip velocity (v_{max}) of 1050 ± 150 mm/yr or 2.9 ± 0.4 mm/day and $\sigma(a - b)/k = 51 \pm 2$ mm. The calculated marginal probability distributions for each parameter (Figure 2.13) show that the sample distributions are approximately normally distributed.

2.7 Discussion

2.7.1 Fault creep and elastic modelling

Our InSAR results show that fault creep reaches the surface along ~ 80 km of the Izmit rupture, from the Gulf of Izmit to the eastern edge of the Adapazari basin. High creep rates on the fault where it enters the Gulf (Figure 2.5) suggest that aseismic creep may continue into the Gulf, extending the length of the creeping segment of the Izmit rupture. Over the InSAR time interval, our time-averaged fault creep rate has a maximum value of 11 ± 2 mm/yr (between 2002-2010) near the city of Izmit.

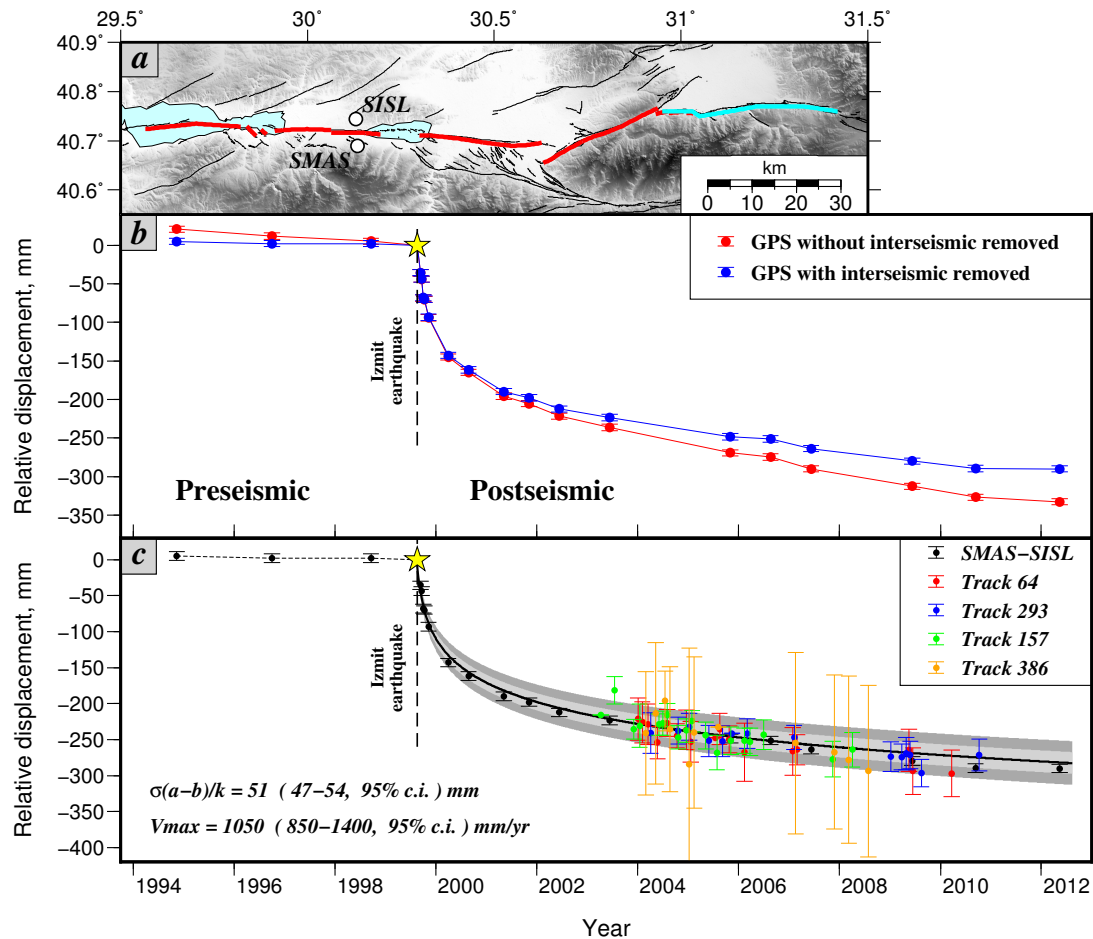


Figure 2.12: (b) A time series of relative displacement between two GPS stations SMAS and SISL (location shown in (a)). Red points represent the observed east-west relative displacements while the blue show the times series corrected for interseismic loading using our best fit parameters from Figure 2.9b. (c) The black model shows the baseline changes predicted by our afterslip model with the best fit model parameters and the points show the corresponding InSAR time series for pixels near the GPS station, colour coded by track. This model predicts a rapid deceleration in shallow fault creep rate from 2.9 ± 0.4 mm/day immediately after the Izmit earthquake to a near steady-state value of ~ 5 mm/yr after 5 years. The dark and grey bands are 2σ and 1σ model uncertainties.

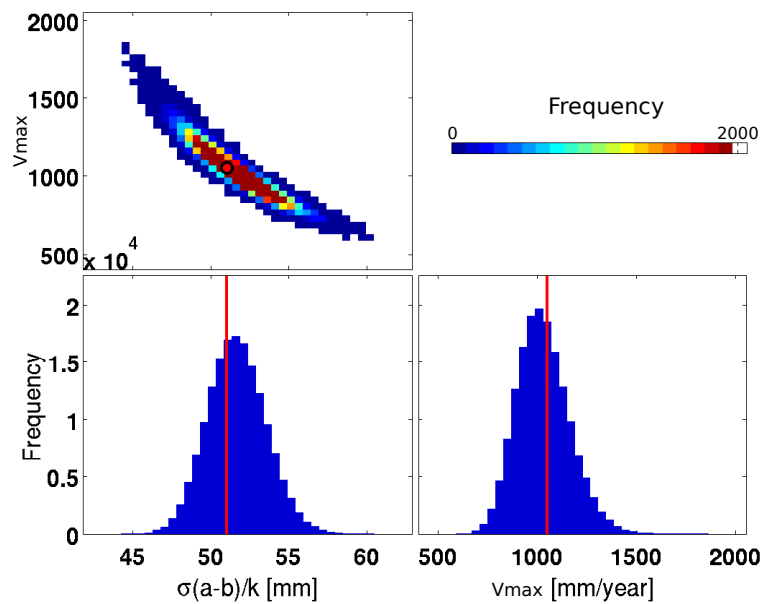


Figure 2.13: The sampled marginal probability distributions of the model parameters. The maximum a posteriori probability solution is highlighted by the red marker and line.

Our simple elastic model fits the data on each profile (Figure 2.9) within the 95% confidence bound, with a maximum a posteriori probability (MAP) estimate of the fault creep rate of 5 mm/yr occurring from the surface to a depth of 8 km. Note that 5 mm/yr is the average fault creep rate along the width of the profile (30 km), while 11 mm/yr is the maximum local creep rate near the city of Izmit. This is less than half that estimated by *Cakir et al. (2012)* (27 mm/yr) using velocities from ascending tracks alone. Much of this difference, particularly in the Adapazari basin, is likely from contamination of the horizontal displacement rates by vertical motion, which was neglected by *Cakir et al. (2012)*. Using only our ascending velocities and ignoring vertical motion we obtain creep rates of ~ 25 mm/yr in the Adapazari basin.

For the first 10 km east of Izmit, our fault creep estimates agree well with that of *Cakir et al. (2012)*. Further east of this and into the Adapazari basin our estimates of fault parallel creep decreases to ~ 6 mm/yr, while *Cakir et al. (2012)*'s begin to increase to about 27 mm/yr. In their model this coincides with a deepening of the depth to the top (0 km to 1 km) and bottom (5 km to 12 km) of the creeping segment, i.e. fault creep is extending down to deeper depths but not reaching the ground surface. In our models the maximum depth of the creeping segment (equivalent to *Cakir et al. (2012)*'s bottom depth) remains fairly constant at ~ 7 km. We do not solve for a top depth because offsets in the velocity gradients across the fault (section 3) imply that fault creep reaches the ground surface along the entire 80 km of the creeping segment, therefore we implicitly assume a top depth of 0 km.

Figure 2.14 compares our MAP solution (in grey) with the prediction from the best

fit parameters estimated by *Cakir et al. (2012)* (in blue). Note that we assume the the top depth for the fault creep reaches the ground surface. It is clear that they overestimate the fault creep rate at both locations. The green line is the MAP result when the far field slip rate and locking depth are fixed to the values used by *Cakir et al. (2012)*. The fit, although within our 95% confidence range, is poor at far-field locations from the fault compared to our solution, and the fit is also poor at these locations to existing GPS data. However, the creep rate and depth estimates are similar to our MAP results implying that these parameters are fairly insensitive to the far-field fault slip rate and locking depth.

Cakir et al. (2012) processed their InSAR data using a persistent scatterer single master approach while we use the persistent scatterer small baseline technique. In the single master case, unwrapping errors can only be assessed visually while we use a more robust loop closure technique to systematically identify and remove (or fix) interferograms with unwrapping errors increasing the chances that the final LOS velocity is estimated using good quality data (see Section 2.2). An interferogram network containing unwrapping errors would translate into an inaccurate LOS velocity map. In areas of poor coherence we recommend using the small baseline processing technique in order to minimise the influence of these errors in the final LOS velocity estimate.

Furthermore, our creep estimates from direct offset measurements at the fault (Figure 2.5) agree well with the estimates from the profile modelling (Figure 2.9). For profile A-A', the direct offset method gives ~ 8 mm/yr compared to 5 (2-8, 95% CI) mm/yr from the model; for profile B-B', the direct offset method gives ~ 6 mm/yr compared to 5 (3-8, 95% CI) mm/yr from the model, and for profile C-C', the direct offset give ~ 3 mm/yr compared to 2 (0-13, 95% CI) mm/yr from the model. The corrected GPS displacement time series (Figure 2.12b) allows us to directly estimate the fault creep rate for the Envisat period (2002-2010). From the GPS alone we estimate a creep rate of 9 ± 4 mm/yr, which compares well with our estimate of ~ 6 mm/yr (from the direct offsets at location of profile B-B').

Our estimates for interseismic locking depth and fault slip rate show a clear trade-off (upper left in Figure 2.11). This is an expected feature of *Savage and Burford (1973)*-type elastic models (e.g. *Wright et al., 2001a*, *Walters et al., 2011*), where a larger slip rate can be compensated by a deeper locking depth. This trade-off is the main cause of the large confidence interval on these parameters. Therefore, we cannot discount a deeper locking depth and faster slip rate than our MAP estimates as these still fall within the confidence limit of our solutions. We have also tried a model for profile B-B' where we fix just the locking depth to 15 km. Our best-fit results for the slip rate, creep rate and creep depth are 20 mm/yr, 6 mm/yr and 10 km respectively. As expected from the trade-offs the slip rate is higher but the creep rate is similar to our MAP solution of 5 mm/yr. The creep depth is a little deeper than the MAP estimate of 8km.

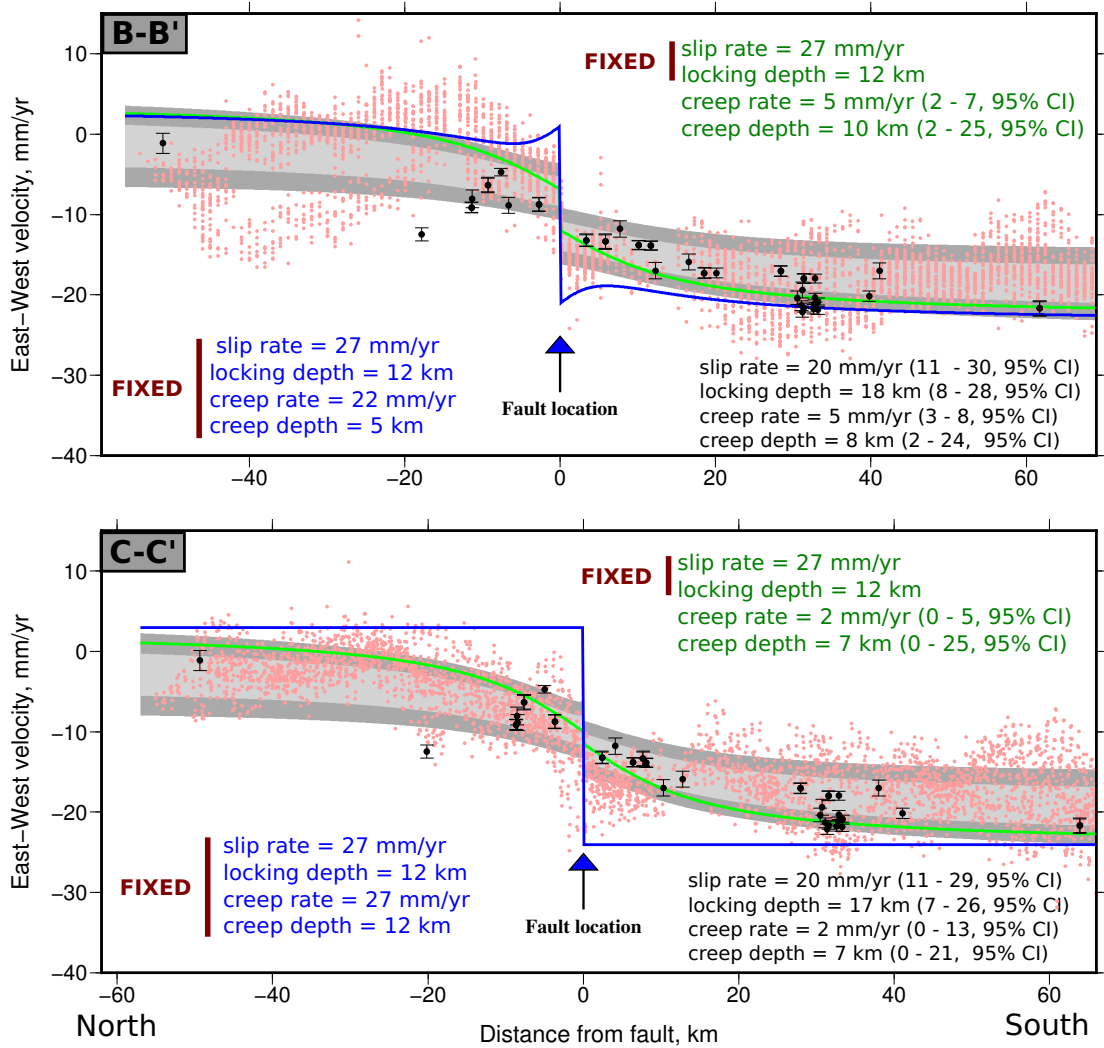


Figure 2.14: Projected east-west velocities along the profiles B-B' and C-C' indicated in Figure 2.6a in the paper. The dark and light grey areas represent the 95% and 68% confidence bounds for our preferred MAP solution shown in Figure 2.9. The green line shows the best fit result when we fix the fault slip rate and locking depth to the values used in *Cakir et al. (2012)* (27 mm/yr for the slip rate and 12 km for the locking depth) and invert for the creep rate and creep depth. In blue is a forward calculation using the best-fit parameter values for this location from *Cakir et al. (2012)*.

Our MAP fault slip rates are consistent with previous work in this region using GPS alone (19 mm/yr, 20 mm/yr and 20 mm/yr from our profiles compared to 11-26 mm/yr from published GPS studies) (e.g. *Straub et al., 1997, Ayhan et al., 2002, Reilinger et al., 2006, Aktug et al., 2009, Ergintav et al., 2014*).

2.7.2 Time series

Our displacement time series model based on rate-and-state-dependent friction is consistent with both the GPS and InSAR displacements (Figure 2.12). Note that this model assumes that the maximum coseismic slip is not collocated with the postseismic creep. This is required because in regions that have undergone coseismic slip the change in stress due to the earthquake, $\Delta\tau$, is negative and this rate-and-state model predicts re-locking. However, if the maximum coseismic slip zone is not collocated with the creeping zone then afterslip can occur. The assumptions holds in our case because the maximum coseismic slip occurred at depths of around 11 km (*Feigl et al., 2002*) while our observed creep occurs in the upper ~ 8 km or less (Figure 2.9).

The model predicts that following the 1999 Izmit earthquake the fault experienced a period of rapid afterslip with an initial maximum rate of 2.9 ± 0.4 mm/day or 1.1 ± 0.2 m/year. This estimate is slightly lower than that of *Bürgmann et al. (2002b)* who found a maximum afterslip rate of ~ 1.4 m/yr in this region using GPS alone. This discrepancy could be due to the simplicity of our model and the fact that our maximum afterslip velocity is a depth-averaged value and neglects any off-fault deformation. The marginalised probability distributions for the rate-and-state model parameters show a clear trade-off between the two model parameters (Figure 2.13), where a faster maximum afterslip, v_{max} , rate can be compensated for by a smaller value of $\sigma(a-b)/k$.

Over the 5 years after the earthquake, the afterslip rate decays to a rate of ~ 5 mm/yr. Continued afterslip five years after the earthquake is not completely unexpected. *Rubin and Ampuero (2005)* define the end of the afterslip period to be the time at which the deceleration vanishes. *Segall (2010)* showed that an estimate of the duration of postseismic afterslip can be determined by:

$$t_{post} = \frac{d_c}{v_{plate}} \frac{k_c}{k}, \quad (2.6)$$

where d_c is the critical slip distance from rate-and-state-dependent friction laws, v_{plate} is the long term fault parallel loading rate, k_c the critical stiffness and k , the stiffness. It is reasonable to associate k_c/k with the ratio of the area of the rupture to that of the nucleation zone. Using laboratory estimates of d_c (e.g. *Scholz, 1988, Dieterich and Kilgore, 1994*), the values for d_c/v_{plate} are of the order 10^4 to 10^5 seconds, so t_{post} could range from months to years.

Hearn et al. (2002) calculated a 1-3 MPa change in coseismic shear stress, $\Delta\tau$, for the uppermost 5 km of the crust at the fault location where we calculate the maximum

fault creep. Assuming $\Delta\tau$ is positive at steady state we can use equation 2.7 (Segall, 2010) to estimate $\sigma(a - b)$.

$$v_{max} = v_p \exp(\Delta\tau / (a - b)\sigma), \quad (2.7)$$

From our displacement time series, we have $\sigma(a - b)/k = 51$ mm, giving stiffness, k , equal to 3-8 MPa/m. The normal stress between 1 and 5 km is 30-130 MPa (assuming lithostatic pressures), which gives us an estimate for the rate-and-state parameter $(a - b)$ of 0.001-0.014. Using a steady-state fault creep rate of 5 mm/yr we arrive at a frictional shear stressing rate of 0.015-0.04 MPa/yr. Our estimate for the rate-and-state parameter $(a - b)$ compares well with the results of Kaneko *et al.* (2013) who determined a value between 0.002 and 0.008 for the Ismetpasa section of the NAF. Our estimates are larger than the range estimated for the Parkfield segment of the San Andreas Fault (0.0006-0.0018) by Johnson *et al.* (2006). However, the authors of that study acknowledge that their estimates for $(a - b)$ are low and explain it by assuming the afterslip occurs in a transition zone between velocity-weakening (negative $a - b$) and velocity-strengthening (positive $a - b$). Laboratory experiments give values for $a - b$, in the range -0.0019-0.0070 for upper crustal rocks such as sandstones, slates, marbles and granites (Ikari *et al.*, 2011). However, as noted by Marone (1998), laboratory friction experiments are highly idealised relative to natural faults and so it is not clear whether a comparison of laboratory-derived friction parameters are relevant to earthquake faulting.

The simple afterslip model used in this study has several important limitations. Firstly the model is 1-D and therefore assumes the fault has homogeneous properties. There have been several successful attempts in describing the general aseismic behaviour of faults and its spatial variability using 2D spring slider fault models (e.g. Dieterich, 1992, Perfettini *et al.*, 2003a) as well as new 3D modelling techniques (e.g. Jolivet *et al.*, 2015).

As noted by Perfettini and Avouac (2004), 1D afterslip models like the one used in this study do not take into account the viscous relaxation of the deep crust or upper mantle. For large events like the Mw 7.4 Izmit earthquake we can expect a transfer of stress to regions below the seismogenic zone.

Another limitation is that we do not consider the role of aftershocks after the Izmit earthquake, which may also accumulate slip.

2.7.3 Moment release

The total moment released by the aseismic creep at the Izmit rupture between 1999 and 2012 (assuming fault creep extends down to 8 km along the 80 km length of the creeping segment) is of the order of 10^{18} Nm. The total moment released in the Izmit earthquake was on the order of 10^{20} Nm (Pinar *et al.*, 2001, Delouis *et al.*, 2002).

Bürgmann et al. (2002b) modelled the complete distribution of afterslip on and below the coseismic slip patch in the 87-day period after the Izmit earthquake and found that the total moment released due to afterslip on the entire fault was of the order 10^{19} Nm. This is still only 10% of the coseismic moment release but it would have altered the stresses in the surrounding crust and could have contributed to the triggering of the Düzce earthquake a few months later.

Currently, the near steady-state creep rate of 5 mm/yr is only releasing about 5-40% of the accumulating moment from plate loading (assuming creep extends down to 8 km depth and fault loading rate of 20 mm/yr (9-27, 95% CI) to a locking depth of 17 km (8-28, 95% CI)). Therefore, in terms of the moment budget, and thus stress transfer and seismic hazard, the effect of the shallow, aseismic slip in the past decade is small compared to that from plate loading.

2.7.4 Implications for the shallow slip deficit

Inversions of coseismic surface deformation data from large ($M_w \sim 7$) strike-slip earthquakes indicate that the coseismic slip in the uppermost section of the seismogenic crust is often systematically less than that at seismogenic depths (4-10 km) (e.g. *Simons et al., 2002*, *Fialko et al., 2005*, *Bilham, 2010*, *Dolan and Haravitch, 2014*). Despite variations between different inversion results, coseismic slip studies of the Izmit earthquake also show this so-called ‘shallow slip deficit’. *Delouis et al. (2002)* and *Feigl et al. (2002)*’s slip inversions reveal that the average coseismic slip in the mid-crust (between 6-15 km) beneath the western margin of Lake Sapanca was 5-7 m while in the shallow crust (<6 km) the average coseismic slip was 3-4 m, producing a coseismic slip deficit of 2-3 m in the shallow crust.

There are two possible explanations for the origin of the shallow slip deficit: the deficit arises due to distributed off-fault deformation in the uppermost crust, in which case it is not strictly speaking a deficit as such, or the shallow slip deficit is accounted for by aseismic slip on the shallow fault.

The mean recurrence time for earthquakes along the North Anatolian Fault is ~ 200 years (*Stein et al., 1997*). Projecting our afterslip model 200 years into the future we find the total average displacement due to afterslip is 1-1.3 m, which is 30-65% of the slip deficit. Therefore, the total steady-state afterslip (integrated over the earthquake cycle) is insufficient to account for all of the shallow coseismic slip deficit. If the deficit is to be explained by slip on the fault during the period between earthquakes (but not by afterslip), it must therefore occur during phases of transient creep. No such events have been observed at this location during the period of good geodetic observations (since ~ 1995). Alternatively, the slip deficit could be due to distributed inelastic coseismic deformation in the uppermost few kilometres of the crust.

Whether this deformation occurs in the coseismic period or in the interseismic period is difficult to tell. *Wright et al. (2001b)* noted that the Izmit earthquake triggered

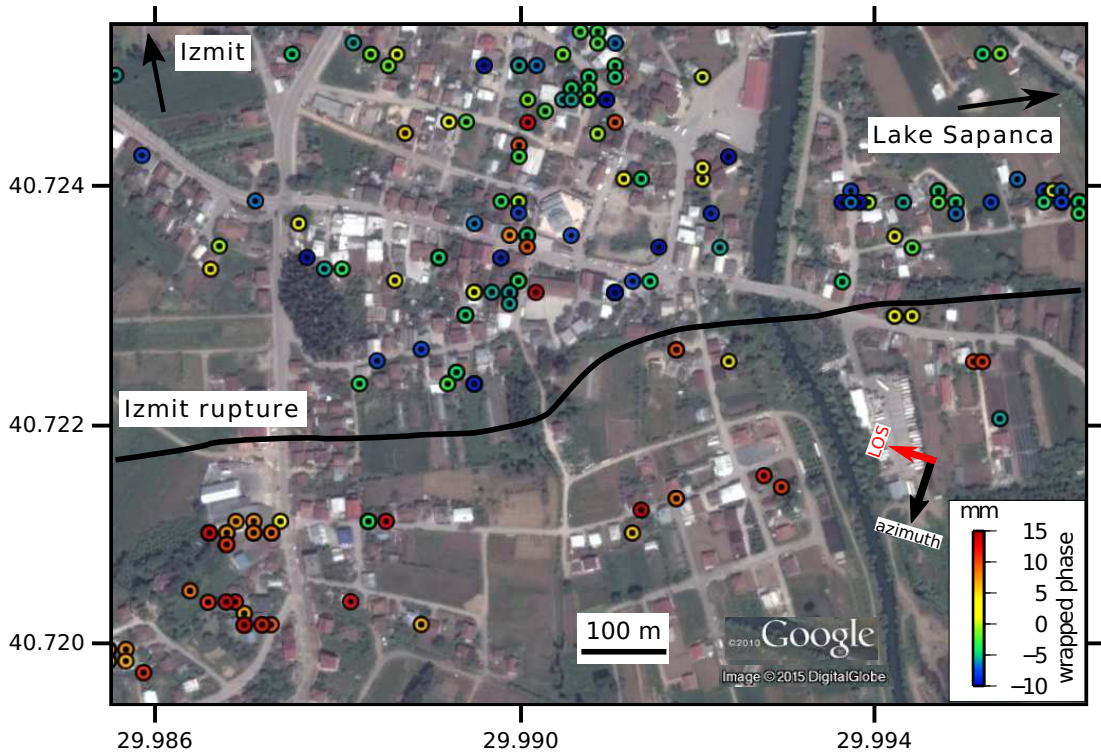


Figure 2.15: A zoom-in of the region around the fault south of the city of Izmit, for an interferogram spanning two and a half years (20070212-20090810) for descending track 293. The bold black line marks the 1999 Izmit rupture. The circles are the InSAR Persistent Scatterer (PS) pixels, colour coded by the wrapped phase. Negative phase values correspond to a decrease in range, i.e. motion towards the satellite, while positive values are an increase in range indicating motion away from the satellite. There is a clear discontinuity between the dominantly green and blue (-10 to -5 mm) pixels to the north and the red pixels to the south (7 to 13 mm) of the fault, consistent with fault creep with a right-lateral sense of motion across the fault. The distance between pixels either side of the fault that show a clear displacement discontinuity is around 100 m.

shallow slip on a smaller fault south of the main rupture. Their coseismic interferogram also shows small off-fault movements on other local faults. The integrated slip from all the small triggered slip events since 1999 has not been clearly documented, but it is unlikely to be of the order of a few metres. Nevertheless, it could help explain a portion of the shallow slip deficit (*Dolan and Haravitch, 2014*).

Slow, long-term distributed deformation (*Fialko et al., 2005*), possibly due to viscous creep mechanisms, is also difficult to resolve due to the noise in the InSAR data. Figure 2.15 shows that we can constrain the surface deformation to be occurring within ~ 50 metres either side of the fault, if not on the fault plane itself. Our fault creep time series uses GPS stations located ~ 3 km from the fault. Thus any off-fault deformation within this distance would have been subsumed and represented as fault creep in our time series model. Distributed deformation mechanisms active during the interseismic period in any case would be expected to produce deformation at longer wavelengths.

A dense network of long-term continuous GPS measurements near the fault would help to constrain the role of viscoelastic relaxation.

2.8 Conclusion

We have investigated the spatial distribution of aseismic creep on the Izmit and Düzce sections of the North Anatolian Fault using Envisat ASAR images in both ascending and descending geometries between 2002 and 2010. Our results show a discontinuity in the LOS velocities at the surface trace of the 1999 Izmit earthquake, consistent with aseismic creep on the shallow fault. Fault creep on the Izmit rupture at the end of our InSAR observation period (2010) occurs at an average rate of ~ 5 mm/yr and extends about 80 km from the Gulf of Izmit in the west to about 30.7° E in the east. However, it is likely that this extends further west into the Gulf making our estimate of the length of the creeping segment a lower bound. We observe a time-averaged maximum fault creep rate of 11 ± 2 mm/yr near the city of Izmit for the period 2002-2010. We also find that the Adapazari basin region is subsiding at a rate of about 6 mm/yr. The causes of this subsidence remain unclear but could be related to water pumping or tectonic subsidence related to movement on a non-planar fault. The time series of relative displacement change between two points either side of the fault is consistent with an afterslip model that predicts a period of rapid deceleration from a maximum velocity of 2.9 ± 0.4 mm/day immediately after the earthquake to a near steady-state value of ~ 5 mm/yr after about 5 years, implying that aseismic creep could continue for many years. The moment released by the shallow aseismic slip between the period 1999-2012 is small compared to the moment released by the Izmit earthquake. The current rate of moment release due to aseismic slip is about 5-40% of the rate of moment accumulation from plate loading. Therefore, we conclude that the NAF in this region is mostly locked and accumulating strain, and the long-term impact of shallow aseismic creep is negligible in terms of stress transfer and seismic hazard. Projecting our afterslip model 200 years into the future we predict the total displacement due to shallow afterslip to be 1-1.3 m. This is insufficient to account for the 2-3 m slip deficit in the shallow crust (< 6 km) observed in coseismic slip studies of the Izmit earthquake. Distributed inelastic deformation in the uppermost few kilometres of the crust or slip transients during the interseismic period are likely to be important mechanisms for generating the shallow slip deficit.

Acknowledgments

This work has been supported by the Natural Environment Research Council project grant number: NE/I028017/1, which supports the lead author's research studentship via the FaultLab project at the University of Leeds. The Envisat satellite data is freely

available and were obtained from the European Space Agency's Geohazard Supersites project. Our MCMC algorithm was developed using Aslak Grinsted's open source GWCMC Hammer algorithm available on the mathworks website. The GPS data were obtained from the Global Strain Rate Model project website (<http://gsrm.unavco.org>). Most of the figures in this paper were made using the public domain Generic Mapping Tools (GMT) software (*Wessel and Smith, 2001*). COMET is the Centre for the Observation and Monitoring of Earthquakes, Volcanoes and Tectonics. We would like to thank Romain Jolivet and Eric Lindsey for providing useful suggestions that helped improve the quality of the manuscript. Results can be obtained by contacting the lead author (eeehu@leeds.ac.uk).

References

- Aktug, B., J. Nocquet, A. Cingöz, B. Parsons, Y. Erkan, P. England, O. Lenk, M. Gürdal, A. Kilicoglu, H. Akdeniz, et al. (2009), Deformation of western Turkey from a combination of permanent and campaign GPS data: Limits to block-like behavior, *Journal of Geophysical Research: Solid Earth (1978–2012)*, 114(B10). [2.1](#), [2.7.1](#)
- Akyuz, H. S. (2002), Surface rupture and slip distribution of the 12 november 1999 Duzce earthquake (M 7.1), North Anatolian Fault, Bolu, Turkey, *The Bulletin of the Seismological Society of America*, 92, 61–66, doi:[10.1785/0120000840](#). [2.1](#)
- Avouac, J.-P. (2015), From geodetic imaging of seismic and aseismic fault slip to dynamic modeling of the seismic cycle, *Annual Review of Earth and Planetary Sciences*, 43(1), 233–271, doi:[10.1146/annurev-earth-060614-105302](#). [2.1](#)
- Ayhan, M. E., C. Demir, O. Lenk, A. Kiliçoglu, Y. Altiner, A. A. Barka, S. Ergintav, and H. Özener (2002), Interseismic strain accumulation in the Marmara Sea region, *Bulletin of the Seismological Society of America*, 92(1), 216–229. [2.1](#), [2.7.1](#)
- Barka, A. (1996), Slip distribution along the North Anatolian Fault associated with the large earthquakes of the period 1939 to 1967, *The Bulletin of the Seismological Society of America*, 86, 1238–1254. [2.1](#)
- Barka, A., H. S. Akyz, E. Altunel, G. Sunal, Z. akir, A. Dikbas, B. Yerli, R. Armijo, B. Meyer, J. B. de Chabalier, T. Rockwell, J. R. Dolan, R. Hartleb, T. Dawson, S. Christofferson, A. Tucker, T. Fumal, R. Langridge, H. Stenner, W. Lettis, J. Bachhuber, and W. Page (2002), The surface rupture and slip distribution of the 17 august 1999 Izmit earthquake (M 7.4), North Anatolian Fault, *Bulletin of the Seismological Society of America*, 92(1), 43–60, doi:[10.1785/0120000841](#). [2.1](#)
- Bekaert, D., A. Hooper, and T. Wright (2015b), Reassessing the 2006 Guerrero slow-slip event, Mexico: Implications for large earthquakes in the Guerrero Gap, *Journal of Geophysical Research: Solid Earth*, 120(2), 1357–1375, doi:[10.1002/2014JB011557](#). [2.3](#)
- Bekaert, D., R. Walters, T. Wright, A. Hooper, and D. Parker (2015c), Statistical comparison of InSAR tropospheric correction techniques, *Remote Sensing of Environment*, 170, 40–47, doi:[10.1002/2014JB011557](#). [2.2.1](#)
- Bekaert, D. P. S., A. Hooper, and T. J. Wright (2015a), A spatially variable power-law tropospheric correction technique for InSAR data, *Journal of Geophysical Research (Solid Earth)*, 120, 1345–1356, doi:[10.1002/2014JB011558](#). [2.2.1](#)
- Biggs, J., T. Wright, Z. Lu, and B. Parsons (2007), Multi-interferogram method for measuring interseismic deformation: Denali Fault, Alaska, *Geophysical Journal International*, 170(3), 1165–1179, doi:[10.1111/j.1365-246X.2007.03415.x](#). [2.2](#)
- Bilgin, T. (1984), Alluvial geomorphology and Quaternary geomorphological evolution of Adapazar Plain and Sapanca depression (in Turkish), *Istanbul University, Faculty of Letters Publication*, (2572), 1–199. [2.4.1](#)

- Bilham, R. (2010), Lessons from the Haiti earthquake, *Nature*, 463(7283), 878–879. [2.7.4](#)
- Bürgmann, R., D. Schmidt, R. M. Nadeau, M. d’Alessio, E. Fielding, D. Manaker, T. V. McEvilly, and M. H. Murray (2000), Earthquake potential along the Northern Hayward Fault, California, *Science*, 289, 1178–1182, doi:[10.1126/science.289.5482.1178](#). [2.1](#)
- Bürgmann, R., S. Ergintav, P. Segall, E. H. Hearn, S. McClusky, R. E. Reilinger, H. Woith, and J. Zschau (2002b), Time-dependent distributed afterslip on and deep below the Izmit earthquake rupture, *Bulletin of the Seismological Society of America*, 92(1), 126–137. [2.1](#), [2.7.2](#), [2.7.3](#)
- Cakir, Z., S. Ergintav, H. Ozener, U. Dogan, A. M. Akoglu, M. Meghraoui, and R. Reilinger (2012), Onset of aseismic creep on major strike-slip faults, *Geology*, 40, 1115–1118, doi:[10.1130/G33522.1](#). [2.1](#), [2.3](#), [2.4.1](#), [2.6](#), [2.7.1](#), [2.7.1](#), [2.14](#)
- Cetin, E., Z. Cakir, M. Meghraoui, S. Ergintav, and A. M. Akoglu (2014), Extent and distribution of aseismic slip on the Isetmpasa segment of the North Anatolian Fault (Turkey) from persistent scatterer InSAR, *Geochemistry, Geophysics, Geosystems*, 15, 2883–2894, doi:[10.1002/2014GC005307](#). [2.1](#)
- Champanois, J., B. Fruneau, E. Pathier, B. Deffontaines, K.-C. Lin, and J.-C. Hu (2012), Monitoring of active tectonic deformations in the Longitudinal Valley (Eastern Taiwan) using persistent scatterer InSAR method with ALOS PALSAR data, *Earth and Planetary Science Letters*, 337, 144–155, doi:[10.1016/j.epsl.2012.05.025](#). [2.1](#)
- Dee, D. P., S. M. Uppala, A. J. Simmons, P. Berrisford, P. Poli, S. Kobayashi, U. Andrae, M. A. Balmaseda, G. Balsamo, P. Bauer, P. Bechtold, A. C. M. Beljaars, L. van de Berg, J. Bidlot, N. Bormann, C. Delsol, R. Dragani, M. Fuentes, A. J. Geer, L. Haimberger, S. B. Healy, H. Hersbach, E. V. Hólm, L. Isaksen, P. Kállberg, M. Köhler, M. Matricardi, A. P. McNally, B. M. Monge-Sanz, J.-J. Morcrette, B.-K. Park, C. Peubey, P. de Rosnay, C. Tavolato, J.-N. Thépaut, and F. Vitart (2011), The ERA-Interim reanalysis: configuration and performance of the data assimilation system, *Quarterly Journal of the Royal Meteorological Society*, 137, 553–597, doi:[10.1002/qj.828](#). [2.2.1](#)
- Delouis, B., D. Giardini, P. Lundgren, and J. Salichon (2002), Joint inversion of InSAR, GPS, teleseismic, and strong-motion data for the spatial and temporal distribution of earthquake slip: Application to the 1999 Izmit mainshock, *Bulletin of the Seismological Society of America*, 92(1), 278–299. [2.7.3](#), [2.7.4](#)
- Dieterich, J. H. (1992), Earthquake nucleation on faults with rate-and state-dependent strength, *Tectonophysics*, 211(1), 115–134. [2.7.2](#)
- Dieterich, J. H., and B. D. Kilgore (1994), Direct observation of frictional contacts: New insights for state-dependent properties, *Pure and Applied Geophysics*, 143(1-3), 283–302. [2.7.2](#)
- Doin, M.-P., C. Lasserre, G. Peltzer, O. Cavali, and C. Doubre (2009), Corrections of stratified tropospheric delays in SAR interferometry: Validation with global atmospheric models, *Journal of Applied Geophysics*, 69(1), 35 – 50, doi:[http://dx.doi.org/10.1016/j.jappgeo.2009.03.010](#). [2.2.1](#)
- Dolan, J. F., and B. D. Haravitch (2014), How well do surface slip measurements track slip at depth in large strike-slip earthquakes? The importance of fault structural maturity in controlling on-fault slip versus off-fault surface deformation, *Earth and Planetary Science Letters*, 388, 38–47. [2.7.4](#)
- Efron, B., and R. Tibshirani (1986), Bootstrap methods for standard errors, confidence intervals, and other measures of statistical accuracy, *Statistical science*, pp. 54–75. [2.3](#)

- Emre, Ö., T. Erkal, A. Tchepalyga, N. Kazancı, M. Keçer, and E. Ünay (1998), Neogene-quaternary evolution of the eastern Marmara region, Northwest Turkey, *Bulletin of the Mineral Research and Exploration Institute of Turkey*, 120, 119–145. [2.4.1](#)
- Ergintav, S., R. Bürgmann, S. McClusky, R. Cakmak, R. Reilinger, O. Lenk, A. Barka, and H. Özener (2002), Postseismic deformation near the Izmit earthquake (17 August 1999, M 7.5) rupture zone, *Bulletin of the Seismological Society of America*, 92(1), 194–207. [2.2.2](#)
- Ergintav, S., S. McClusky, E. Hearn, R. Reilinger, R. Cakmak, T. Herring, H. Ozener, O. Lenk, and E. Tari (2009), Seven years of postseismic deformation following the 1999, M = 7.4 and M = 7.2, Izmit-Düzce, Turkey earthquake sequence, *Journal of Geophysical Research (Solid Earth)*, 114, B07403, doi:[10.1029/2008JB006021](#). [2.1](#)
- Ergintav, S., R. Reilinger, R. Çakmak, M. Floyd, Z. Cakir, U. Doğan, R. King, S. McClusky, and H. Özener (2014), Istanbul’s earthquake hot spots: Geodetic constraints on strain accumulation along faults in the Marmara seismic gap, *Geophysical Research Letters*, 41(16), 5783–5788. [2.1](#), [2.7.1](#)
- Erinç, S., and N. Tunçdilek (1952), The agricultural regions of Turkey, *Geographical Review*, pp. 179–203. [2.4.1](#)
- Farr, T. G., P. A. Rosen, E. Caro, R. Crippen, R. Duren, S. Hensley, M. Kobrick, M. Paller, E. Rodriguez, L. Roth, D. Seal, S. Shaffer, J. Shimada, J. Umland, M. Werner, M. Oskin, D. Burbank, and D. Alsdorf (2007), The shuttle radar topography mission, *Reviews of Geophysics*, 45, RG2004, doi:[10.1029/2005RG000183](#). [2.2](#)
- Feigl, K. L., F. Sarti, H. Vadon, S. McClusky, S. Ergintav, P. Durand, R. Bürgmann, A. Rigo, D. Massonnet, and R. Reilinger (2002), Estimating slip distribution for the Izmit mainshock from coseismic GPS, ERS-1, RADARSAT, and SPOT measurements, *Bulletin of the Seismological Society of America*, 92(1), 138–160. [2.7.2](#), [2.7.4](#)
- Fialko, Y., D. Sandwell, M. Simons, and P. Rosen (2005), Three-dimensional deformation caused by the Bam, Iran, earthquake and the origin of shallow slip deficit, *Nature*, 435(7040), 295–299. [2.7.4](#), [2.7.4](#)
- Foreman-Mackey, D., D. W. Hogg, D. Lang, and J. Goodman (2013), emcee: The MCMC hammer, *Publications of the Astronomical Society of the Pacific*, 125(925), 306–312. [2.5](#)
- Gedikli, B. (2004), Urbanization and land-use planning in Adapazari (Turkey) reconsidered after the 1999 earthquake, *Journal of Housing and the Built Environment*, 20(1), 79–91. [2.4.1](#)
- Goodman, J., and J. Weare (2010), Ensemble samplers with affine invariance, *Communications in Applied Mathematics and Computational Science*, 5, 65–80, doi:[10.2140/camcos.2010.5.65](#). [2.5](#)
- Hearn, E. H., R. Bürgmann, and R. E. Reilinger (2002), Dynamics of Izmit earthquake postseismic deformation and loading of the Düzce earthquake hypocenter, *Bulletin of the Seismological Society of America*, 92(1), 172–193. [2.7.2](#)
- Hooper, A. (2008), A multi-temporal InSAR method incorporating both persistent scatterer and small baseline approaches, *Geophysical Research Letters*, 35, L16302, doi:[10.1029/2008GL034654](#). [2.2](#)
- Hooper, A., D. Bekaert, K. Spaans, and M. Arikan (2012), Recent advances in SAR interferometry time series analysis for measuring crustal deformation, *Tectonophysics*, 514, 1–13, doi:[10.1016/j.tecto.2011.10.013](#). [2.2](#)

- Hubert-Ferrari, A., A. Barka, E. Jacques, S. S. Nalbant, B. Meyer, R. Armijo, P. Tapponnier, and G. C. P. King (2000), Seismic hazard in the Marmara Sea region following the 17 August 1999 Izmit earthquake, *Nature*, *404*, 269–273. [2.1](#), [2.1](#)
- Ikari, M. J., A. R. Niemeijer, and C. Marone (2011), The role of fault zone fabric and lithification state on frictional strength, constitutive behavior, and deformation microstructure, *Journal of Geophysical Research: Solid Earth*, *116*(B8). [2.7.2](#)
- Ikiel, C., A. A. Tutucu, B. Ustaoglu, and D. E. Kilic (2012), Land use and land cover (LULC) classification using Spot-5 image in the Adapazari Plain and its surroundings, Turkey, *The Online Journal of Science and Technology*, *2*(2). [2.4.1](#)
- Jackson, J., and D. McKenzie (1984), Active tectonics of the Alpine/Himalayan belt between western Turkey and Pakistan, *Geophysical Journal*, *77*, 185–264, doi:10.1111/j.1365-246X.1984.tb01931.x. [2.6](#), [2.4.1](#)
- Johnson, K. M., R. Bürgmann, and K. Larson (2006), Frictional properties on the San Andreas fault near Parkfield, California, inferred from models of afterslip following the 2004 earthquake, *Bulletin of the Seismological Society of America*, *96*(4B), S321–S338. [2.7.2](#)
- Jolivet, R., R. Grandin, C. Lasserre, M.-P. Doin, and G. Peltzer (2011), Systematic InSAR tropospheric phase delay corrections from global meteorological reanalysis data, *Geophysical Research Letters*, *38*, L17311, doi:10.1029/2011GL048757. [2.2.1](#)
- Jolivet, R., P. S. Agram, N. Y. Lin, M. Simons, M.-P. Doin, G. Peltzer, and Z. Li (2014), Improving InSAR geodesy using global atmospheric models, *Journal of Geophysical Research: Solid Earth*, *119*(3), 2324–2341. [2.2.1](#)
- Jolivet, R., M. Simons, P. Agram, Z. Duputel, and Z.-K. Shen (2015), Aseismic slip and seismogenic coupling along the central San Andreas Fault, *Geophysical Research Letters*, *42*(2), 297–306. [2.1](#), [2.7.2](#)
- Kampes, B. M., R. F. Hanssen, and Z. Perski (2003), Radar interferometry with public domain tools, in *FRINGE 2003 Workshop, ESA Special Publication*, vol. 550, p. 10. [2.2](#)
- Kaneko, Y., Y. Fialko, D. T. Sandwell, X. Tong, and M. Furuya (2013), Interseismic deformation and creep along the central section of the North Anatolian Fault (Turkey): InSAR observations and implications for rate-and-state friction properties, *Journal of Geophysical Research (Solid Earth)*, *118*, 316–331, doi:10.1029/2012JB009661. [2.1](#), [2.6](#), [2.7.2](#)
- Karahan, A. E., H. Berckhemer, and B. Baier (2001), Crustal structure at the western end of the North Anatolian Fault Zone from deep seismic sounding, *Annali Di Geofisica*, *44*(1). [2.4.1](#)
- Kreemer, C., G. Blewitt, and E. C. Klein (2014), A geodetic plate motion and global strain rate model, *Geochemistry, Geophysics, Geosystems*, *15*(10), 3849–3889. [2.1](#), [2.2.2](#)
- Le Pichon, X., N. Chamot-Rooke, C. Rangin, and A. Sengör (2003), The North Anatolian fault in the Sea of Marmara, *Journal of Geophysical Research: Solid Earth (1978–2012)*, *108*(B4). [2.1](#)
- Marinkovic, P., and Y. Larsen (2013), Consequences of long-term ASAR local oscillator frequency decay—an empirical study of 10 years of data, in *Living Planet Symposium, Edinburgh. Frascati: European Space Agency (2013, September)*. [2.2](#)
- Marone, C. (1998), Laboratory-derived friction laws and their application to seismic faulting, *Annual Review of Earth and Planetary Sciences*, *26*(1), 643–696. [2.7.2](#)

- Marone, C. J., C. Scholtz, and R. Bilham (1991), On the mechanics of earthquake afterslip, *Journal of Geophysical Research: Solid Earth (1978–2012)*, *96*(B5), 8441–8452. [2.6](#)
- Maurer, J., and K. Johnson (2014), Fault coupling and potential for earthquakes on the creeping section of the central San Andreas Fault, *Journal of Geophysical Research: Solid Earth*, *119*(5), 4414–4428. [2.1](#)
- Meade, B. J., B. H. Hager, S. C. McClusky, R. E. Reilinger, S. Ergintav, O. Lenk, A. Barka, and H. Özener (2002), Estimates of seismic potential in the Marmara Sea region from block models of secular deformation constrained by global positioning system measurements, *The Bulletin of the Seismological Society of America*, *92*, 208–215, doi:[10.1785/0120000837](#). [2.1](#)
- Michel, R., and J.-P. Avouac (2002), Deformation due to the 17 August 1999 Izmit, Turkey, earthquake measured from SPOT images, *Journal of Geophysical Research: Solid Earth (1978–2012)*, *107*(B4), ETG–2. [2.5](#)
- Neugebauer, J. (1995), Structures and kinematics of the north Anatolian Fault zone, Adapazarı-Bolu region, northwest Turkey, *Tectonophysics*, *243*(1), 119–134. [2.4.1](#)
- Neugebauer, J., M. Löffler, H. Berckhemer, and A. Yatman (1997), Seismic observations at an overstep of the western North Anatolian Fault (Abant–Sapanca region, Turkey), *Geologische rundschau*, *86*(1), 93–102. [2.4.1](#)
- Perfettini, H., and J.-P. Avouac (2004), Postseismic relaxation driven by brittle creep: A possible mechanism to reconcile geodetic measurements and the decay rate of aftershocks, application to the Chi-Chi earthquake, Taiwan, *Journal of Geophysical Research: Solid Earth*, *109*(B2). [2.7.2](#)
- Perfettini, H., J. Schmittbuhl, and A. Cochard (2003a), Shear and normal load perturbations on a two-dimensional continuous fault: 1. static triggering, *Journal of Geophysical Research: Solid Earth*, *108*(B9). [2.7.2](#)
- Pinar, A., Y. Honkura, and K. Kuge (2001), Seismic activity triggered by the 1999 Izmit earthquake and its implications for the assessment of future seismic risk, *Geophysical Journal International*, *146*(1), F1–F7. [2.7.3](#)
- Poyraz, S. A., M. U. Teoman, N. Türkelli, M. Kahraman, D. Cambaz, A. Mutlu, S. Rost, G. A. Houseman, D. A. Thompson, D. Cornwell, et al. (2015), New constraints on micro-seismicity and stress state in the western part of the North Anatolian Fault Zone: Observations from a dense seismic array, *Tectonophysics*, *656*, 190–201. [2.4.1](#)
- Reilinger, R., S. Ergintav, R. Bürgmann, S. McClusky, O. Lenk, A. Barka, O. Gurkan, L. Hearn, K. Feigl, R. Cakmak, et al. (2000), Coseismic and postseismic fault slip for the 17 August 1999, M= 7.5, Izmit, Turkey earthquake, *Science*, *289*(5484), 1519–1524. [2.2.2](#), [2.5](#)
- Reilinger, R., S. McClusky, P. Vernant, S. Lawrence, S. Ergintav, R. Cakmak, H. Özener, F. Kadirov, I. Guliev, R. Stepanyan, M. Nadariya, G. Hahubia, S. Mahmoud, K. Sakr, A. ArRajehi, D. Paradissis, A. Al-Aydrus, M. Prilepin, T. Guseva, E. Evren, A. Dmitrotsa, S. V. Filikov, F. Gomez, R. Al-Ghazzi, and G. Karam (2006), GPS constraints on continental deformation in the Africa-Arabia-Eurasia continental collision zone and implications for the dynamics of plate interactions, *Journal of Geophysical Research: Solid Earth*, *111*(B5), doi:[10.1029/2005JB004051](#). [2.1](#), [2.2.2](#), [2.7.1](#)
- Rice, J. R. (1993), Spatio-temporal complexity of slip on a fault, *Journal of Geophysical Research*, *98*, 9885–9907, doi:[10.1029/93JB00191](#). [2.1](#), [2.6](#)
- Rice, J. R., and A. L. Ruina (1983), Stability of steady frictional slipping, *Journal of Applied Mechanics*, *50*, 343, doi:[10.1115/1.3167042](#). [2.1](#), [2.6](#)

- Rosen, P. A., S. Hensley, G. Peltzer, and M. Simons (2004), Updated repeat orbit interferometry package released, *Eos, Transactions American Geophysical Union*, 85(5), 47–47, doi:10.1029/2004EO050004. 2.2
- Rubin, A. M., and J.-P. Ampuero (2005), Earthquake nucleation on (aging) rate and state faults, *Journal of Geophysical Research (Solid Earth)*, 110, B11312, doi:10.1029/2005JB003686. 2.7.2
- Ruina, A. (1983), Slip instability and state variable friction laws, *Journal of Geophysical Research*, 88, 10,359, doi:10.1029/JB088iB12p10359. 2.1, 2.6
- Savage, J. (1983), A dislocation model of strain accumulation and release at a subduction zone, *J. geophys. Res.*, 88(6), 4984–4996. 2.5
- Savage, J. C., and R. O. Burford (1973), Geodetic determination of relative plate motion in central California, *Journal of Geophysical Research*, 78, 832–845, doi:10.1029/JB078i005p00832. 2.5, 2.6, 2.7.1
- Schmidt, D. A., R. Bürgmann, R. M. Nadeau, and M. D’Alessio (2005), Distribution of aseismic slip rate on the Hayward fault inferred from seismic and geodetic data, *Journal of Geophysical Research (Solid Earth)*, 110, B08406, doi:10.1029/2004JB003397. 2.1
- Scholz, C. (1988), *The critical slip distance for seismic faulting*, Nature Publishing Group. 2.7.2
- Scholz, C. H. (2002), *The mechanics of earthquakes and faulting*, Cambridge university press. 2.6
- Segall, P. (2010), *Earthquake and Volcano Deformation*, Princeton University Press. 2.1, 2.6, 2.6, 2.7.2, 2.7.2
- SHW (1983), Sakarya Plain, *Hydrological Investigation Report, State Hydraulic Works, Ankara, Turkey in Turkish*. 2.4.1
- Simons, M., Y. Fialko, and L. Rivera (2002), Coseismic deformation from the 1999 Mw 7.1 Hector Mine, California, earthquake as inferred from InSAR and GPS observations, *Bulletin of the Seismological Society of America*, 92(4), 1390–1402. 2.7.4
- Stein, R. S., A. A. Barka, and J. H. Dieterich (1997), Progressive failure on the North Anatolian Fault since 1939 by earthquake stress triggering, *Geophysical Journal International*, 128, 594–604, doi:10.1111/j.1365-246X.1997.tb05321.x. 2.1, 2.7.4
- Straub, C., H.-G. Kahle, and C. Schindler (1997), GPS and geologic estimates of the tectonic activity in the Marmara Sea region, NW Anatolia, *Journal of Geophysical Research: Solid Earth (1978–2012)*, 102(B12), 27,587–27,601. 2.1, 2.7.1
- Thomas, M. Y., J.-P. Avouac, J. Champenois, J.-C. Lee, and L.-C. Kuo (2014), Spatiotemporal evolution of seismic and aseismic slip on the Longitudinal Valley Fault, Taiwan, *Journal of Geophysical Research: Solid Earth*, 119(6), 5114–5139. 2.1
- Tse, S. T., and J. R. Rice (1986), Crustal earthquake instability in relation to the depth variation of frictional slip properties, *Journal of Geophysical Research*, 91, 9452–9472, doi:10.1029/JB091iB09p09452. 2.1, 2.6
- Ulutaş, E., Ö. Coruk, and A. Karakaş (2011), A study of residuals for strong ground motions in Adapazari basin, NW Turkey, by ground motion prediction equations (GMPEs), *Studia Geophysica et Geodaetica*, 55(2), 213–240. 2.4.1
- Ünay, E., Ö. Emre, T. Erkal, and M. Keçer (2001), The rodent fauna from the Adapazari pull-apart basin (NW Anatolia): its bearings on the age of the North Anatolian fault, *Geodinamica Acta*, 14(1-3), 169–175. 2.4.1

- Walters, R., R. Holley, B. Parsons, and T. Wright (2011), Interseismic strain accumulation across the North Anatolian Fault from Envisat InSAR measurements, *Geophysical research letters*, *38*(5). [2.7.1](#)
- Walters, R. J., J. R. Elliott, Z. Li, and B. Parsons (2013), Rapid strain accumulation on the Ashkabad Fault (Turkmenistan) from atmosphere-corrected InSAR, *Journal of Geophysical Research: Solid Earth*, *118*(7), 3674–3690. [2.2.1](#)
- Weertman, J., and J. R. Weertman (1964), *Elementary Dislocation Theory*, New York: Macmillan. Pub. [2.5](#)
- Wessel, P., and W. H. Smith (2001), The Generic Mapping Tools. [2.8](#)
- Wright, T., B. Parsons, and E. Fielding (2001a), Measurement of interseismic strain accumulation across the North Anatolian Fault by satellite radar interferometry, *Geophysical Research Letters*, *28*(10), 2117–2120. [2.7.1](#)
- Wright, T., E. Fielding, and B. Parsons (2001b), Triggered slip: observations of the 17 August 1999 Izmit (Turkey) earthquake using radar interferometry, *Geophysical Research Letters*, *28*(6), 1079–1082. [2.1](#), [2.5](#), [2.7.4](#)
- Wright, T. J., B. E. Parsons, and L. Zhong (2004), Toward mapping surface deformation in three dimensions using InSAR, *Geophysical research letters*, *31*(1), L01,607–1. [2.4](#)
- Yigitbas, E., A. Elmas, A. Sefunc, and N. Ozer (2004), Major neotectonic features of eastern marmara region, turkey: development of the adapazari-karasu corridor and its tectonic significance, *Geological Journal*, *39*(2), 179–198. [2.4.1](#)

Chapter 3

Interseismic strain accumulation across the central North Anatolian Fault from iteratively unwrapped InSAR measurements

E. Hussain¹, A. Hooper¹, T.J. Wright¹, R.J. Walters², D.P.S. Bekaert³

¹ *COMET, School of Earth and Environment, University of Leeds, UK*

² *COMET, Department of Earth Sciences, University of Durham, UK*

³ *Jet Propulsion Laboratory, California Institute of Technology, Pasadena, USA.*

Formerly at COMET, University of Leeds, UK

Abstract

The North Anatolian Fault (NAF) is a major tectonic feature in the Middle-East and is the most active fault in Turkey. The central portion of the NAF is a region of GNSS scarcity. Previous studies of interseismic deformation have focused on the aseismic creep near the town of Ismetpasa using radar data acquired in a single line-of-sight direction, requiring several modelling assumptions. We have measured interseismic deformation across the NAF using both ascending and descending data from the Envisat satellite mission acquired between 2003-2010. Rather than rejecting incorrectly unwrapped areas in the interferograms, we develop a new iterative unwrapping procedure for small baseline Interferometric Synthetic Aperture Radar (InSAR) processing that expands the spatial coverage. Our method corrects unwrapping errors iteratively and increases the robustness of the unwrapping procedure. We remove long wavelength trends from the InSAR data using GNSS observations and deconvolve the InSAR velocities into fault-parallel motion. Profiles of fault-parallel velocity reveal a systematic eastward decrease in fault slip rate from 30 mm/yr (25-34, 95% CI) to 21 mm/yr (14-27, 95% CI) over a distance of ~ 200 km. Direct offset measurements across the fault reveal fault creep along a ~ 130 km section of the central NAF, with an average creep rate of 8 ± 2 mm/yr, and a maximum creep rate of 14 ± 2 mm/yr located ~ 30 km east of Ismetpasa. As fault creep is releasing only 30-40% of the long-term strain in the shallow crust, the fault is still capable of producing large, damaging earthquakes in this region.

3.1 Introduction

The North Anatolian Fault (NAF) is a major continental right-lateral transform fault located in northern Turkey. Together with the East Anatolian Fault, it facilitates the westward motion of Anatolia, caught in the convergence zone of the Eurasian plate with the Arabian plate (*McKenzie, 1972*). Since the 1939 Mw 7.9 Erzincan earthquake in eastern Turkey, the NAF has ruptured in a sequence of large (Mw >6.7) earthquakes with a dominant westward progression in seismicity (*Barka, 1996, Stein et al., 1997*). *Stein et al. (1997)* and *Hubert-Ferrari et al. (2000)* have interpreted this sequence to result from stress transfer along strike, where one earthquake brings the adjacent segment closer to failure.

In order to understand the role that the NAF plays in regional tectonics and seismic hazard, there have been numerous estimates of the fault slip rate for the NAF using present-day deformation measured with GNSS (e.g. *Straub et al., 1997, Reilinger et al., 2006, Ergintav et al., 2009*) or offset geological features (e.g. *Hubert-Ferrari et al., 2002, Pucci et al., 2008, Kozaci et al., 2009*). There have also been several InSAR-derived estimates of the fault slip rate, which have focused on the western or eastern regions of the NAF where the InSAR coherence is better (e.g. *Wright et al., 2001a, Cakir et al.,*

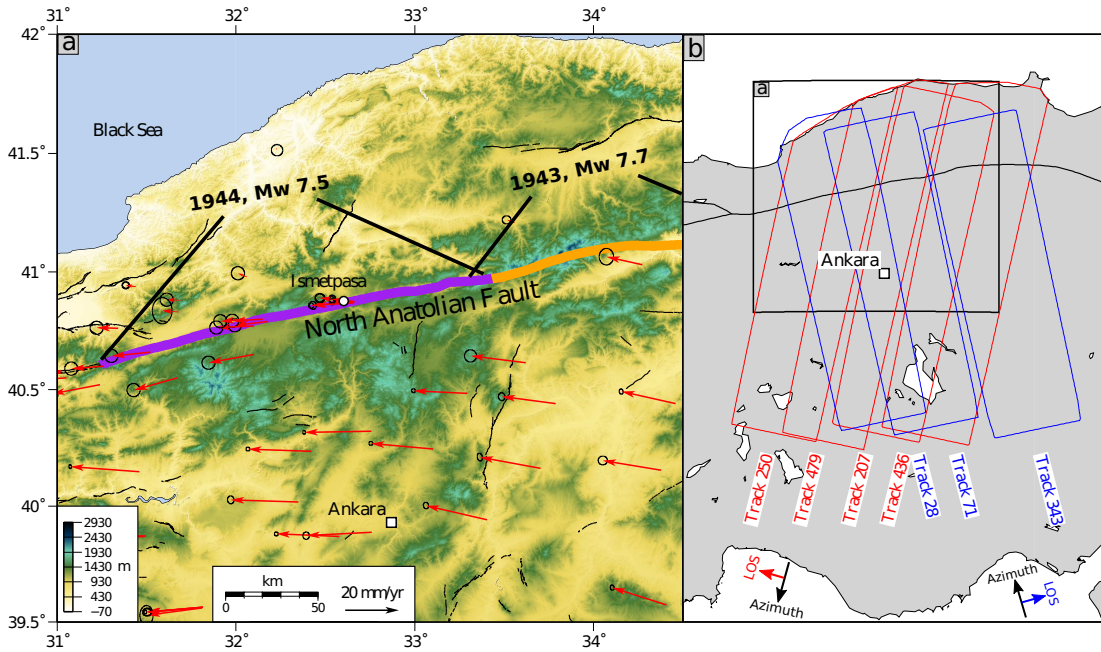


Figure 3.1: (a) The central section of the North Anatolian Fault. The red arrows are published GNSS velocities from the Global Strain Rate Model project ([Kreemer et al., 2014](#)). The coloured sections indicate previous ruptures along this section of the fault. (b) The Envisat satellite data tracks used in this study. Descending tracks are coloured in red and ascending tracks in blue.

2005, [Walters et al., 2011](#), [Kaneko et al., 2013](#), [Cakir et al., 2014](#), [Cetin et al., 2014](#), [Walters et al., 2014](#), [Cavalié and Jónsson, 2014](#), [Hussain et al., 2016](#)).

However, slip rate estimates for the central NAF are relatively poorly constrained, with sparse GNSS data north of this portion of the fault (Figure 3.1) and wide ranging geological and geodetic estimates. Geological fault slip rate range from as low as 5 mm/yr to as high as 44 mm/yr (e.g. [Barka and Hancock, 1984](#), [Barka, 1992](#), [Hubert-Ferrari et al., 2002](#), [Kozaci et al., 2007](#), [Kozaci et al., 2009](#)), while GNSS studies estimate the slip rate for the region to a range of 17-34 mm/yr (e.g. [Oral et al., 1993](#), [Noomen et al., 1996](#), [Ayhan et al., 2002](#), [Reilinger et al., 2006](#)).

Shallow aseismic slip on the fault plane, i.e. fault creep, on the central portion of the NAF was first documented by [Ambraseys \(1970\)](#), who observed increasing displacements of a wall that was built across the fault near the town of Ismetpasa, over multiple years. [Ambraseys \(1970\)](#) estimated a fault creep rate of ~ 20 mm/yr for the time period 1955-1969. Since this original investigation, the fault creep has been the focus of numerous geodetic studies (e.g. [Cakir et al., 2005](#), [Kutoglu et al., 2010](#), [Karabacak et al., 2011](#), [Ozener et al., 2013](#), [Cetin et al., 2014](#)). [Cetin et al. \(2014\)](#) suggested that the fault creep rate has been decaying since the first measurements in 1970 to a current steady-state value of $\sim 6-8$ mm/yr. Most previous InSAR studies in this region have only used satellite data from a single look direction, e.g. the use of descending Envisat data by [Cakir et al. \(2005\)](#) and [Cetin et al. \(2014\)](#). [Kaneko et al. \(2013\)](#) used

Table 3.1: Data coverage for each Envisat track used in this study

Track	Geometry	Time span	No. of images	Total ints created	Ints used
250	Descending	20031212 - 20100723	38	115	59
479	Descending	20031228 - 20100704	30	90	50
207	Descending	20040113 - 20100928	40	88	53
436	Descending	20030703 - 20100318	36	96	65
28	Ascending	20040728 - 20100707	14	30	21
71	Ascending	20040103 - 20090829	19	48	29
343	Ascending	20040610 - 20100415	14	27	20

a combination of ascending tracks from the ALOS satellite and one descending frame from Envisat track 207, limiting their observational period to 2007-2011. They suggested that aseismic creep at a rate of ~ 9 mm/yr, is limited to the upper 5.5-7 km of the crust which exhibits velocity strengthening frictional behaviour.

Recently, [Rousset et al. \(2016\)](#) used high resolution COSMO-SkyMed satellite data spanning the time window between July 2013 to May 2014 to show evidence of periods of elevated fault creep spanning a month with total slip of 20 mm, indicating that episodic creep events may be an important mechanism producing aseismic slip.

In this study we use a more complete dataset covering the entire central NAF in both ascending and descending geometries and spanning the ~ 8 year time window between 2003-2010. We remove long wavelength trends from the InSAR data using published GNSS velocities ([Kreemer et al., 2014](#)), and deconvolve the InSAR line-of-sight velocities into fault-parallel and vertical motion.

We use simple elastic dislocation models to estimate geodetic fault slip rates and locking depths, and investigate the spatial variation of fault creep along the central NAF. We also develop and apply a new iterative unwrapping algorithm that minimises unwrapping errors during the InSAR processing.

3.2 InSAR processing

Our dataset consists of 191 Envisat images from 4 descending tracks (250, 479, 207, 436) and 3 ascending tracks (28, 71, 343) (Figure 3.1b). Together these cover the central NAF between 31.5°E and 35°E , and span the time interval 2003-2010. Details of the processed data for each track are given in Table 3.1.

We focus the Envisat images using ROI_PAC ([Rosen et al., 2004](#)) and use the DORIS software ([Kampes et al., 2003](#)) to construct 494 interferograms. For each track we produce a redundant connected network of interferograms while minimising the temporal separation between acquisitions and the spatial separation of the satellite (the perpendicular baseline) (Figure C.1). We correct topographic contributions to the radar phase using the 90 m SRTM Digital Elevation Model ([Farr et al., 2007](#)) and

account for the known oscillator drift for Envisat according to [Marinkovic and Larsen \(2013\)](#). We unwrap the interferometric phase using a new iterative unwrapping process described in section 3.3.

We apply the StaMPS (Stanford Method for Persistent Scatterers) small baseline time series technique ([Hooper, 2008](#), [Hooper et al., 2012](#)) to remove incoherent pixels and reduce the noise contribution to the deformation signal, by selecting only those pixels that have low phase noise on average in the small baseline interferograms used in the analysis.

The atmospheric contribution is often the largest source of error in radar interferograms (e.g. [Doin et al., 2009](#), [Walters et al., 2013](#), [Jolivet et al., 2014](#), [Bekaert et al., 2015a](#)). To mitigate this we estimated a troposphere correction using auxiliary data from the ERA-Interim global atmospheric model reanalysis product ([Dee et al., 2011](#)). We use the TRAIN (Toolbox for Reducing Atmospheric InSAR Noise) software package ([Bekaert et al., 2015c](#)) to correct each individual interferogram for tropospheric noise. After removing a planar phase ramp from each interferogram, the ERA-I correction reduces the standard deviation of our tracks by 8% on average. The average reduction in standard deviation is small after correction, implying that some residual atmospheric signals remain in the interferograms after the ERA-I correction. The average reduction in standard deviation for each track are 10% for track 207, 1% for track 250, 2% for track 436, 12% for track 479, 10% for track 28, 16% for track 71 and 6% for track 343 (Figures C.2 and C.3).

Our final redundant small baseline networks consist of a total of 297 interferograms over the seven tracks (Figure S1). We use these networks to calculate the average line-of-sight (LOS) velocity map for each track.

Any non-tectonic long wavelength signals (>100 km), including those due to orbital errors, are effectively removed from each track when the InSAR line-of-sight (LOS) velocities are transformed into a Eurasia-fixed GNSS reference frame (details in section 3.4). The uncertainties on the final velocity for each pixel are calculated using bootstrap resampling ([Efron and Tibshirani, 1986](#)) and are presented at the 1 sigma level in the following work.

We calculate the LOS variance-covariance matrix of the noise for each InSAR track by computing the average radial covariance vs. distance (autocorrelation) using the velocities in a 50 km by 50 km region ~250 km to the south of the fault. This region is assumed to have no tectonic deformation and contain only atmospheric noise. We fit an exponential covariance function (e.g. [Lohman and Simons, 2005](#), [Sudhaus and Sigurjón, 2009](#)), $C(r)$, as:

$$C(r) = \sigma^2 e^{-\frac{r}{\lambda}}, \quad (3.1)$$

where we estimate the variance (σ^2) and the characteristic length (λ), which gives the

Table 3.2: The centre of the 50 km by 50 km region used to estimate the noise covariance function parameters.

Track	Centre (lon, lat)	Variance, σ^2 (mm/yr) ²	Characteristic Length, λ (km)
207	33°E, 39.5°N	8.91	53
250	31.75°E, 39.5°N	4.95	27
436	34°E, 39.5°N	3.91	22
479	32.5°E, 39.5°N	2.88	10
28	34.5°E, 39.5°N	6.12	25
71	33.2°E, 39.5°N	4.00	19
343	32.5°E, 39.5°N	1.00	4

spatial correlation of noise as a function of distance between pixels (r). Our values for each track and the centre of the region used to calculate the covariance function are shown in Table 3.2. These covariances are used in section 3.5 when modelling the horizontal velocities and fault creep rates.

3.3 Iterative phase unwrapping

3.3.1 Method description

Phase unwrapping is the process of recovering continuous phase values from phase data that are measured modulo 2π radians (wrapped data) (*Ghiglia and Pritt, 1998*). Original 2D phase unwrapping algorithms unwrapped the phase of each individual interferogram independently (e.g. *Goldstein et al., 1988, Costantini, 1998, Zebker and Lu, 1998*). However, a time series of selected interferogram pixels can be considered a 3D data set, the third dimension being that of time. *Hooper and Zebker (2007)* showed that treating the unwrapping problem as one 3D problem as opposed to a series of 2D problems leads to an improvement in the accuracy of the solution in a similar way to which 2D unwrapping provides an improvement over one-dimensional spatial methods.

Fully 3D phase-unwrapping algorithms commonly assume that the phase difference between neighbouring pixels is generally less than half a phase cycle (2π radians) in all dimensions (*Hooper and Zebker, 2007*). However, due to atmospheric delays, InSAR signals are effectively uncorrelated in time, violating this assumption. Other unwrapping algorithms require the assumption of a temporal parametric function, such as a linear phase evolution in time (*Ferretti et al., 2001*), to unwrap the phase signals.

The standard unwrapping algorithm used in the Stanford Method for Persistent Scatterers (StaMPS) software (*Hooper, 2010*) uses the actual phase evolution in time to guide unwrapping in the spatial dimension without assuming a particular temporal evolution model. The phase difference between nearby pixels (double-difference phase) is filtered in time to give an estimate of the unwrapped displacement phase for each satellite acquisition and an estimate of the phase noise. This is used to construct prob-

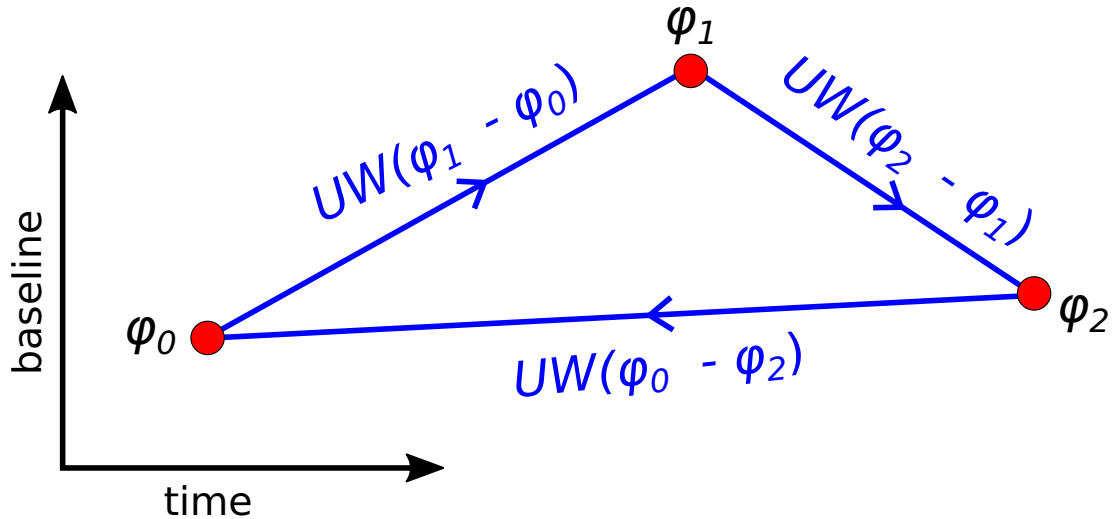


Figure 3.2: A simple interferometric loop consisting of 3 acquisitions (red points) with phase $\phi_{0:2}$. The interferograms are denoted by the blue lines, and are the difference in phase for two acquisitions. UW is the StaMPS unwrapping operator, see text for details. For every pixel unwrapped correctly in each interferogram the phase sum around the loop is equal to zero, i.e. $UW(\phi_1 - \phi_0) + UW(\phi_2 - \phi_1) + UW(\phi_0 - \phi_2) = 0$.

ability density functions for each unwrapped double-difference phase in every interferogram. An efficient algorithm (SNAPHU (*Chen and Zebker, 2000, 2001*)) then searches for the solution in space that maximises the total joint probability, i.e. minimises the total ‘cost’.

For a connected network of small baseline interferograms, the phase-unwrapping of individual interferograms can be checked for network consistency by summing the phase around closed interferometric loops (e.g. *Pepe and Lanari, 2006, Biggs et al., 2007, Cavalié et al., 2007, Jolivet et al., 2011*) (Figure 3.2). In the standard unwrapping approach used in StaMPS, any interferograms identified to have large unwrapping errors are removed from the small baseline network, which can result in loss of information and/or reduction in network redundancy. Note that some other InSAR practitioners (e.g. *Biggs et al., 2007, Wang et al., 2009, Walters et al., 2011*) generally do not drop badly unwrapped interferograms, but attempt to correct unwrapping errors by manually adding integer multiples of 2π to badly unwrapped regions of pixels. However, this is a time consuming process.

In our method, we iterate the standard StaMPS unwrapping procedure while calculating the sum of the unwrapped phase around closed loops for every pixel in every interferogram, using the following equation:

$$\sum_{i=0}^{n-1} UW\{\phi_{(i+1)\bmod n} - \phi_i\} + \epsilon = 0, \quad (3.2)$$

where UW is the StaMPS unwrapping operator, n is the number of interferograms on

the path around an interferometric loop, $(\phi_{i+1} - \phi_i)$ are the interferometric phase values of a pixel in the interferograms created by calculating the phase difference between image $i+1$ and i relative to a reference point, and ϵ is the error term. The reference point is chosen to be north of the fault for all tracks. Any pixels satisfying the requirement of $|\epsilon| < 1$ rad are defined as “error-free pixels” and are assumed to be correctly unwrapped. An error term is needed because the interferograms are multilooked before unwrapping and so we do not expect to have full closure around each interferometric loop. Using $\epsilon = 1$, is reasonable as it is well below the 2π radians required to produce unwrapping errors and allows for a small amount of closure error introduced by the nonlinear nature of multilooking. In our tests setting ϵ to 0.5 made no significant impact on the acceptance rates.

In each iteration, we keep all unwrapping parameters fixed (such as the number of interferograms, the filter strength and the unwrap grid size) but assume that pixels identified as error-free in the previous iteration are unwrapped correctly, and apply a high cost to changing the phase difference between these pixels in the next iteration. The StaMPS unwrapping algorithm uses the double difference phase evolution in time to calculate the probability density function for each pixel pair. For pixels identified as unwrapped correctly we set the weighting for these pixels to 100 times the badly unwrapped pixels to effectively ensure the evolution in time is fixed. In this way, the iterative unwrapping method uses the error-free pixels as a guide to unwrapping the regions that contained unwrapping errors in previous iterations.

López-Quiroz et al. (2009) describe a processes where unwrapping is iterated on the residual interferogram after the removal of an estimate of the deformation signal. However, our technique does not require an assumption of the deformation signal.

3.3.2 Testing the iterative unwrapping procedure

We tested the new algorithm on data from Envisat descending track 207, which covers a region roughly 100 km by 400 km in central Turkey (Figure 3.1b). Each iteration consists of the following steps: running the StaMPS unwrapping algorithm, determining the pixels unwrapped correctly in each interferogram using the method described above and in the appendix, applying a high cost to unwrapping across these pixels and re-running the unwrapping algorithm again. We iterate this procedure 30 times. The results from standard unwrapping does not change as no modifications are made to its inputs and is represented by the straight line indicating no change in the number of error-free pixels per iteration. Figure 3.3 shows that the percentage of error-free pixels in the entire small baseline network increases sharply with the first 8 iterations from 70% to 83%, reaching a maximum of 84% after 30 iterations; meaning that there are some unwrapping errors the method is unable to fix. This is also evident from the individual interferograms (Figure 3.4), which show this same rapid increase in the percentage of error-free pixels followed by a plateau. It is clear that there are some unwrapping

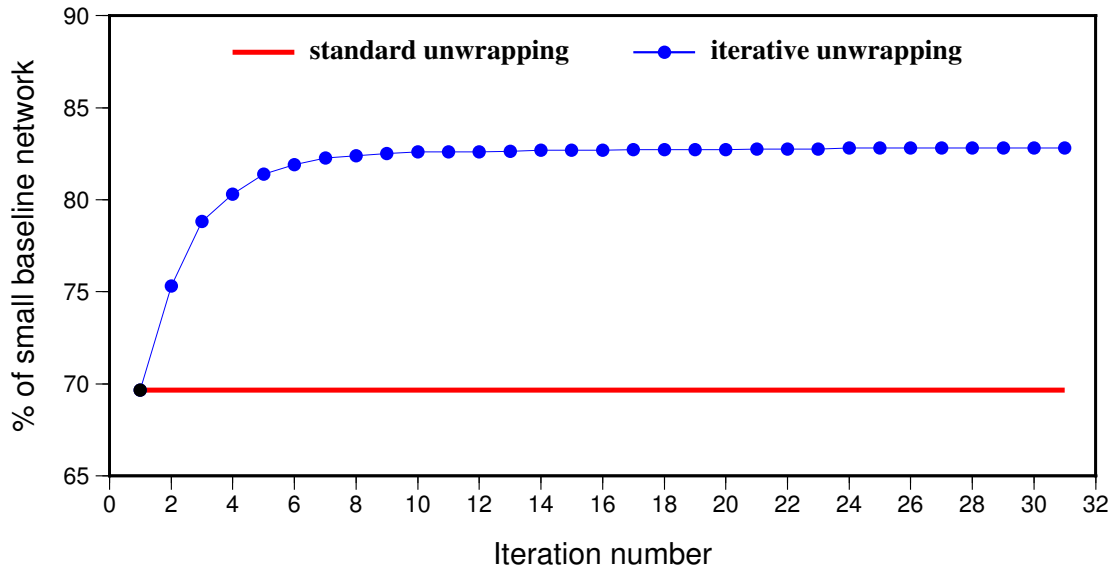


Figure 3.3: Total percentage of pixels in the small baseline network for descending track 207 that were identified as closed, i.e. correctly unwrapped, using our iterative unwrapping procedure (blue) and the standard unwrapping (red) algorithm. There is a rapid increase in the number of error-free pixels for the first 8 iterations after which it reaches a plateau. As no modification is made to the input of the unwrapping algorithm, there is no change for each iteration of the standard unwrapping algorithm.

errors that cannot be corrected (blue colours in Figure 3.5) using the iterative method. However the iterative procedure greatly reduces the total number of unwrapping errors and thus, increases the InSAR coverage whilst minimising errors.

After 8 iterations the percentage of error-free pixels increased from 90 to 94% for track 250, from 65 to 80% for track 436, from 92 to 95% for track 479, from 83 to 87% for track 343, from 71 to 77% for track 28, and from 91 to 93% for track 71.

3.4 Interseismic velocity field across the central NAF

To investigate the pattern of interseismic strain accumulation along the fault we decompose our full InSAR velocity field into the fault-parallel and fault-perpendicular components of motion. Following the method described in *Hussain et al. (2016)*, we do this first by resampling our InSAR LOS velocities (Figure 3.6) onto a 1 km by 1 km grid encompassing the spatial extent of all our tracks. We use a nearest neighbour resampling technique including only those persistent scatterer pixels with a nearest neighbour within 1 km of the centre of each grid point. We reference each track to a Eurasia-fixed GNSS reference frame by first averaging the InSAR velocities that fall in a 1 km radius around every GNSS station within the boundaries of each InSAR track. We project the GNSS velocities into the local satellite line-of-sight and calculate the difference from the InSAR velocities. The vertical component of the GNSS velocities are not available on the Global Strain Rate Model website. *Ergintav et al. (2009)* showed that the ver-

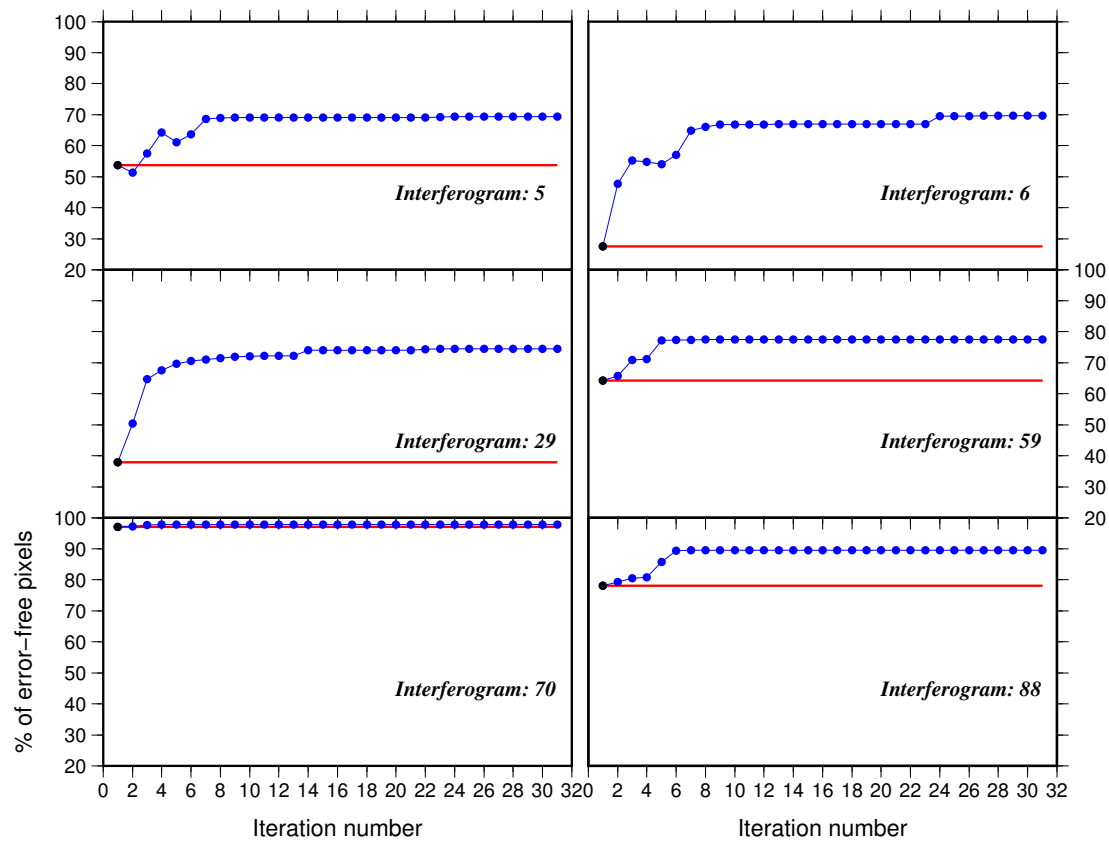


Figure 3.4: Changes in the percentage of error-free pixels (correctly unwrapped pixels) per iteration shown for selected interferograms. In blue are the changes for the iterative unwrapping algorithm while red indicates the standard unwrapping.

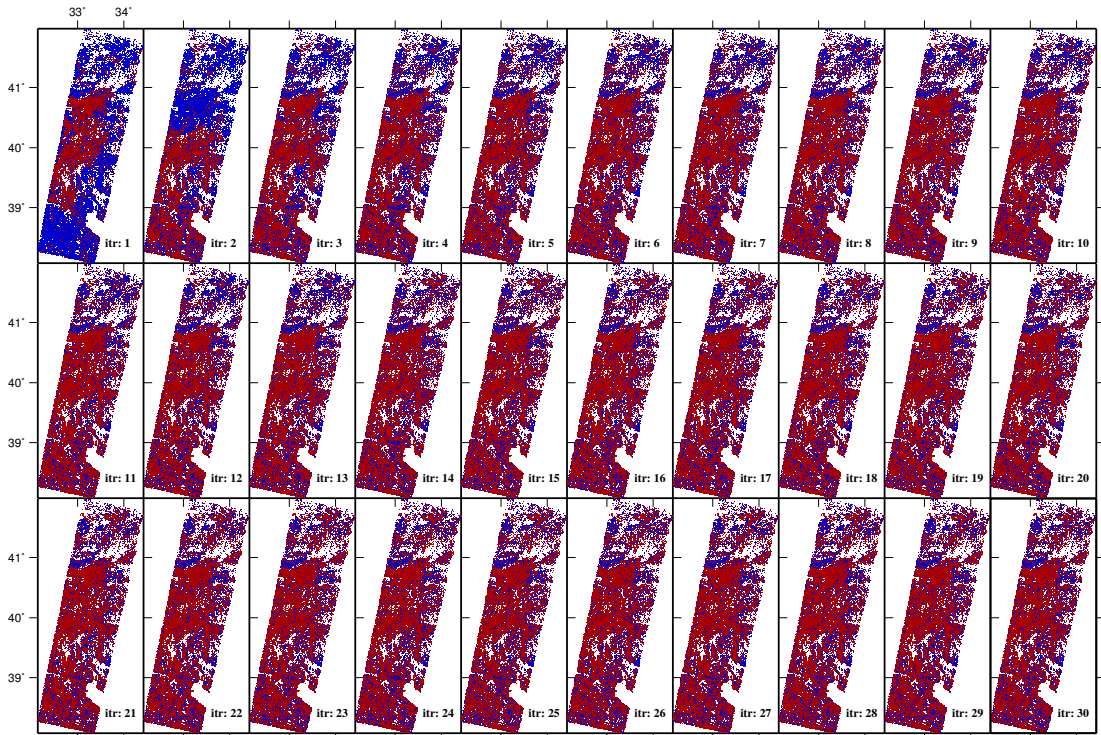


Figure 3.5: Evolution of the number of error-free pixels (correctly unwrapped pixels) per iteration shown for interferogram 29. error-free pixels are identified in red while pixels that did not close, i.e. have unwrapping errors, are in blue.

tical GNSS component is small and very noisy over western Turkey, therefore we only use the horizontal velocities in our analysis. We determine the best-fit plane through the residual velocities and remove this from the InSAR velocities to transform the LOS velocities into a Eurasia-fixed GNSS reference frame. This procedure is done separately for each track.

For every pixel where information from both ascending and descending geometries are available, we use equation 3.3 to invert for the east-west and vertical components of motion following the method described by *Wright et al. (2004)*, *Hussain et al. (2016)*, while taking into account the local incidence angles:

$$D_{LOS} = [\sin(\theta)\cos(\alpha) \quad -\sin(\theta)\sin(\alpha) \quad -\cos(\theta)] \begin{bmatrix} D_E \\ D_N \\ D_U \end{bmatrix}, \quad (3.3)$$

where D_{LOS} is the LOS velocity, θ is the local radar incidence angle, α the azimuth of the satellite heading vector, and $[D_E, D_N, D_U]^T$ is a vector with the east, north and vertical components of motion respectively.

Equation 3.3 contains three unknowns (D_E , D_N and D_U) but we only have two input velocities with large differences in satellite look angle in the inversion (the ascending and descending InSAR LOS velocities). Therefore it is impossible to calculate the full 3-D

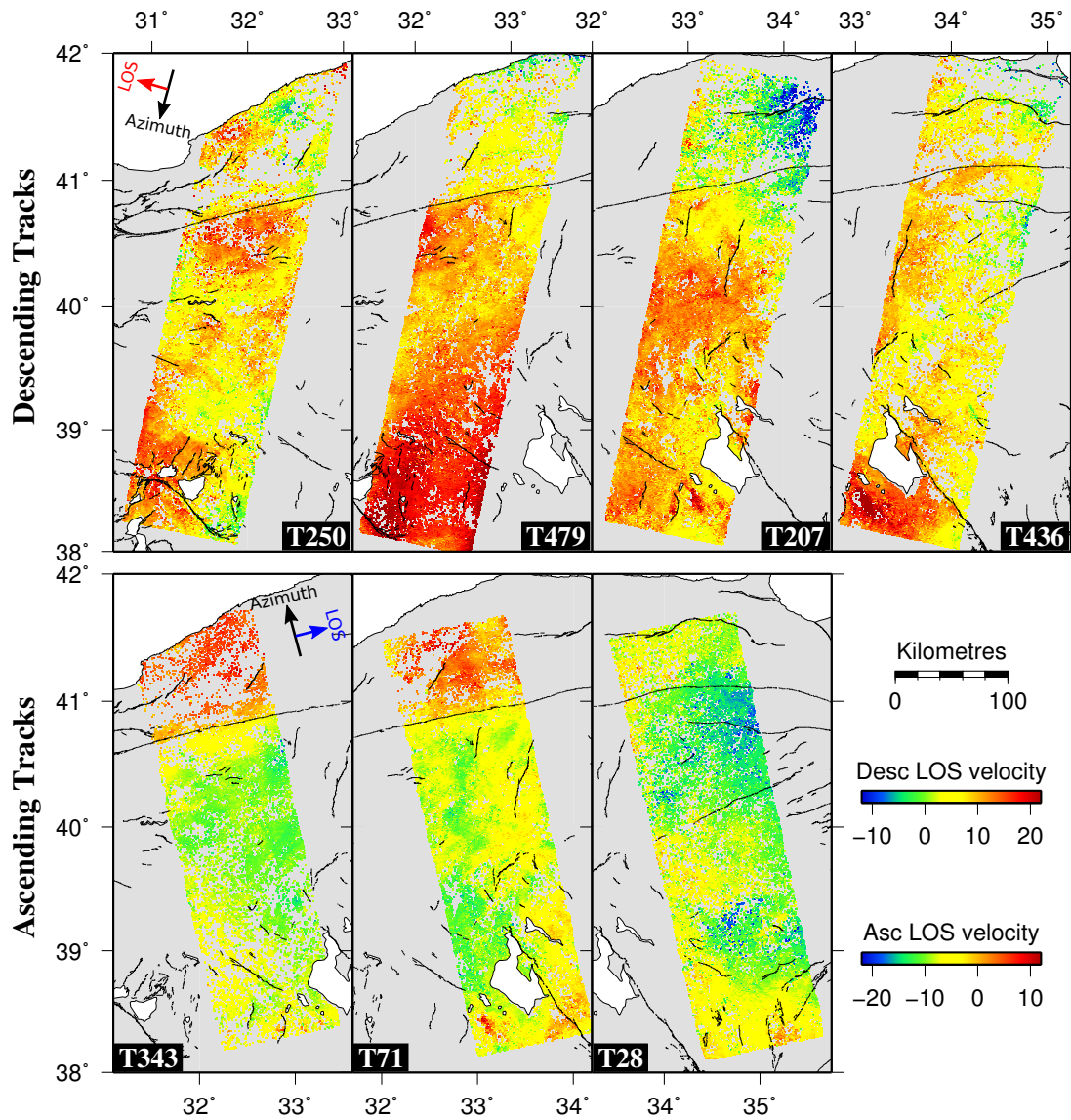


Figure 3.6: Descending and ascending line-of-sight velocities with each track referenced to a Eurasia fixed GNSS reference frame. Red colours indicate motion away from the satellite while blue colours indicate motion towards the satellite.

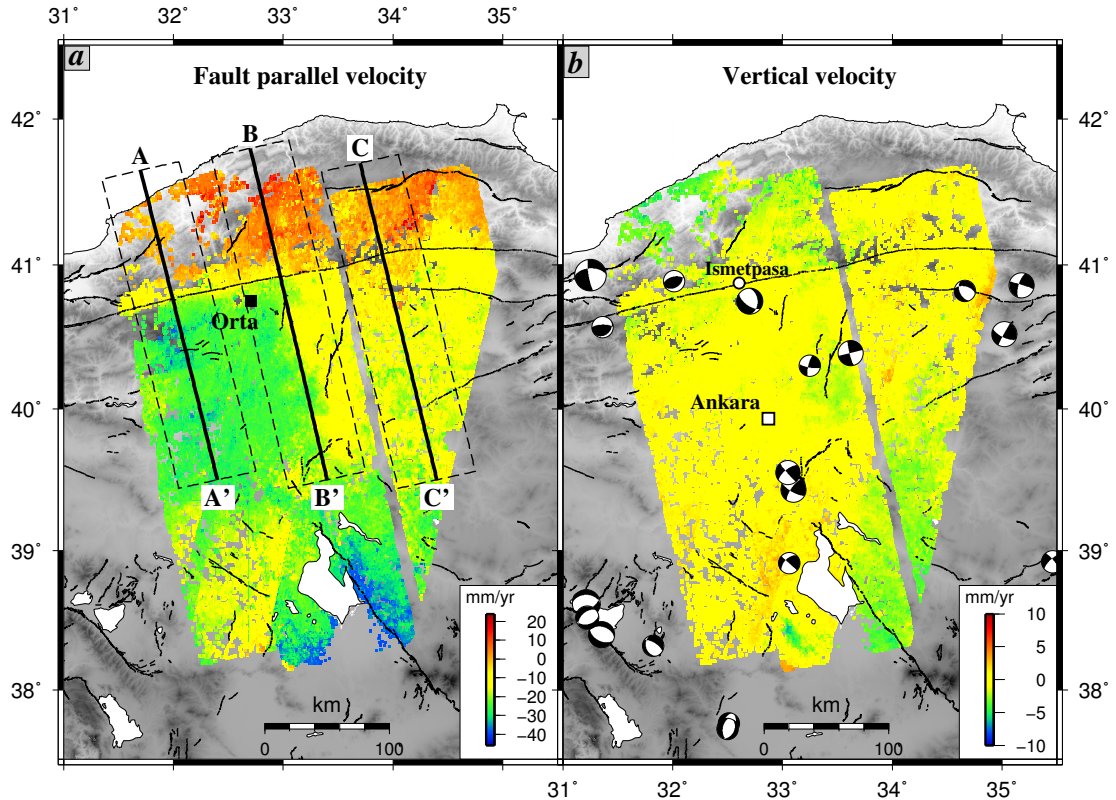


Figure 3.7: (a) LOS InSAR velocities decomposed into the fault parallel and vertical (b) components of motion, where the north-south component is constrained by the GNSS north component (Figure C.5), see text for description. Negative fault parallel velocities indicate motion towards the west and negative fault perpendicular velocities indicate motion to the south. Uncertainty maps for these components are in Figure C.5. The lines labelled A-A', B-B' and C-C' are profiles through the fault parallel velocity shown in Figure 3.8. Earthquake moment tensors are from the Global Centroid Moment Tensor catalogue for all events greater than magnitude 4 between 1976 and 2016. The 2000 Mw 6 Orta earthquake location is shown in (a).

velocity field without a prior assumption. The common assumption made in previous studies is that there is no vertical motion across the region of interest (e.g. [Walters et al., 2014](#), [Hussain et al., 2016](#)). In our case we note that both the ascending and descending tracks are equally insensitive to motion in the north-south direction. We therefore use the smooth interpolated north component of the GNSS velocities (Figure C.4) to constrain the north-south component (D_N) in the inversion, and solve for the east-west and vertical components of motion using the InSAR LOS velocities. We calculate the fault-parallel component of the horizontal velocity by assuming motion occurs on a strike-slip fault trending at $N81^\circ E$.

Our fault parallel velocities (Figure 3.7a) show the expected right-lateral interseismic motion across the NAF, with red colours representing motion to the north-east and blue to the south-west. Our estimated vertical component show that there is little vertical motion across the NAF in this region (Figure 3.7b).

There is a relatively sharp change in fault-parallel velocity south of the NAF (Figure 3.7) that coincides with the B-B' profile line. We believe that this is due to a combination of postseismic deformation from the 2000 Orta earthquake (Mw 6) (*Taymaz et al., 2007*), residual atmosphere introduced mainly from ascending track 71 and postseismic deformation from the 1999 Izmit and Düzce earthquakes.

3.5 Modelling profile velocities

We analyse three profiles across the fault where velocities from within 20 km are projected onto the profiles shown in Figure 3.7a. *Walters et al. (2014)* noted that there is a variation in the fault parallel velocity away from the fault that is not due to interseismic loading but due to the proximity to the Euler pole of rotation. For example, GNSS velocities presented by *Nocquet (2012)* show fault parallel velocity vectors with magnitude ~ 25 mm/yr close to the NAF but ~ 8 mm/yr in Cyprus roughly 800 km away from the fault. This variation is mostly due to the proximity of the Cyprus GNSS stations to the pole of rotation of Anatolia with respect to Eurasia. We use the pole of rotation calculated for Anatolia with respect to Eurasia by *Reilinger et al. (2006)*, who estimated a rotation rate of 1.23 degrees/Myr about a pole located at 32.1°E , 30.8°N near the Nile delta. In a Eurasia-fixed reference frame this rotation effect only applies to the region south of the NAF and corresponds to a value of $\theta_{rot} = 0.0215$ mm/yr/km or 2.15 mm/yr at a distance of 100 km from the fault.

Assuming the fault parallel velocities far to south of the fault (>200 km) are mostly due to atmospheric noise and contain no tectonic deformation, we calculate the variance-covariance matrix of the noise using the method described in section 3.2, using velocities from a 50 km by 50 km region centered on 32.5°E , 39°N . The estimated variance (σ^2) and characteristic length (λ) for the covariance function (equation 3.1) is 6.35 (mm/yr) 2 and 35.8 km respectively.

Profiles A-A' and C-C' do not cross the creeping section of the fault. For these profiles we fit a 1-D model (*Savage and Burford, 1973*) through the profiles where the fault parallel velocity, v_{par} , at a fault normal distance x , is a function of the fault slip rate, S , and the locking depth, d_1 . Including the rotation effect discussed above, our 1-D model is:

$$v_{par}(x) = \frac{S}{\pi} \arctan\left(\frac{x}{d_1}\right) + x\theta_{rot} + a, \text{ where } \theta_{rot} = \begin{cases} 0.0215, & \text{if } x > 0 \\ 0, & \text{if } x \leq 0 \end{cases}, \quad (3.4)$$

where a is a static offset.

However, profile B-B' crosses the creeping section of the fault. For this profile we model the fault parallel velocity as a combination of two signals: a long wavelength

signal that represents interseismic loading at rate S and locking depth d_1 , and a short wavelength signal that represents the fault creep at a rate C from the surface down to depth d_2 (e.g. [Wright et al., 2001a](#), [Elliott et al., 2008](#), [Hussain et al., 2016](#)).

$$v_{par}(x) = -\frac{S}{\pi} \arctan\left(\frac{x}{d_1}\right) + C \left[\frac{1}{\pi} \arctan\left(\frac{x}{d_2}\right) - \mathcal{H}(x) \right] + x\theta_{rot} + a, \quad (3.5)$$

$$\text{where } \theta_{rot} = \begin{cases} 0.0215, & \text{if } x > 0 \\ 0, & \text{if } x \leq 0 \end{cases},$$

where $\mathcal{H}(x)$ is the Heaviside function.

We find best-fit values for each model parameter (S , d_1 , C , d_2) and an offset a , using a Bayesian approach, implementing the [Goodman and Weare \(2010\)](#) affine-invariant ensemble Markov Chain Monte Carlo (MCMC) sampler. For details see [Hussain et al. \(2016\)](#).

Our MCMC sampler uses 600 walkers to explore the parameter space constrained by: $0 < S$ (mm/yr) < 60 , $0 < d_1$ (km), < 60 , $0 < C$ (mm/yr), < 30 , $0 < d_2$ (km), < 40 , $-40 < a$ (mm/yr) < 40 , assuming a uniform prior probability distribution over each range. An important constraint we impose is that the maximum creep depth cannot be greater than the locking depth, i.e. $d_2 \leq d_1$. Our MCMC model runs over 300,000 iterations and produces 48,000 random samples from which we estimate both the maximum a posteriori probability (MAP) solution and corresponding parameter uncertainties.

The results of our analysis are shown in [Figure 3.8](#), with the observed profile velocity in red and the MAP solution in the bold dashed line. The sampled marginal probability distributions for the fault slip rate, the locking depth, creep rate and the static offset are approximately normally distributed ([Figure 3.9](#)). As expected of elastic dislocation models there is a strong trade-off between the fault slip rate and the locking depth (top left box for each profile in [Figure 3.9](#)) where a slower slip rate can be compensated by a shallower locking depth.

Our MAP estimates for the fault slip rate of 30 mm/yr (25-34, 95% CI), 28 mm/yr (23-33, 95% CI) and 21 mm/yr (14-27, 95% CI) appear to decrease eastward from profile A-A' to C-C' with no such pattern in the locking depths: 13 km (6-20, 95% CI), 13 km (5-22, 95% CI) and 17 km (10-25, 95% CI).

To test whether the difference in MAP slip rate between profiles A-A' and C-C' is significant we consider the null hypothesis that each of the estimated slip rates are one draw from a Gaussian distribution with the same expected value (but with different standard deviations).

If the hypothesis is true, the distribution of the difference in MAP slip rates will be Gaussian with a mean of zero and standard deviation $= \sqrt{\sigma_A^2 + \sigma_C^2}$, where σ_A^2

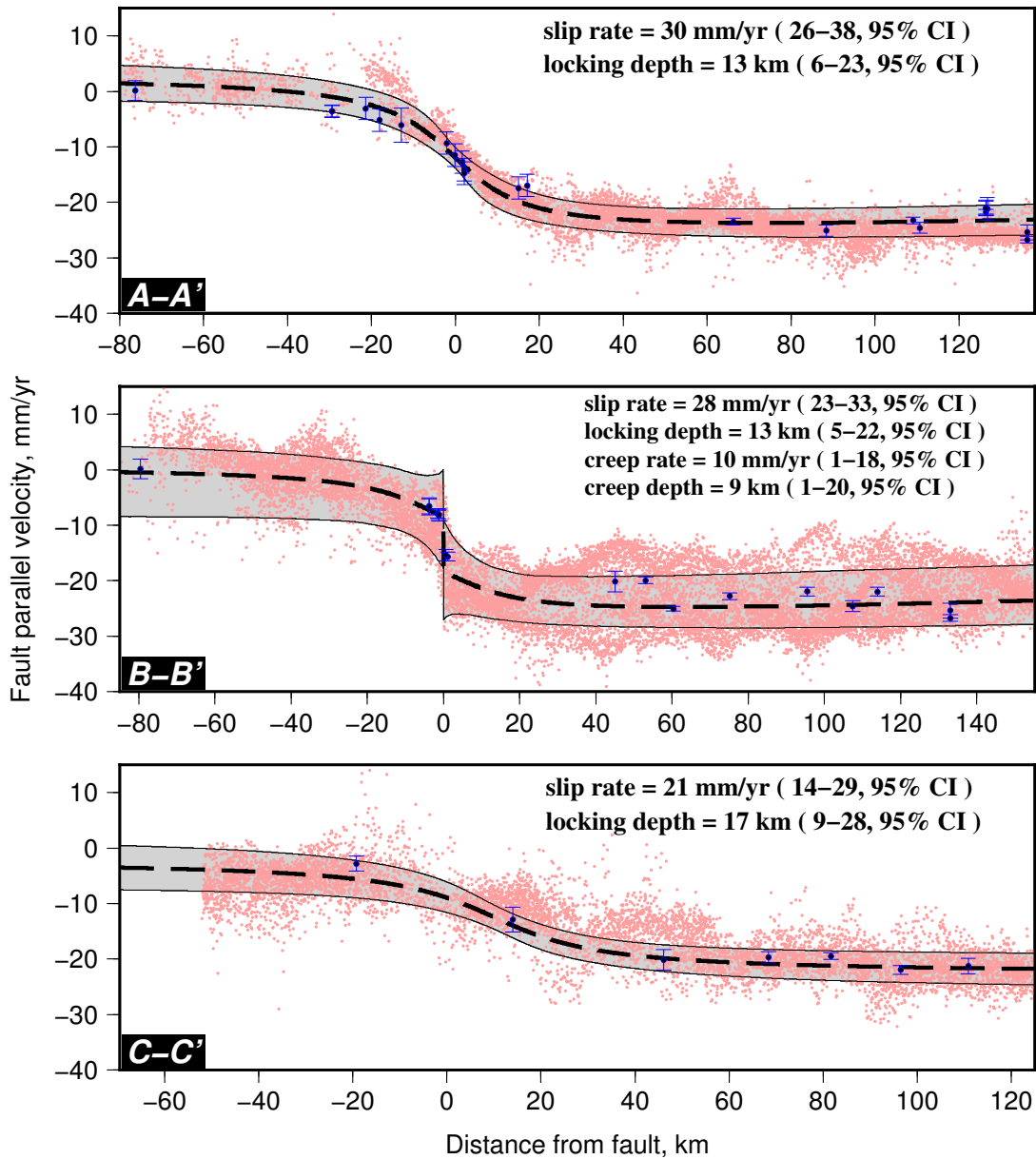


Figure 3.8: Profiles through the fault parallel velocities along three lines shown in Figure 3.7. The red points are fault parallel velocities projected from within ± 25 km distance onto the profile. The blue points are the fault parallel component of the GNSS velocities. The bold black dashed line is the best fit, maximum a posteriori probability (MAP), solution while the light grey shaded region is the 95% model confidence range. The best fit model parameters are shown in the text with the 95% confidence range in brackets.

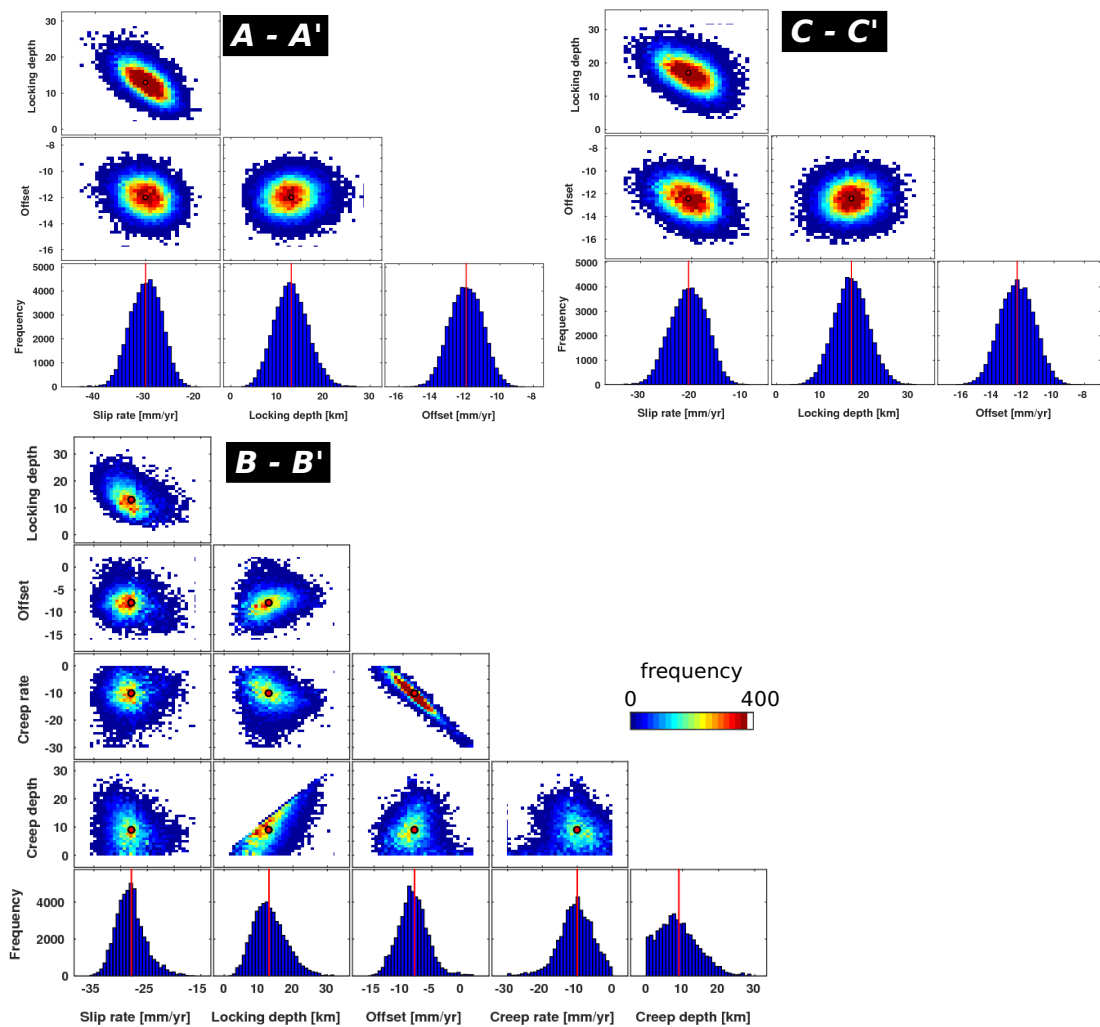


Figure 3.9: Marginal probability distributions for profile A-A', B-B' and C-C'. The red line and dot indicate the maximum a posteriori probability (MAP) solution from our Markov Chain Monte Carlo (MCMC) analysis.

and σ_C^2 are the variance of the estimator for slip rate between profiles A-A' and C-C' respectively. The ratio of $(S_A - S_C)/\sqrt{(\sigma_A^2 + \sigma_C^2)}$, where S_A and S_C are the MAP slip rates for A-A' and C-C' respectively, can therefore be used to test the null hypothesis. A value of 1.96 or more should only occur 5% of the time if the null hypothesis is true. In our case we find the ratio to be equal to 2.28, so we reject the null hypothesis at the 5% level meaning our results indicate that the rates are different with >95% confidence.

Our map of fault parallel velocity (Figure 3.7a) shows a lateral variation in far-field velocities. For example at 40°N the fault parallel velocity decreases from 28-30 mm/yr on profile A-A' to 15-20 mm/yr on profile C-C'. Assuming the far-field to the north is pinned to zero, as would be the case in a Eurasia-fixed reference frame, the fault parallel velocities show an eastward decrease in relative velocity between the region north of the fault and the region to the south, which would result in decreasing fault slip rate.

The GNSS study of *Yavaşoğlu et al. (2011)*, which overlaps with the eastern edge of our fault parallel InSAR velocities estimated a fault slip rate of 20.5 ± 1.8 mm/yr, which is directly comparable with our estimate of 21 mm/yr (14-27, 95% CI) for the eastern profile (C-C'). In general our estimates are comparable with the slip rate estimates from GNSS studies in this region, which range between 17 and 34 mm/yr (e.g. *Oral et al., 1993*, *Noomen et al., 1996*, *Ayhan et al., 2002*, *Reilinger et al., 2006*). However our rate of 30 mm/yr to the west are at the faster edge of the spectrum of published estimates.

An important limitation of the simple dislocation models used in this study is that it assumes the elastic properties of the crust do not vary along the fault, which is not always the case for faults in the field. These differences may arise due to changes in fault geometry, geology and the presence of fluids (e.g. *Perrin et al., 2016*). Variations in crustal rheological could change the strain accumulation on the fault, which would result in slightly different slip rates. However, the simple elastic dislocation model matches the data well and is able to give a first order estimate of the fault slip rate and locking depth.

3.6 Fault creep along the central NAF

To investigate the pattern of aseismic creep along the central NAF we plot short profiles extending 5 km either side of the fault at regular locations (every ~5 km) along the central NAF (Figure 3.10b), projecting the LOS velocities from within 2.5 km onto each profile. We fit two straight lines through the velocities on either side of the fault, taking into account of the covariance, and determine the offset at the fault trace, which corresponds to the LOS creep rate.

Our results (Figure 3.10a) clearly show that a ~130 km section of the central NAF is undergoing aseismic creep at average rate of ~4 mm/yr in the LOS for descending

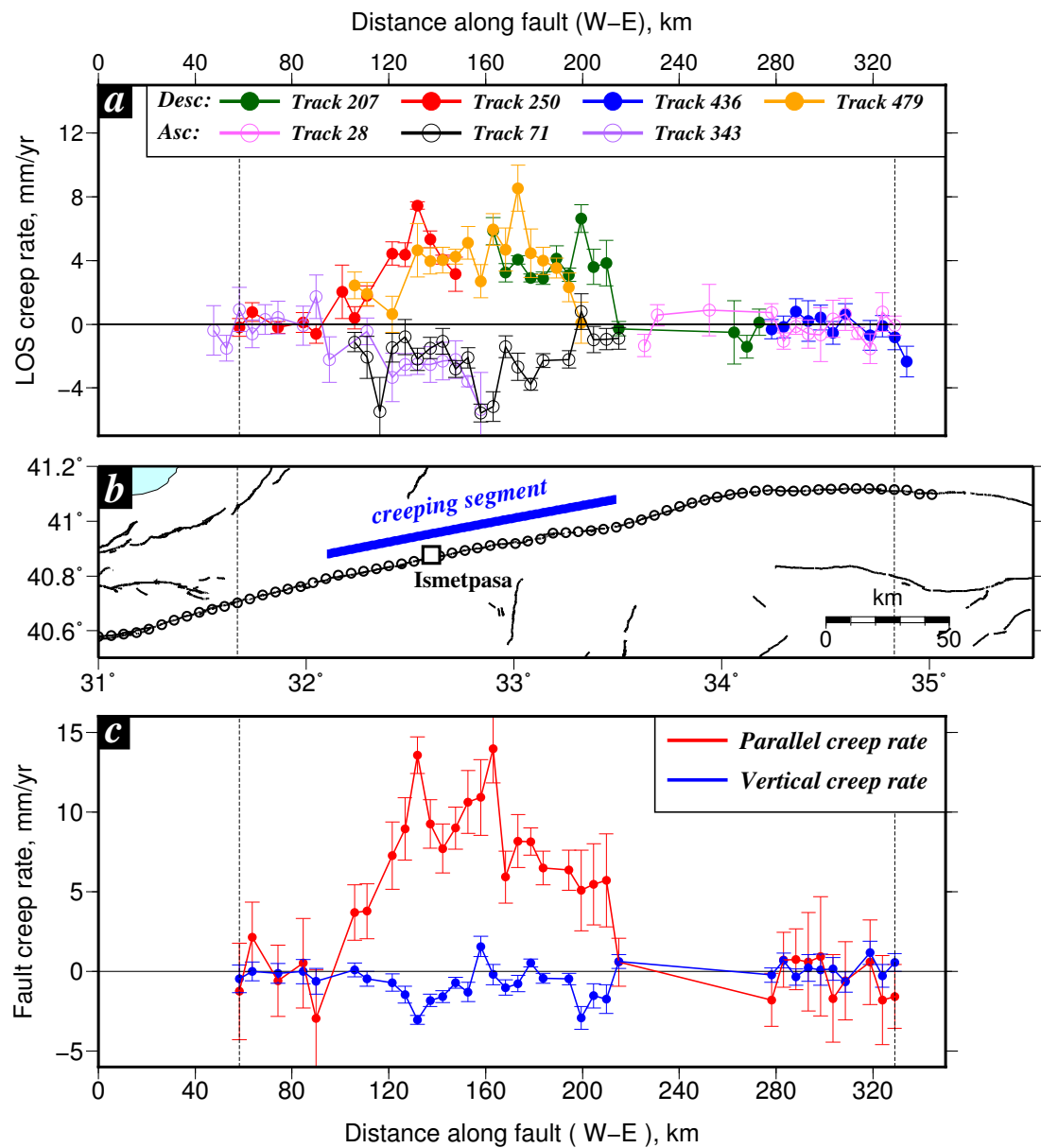


Figure 3.10: (a) The variation in LOS fault creep rate along the central NAF with the creep calculated by determining the offset in LOS velocity across the fault at the locations indicated in (b). The ascending tracks are shown with open circles while the descending are in solid circles. (c) The fault creep rate decomposed into the east-west and vertical components, with the north component constrained by the interpolated GNSS north velocities (Figure S4), for locations with both ascending and descending information. Positive creep values in E-W indicate right-lateral motion, while positive values in the vertical represent subsidence of the north with respect to the south side of the fault. All error bars indicate 1 σ uncertainty.

and ~ 3 mm/yr for ascending. The extent of creep is in agreement with the ~ 125 km estimated by *Cetin et al. (2014)* but larger than the ~ 70 -80 km estimated by *Cakir et al. (2005)* and *Kaneko et al. (2013)*. We find no fault creep above our noise level (~ 1 mm/yr in the LOS) west of about 31.2°E and east of about 33.5°E .

Hussain et al. (2016) showed that creep estimates can be contaminated by vertical motions. To test this we use the estimated north-south component of motion from the interpolated GNSS velocities (Figure C.4) along with the creep estimates from both ascending and descending tracks to calculate the east-west and vertical components of motion using Equation 3.3. We calculate the fault parallel component of the creep rate assuming the fault strikes at $\text{N}81^\circ\text{E}$.

Figure 3.10c shows our estimated fault parallel (in red) and vertical (in blue) components of motion for the fault creep rate. There appears to be little vertical motion along the creeping segment. The maximum fault creep rate is 14 ± 2 mm/yr along a portion of the fault located ~ 30 km east of Ismetpasa. The average rate for the entire creeping section is 8 ± 2 mm/yr.

3.7 Discussion

3.7.1 Iterative unwrapping benefits and limitations

Our new iterative unwrapping procedure reduces the number of unwrapping errors in the overall small baseline network and thus improves the InSAR coverage as more correctly unwrapped pixels are added to the network instead of being discarded. However, it is clear that the process cannot fix all unwrapping errors (Figure 3.5). We find that there is a sharp increase in the total number of error-free pixels within the first 8 iterations after which the improvements are small. Therefore, to minimise unwrapping errors from the network some interferograms with particularly poor unwrapping still need to be removed. An efficient procedure would be to run the unwrapping process for 8-10 iterations, remove any particularly bad interferograms (therefore modifying the input to the unwrapping algorithm) and repeat the iterations.

Traditionally, interferograms with unwrapping errors have either been discarded (e.g. *Pinel et al., 2011*, *Hussain et al., 2016*) or have been fixed manually (e.g. *Hamlyn et al., 2014*, *Pagli et al., 2014*). Manual fixing requires drawing a polygon around the unwrapping errors in every interferogram and adding or subtracting an arbitrary integer multiple of 2π until the phase sum around an interferometric loop equals to zero. This can be a very time-consuming and labour intensive process. The strength of our procedure is that the process is automated. However, as we show in Figure 3.4, our procedure cannot fix all unwrapping errors and so does require some manual intervention in discarding (or correcting) particularly bad interferograms.

An important limitation using our technique is that it requires a redundant small

baseline network in order to compute the phase sum around closed interferometric loops. We cannot automatically detect unwrapping errors in individual isolated interferograms.

The aim of this method is to fix pixels that are unwrapped correctly. By adding a high cost to amending the unwrapped values for these pixels, the hope is that the next iteration of unwrapping will correctly unwrap the phase of nearby pixels. The method does not address the cause of the unwrapping error, however, which in some cases cannot be overcome simply by repeating the unwrapping process. Hence some pixels remain badly unwrapped after any number of iterations.

Another limitation is that we inherently assume a “error-free” pixel, i.e. a pixel that undergoes loop closure, is unwrapped correctly. There may be special circumstances in which this may not be the case. Consider the simplest loop consisting of three acquisitions A , B and C with interferograms AB and BC along the forward arc and CA on the return arc. If a particular set of pixels in either one of the forward arc interferograms (AB or BC) has an unwrapping error and these exact same pixels have the same magnitude error but with the opposite sign in interferogram CA then those pixels will still undergo loop closure and be classed as “error-free” in our technique.

However, in reality most interferograms are a part of multiple interferometric loops. And so if this error occurs in one loop and not the other our method can still detect it, i.e. interferogram BC is part of triangular loops ABC and BEC . Our unwrapping procedure becomes more robust with greater network redundancy. However care should be taken not to introduce interferograms with large perpendicular and/or temporal baselines as they are likely to have unwrapping errors.

3.7.2 Interseismic slip rates

Our horizontal velocity field created by combining velocities from seven InSAR tracks, in both ascending and descending geometries in a GNSS-fixed Eurasia reference frame (Figure 3.7) confirms the right-lateral sense of motion expected from the North Anatolian Fault. Our simple elastic dislocation models fit the fault parallel velocities within the 95% confidence range (Figure 3.8) with a statistically significant decrease in fault slip rate from 30 mm/yr (25-34, 95% CI) in the east, through 28 mm/yr (23-33, 95% CI) to 21 mm/yr (14-27, 95% CI). Our estimated locking depths of 13 km (6-20, 95% CI), 13 km (5-22, 95% CI), 17 km (10-25, 95% CI) show no such pattern. Our statistical test to discard the hypothesis of a constant slip rate assumes the the uncertainty attributed to the data is correct. If the uncertainty were underestimated due to the possibility that the apparent change in slip rates could result from other physical mechanisms such as other deformations or change in crust rheology, the level of confidence could be overestimated (e.g. [Duputel et al., 2014](#)).

The positive trade-off between the fault slip and locking depths means that a decreasing fault slip can be compensated by a decreasing locking depth near the fault.

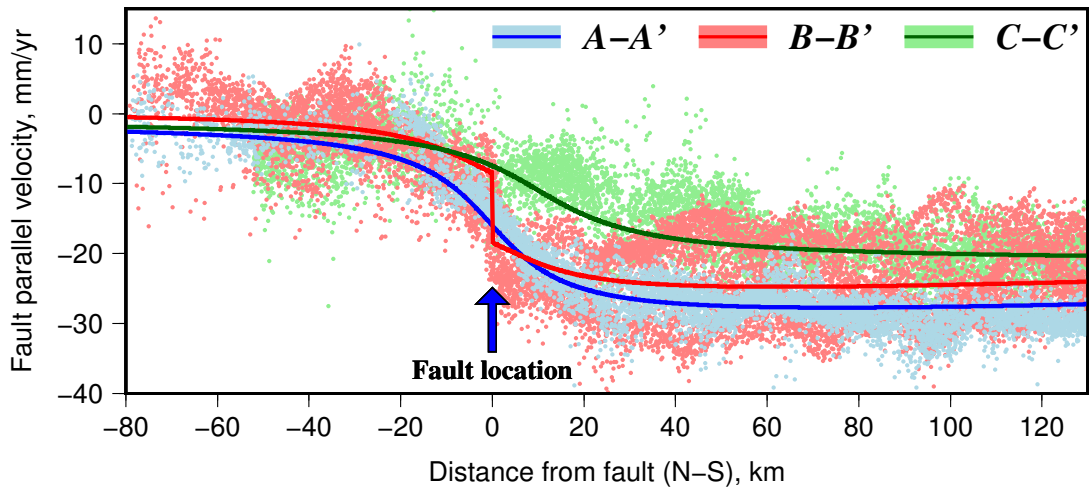


Figure 3.11: Fault parallel velocities for each profile shown in Figure 3.8 with the velocities in pale blue, pale red and pale green corresponding to profile A-A', B-B' and C-C' respectively. Our best fit (MAP solution) model is shown by the bold line through the velocities. It is clear that there is a far field decrease in velocity from profile A-A' to profile C-C'.

This would explain the large confidence intervals for these parameters and could explain the lateral variation in these parameters. However, if we assume the velocities in the far field to the north are zero, as we would expect with velocities in a Eurasia-fixed reference frame, then the far-field plate velocities (velocities to the far south on each profile) do appear to be decreasing eastwards along the fault, from ~ 30 mm/yr in profile A-A' to ~ 20 mm/yr in profile C-C' (Figure 3.11), implying that the lateral change in these parameters are real variations along the fault. This pattern is also observed in the GNSS velocities (Figure 3.8).

There is a relatively sharp change in fault-parallel velocity south of the NAF (Figure 3.7) that coincides with the B-B' profile line. The feature does not correspond to a track boundary (Figure 3.1). Figure 3.12 shows the fault parallel velocities projected onto profile D-D' that shows this gradient between 100 km and 140 km. It is clear that the variation along the profile broadly matches the GNSS velocities, although the gradient at 120 km is steeper in the InSAR than the GNSS. This might be due to local atmospheric residuals in the InSAR velocities. The gradient does not correspond to any topographic changes along the profile.

Ergintav et al. (2009) showed that the 1999 earthquakes resulted in postseismic deformation as far as Ankara, which is less than 100 km south of the NAF in this region. Therefore, the faster velocities to the west of the study region could be due to postseismic deformation from the 1999 earthquakes with the sharp gradient representing the eastern limit of postseismic deformation.

The largest recent earthquakes on the central portion of the NAF in recent times were the 1943 Tosya (Mw 7.7), the 1944 Bolu-Gerede (Mw 7.5) and the 1951 Kursunlu (Mw 6.9) earthquakes (Figure 3.13). Our fastest slip rate of 30 mm/yr corresponds

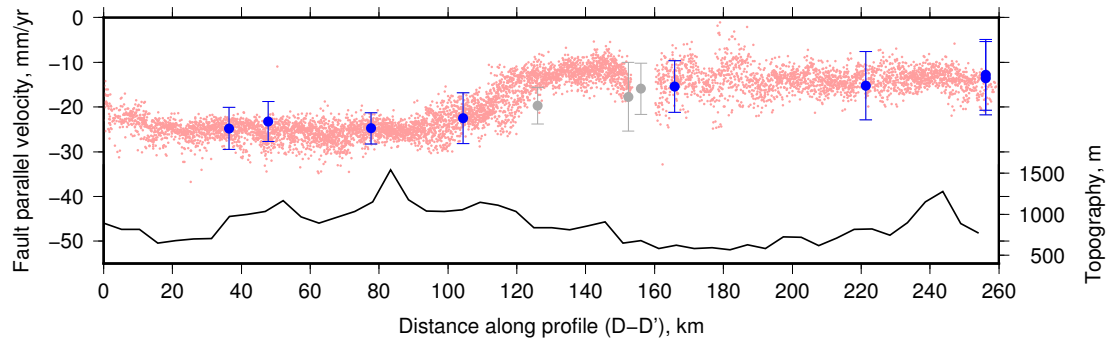


Figure 3.12: Fault parallel velocities along profile D-D' indicated in Figure 3.7. The InSAR velocities are shown in red and the GNSS in blue, with points projected from within a 30 km window centered on the profile. The grey points are GNSS velocities projected from within a 60 km window centered on the profile.

to the peak coseismic slip region of the 1944 earthquake while the central profile with 28 mm/yr corresponds to the 1951 earthquake slip, and the easternmost profile with the slowest slip rate of 21 mm/yr covers the 1943 earthquake rupture. In the case of the two largest earthquakes the coseismic surface slip decreases to the east. Previous studies have shown that overall coseismic slip decrease is indicative of off-fault strain dissipation (e.g. [Manighetti et al., 2005](#)). If this pattern of off-fault strain dissipation also occurs during the interseismic period then our model, which assumes all the slip occurs on the fault, would overestimate the slip rate on the fault. However, it remains unclear if distributed off-fault fault deformation occurs during the interseismic period. A dense network of long-term continuous GNSS measurements around the fault would help determine if this is an important mechanism of long term strain dissipation.

The change in slip rate along the fault could also arise from east-west extension within Anatolia. Earthquake moment tensors show significant number of earthquakes within Anatolia (Figure 3.7b), several with normal faulting mechanisms, implying that there is ongoing internal deformation within Anatolia. [Aktuğ et al. \(2013\)](#) also found significant ongoing deformation within Anatolia from detailed analysis of GNSS velocities in central Anatolia, which were more consistent with east-west elastic elongation rather than a rigid-body rotation ([Reilinger et al., 1997](#), [McClusky et al., 2000](#)) or simple transport ([Reilinger et al., 2006](#)).

The average fault slip rate across the central NAF from our three profiles is 26 mm/yr, which is similar to the slip rate determined using GNSS alone for the region (e.g. [Reilinger et al., 2006](#), [Nocquet, 2012](#)).

3.7.3 Fault creep

Our estimates of fault creep rate by direct offset measurements of LOS velocity across the fault reveal that a ~ 130 km portion of the central NAF is undergoing aseismic creep that reaches the ground surface.

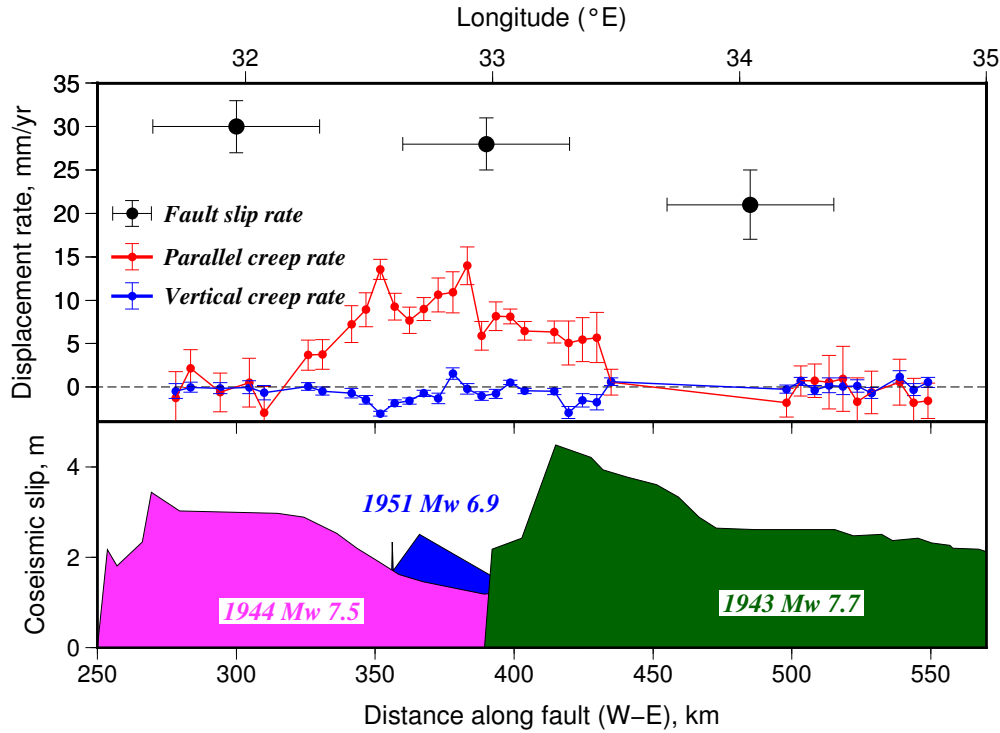


Figure 3.13: Fault slip rate estimates from our elastic dislocation models (Figure 3.8) and aseismic creep rate (Figure 3.10) shown against coseismic surface slip distribution (after *Stein et al. (1997)*).

Over the InSAR time interval, the fault creep rate has a maximum of 14 ± 2 mm/yr around 30 km east of Ismetpasa, which is slightly slower than the value determined by *Cetin et al. (2014)*, who found the maximum creep to be 20 ± 2 mm/yr at the same location. This discrepancy can be explained by the fact that they used LOS velocities from a single look direction (descending). Using our descending velocities alone, which is the same dataset used by *Cetin et al. (2014)*, we estimate a similar maximum fault creep rate of 21 ± 2 mm/yr.

This study is a confirmation that where available, both ascending and descending information can be used to estimate accurate and unbiased values of creep or other surface deformation that is not contaminated by vertical motions

Our average creep rate for the entire portion of the creeping sections is 8 ± 2 mm/yr. This is similar to our MAP solution from our elastic model for profile B-B' (10 mm/yr). Our estimate for the average fault creep rate is similar to recent estimates by *Karabacak et al. (2011)*, *Ozener et al. (2013)*, *Kaneko et al. (2013)* and *Cetin et al. (2014)* who estimate average creep rates of 6-9 mm/yr, 7.6 ± 1 , 9 mm/yr and 8 ± 2 mm/yr respectively. Our MAP solution for the depth extent of aseismic fault creep (9 km) is deeper than the 5 km estimated by *Cetin et al. (2014)* and 4 km estimated by *Rousset et al. (2016)*. However, our 95% confidence bound on this parameter is large (1-20 km). It is possible that we are biased towards deeper depths because we resample our velocities to

a 1km by 1km grid, which could be insensitive to very shallow creep depths. However, [Hussain et al. \(2016\)](#) showed that changing the creep depths over a large range (4 km to 12 km) only results in a small difference in the shape of the profile close to the fault, which is below the estimated uncertainty in the fault parallel velocities. Therefore, it is more likely that the large confidence bound on the creep depth extent is due to the noise in the data.

The average creep rate is about a third of the average fault slip rate (26 mm/yr) for this portion of the NAF implying that strain is still accumulating along the fault. Shallow aseismic creep reduces the rate of interseismic strain accumulation by 30-40% compared to if the fault was fully locked. Assuming a uniform steady-state creep rate of 8 ± 2 mm/yr down to 6 ± 3 km depth (average of [Cetin et al. \(2014\)](#), [Rousset et al. \(2016\)](#) and our MAP solution) along the entire 130 km creeping segment of the fault and 26 mm/yr (21-32, 95% CI) down to a locking depth of 14 (7-22, 95% CI) km, in 200 years (approximate earthquake repeat time ([Stein et al., 1997](#))) the creeping segment of the fault will have accumulated strain equivalent to an earthquake with moment magnitude between 7.4 and 8. This large range is mostly due to the large confidence range for our model parameters. Using the average MAP solution from the three profiles gives a strain deficit equivalent to a moment magnitude 7.7 earthquake in a 200 year period.

3.8 Conclusion

We have presented a new iterative unwrapping technique for small baseline InSAR processing that can be used to iteratively identify and mitigate unwrapping errors, therefore increasing the number of correctly unwrapped pixels in the small baseline network and improving the InSAR coverage compared to methods where unwrapping errors are rejected or masked. We have used this technique to process Envisat SAR data from 7 tracks in both ascending and descending geometries spanning the time window between 2003 and 2010. The footprint of our tracks cover the entire central portion of the North Anatolian Fault in both viewing geometries. We combine the InSAR LOS velocities with published GNSS to create a horizontal velocity field for the region (assuming negligible vertical motions). Profiles through the fault parallel velocities reveal an eastward decreasing fault slip rate (30 mm/yr, 28 mm/yr and 21 mm/yr) with no such pattern in the locking depths (13 km, 13 km, 17 km). Direct offset measurements of LOS velocity across the fault reveal that a ~ 130 km portion of the central NAF is undergoing aseismic fault creep that reaches the ground surface at an average rate of 8 ± 2 mm/yr. The maximum creep rate of 14 ± 2 mm/yr is slower than previous estimates, which were biased by using data from only a single satellite look direction. We conclude that shallow aseismic creep on the central section of the NAF reduces the rate of interseismic strain accumulation by 30-40% compared to if

it was fully locked. Nevertheless, the fault is still accumulating strain and remains capable of producing a large earthquake in the future.

Appendix: Automatic selection of interferometric loops

In this study we created an algorithm that automatically selects and computes the phase sum around closed interferometric loops. This method is based on the methods developed by *Biggs et al. (2007)* and *Wang et al. (2009)*. For simplicity, we assume interferograms are always generated as the difference of the earlier and later SAR acquisitions. Given a small baseline network of such interferograms our algorithm has 4 main steps:

1. For each acquisition date t_1 , determine all other acquisitions it connects to. To avoid duplication we only consider acquisitions forward in time, i.e. t_2, t_3, t_4, \dots where $t_i > t_1$
2. Determine all possible triangles that can be made involving t_1 , using the connecting interferograms and ensuring the nodes remain in chronological order. E.g. the triangle T_{123} consists of the interferograms $\phi_{1,2}$, $\phi_{2,3}$, and $\phi_{1,3}$
3. The first two interferograms ($\phi_{1,2}$ and $\phi_{2,3}$) are classed as being on the “forward path” of the interferometric loop, while the last interferogram is on the “return path”. Therefore the phase sum around the loop for a correctly unwrapped pixel is: $\phi_{1,2} + \phi_{2,3} - \phi_{1,3} = \epsilon$, where $|\epsilon| < 1$
4. Progress through all nodes within the small baseline network in this manner attempting to connect all interferograms with triangular loops. If any interferograms remain at the end we use Dijkstra’s algorithm (*Dijkstra, 1959*) to determine the shortest interferometric path through the network that connects the two nodes of the remaining interferogram.

Acknowledgments

This work has been supported by the Natural Environment Research Council project grant number: NE/I028017/1, which supports the lead author’s research studentship as part of the FaultLab project at the University of Leeds. The Envisat satellite data are freely available and were obtained from the European Space Agency’s Geohazard Supersites project. The GNSS data were obtained from the Global Strain Rate Model project website (<http://gsm2.unavco.org>). Many of the figures in this paper were made using the public domain Generic Mapping Tools (GMT) software (*Wessel and Smith, 2001*). Part of this work was carried out at the Jet Propulsion Laboratory, California Institute of Technology, under a contract with the National Aeronautics and

Space Administration. COMET is the Centre for the Observation and Monitoring of Earthquakes, Volcanoes and tectonics. Results can be obtained by contacting the lead author (eehu@leeds.ac.uk). We would like to thank two anonymous reviewers for their helpful feedback and suggestions, which have improved the quality of the paper.

References

- Aktuğ, B., E. Parmaksız, M. Kurt, O. Lenk, A. Kılıçoğlu, M. A. Gürdal, and S. Özdemir (2013), Deformation of Central Anatolia: GPS implications, *Journal of Geodynamics*, *67*, 78–96. [3.7.2](#)
- Ambraseys, N. N. (1970), Some characteristic features of the Anatolian fault zone, *Tectonophysics*, *9*(2), 143–165. [3.1](#)
- Ayhan, M. E., C. Demir, O. Lenk, A. Kiliçoğlu, Y. Altiner, A. A. Barka, S. Ergintav, and H. Özener (2002), Interseismic strain accumulation in the Marmara Sea region, *Bulletin of the Seismological Society of America*, *92*(1), 216–229. [3.1](#), [3.5](#)
- Barka, A. (1992), The north Anatolian fault zone, in *Annales tectonicae*, vol. 6, pp. 164–195. [3.1](#)
- Barka, A. (1996), Slip distribution along the North Anatolian Fault associated with the large earthquakes of the period 1939 to 1967, *The Bulletin of the Seismological Society of America*, *86*, 1238–1254. [3.1](#)
- Barka, A. A., and P. L. Hancock (1984), Neotectonic deformation patterns in the convex-northwards arc of the North Anatolian fault zone, *Geological Society, London, Special Publications*, *17*(1), 763–774. [3.1](#)
- Bekaert, D., R. Walters, T. Wright, A. Hooper, and D. Parker (2015c), Statistical comparison of InSAR tropospheric correction techniques, *Remote Sensing of Environment*, *170*, 40–47, doi:[10.1002/2014JB011557](#). [3.2](#)
- Bekaert, D. P. S., A. Hooper, and T. J. Wright (2015a), A spatially variable power-law tropospheric correction technique for InSAR data, *Journal of Geophysical Research (Solid Earth)*, *120*, 1345–1356, doi:[10.1002/2014JB011558](#). [3.2](#)
- Biggs, J., T. Wright, Z. Lu, and B. Parsons (2007), Multi-interferogram method for measuring interseismic deformation: Denali Fault, Alaska, *Geophysical Journal International*, *170*(3), 1165–1179, doi:[10.1111/j.1365-246X.2007.03415.x](#). [3.3.1](#), [3.8](#)
- Cakir, Z., A. M. Akoglu, S. Belabbes, S. Ergintav, and M. Meghraoui (2005), Creeping along the ismetpasa section of the North Anatolian fault (Western Turkey): Rate and extent from InSAR, *Earth and Planetary Science Letters*, *238*(1), 225–234. [3.1](#), [3.6](#)
- Cakir, Z., S. Ergintav, A. M. Akoğlu, R. Çakmak, O. Tatar, and M. Meghraoui (2014), InSAR velocity field across the North Anatolian Fault (eastern Turkey): Implications for the loading and release of interseismic strain accumulation, *Journal of Geophysical Research: Solid Earth*, *119*(10), 7934–7943. [3.1](#)
- Cavalié, O., and S. Jónsson (2014), Block-like plate movements in eastern Anatolia observed by InSAR, *Geophysical Research Letters*, *41*(1), 26–31. [3.1](#)
- Cavalié, O., M.-P. Doin, C. Lasserre, and P. Briole (2007), Ground motion measurement in the Lake Mead area, Nevada, by differential synthetic aperture radar interferometry time series analysis: Probing the lithosphere rheological structure, *Journal of Geophysical Research: Solid Earth*, *112*(B3). [3.3.1](#)

- Cetin, E., Z. Cakir, M. Meghraoui, S. Ergintav, and A. M. Akoglu (2014), Extent and distribution of aseismic slip on the Isetpasa segment of the North Anatolian Fault (Turkey) from persistent scatterer InSAR, *Geochemistry, Geophysics, Geosystems*, *15*, 2883–2894, doi:[10.1002/2014GC005307](https://doi.org/10.1002/2014GC005307). 3.1, 3.6, 3.7.3
- Chen, C. W., and H. A. Zebker (2000), Network approaches to two-dimensional phase unwrapping: Intractability and two new algorithms, *JOSA A*, *17*(3), 401–414. 3.3.1
- Chen, C. W., and H. A. Zebker (2001), Two-dimensional phase unwrapping with use of statistical models for cost functions in nonlinear optimization, *JOSA A*, *18*(2), 338–351. 3.3.1
- Costantini, M. (1998), A novel phase unwrapping method based on network programming, *Geoscience and Remote Sensing, IEEE Transactions on*, *36*(3), 813–821. 3.3.1
- Dee, D. P., S. M. Uppala, A. J. Simmons, P. Berrisford, P. Poli, S. Kobayashi, U. Andrae, M. A. Balmaseda, G. Balsamo, P. Bauer, P. Bechtold, A. C. M. Beljaars, L. van de Berg, J. Bidlot, N. Bormann, C. Delsol, R. Dragani, M. Fuentes, A. J. Geer, L. Haimberger, S. B. Healy, H. Hersbach, E. V. Hólm, L. Isaksen, P. Kállberg, M. Köhler, M. Matricardi, A. P. McNally, B. M. Monge-Sanz, J.-J. Morcrette, B.-K. Park, C. Peubey, P. de Rosnay, C. Tavolato, J.-N. Thépaut, and F. Vitart (2011), The ERA-Interim reanalysis: configuration and performance of the data assimilation system, *Quarterly Journal of the Royal Meteorological Society*, *137*, 553–597, doi:[10.1002/qj.828](https://doi.org/10.1002/qj.828). 3.2
- Dijkstra, E. W. (1959), A note on two problems in connexion with graphs, *Numerische mathematik*, *1*(1), 269–271. 4
- Doin, M.-P., C. Lasserre, G. Peltzer, O. Cavali, and C. Doubre (2009), Corrections of stratified tropospheric delays in SAR interferometry: Validation with global atmospheric models, *Journal of Applied Geophysics*, *69*(1), 35 – 50, doi:<http://dx.doi.org/10.1016/j.jappgeo.2009.03.010>. 3.2
- Duputel, Z., P. S. Agram, M. Simons, S. E. Minson, and J. L. Beck (2014), Accounting for prediction uncertainty when inferring subsurface fault slip, *Geophysical Journal International*, p. ggt517. 3.7.2
- Efron, B., and R. Tibshirani (1986), Bootstrap methods for standard errors, confidence intervals, and other measures of statistical accuracy, *Statistical science*, pp. 54–75. 3.2
- Elliott, J., J. Biggs, B. Parsons, and T. Wright (2008), InSAR slip rate determination on the Altyn Tagh Fault, northern Tibet, in the presence of topographically correlated atmospheric delays, *Geophysical Research Letters*, *35*(12). 3.5
- Ergintav, S., S. McClusky, E. Hearn, R. Reilinger, R. Cakmak, T. Herring, H. Ozener, O. Lenk, and E. Tari (2009), Seven years of postseismic deformation following the 1999, M = 7.4 and M = 7.2, Izmit-Düzce, Turkey earthquake sequence, *Journal of Geophysical Research (Solid Earth)*, *114*, B07403, doi:[10.1029/2008JB006021](https://doi.org/10.1029/2008JB006021). 3.1, 3.4, 3.7.2
- Farr, T. G., P. A. Rosen, E. Caro, R. Crippen, R. Duren, S. Hensley, M. Kobrick, M. Paller, E. Rodriguez, L. Roth, D. Seal, S. Shaffer, J. Shimada, J. Umland, M. Werner, M. Oskin, D. Burbank, and D. Alsdorf (2007), The shuttle radar topography mission, *Reviews of Geophysics*, *45*, RG2004, doi:[10.1029/2005RG000183](https://doi.org/10.1029/2005RG000183). 3.2
- Ferretti, A., C. Prati, and F. Rocca (2001), Permanent scatterers in SAR interferometry, *Geoscience and Remote Sensing, IEEE Transactions on*, *39*(1), 8–20. 3.3.1
- Ghiglia, D. C., and M. D. Pritt (1998), *Two-dimensional phase unwrapping: Theory, algorithms, and software*, vol. 4, Wiley New York. 3.3.1

- Goldstein, R. M., H. A. Zebker, and C. L. Werner (1988), Satellite radar interferometry: Two-dimensional phase unwrapping, *Radio science*, *23*(4), 713–720. [3.3.1](#)
- Goodman, J., and J. Weare (2010), Ensemble samplers with affine invariance, *Communications in Applied Mathematics and Computational Science*, *5*, 65–80, doi:[10.2140/camcos.2010.5.65](#). [3.5](#)
- Hamlyn, J. E., D. Keir, T. J. Wright, J. W. Neuberg, B. Goitom, J. O. Hammond, C. Pagli, C. Oppenheimer, J. Kendall, R. Grandin, et al. (2014), Seismicity and subsidence following the 2011 Nabro eruption, Eritrea: Insights into the plumbing system of an off-rift volcano, *Journal of Geophysical Research: Solid Earth*, *119*(11), 8267–8282. [3.7.1](#)
- Hooper, A. (2008), A multi-temporal InSAR method incorporating both persistent scatterer and small baseline approaches, *Geophysical Research Letters*, *35*, L16302, doi:[10.1029/2008GL034654](#). [3.2](#)
- Hooper, A. (2010), A statistical-cost approach to unwrapping the phase of insar time series, in *Proceeding of International Workshop on ERS SAR Interferometry, Frascati, Italy*, vol. 30. [3.3.1](#)
- Hooper, A., and H. A. Zebker (2007), Phase unwrapping in three dimensions with application to insar time series, *JOSA A*, *24*(9), 2737–2747. [3.3.1](#)
- Hooper, A., D. Bekaert, K. Spaans, and M. Arkan (2012), Recent advances in SAR interferometry time series analysis for measuring crustal deformation, *Tectonophysics*, *514*, 1–13, doi:[10.1016/j.tecto.2011.10.013](#). [3.2](#)
- Hubert-Ferrari, A., A. Barka, E. Jacques, S. S. Nalbant, B. Meyer, R. Armijo, P. Tapponnier, and G. C. P. King (2000), Seismic hazard in the Marmara Sea region following the 17 August 1999 Izmit earthquake, *Nature*, *404*, 269–273. [3.1](#)
- Hubert-Ferrari, A., R. Armijo, G. King, B. Meyer, and A. Barka (2002), Morphology, displacement, and slip rates along the North Anatolian Fault, Turkey, *Journal of Geophysical Research: Solid Earth (1978–2012)*, *107*(B10), ETG–9. [3.1](#)
- Hussain, E., T. J. Wright, R. J. Walters, D. Bekaert, A. Hooper, and G. A. Houseman (2016), Geodetic observations of postseismic creep in the decade after the 1999 izmit earthquake, turkey: Implications for a shallow slip deficit, *Journal of Geophysical Research: Solid Earth*, *121*(4), 2980–3001. [3.1](#), [3.4](#), [3.4](#), [3.4](#), [3.5](#), [3.5](#), [3.6](#), [3.7.1](#), [3.7.3](#)
- Jolivet, R., R. Grandin, C. Lasserre, M.-P. Doin, and G. Peltzer (2011), Systematic InSAR tropospheric phase delay corrections from global meteorological reanalysis data, *Geophysical Research Letters*, *38*, L17311, doi:[10.1029/2011GL048757](#). [3.3.1](#)
- Jolivet, R., P. S. Agram, N. Y. Lin, M. Simons, M.-P. Doin, G. Peltzer, and Z. Li (2014), Improving InSAR geodesy using global atmospheric models, *Journal of Geophysical Research: Solid Earth*, *119*(3), 2324–2341. [3.2](#)
- Kampes, B. M., R. F. Hanssen, and Z. Perski (2003), Radar interferometry with public domain tools, in *FRINGE 2003 Workshop, ESA Special Publication*, vol. 550, p. 10. [3.2](#)
- Kaneko, Y., Y. Fialko, D. T. Sandwell, X. Tong, and M. Furuya (2013), Interseismic deformation and creep along the central section of the North Anatolian Fault (Turkey): InSAR observations and implications for rate-and-state friction properties, *Journal of Geophysical Research (Solid Earth)*, *118*, 316–331, doi:[10.1029/2012JB009661](#). [3.1](#), [3.6](#), [3.7.3](#)
- Karabacak, V., E. Altunel, and Z. Cakir (2011), Monitoring aseismic surface creep along the North Anatolian Fault (Turkey) using ground-based LIDAR, *Earth and Planetary Science Letters*, *304*(1), 64–70. [3.1](#), [3.7.3](#)

- Kozaci, Ö., J. Dolan, R. Finkel, and R. Hartleb (2007), Late Holocene slip rate for the North Anatolian Fault, Turkey, from cosmogenic ^{36}Cl geochronology: Implications for the constancy of fault loading and strain release rates, *Geology*, *35*(10), 867–870. [3.1](#)
- Kozaci, Ö., J. F. Dolan, and R. C. Finkel (2009), A late Holocene slip rate for the central North Anatolian fault, at Tahtaköprü, Turkey, from cosmogenic ^{10}Be geochronology: Implications for fault loading and strain release rates, *Journal of Geophysical Research: Solid Earth (1978–2012)*, *114*(B1). [3.1](#)
- Kreemer, C., G. Blewitt, and E. C. Klein (2014), A geodetic plate motion and global strain rate model, *Geochemistry, Geophysics, Geosystems*, *15*(10), 3849–3889. [3.1](#)
- Kutoglu, H., H. Akcin, O. Gundogdu, K. Gormus, and E. Koksal (2010), Relaxation on the Ismetpasa segment of the North Anatolian Fault after the Golcuk Mw = 7.4 and Duzce Mw = 7.2 shocks, *Natural Hazards and Earth System Science*, *10*(12), 2653–2657. [3.1](#)
- Lohman, R. B., and M. Simons (2005), Some thoughts on the use of InSAR data to constrain models of surface deformation: Noise structure and data downsampling, *Geochemistry, Geophysics, Geosystems*, *6*(1). [3.2](#)
- López-Quiroz, P., M.-P. Doin, F. Tupin, P. Briole, and J.-M. Nicolas (2009), Time series analysis of Mexico City subsidence constrained by radar interferometry, *Journal of Applied Geophysics*, *69*(1), 1–15. [3.3.1](#)
- Manighetti, I., M. Campillo, C. Sammis, P. Mai, and G. King (2005), Evidence for self-similar, triangular slip distributions on earthquakes: Implications for earthquake and fault mechanics, *Journal of Geophysical Research: Solid Earth*, *110*(B5). [3.7.2](#)
- Marinkovic, P., and Y. Larsen (2013), Consequences of long-term ASAR local oscillator frequency decay—an empirical study of 10 years of data, in *Living Planet Symposium, Edinburgh. Frascati: European Space Agency (2013, September)*. [3.2](#)
- McClusky, S., S. Balassanian, A. Barka, C. Demir, M. Hamburger, H. Kahle, K. Kastors, G. Kekelidse, R. King, V. Kotzev, et al. (2000), Gps constraints on crustal movements and deformations for plate dynamics, *J Geophys Res*, *105*, 5695–5720. [3.7.2](#)
- McKenzie, D. (1972), Active tectonics of the Mediterranean region, *Geophysical Journal International*, *30*(2), 109–185. [3.1](#)
- Nocquet, J.-M. (2012), Present-day kinematics of the Mediterranean: A comprehensive overview of GPS results, *Tectonophysics*, *579*, 220–242. [3.5](#), [3.7.2](#)
- Noomen, R., T. Springer, B. Ambrosius, K. Herzberger, D. Kuijper, G.-J. Mets, B. Overgaauw, and K. Wakker (1996), Crustal deformations in the Mediterranean area computed from SLR and GPS observations, *Journal of geodynamics*, *21*(1), 73–96. [3.1](#), [3.5](#)
- Oral, M. B., R. E. Reilinger, M. N. Toksöz, A. A. Barka, and I. Kinik (1993), Preliminary results of 1988 and 1990 GPS measurements in western Turkey and their tectonic implications, *Contributions of Space Geodesy to Geodynamics: Crustal Dynamics*, pp. 407–416. [3.1](#), [3.5](#)
- Ozener, H., A. Dogru, and B. Turgut (2013), Quantifying aseismic creep on the ismetpasa segment of the north anatolian fault zone (turkey) by 6 years of gps observations, *Journal of Geodynamics*, *67*, 72–77. [3.1](#), [3.7.3](#)
- Pagli, C., H. Wang, T. J. Wright, E. Calais, and E. Lewi (2014), Current plate boundary deformation of the Afar rift from a 3-D velocity field inversion of InSAR and GPS, *Journal of Geophysical Research: Solid Earth*, *119*(11), 8562–8575. [3.7.1](#)

- Pepe, A., and R. Lanari (2006), On the extension of the minimum cost flow algorithm for phase unwrapping of multitemporal differential SAR interferograms, *Geoscience and Remote Sensing, IEEE Transactions on*, 44(9), 2374–2383. 3.3.1
- Perrin, C., I. Manighetti, J.-P. Ampuero, F. Cappa, and Y. Gaudemer (2016), Location of largest earthquake slip and fast rupture controlled by along-strike change in fault structural maturity due to fault growth, *Journal of Geophysical Research: Solid Earth*. 3.5
- Pinel, V., A. Hooper, S. De la Cruz-Reyna, G. Reyes-Davila, M. Doin, and P. Bascou (2011), The challenging retrieval of the displacement field from InSAR data for andesitic stratovolcanoes: Case study of Popocatepetl and Colima Volcano, Mexico, *Journal of Volcanology and Geothermal Research*, 200(1), 49–61. 3.7.1
- Pucci, S., P. De Martini, and D. Pantosti (2008), Preliminary slip rate estimates for the Düzce segment of the North Anatolian Fault Zone from offset geomorphic markers, *Geomorphology*, 97(3), 538–554. 3.1
- Reilinger, R., S. McClusky, M. Oral, R. King, M. Toksoz, A. Barka, I. Kinik, O. Lenk, and I. Sanli (1997), Global Positioning System measurements of present-day crustal movements in the Arabia-Africa-Eurasia plate collision zone, *Journal of Geophysical Research: Solid Earth*, 102(B5), 9983–9999. 3.7.2
- Reilinger, R., S. McClusky, P. Vernant, S. Lawrence, S. Ergintav, R. Cakmak, H. Ozener, F. Kadirov, I. Guliev, R. Stepanyan, M. Nadariya, G. Hahubia, S. Mahmoud, K. Sakr, A. ArRajehi, D. Paradissis, A. Al-Aydrus, M. Prilepin, T. Guseva, E. Evren, A. Dmitrotsa, S. V. Filikov, F. Gomez, R. Al-Ghazzi, and G. Karam (2006), GPS constraints on continental deformation in the Africa-Arabia-Eurasia continental collision zone and implications for the dynamics of plate interactions, *Journal of Geophysical Research: Solid Earth*, 111(B5), doi:10.1029/2005JB004051. 3.1, 3.5, 3.5, 3.7.2
- Rosen, P. A., S. Hensley, G. Peltzer, and M. Simons (2004), Updated repeat orbit interferometry package released, *Eos, Transactions American Geophysical Union*, 85(5), 47–47, doi:10.1029/2004EO050004. 3.2
- Rousset, B., R. Jolivet, M. Simons, C. Lassarre, B. Riel, P. Milillo, Z. Cakir, and F. Renard (2016), An aseismic slip transient on the North Anatolian Fault, *Geophysical Research Letters*, p. 4, doi:10.1002/2016GL068250. 3.1, 3.7.3
- Savage, J. C., and R. O. Burford (1973), Geodetic determination of relative plate motion in central California, *Journal of Geophysical Research*, 78, 832–845, doi:10.1029/JB078i005p00832. 3.5
- Stein, R. S., A. A. Barka, and J. H. Dieterich (1997), Progressive failure on the North Anatolian Fault since 1939 by earthquake stress triggering, *Geophysical Journal International*, 128, 594–604, doi:10.1111/j.1365-246X.1997.tb05321.x. 3.1, 3.13, 3.7.3
- Straub, C., H.-G. Kahle, and C. Schindler (1997), GPS and geologic estimates of the tectonic activity in the Marmara Sea region, NW Anatolia, *Journal of Geophysical Research: Solid Earth (1978–2012)*, 102(B12), 27,587–27,601. 3.1
- Sudhaus, H., and J. Sigurjón (2009), Improved source modelling through combined use of InSAR and GPS under consideration of correlated data errors: Application to the June 2000 Kleifarvatn earthquake, Iceland, *Geophysical Journal International*, 176(2), 389–404. 3.2
- Taymaz, T., T. Wright, S. Yolsal, O. Tan, E. Fielding, and G. Seyitolu (2007), Source characteristics of the 6 June 2000 Orta-çankırı (central Turkey) earthquake: A synthesis of seismological, geological and geodetic (InSAR) observations, and internal deformation of the Anatolian plate, *Geological Society, London, Special Publications*, 291(1), 259–290. 3.4

- Walters, R., R. Holley, B. Parsons, and T. Wright (2011), Interseismic strain accumulation across the North Anatolian Fault from Envisat InSAR measurements, *Geophysical research letters*, *38*(5). [3.1](#), [3.3.1](#)
- Walters, R., B. Parsons, and T. Wright (2014), Constraining crustal velocity fields with InSAR for Eastern Turkey: Limits to the block-like behavior of Eastern Anatolia, *Journal of Geophysical Research: Solid Earth*, *119*(6), 5215–5234. [3.1](#), [3.4](#), [3.5](#)
- Walters, R. J., J. R. Elliott, Z. Li, and B. Parsons (2013), Rapid strain accumulation on the Ashkabad Fault (Turkmenistan) from atmosphere-corrected InSAR, *Journal of Geophysical Research: Solid Earth*, *118*(7), 3674–3690. [3.2](#)
- Wang, H., T. Wright, and J. Biggs (2009), Interseismic slip rate of the northwestern Xianshuihe fault from InSAR data, *Geophysical Research Letters*, *36*(3). [3.3.1](#), [3.8](#)
- Wessel, P., and W. H. Smith (2001), The Generic Mapping Tools. [3.8](#)
- Wright, T., B. Parsons, and E. Fielding (2001a), Measurement of interseismic strain accumulation across the North Anatolian Fault by satellite radar interferometry, *Geophysical Research Letters*, *28*(10), 2117–2120. [3.1](#), [3.5](#)
- Wright, T. J., B. E. Parsons, and L. Zhong (2004), Toward mapping surface deformation in three dimensions using InSAR, *Geophysical research letters*, *31*(1), L01,607–1. [3.4](#)
- Yavaşoğlu, H., E. Tarı, O. Tüysüz, Z. Çakır, and S. Ergintav (2011), Determining and modeling tectonic movements along the central part of the North Anatolian Fault (Turkey) using geodetic measurements, *Journal of Geodynamics*, *51*(5), 339–343. [3.5](#)
- Zebker, H. A., and Y. Lu (1998), Phase unwrapping algorithms for radar interferometry: residue-cut, least-squares, and synthesis algorithms, *JOSA A*, *15*(3), 586–598. [3.3.1](#)

Chapter 4

Strong lower crust required by strain observations spanning an entire earthquake cycle

E. Hussain¹, T.J. Wright¹, R.J. Walters², D.P.S. Bekaert³ and R. Lloyd⁴

¹ *COMET, School of Earth and Environment, University of Leeds, UK*

² *COMET, Department of Earth Sciences, University of Durham, UK*

³ *Jet Propulsion Laboratory, California Institute of Technology, Pasadena, USA*

⁴ *COMET, School of Earth Sciences, University of Bristol, UK*

Abstract

Earthquakes are caused by the release of tectonic strain accumulated in the interseismic period. Recent advances in satellite geodesy mean we can now measure this interseismic strain accumulation with sufficient accuracy such that strain data can be useful for seismic hazard assessment. However, it remains unclear whether these short-term (decadal) geodetic observations can be useful when assessing the seismic hazard of faults that accumulate strain over centuries to millenia. Here we show that interseismic strain around a major continental transform fault reaches a near-steady state within a few years after major earthquakes. We use InSAR observations acquired by Envisat between 2002 and 2010 to measure the rates of tectonic strain accumulation along the entire North Anatolian Fault, where the time period since the last earthquake varies from ~ 7 years to ~ 70 years. When combined with GNSS observations collected prior to two major earthquakes in 1999, we show that the shear strain rate is independent of the time since the last earthquake. Short-term geodetic strain observations can therefore usefully contribute to seismic hazard assessment. Geodetic observations for an entire earthquake cycle can only be explained if a weak shear zone is embedded within a strong lower crust with viscosity $\geq \sim 10^{20}$ Pas.

4.1 Introduction

Early viscoelastic models of earthquake cycle deformation, based on sparse geodetic observations around the San Andreas Fault suggest that strain rate varies as a function of time throughout the earthquake cycle (*Savage and Prescott, 1978, Thatcher, 1983, Savage, 2000*). The models predict a decreasing shear strain on the fault and a widening deformation zone with time (e.g. *Wright et al., 2013*). If this is true then short-term geodetic estimates of strain accumulation rate will not represent the long-term strain rate; using observations from early in the cycle will overestimate the long-term strain (and the seismic hazard) and those from late in the cycle will underestimate the strain rate.

Earthquake recurrence rate has been shown to closely follow the strain rate on a fault (e.g. *Bird et al., 2010, Bird and Kreemer, 2015*), therefore accurate estimates of the long-term strain rates are critical for seismic hazard assessment and probabilistic forecasting.

However, the long inter-event time in many large fault zones, typically hundreds to thousands of years, means we do not have deformation observations with modern instruments spanning a complete earthquake cycle for any single location (*Meade et al., 2013*). Here, we instead use observations of surface deformation from different portions of a single fault at different stages of the cycle, the North Anatolian Fault (NAF) in Turkey. In the last 80 years the NAF has failed in 10 large earthquakes ($M_w > 6.5$) that

Table 4.1: Data coverage for each Envisat track used in this study.

Track	Geometry	Time span	No. of images	Ifigs created	Ifigs used	ERA-I improvement ^a , %
64	Descending	20040103 - 20100327	21	61	27	13
293	Descending	20040119 - 20101004	20	46	28	3
21	Descending	20021106 - 20090930	25	76	35	8
250	Descending	20031212 - 20100723	38	115	59	1
479	Descending	20031228 - 20100704	30	90	50	12
207	Descending	20040113 - 20100928	40	88	53	10
436	Descending	20030703 - 20100318	36	96	65	2
164	Descending	20031206 - 20100717	44	104	75	1
393	Descending	20031013 - 20100104	29	70	59	-6
350	Descending	20030207 - 20100730	34	79	41	4
429	Ascending	20021204 - 20090819	21	63	29	4
157	Ascending	20030404 - 20080328	19	44	26	7
386	Ascending	20040229 - 20080727	12	29	17	-2
343	Ascending	20040610 - 20100415	14	27	20	6
71	Ascending	20040103 - 20090829	19	48	29	16
28	Ascending	20040728 - 20100707	14	30	21	10
128	Ascending	20041013 - 20100609	12	25	17	-3

^a The percentage noise reduction for each track after the ERA-I weather model correction for tropospheric noise. We remove a ramp from each interferogram before computing the standard deviation.

have ruptured over 1000 km of the fault with an average slip of $\sim 2\text{--}4$ m ([Barka, 1996](#), [Stein et al., 1997](#), [Parsons et al., 2000](#)).

We present the first high-resolution observations of surface deformation for the entire continental expression of the NAF (~ 1000 km) made using InSAR analysis of data spanning 2002 to 2010. Using these data and GNSS observations collected before the 1999 earthquakes, i.e. 245 years late in the cycle, and assuming the entire fault behaves in a similar way, gives us geodetic observations spanning a full ~ 250 year earthquake cycle on the NAF. We show that strain accumulation reaches near steady state within ~ 10 years of an earthquake and discuss the implications for seismic hazard assessment and the rheology of the continental lithosphere.

4.2 Surface deformation from InSAR

We mapped the surface deformation along the entire North Anatolian Fault with InSAR, using satellite radar data from the European Space Agency’s Envisat mission. Our dataset consists of a total of 608 Synthetic Aperture Radar (SAR) images from 14 descending and 9 ascending satellite tracks that span the time interval between 2002 and 2010 (Figure 4.1a-b). Details of the data processing for each track are given in Table 4.1 and the Methods section.

Ascending and descending data are complete for the entire fault except for a gap in ascending data between about 35°E and 37°E (Figure 4.1b), where too few acquisitions were made in the ascending mode.

We transform all estimated LOS velocities to a Eurasia-fixed GNSS reference frame by firstly resampling our InSAR LOS velocities onto a 1 km by 1 km regular grid. For each track, we then determine the best-fit plane between the GNSS velocities projected into the LOS and the InSAR velocities within 1km of each GNSS site, and remove this from the InSAR rate maps.

To estimate the uncertainties in the data we calculate the RMS misfit in horizontal velocities in the overlapping areas between neighbouring tracks (Figure D3), using the average incidence angle $\sim 23^\circ$ and assuming negligible vertical motion. The residuals between neighbouring tracks are approximately Gaussian with mean values close to zero. The average RMS misfits between these independent estimates of horizontal velocities are 4.1 mm/yr for descending tracks and 5.5 mm/yr for ascending tracks, giving empirical uncertainties of ~ 3 and ~ 4 mm/yr respectively for the individual tracks.

For pixels with both ascending and descending LOS velocities, we invert for the east-west and vertical components of motion using the smooth, interpolated north component of the GNSS velocities (Figure D4) to constrain the north-south component in the inversion (e.g. *Hussain et al., 2016 in revision*). While most of our region of interest is covered by both ascending and descending data (blue polygons in Figure 4.1c), some areas have only ascending or descending data. For these locations we also assume no vertical motion, allowing us to still invert for the east-west component of motion.

Our resulting velocity field is shown in Figure 4.1c. The east-west velocities clearly show strain accumulation along the entire NAF with the expected right-lateral sense of motion. There is no systematic pattern in vertical velocities across the fault (Figure D5)

4.3 Variation in strain accumulation along the NAF

To investigate the spatial variation in strain accumulation we plot profiles of fault parallel velocity at regular locations along the fault (every ~ 50 km) and use simple dislocation models to estimate fault slip rate and locking depth. We use a screw dislocation model (*Savage and Burford, 1973*) for most of the fault (with a rotation term as in *Hussain et al. (2016 in revision)*). For sections with shallow fault creep (identified by *Hussain et al. (2016)* and *Cetin et al. (2014)*), we also solve for creep rate and maximum creep depth (see Methods for details).

The results (Figures 4.2, 4.3 and D8) show the variation in slip rate and locking depth along the NAF. There is no clear spatial correlation in slip rate or locking depth with the location of previous large ruptures along the NAF. We see a general pattern

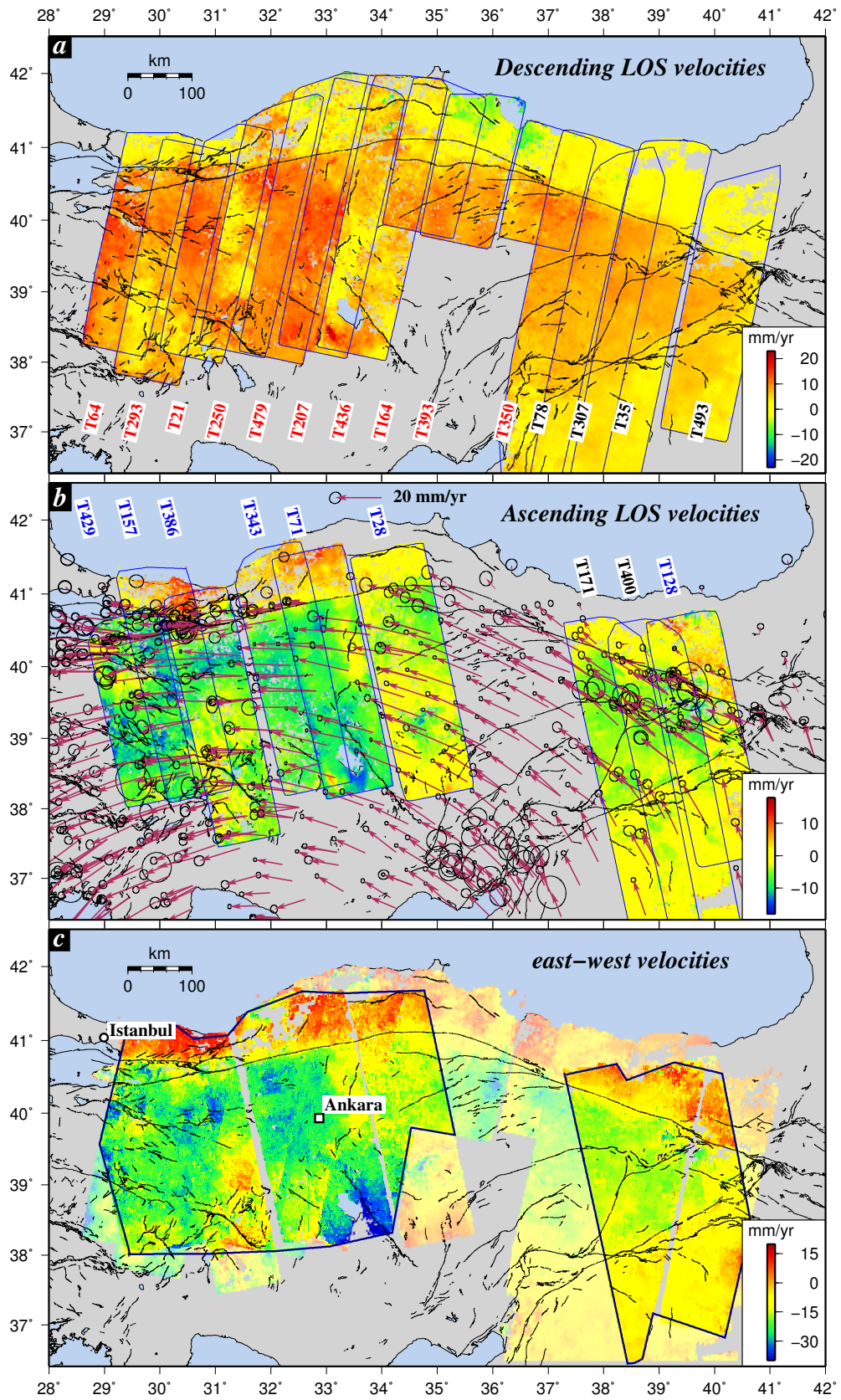


Figure 4.1: The line-of-sight (LOS) velocities for the descending (a) and ascending (b) tracks used in this study. The maroon vectors are published GNSS velocities from the Global Strain Rate Model (*Kreemer et al., 2014*). (c) The east-west component of motion decomposed from the LOS measurements and the interpolated GNSS north velocities, see text for details. The polygons indicate regions with both ascending and descending data. The pale regions outside the polygons are covered by only ascending or descending data.

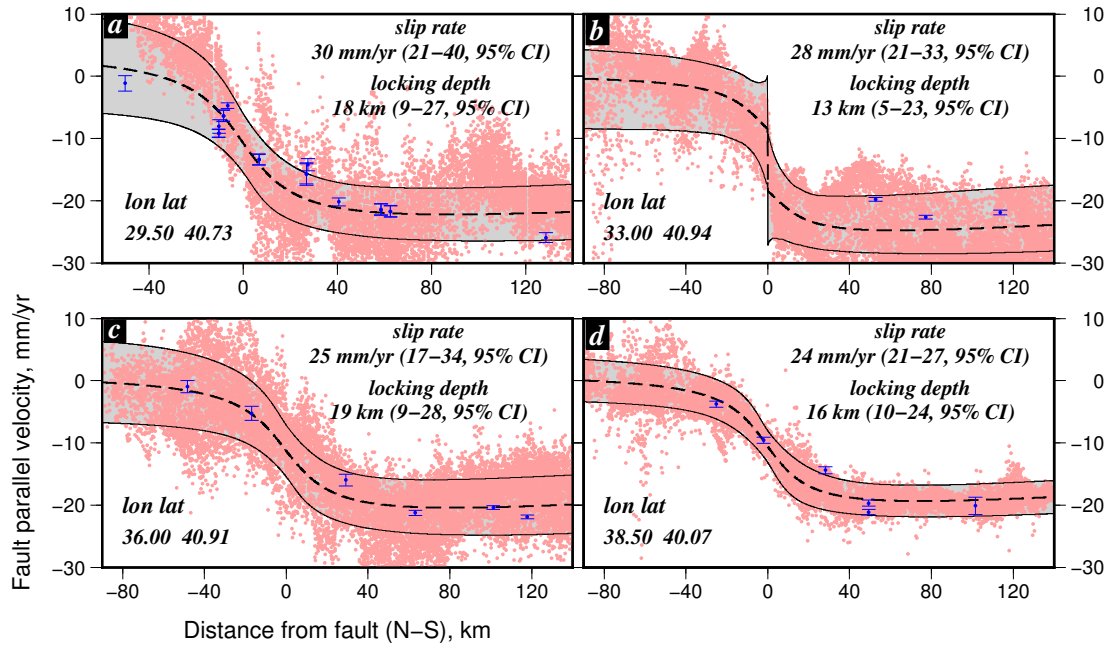


Figure 4.2: A selection of profiles used to estimate the fault slip rate and locking depth (red points in Figure 4.3). All 22 profiles are shown in Figure D8 in the supplementary material. The red points are the fault parallel InSAR velocities projected from within 25 km perpendicular distance onto each profile. The blue points are the fault parallel component of the GNSS velocities. The black dashed line is our maximum a posteriori probability (MAP) solution with the grey shaded area representing the 95% confidence interval.

of westward increasing slip rates from an average 22 ± 3 mm/yr on the eastern section of the NAF to 30 ± 3 mm/yr in the west (Figure 4.3b). Our maximum a posteriori probability (MAP) solutions for the locking depth show no clear variation along strike. Although slip rate and locking depth estimates covary (e.g. Wang *et al.*, 2009), the slip rates are not greatly affected by locking depth (Figure D6). Our profiles show that surface strain is localised with about 90% of the interseismic deformation occurring in a roughly 70 km wide region centred on the fault.

If we assume no internal deformation within central Turkey then the projection of far field GNSS velocities onto the fault gives the estimated slip rate from GNSS alone with no required prior assumption on the deformation model. These velocities are indicated by the purple lines in Figure 4.3b for five broad profiles (~ 150 km wide, Figure D7), which show good agreement with the MAP slip rates from the joint inversion.

We use our estimates of the slip rate and locking depth for each of our profiles to estimate the shear strain rate along the fault caused by motion below the locked seismogenic crust, ensuring we propagate the full covariance information. Our estimates of the strain rate (Figure 4.3d) show no clear spatial correlation with any previous ruptures, with the strain rates consistent with a near constant value of ~ 0.5 microstrain/yr along the fault. Interseismic strain rate therefore appears to be independent of time since the last earthquake for most of the earthquake cycle.

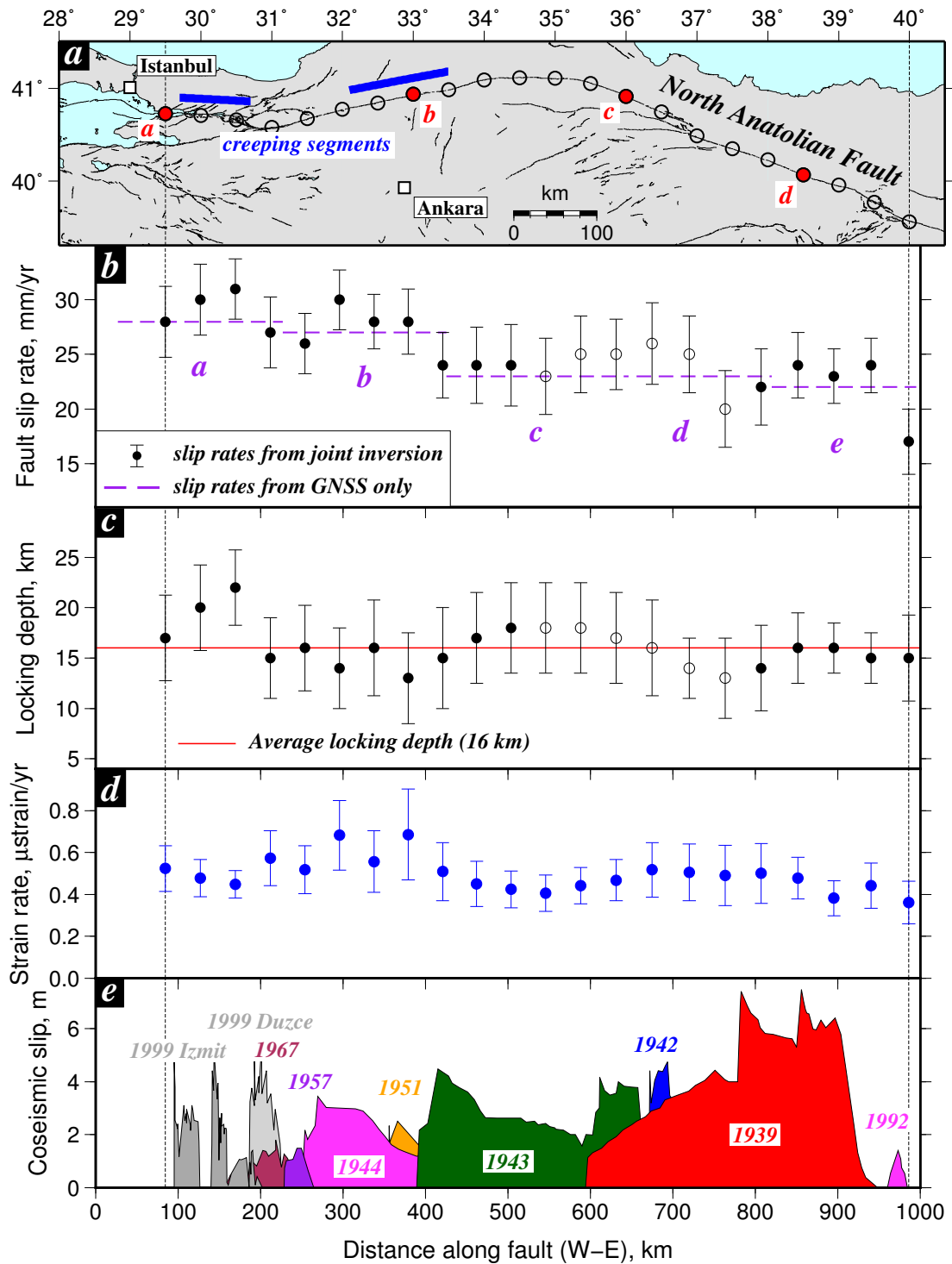


Figure 4.3: The variation in fault slip rate (b) and locking depth (c) along strike of the NAF at the locations indicated by the black circles in (a). The error bars represent the 68% confidence bound on the parameter estimates. The solid circles are results from profiles that are in the high confidence polygons indicated in Figure 4.1c while the open circles are profiles that are in areas where only ascending or descending data are available. The slip rates are consistent with a constant locking depth of 16 ± 4 km along the entire fault (Figure D6). The purple lines in (b) are the slip rate estimates from GNSS alone (Figure D7). We use the slip rate and locking depth estimates to calculate the strain rate along the fault (d), as described in the text. (e) The surface coseismic slip distributions of major earthquakes (Mw > 6.5) along the NAF since 1939 (Stein *et al.*, 1997, Barka *et al.*, 2002, Akyuz, 2002).

4.4 Discussion and Conclusions

Viscoelastic-coupling models of the earthquake cycle, with repeating earthquakes in an elastic layer overlying a viscoelastic half space, predict a decreasing shear strain with time after an earthquake (*Savage and Prescott, 1978, Thatcher, 1983, Savage, 1990*).

The key parameter that controls the temporal behaviour of these models is τ_0 : the ratio of Maxwell relaxation time ($2\eta/\mu$) to inter-event time (T), where η is the viscosity of the lower crust and μ is the shear modulus. Models with $\tau_0 \ll 1$, i.e. Maxwell relaxation time \ll inter-event time, predict a rapidly decreasing strain rate with time, while models with $\tau_0 \gtrsim 1$ predict a constant strain rate with time (Figure 4.4).

We compare our observations with predictions of the strain rate variation with time for different lower crustal viscosities using the viscoelastic-coupling model for the NAF using $T \sim 250$ years (*Stein et al., 1997*) and $\mu = 3 \times 10^{10}$ Pa (Figure 4.4). τ_0 values of 0.01, 0.1, 1 and 10 correspond to lower crustal viscosities of $\sim 10^{18}$ Pas, $\sim 10^{19}$ Pas, $\sim 10^{20}$ Pas and $\sim 10^{21}$ Pas respectively.

We also calculate the evolution of postseismic strain rates from GNSS observations following the 1999 Izmit earthquake (*Ergintav et al., 2009*). These show velocities that decay according to a $1/(t+c)$ law with strain rates small after ~ 7 -10 years (Figure 4.4).

After the initial postseismic period, the shear strain rates do not vary with time for the North Anatolian Fault. Viscoelastic coupling models with low τ_0 cannot explain time-invariance for most of the earthquake cycle. A time-invariant strain accumulation requires a strong substrate with a viscosity $\geq 10^{20}$ Pas.

No value of τ_0 can explain the observed evolution of postseismic strain that dominates the geodetic signals for the first few years following a large earthquake. The observations fit a model in which velocities are proportional to $1/(t+c)$, analogous to a modified Omori law that governs aftershock decay (*Omori, 1894*). This is consistent with either rate-and-state friction controlled afterslip on a deep portion of the fault or viscoelastic relaxation of a power-law shear zone with a large stress exponent (*Montési, 2004*).

Earlier geodetic investigations of the slip rate on the NAF treated the fault as rotating along a great circle about an Euler pole located in the Nile delta (e.g. *Reilinger et al., 1997, McClusky et al., 2000*). This method assumes all the relative motion between Eurasia and Anatolia is taken up on the fault, meaning that there is no internal deformation within Anatolia. However *Aktuğ et al. (2013)* showed that there is significant deformation within central Anatolia. They computed linear gradients of 0.7–1.3 mm per 100 km along great circle paths about the Euler pole, which is mechanically inconsistent with the assumptions of coherent transport or rigid body rotation. For the NAF this linear gradient predicts a change in velocity of 6.3-11.7 mm/yr between the

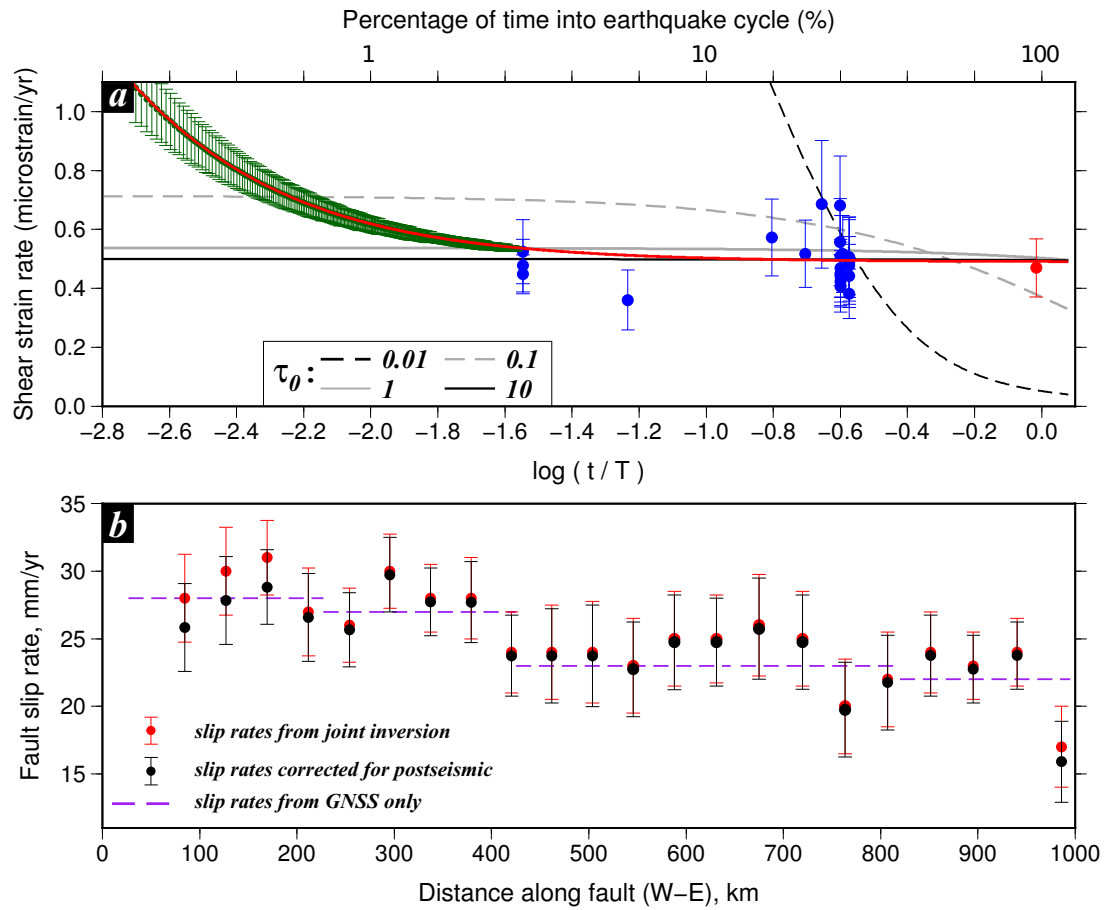


Figure 4.4: (a) The shear strain rates estimated using our estimates of the slip rate and locking depths along the NAF plotted against the time since the last earthquake, in blue. The red circle is the estimate using pre-1999 earthquake GNSS measurements. The darkgreen points are the postseismic strain rates estimated from the weekly velocity timeseries of two GNSS stations located ~ 10 km either side of the fault (SEFI and KAZI) (*Ergintav et al., 2009*). The red line is the best fit to the postseismic and interseismic GNSS strain rates. The black and grey lines are the expected variation in strain rate with time for different lower crustal viscosities away from the fault (*Savage and Prescott, 1978, Savage, 2000*). τ_0 values of 0.01, 0.1, 1 and 10 correspond to lower crustal viscosities of $\sim 10^{18}$ Pas, $\sim 10^{19}$ Pas, $\sim 10^{20}$ Pas and $\sim 10^{21}$ Pas respectively. (b) Fault slip rate variation along the NAF corrected for the postseismic slip rate, assuming a fixed locking depth at 16 km.

eastern and western most sections of the fault. Our estimates show an increase in fault slip rate of 6 ± 3 mm/yr from an average 22 ± 3 mm/yr in the east to 28 ± 3 mm/yr in the west (corrected for postseismic velocities, Figure 4.4b), which is consistent with the prediction of *Aktuğ et al. (2013)* and implies east-west extension within Anatolia.

Our results imply that short term snapshots of the present-day strain accumulation (as long as it is after the postseismic period) are representative of the entire earthquake cycle, and therefore geodetic estimates of the strain rate can be used to estimate the total strain accumulation since the last earthquake on a fault, and be used as a proxy for the seismic hazard (*Bird et al., 2010, Bird and Kreemer, 2015*).

Previous studies have used the depth distribution of earthquakes in the continents to suggest that the strength of the lithosphere resides in the upper crust (e.g. *Maggi et al., 2000, Jackson et al., 2008*). However, our analysis of the strain rate shows that the lower crust away from the fault zone is also strong, implying that seismogenic thickness is not a useful indicator for crustal strength. A time-invariant strain rate for most of the seismic cycle can only be explained if a weak shear zone is embedded within a strong lower crust.

Acknowledgments

This work has been supported by the Natural Environment Research Council project grant number: NE/I028017/1, which supports the lead author's PhD studentship as part of the FaultLab project at the University of Leeds. The Envisat satellite data are freely available and were obtained from the European Space Agency's Geohazard Supersites project. The GNSS data were obtained from the Global Strain Rate Model project website (<http://gsm.unavco.org>). Many of the figures in this paper were made using the public domain Generic Mapping Tools (GMT) software (*Wessel and Smith, 2001*). Part of this work was carried out at the Jet Propulsion Laboratory, California Institute of Technology, under a contract with the National Aeronautics and Space Administration. COMET is the Centre for the Observation and Monitoring of Earthquakes, Volcanoes and tectonics. Results can be obtained by contacting the lead author (eeehu@leeds.ac.uk).

4.5 Methods

InSAR data processing

We focus the Envisat SAR images using ROLPAC (*Rosen et al., 2004*) and use the DORIS software (*Kampes et al., 2003*) to construct interferograms that minimise the temporal and perpendicular baselines while producing a redundant network for each track (Figures D1 and D2). We correct for topographic contributions to the radar phase using a 90 m SRTM Digital Elevation Model (*Farr et al., 2007*) and account

for the oscillator drift for Envisat according to [Marinkovic and Larsen \(2013\)](#). We unwrap the interferograms using an iterative unwrapping procedure for small baseline InSAR measurements described by [Hussain et al. \(2016 in revision\)](#). We correct each interferogram for an estimate of the tropospheric noise using auxiliary data from the ERA-Interim global atmospheric model reanalysis product ([Dee et al., 2011](#), [Bekaert et al., 2015c](#)). On average the ERA-I correction reduces the standard deviation of our tracks by about 5% (Table 4.1). We use the StaMPS (Stanford Method for Persistent Scatterers) small baseline time series technique ([Hooper, 2008](#), [Hooper et al., 2012](#)) to remove incoherent pixels and reduce the noise contribution to the deformation signal, and calculate the average line-of-sight (LOS) velocity for each track. We present 1-sigma uncertainties on the final velocities for each pixel, calculated using bootstrap resampling ([Efron and Tibshirani, 1986](#)).

Our InSAR dataset includes 6 tracks published by [Walters et al. \(2014\)](#) (descending tracks 78, 307, 35 and 493, and ascending tracks 171 and 400), which cover the eastern section of the NAF (Figure 4.1). The interferograms for these tracks were created using ROI-PAC, with the InSAR corrections applied as discussed above, and the velocity maps formed using the π -RATE software package ([Wang and Wright, 2012](#)). The main difference between π -RATE and StaMPS is related to the selection of the pixels, while the mathematical expression for the rate-computation does not change. See [Walters et al. \(2014\)](#) for more details on the processing of these tracks.

Modelling profiles

We use the method described by [Hussain et al. \(2016 in revision\)](#) to fit a simple 1-D elastic dislocation model to the fault parallel velocities (v_{par}), using a simple screw dislocation model (Equation 4.1) for most of the fault to solve for slip rate (S) and locking depth (d_1). For creeping sections we also solve for the creep rate (C) and creep depth (d_2) (Equation 4.2).

$$v_{par}(x) = \frac{S}{\pi} \arctan\left(\frac{x}{d_1}\right) + x\theta_{rot} + a, \quad (4.1)$$

$$v_{par}(x) = \frac{S}{\pi} \arctan\left(\frac{x}{d_1}\right) + C \left[\frac{1}{\pi} \arctan\left(\frac{x}{d_2}\right) - \mathcal{H}(x) \right] + x\theta_{rot} + a, \quad (4.2)$$

where a is a static offset, $\mathcal{H}(x)$ is the Heaviside function and θ_{rot} corrects for the proximity of the profile points to the pole of rotation of Anatolia in a Eurasia-fixed reference frame. θ_{rot} is calculated using the linear trend through the far-field GNSS velocities on 5 broad profiles (Figure D7), and assuming the pole of rotation is fixed. The values used and the longitude extent to which they apply are given in Table 4.2.

We find the best-fit values for each model parameter using a Markov Chain Monte Carlo (MCMC) Bayesian sampler ([Goodman and Weare, 2010](#), [Hussain et al., 2016](#)).

Table 4.2: θ_{rot} values used for the rotation correction.

Profile ID ^a	Lon. extent (°E)	θ_{rot} (mm/yr/km)
a	29 - 31.25	0.0255
b	31.25 - 33.5	0.0307
c	33.5 - 35.5	0.0138
d	35.5 - 38	0.0213
e	38 - 40	0.0308

^a GNSS profiles shown in Figures 4.3b and D7.

The MCMC sampler explores the parameter space constrained by: $-60 < S$ (mm/yr) < 0 , $0 < d_1$ (km), < 60 , $-30 < C$ (km), < 0 , $0 < d_2$ (km), < 40 , $-40 < a$ (mm/yr) < 40 , assuming a uniform prior probability distribution over each range. For creeping profiles an important constraint we impose is that the maximum creep depth cannot be greater than the locking depth, i.e. $d_2 \leq d_1$. Our MCMC model runs over 300,000 iterations and produces 48,000 samples of the posterior distribution from which we estimate both the maximum a posteriori probability (MAP) solution and marginalised probability distributions for each parameter.

References

- Aktuğ, B., E. Parmaksız, M. Kurt, O. Lenk, A. Kılıçoğlu, M. A. Gürdal, and S. Özdemir (2013), Deformation of Central Anatolia: GPS implications, *Journal of Geodynamics*, *67*, 78–96. [4.4](#)
- Akyuz, H. S. (2002), Surface rupture and slip distribution of the 12 november 1999 Duzce earthquake (M 7.1), North Anatolian Fault, Bolu, Turkey, *The Bulletin of the Seismological Society of America*, *92*, 61–66, doi:[10.1785/0120000840](#). [4.3](#)
- Barka, A. (1996), Slip distribution along the North Anatolian Fault associated with the large earthquakes of the period 1939 to 1967, *The Bulletin of the Seismological Society of America*, *86*, 1238–1254. [4.1](#)
- Barka, A., H. S. Akyuz, E. Altunel, G. Sunal, Z. Akir, A. Dikbas, B. Yerli, R. Armijo, B. Meyer, J. B. de Chabalier, T. Rockwell, J. R. Dolan, R. Hartleb, T. Dawson, S. Christofferson, A. Tucker, T. Fumal, R. Langridge, H. Stenner, W. Lettis, J. Bachhuber, and W. Page (2002), The surface rupture and slip distribution of the 17 august 1999 Izmit earthquake (M 7.4), North Anatolian Fault, *Bulletin of the Seismological Society of America*, *92*(1), 43–60, doi:[10.1785/0120000841](#). [4.3](#)
- Bekaert, D., R. Walters, T. Wright, A. Hooper, and D. Parker (2015c), Statistical comparison of InSAR tropospheric correction techniques, *Remote Sensing of Environment*, *170*, 40–47, doi:[10.1002/2014JB011557](#). [4.5](#)
- Bird, P., and C. Kreemer (2015), Revised tectonic forecast of global shallow seismicity based on version 2.1 of the Global Strain Rate Map, *Bulletin of the Seismological Society of America*, *105*(1), 152–166. [4.1](#), [4.4](#)
- Bird, P., C. Kreemer, and W. E. Holt (2010), A long-term forecast of shallow seismicity based on the Global Strain Rate Map, *Seismological Research Letters*, *81*(2), 184–194. [4.1](#), [4.4](#)
- Cetin, E., Z. Cakir, M. Meghraoui, S. Ergintav, and A. M. Akoglu (2014), Extent and distribution of aseismic slip on the Ismetpasa segment of the North Anatolian Fault (Turkey) from persistent scatterer InSAR, *Geochemistry, Geophysics, Geosystems*, *15*, 2883–2894, doi:[10.1002/2014GC005307](#). [4.3](#)
- Dee, D. P., S. M. Uppala, A. J. Simmons, P. Berrisford, P. Poli, S. Kobayashi, U. Andrae, M. A. Balmaseda, G. Balsamo, P. Bauer, P. Bechtold, A. C. M. Beljaars, L. van de Berg, J. Bidlot, N. Bormann, C. Delsol, R. Dragani, M. Fuentes, A. J. Geer, L. Haimberger, S. B. Healy, H. Hersbach, E. V. Hólm, L. Isaksen, P. Kållberg, M. Köhler, M. Matricardi, A. P. McNally, B. M. Monge-Sanz, J.-J. Morcrette, B.-K. Park, C. Peubey, P. de Rosnay, C. Tavolato, J.-N. Thépaut, and F. Vitart (2011), The ERA-Interim reanalysis: configuration and performance of the data assimilation system, *Quarterly Journal of the Royal Meteorological Society*, *137*, 553–597, doi:[10.1002/qj.828](#). [4.5](#)
- Efron, B., and R. Tibshirani (1986), Bootstrap methods for standard errors, confidence intervals, and other measures of statistical accuracy, *Statistical science*, pp. 54–75. [4.5](#)

- Ergintav, S., S. McClusky, E. Hearn, R. Reilinger, R. Cakmak, T. Herring, H. Ozener, O. Lenk, and E. Tari (2009), Seven years of postseismic deformation following the 1999, $M = 7.4$ and $M = 7.2$, Izmit-Düzce, Turkey earthquake sequence, *Journal of Geophysical Research (Solid Earth)*, *114*, B07403, doi:[10.1029/2008JB006021](https://doi.org/10.1029/2008JB006021). 4.4
- Farr, T. G., P. A. Rosen, E. Caro, R. Crippen, R. Duren, S. Hensley, M. Kobrick, M. Paller, E. Rodriguez, L. Roth, D. Seal, S. Shaffer, J. Shimada, J. Umland, M. Werner, M. Oskin, D. Burbank, and D. Alsdorf (2007), The shuttle radar topography mission, *Reviews of Geophysics*, *45*, RG2004, doi:[10.1029/2005RG000183](https://doi.org/10.1029/2005RG000183). 4.5
- Goodman, J., and J. Weare (2010), Ensemble samplers with affine invariance, *Communications in Applied Mathematics and Computational Science*, *5*, 65–80, doi:[10.2140/camcos.2010.5.65](https://doi.org/10.2140/camcos.2010.5.65). 4.5
- Hooper, A. (2008), A multi-temporal InSAR method incorporating both persistent scatterer and small baseline approaches, *Geophysical Research Letters*, *35*, L16302, doi:[10.1029/2008GL034654](https://doi.org/10.1029/2008GL034654). 4.5
- Hooper, A., D. Bekaert, K. Spaans, and M. Arikani (2012), Recent advances in SAR interferometry time series analysis for measuring crustal deformation, *Tectonophysics*, *514*, 1–13, doi:[10.1016/j.tecto.2011.10.013](https://doi.org/10.1016/j.tecto.2011.10.013). 4.5
- Hussain, E., T. J. Wright, R. J. Walters, D. Bekaert, A. Hooper, and G. A. Houseman (2016), Geodetic observations of postseismic creep in the decade after the 1999 izmit earthquake, turkey: Implications for a shallow slip deficit, *Journal of Geophysical Research: Solid Earth*, *121*(4), 2980–3001. 4.3, 4.5
- Hussain, E., A. Hooper, T. J. Wright, R. J. Walters, and D. Bekaert (2016 in revision), Interseismic strain accumulation across the central north anatolian fault from iteratively unwrapped insar measurements, *Submitted*. 4.2, 4.3, 4.5, 4.5
- Jackson, J., D. McKENZIE, K. Priestley, and B. Emmerson (2008), New views on the structure and rheology of the lithosphere, *Journal of the Geological Society*, *165*(2), 453–465. 4.4
- Kampes, B. M., R. F. Hanssen, and Z. Perski (2003), Radar interferometry with public domain tools, in *FRINGE 2003 Workshop, ESA Special Publication*, vol. 550, p. 10. 4.5
- Kreemer, C., G. Blewitt, and E. C. Klein (2014), A geodetic plate motion and global strain rate model, *Geochemistry, Geophysics, Geosystems*, *15*(10), 3849–3889. 4.1
- Maggi, A., J. Jackson, K. Priestley, and C. Baker (2000), A re-assessment of focal depth distributions in southern Iran, the Tien Shan and northern India: Do earthquakes really occur in the continental mantle?, *Geophysical Journal International*, *143*(3), 629–661. 4.4
- Marinkovic, P., and Y. Larsen (2013), Consequences of long-term ASAR local oscillator frequency decay—an empirical study of 10 years of data, in *Living Planet Symposium, Edinburgh. Frascati: European Space Agency (2013, September)*. 4.5
- McClusky, S., S. Balassanian, A. Barka, C. Demir, M. Hamburger, H. Kahle, K. Kasters, G. Kekelidse, R. King, V. Kotzev, et al. (2000), Gps constraints on crustal movements and deformations for plate dynamics, *J Geophys Res*, *105*, 5695–5720. 4.4
- Meade, B. J., Y. Klinger, and E. A. Hetland (2013), Inference of multiple earthquake-cycle relaxation timescales from irregular geodetic sampling of interseismic deformation, *Bulletin of the Seismological Society of America*, *103*(5), 2824–2835. 4.1
- Montési, L. G. (2004), Controls of shear zone rheology and tectonic loading on post-seismic creep, *Journal of Geophysical Research: Solid Earth*, *109*(B10). 4.4

- Omori, F. (1894), *On the after-shocks of earthquakes*, vol. 7, The University. 4.4
- Parsons, T., S. Toda, R. S. Stein, A. Barka, and J. H. Dieterich (2000), Heightened odds of large earthquakes near Istanbul: An interaction-based probability calculation, *Science*, 288, 661–665, doi:10.1126/science.288.5466.661. 4.1
- Reilinger, R., S. McClusky, M. Oral, R. King, M. Toksoz, A. Barka, I. Kinik, O. Lenk, and I. Sanli (1997), Global Positioning System measurements of present-day crustal movements in the Arabia-Africa-Eurasia plate collision zone, *Journal of Geophysical Research: Solid Earth*, 102(B5), 9983–9999. 4.4
- Rosen, P. A., S. Hensley, G. Peltzer, and M. Simons (2004), Updated repeat orbit interferometry package released, *Eos, Transactions American Geophysical Union*, 85(5), 47–47, doi:10.1029/2004EO050004. 4.5
- Savage, J. (1990), Equivalent strike-slip earthquake cycles in half-space and lithosphere-asthenosphere earth models, *Journal of Geophysical Research: Solid Earth*, 95(B4), 4873–4879. 4.4
- Savage, J. (2000), Viscoelastic-coupling model for the earthquake cycle, *Journal of Geophysical Research*, 105. 4.1, 4.4
- Savage, J., and W. Prescott (1978), Asthenosphere readjustment and the earthquake cycle, *Journal of Geophysical Research: Solid Earth*, 83(B7), 3369–3376. 4.1, 4.4, 4.4
- Savage, J. C., and R. O. Burford (1973), Geodetic determination of relative plate motion in central California, *Journal of Geophysical Research*, 78, 832–845, doi:10.1029/JB078i005p00832. 4.3
- Stein, R. S., A. A. Barka, and J. H. Dieterich (1997), Progressive failure on the North Anatolian Fault since 1939 by earthquake stress triggering, *Geophysical Journal International*, 128, 594–604, doi:10.1111/j.1365-246X.1997.tb05321.x. 4.1, 4.3, 4.4
- Thatcher, W. (1983), Nonlinear strain buildup and the earthquake cycle, *Journal of Geophysical Research*, 88, 5893–5902. 4.1, 4.4
- Walters, R., B. Parsons, and T. Wright (2014), Constraining crustal velocity fields with InSAR for Eastern Turkey: Limits to the block-like behavior of Eastern Anatolia, *Journal of Geophysical Research: Solid Earth*, 119(6), 5215–5234. 4.5
- Wang, H., and T. Wright (2012), Satellite geodetic imaging reveals internal deformation of western Tibet, *Geophysical Research Letters*, 39(7). 4.5
- Wang, H., T. Wright, and J. Biggs (2009), Interseismic slip rate of the northwestern Xianshuihe fault from InSAR data, *Geophysical Research Letters*, 36(3). 4.3
- Wessel, P., and W. H. Smith (2001), The Generic Mapping Tools. 4.4
- Wright, T. J., J. R. Elliott, H. Wang, and I. Ryder (2013), Earthquake cycle deformation and the Moho: Implications for the rheology of continental lithosphere, *Tectonophysics*, 609, 504–523. 4.1

Chapter 5

Discussion and Conclusions

In this chapter I summarise the main findings of this thesis from Chapters 2-4, and discuss future opportunities and pathways for using InSAR to probe deeper into the earthquake cycle.

5.1 Summary of results and implications

5.1.1 Chapter 2

In Chapter 2 I used data from 5 Envisat tracks to investigate the spatial pattern and temporal behaviour of aseismic creep on the Izmit section of the North Anatolian Fault (NAF). *Cakir et al. (2012)* showed that this part of the fault was not creeping before the 1999 Izmit earthquake (Mw 7.4), and concluded that fault creep was initiated as a postseismic response to the earthquake. My InSAR dataset covers the time period between 2003 and 2010 and shows fault creep to be localised on a ~ 80 km section of the Izmit rupture. Over the InSAR time interval, the time-averaged fault creep rate has a maximum value of 11 ± 2 mm/yr near the city of Izmit. My estimate is slower than the 27 mm/yr estimated by *Cakir et al. (2012)*. This discrepancy arises mainly due to a bias from their use of satellite data from only a single look direction, which is unable to correct for contamination from vertical motions onto the line-of-sight (LOS).

I showed that fault creep has a steady-state rate of 5 mm/yr down to a maximum depth of 8 km. Therefore, in terms of the moment budget and seismic hazard, the effect of the shallow, aseismic slip in the past decade is small compared to that from plate loading.

Using a rate-and-state friction model to project my displacement time series 200 years later into the earthquake cycle shows that the cumulative shallow slip is insufficient to account for the 2-3 m shallow coseismic slip deficit observed in the Izmit earthquake. Therefore, distributed inelastic deformation in the uppermost few kilometers of the crust or slip transients during the interseismic period are likely to be important mechanisms for generating the shallow slip deficit.

InSAR LOS measurements are most sensitive to motion in the vertical direction - the average vertical component of the look vector is ~ 0.9 compared to ~ 0.4 for the east component and ~ 0.1 for the north component. Therefore, even small motions in the vertical direction will strongly bias estimates of horizontal velocity if using information from only a single look direction. For more robust analysis of horizontal surface deformation it is critical to have InSAR measurements in both ascending and descending geometries, which can be used to decompose the velocities into horizontal and vertical components of motion (either by assuming negligible north-south or fixing this with GNSS velocities).

5.1.2 Chapter 3

One of the key limiting steps for robust InSAR analysis is the phase unwrapping procedure. In Chapter 3 I developed a new phase unwrapping procedure for small baseline InSAR measurements. This method iteratively checks for pixels unwrapped correctly in a previous iteration and applies a high cost to unwrapping across these pixels in the next iteration. In this way the unwrapping algorithm uses the correctly unwrapped pixels as a guide to fix unwrapping errors in subsequent iterations.

I applied this technique to data from 7 Envisat tracks across the central section of North Anatolian Fault, a region of GNSS scarcity. Using information from both ascending and descending LOS velocities I showed that a ~ 130 km section of the NAF in this region is undergoing aseismic creep, consistent with previous studies ([Cetin et al., 2014](#)). However, I found a slight slower maximum creep rate of 14 ± 2 mm/yr compared to 20 ± 2 mm/yr estimated by [Cetin et al. \(2014\)](#). I showed that this discrepancy arises due to the bias from using data from a single satellite geometry; again highlighting the importance of using both ascending and descending information when investigated horizontal velocities.

By fitting a simple elastic dislocation model to three profiles along the fault I showed that there is an eastward decrease in fault slip rate, from 30 mm/yr (25-34, 95% CI) in the west to 21 mm/yr (14-27, 95% CI) in the eastern portion of the study area. This corresponds to a change of 11 ± 3 mm/yr in fault slip rate over a distance of ~ 200 km. There is no such pattern in the locking depth.

The observed change in slip rate could be a result of postseismic deformation from either the 1943 (Mw 7.7) and 1944 (Mw 7.5) earthquakes, or the 1999 Izmit (Mw 7.4) and Düzce (Mw 7.2) earthquakes. [Ergintav et al. \(2009\)](#) showed that the 1999 earthquakes resulted in postseismic deformation as far as Ankara, which is less than 100 km south of this region. Therefore, the rapid change in fault slip rate is probably due to postseismic deformation from the 1999 earthquakes, although we cannot rule out any long-term influence from the 1943 and 1944 earthquakes.

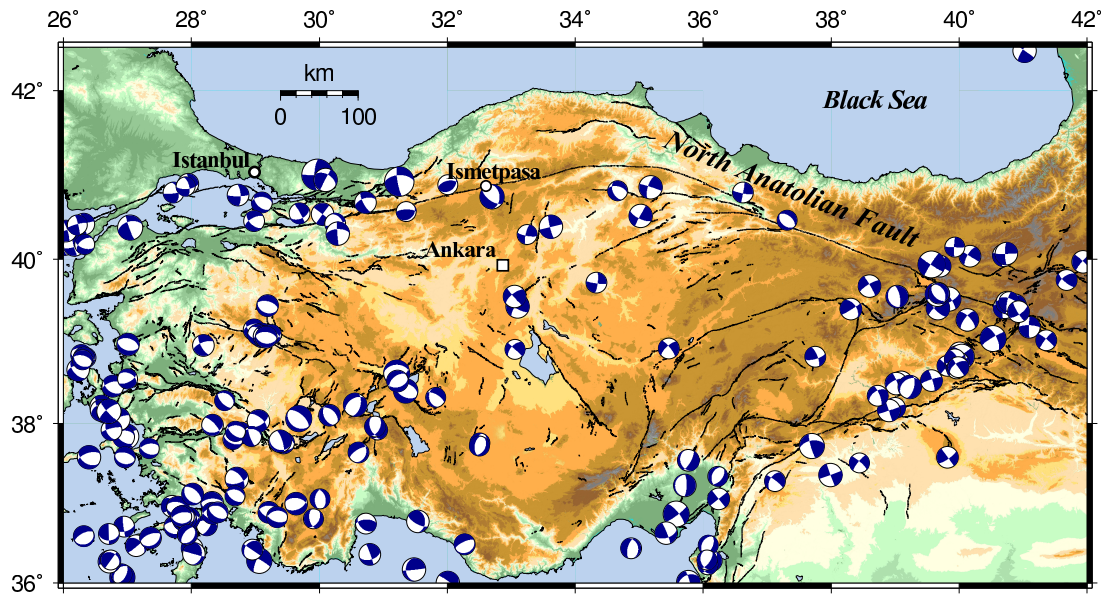


Figure 5.1: A map of seismic activity in Turkey since 1970. Earthquakes shown are all events greater than M_w 4.5. Data from the Global Centroid Moment Catalogue (GCMT).

5.1.3 Chapter 4

In Chapter 4 I combined InSAR data from 23 Envisat tracks (data from 2002 to 2010) with published GNSS velocities to produce a horizontal velocity field for the entire continental expression of the NAF (~ 1000 km). Profiles through fault parallel velocities revealed that interseismic strain is localised on the fault with 90% of the surface deformation occurring within a ~ 70 km region centered on the fault. This is consistent with slip on a single deep fault plane along the entire NAF (*Wright et al., 2001a, Cakir et al., 2014*), although a shear zone narrower than about 70 km cannot be discounted.

I showed that the locking depth does not vary significantly along the fault with an average value of 16 ± 4 km, and since each segment of the NAF is at a different stage of the earthquake cycle, the locking depth is invariant with respect to the time since the last earthquake. This observation is inconsistent with many earthquake cycle models (e.g. *Savage and Prescott, 1978, Thatcher, 1983, Savage, 2000*), which predict an increasingly wider zone of deformation around the fault with time. This translates to a deeper locking depth with time, which we do not see for the North Anatolian Fault. The implication of this is that strain accumulation reaches a steady-state fairly rapidly after an earthquake (< 7 years) after which strain is localised on a narrow shear zone centred on the fault that does not vary with time. A time-invariant strain rate is consistent with a strong lower crust in the region away from the fault with a viscosity $\geq 10^{20}$ Pas.

I also showed that there is an westward increasing fault slip rate from an average 22 ± 3 mm/yr in the east, to 28 ± 3 mm/yr on the western section of the NAF. These

observations are inconsistent with simple block-like motion of Anatolia away from the Arabia-Eurasia collision zone (*Reilinger et al., 1997, McClusky et al., 2000*), which predicts a constant slip rate for motion along a great circle about the Euler rotation pole. My observations are more consistent with *Aktuğ et al. (2013)*, who showed that there is significant internal east-west deformation within Anatolia. However, this study is the first to translate this into changes in slip rate on the NAF itself.

This has important implications for seismic hazard in central Turkey. Figure 5.1 is a map of the seismicity in Turkey since 1970. It shows that most earthquakes are clustered around the North and East Anatolian Fault and southwest Turkey, a region of active extension. However, there are a numerous faults within central Turkey, with a few that have produced earthquakes in the past few decades. An important future piece of work would be to investigate the strain accumulation on these individual faults. This will be very challenging as the strain rates on these faults are expected to be very small and thus, surface displacement rates small compared to the NAF.

5.2 Locking depth and slip rate variation with time

In this thesis I have measured interseismic strain (slip rate and locking depth) across the North Anatolian Fault. These measurements add to a growing catalogue of similar geodetic studies on other large strike-slip faults since the first interseismic study by (*Wright et al., 2001a*).

Viscoelastic models of earthquake cycle deformation on strike-slip faults predict interseismic shear strain at the Earth's surface close to the fault to decrease with time after an earthquake (*Savage and Prescott, 1978, Savage, 1990, 2000*). At the same time surface strain gradually broadens with time (*Thatcher, 1983*). In the case of the screw dislocation model (*Savage and Burford, 1973*), this will give an apparent increase in locking depth or a decrease in slip rate with time.

In Chapter 4 I showed that this does not appear to be the case for the North Anatolian Fault. In order to extend this test to a global dataset, I collected all published geodetic estimates of fault slip rate and locking depth along major strike-slip faults, and the time since the last large ($M_w > 6$) earthquake (Table E.1).

Figure 5.2 shows the variation in locking and depth and slip rate with time. Most estimates of the locking depth are between 8–21 km (grey region in Figure 5.2a), and there is no clear variation with time. Therefore, my conclusions from Chapter 4 appear to be consistent for a global dataset, implying that in general the lower crust in the regions away from the fault zone is strong.

It is also clear that there is no obvious temporal pattern in fault slip rate, with most measurements randomly scattered through time. This is consistent with the observations of *Meade et al. (2013)*, who showed that there is a good agreement between long-term geological slip rates and short term geodetic slip rates on 15 continental

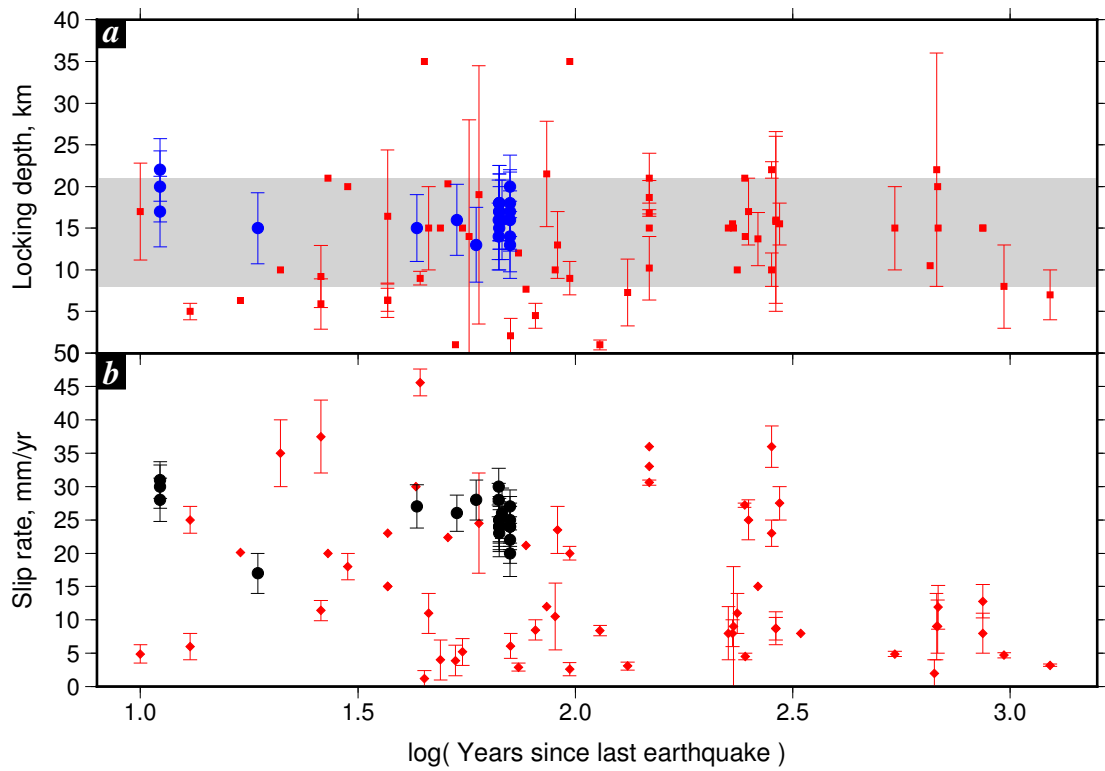


Figure 5.2: (a) The variation in locking depth and slip rate (b) with time. Blue and black circles are results from this study and red points are published estimates. Points with no error bars indicate estimates that were fixed in the original inversion. See Table E.1 for details of the data.

strike-slip faults, implying that fault slip rates do not appear to change much during the interseismic period.

5.3 Detecting fault creep

The last decade has seen a trend towards closer investigations of near fault deformation and has resulted in numerous publications of fault creep with a growing focus on its role in releasing interseismic strain during the earthquake cycle (e.g. [Schmidt et al., 2005](#), [Jolivet et al., 2012](#), [Cetin et al., 2014](#), [Hussain et al., 2016](#)). In this thesis I have shown that fault creep is an important deformation mechanism along the NAF, and we are able to detect small displacement rates using a long time series of InSAR measurements. I believe that careful investigations of other large faults, particularly those less well studied in Tibet, will reveal more faults exhibiting creeping behaviour. The ultimate aim is to produce a robust mechanism to detect either transient or long-term fault creep. There are four possible ways to do this:

1. Use high temporal resolution InSAR measurements
2. Correct for long wavelength signals, assuming fault creep produces a short wavelength deformation signal
3. Use a Network Inversion Filter to detect deviations from steady-state
4. Exploit measurements from other instruments

I elaborate on these suggestions below.

5.3.1 Use high temporal resolution InSAR measurements

In this study I have used data from the Envisat satellite mission, which gives a SAR measurement of the same section of ground every 70 days on average. I have shown that this is sufficient to detect long term aseismic creep on the NAF. However, I am not able to detect transient slip episodes with a duration less than the satellite repeat time.

Recently, [Rousset et al. \(2016\)](#) used data from the COSMO-SkyMed constellation, which produces a SAR image every 1-16 days, to detect a transient creep episode at the Ismetpasa section of the NAF between 2013 and 2014 (Figure 5.3). Using this temporally dense dataset they were able to identify a major burst of aseismic slip spanning 31 days with a maximum slip of 2 cm. Events such as these would be impossible to detect with Envisat data.

The new Sentinel-1 satellite constellation (discussed in Section 5.5), when fully operational, will provide a SAR image every 6-12 days for most of the tectonically active regions around the world. I believe that with careful timeseries analysis of the

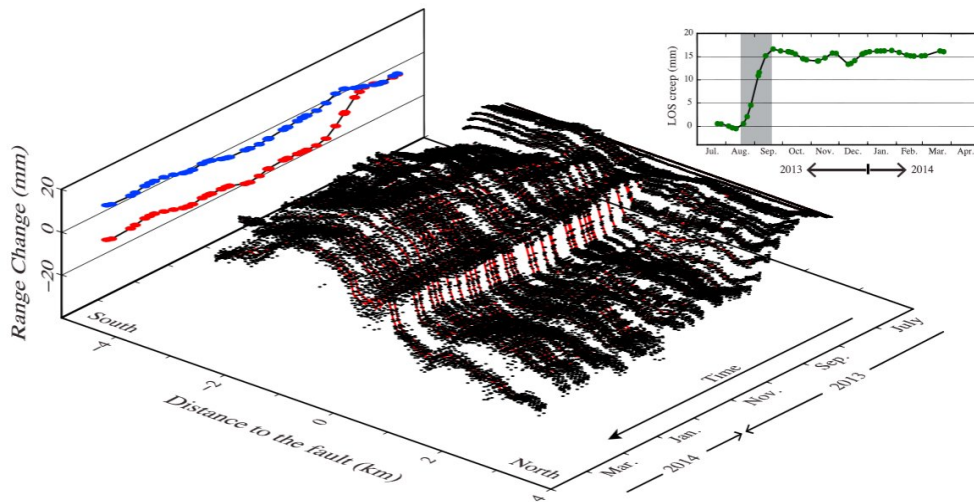


Figure 5.3: Transient slip on the Isetpasa section of the NAF measured with InSAR analysis of high temporal resolution COSMO-SkyMed data. Image from [Rousset et al. \(2016\)](#).

temporally dense data from Sentinel-1, it would be possible to detect transient creep events like the one observed at Isetpasa on most creeping faults around the world.

5.3.2 Correct for long wavelength signals

In Chapter 2 I showed that fault creep has a small wavelength deformation signal (<10 km) compared to the broad signal (10s km) characteristic of interseismic deformation (Figure 5.4). One way of detecting fault creep is to therefore correct high resolution horizontal velocities obtained from InSAR, for the long wavelength interseismic deformation.

In regions with good GNSS coverage, like Turkey, we can use the smoothed, interpolated GNSS velocities to obtain the long wavelength smooth velocity field. This has the added benefit of correcting for not only the long wavelength interseismic deformation but also any other non-tectonic deformation patterns such as “block” rotation, which is particularly strong in Turkey (see Chapter 3). Figure 5.5a shows the east-west component of the smoothed GNSS velocity field created using the VELMAP software ([Wang and Wright, 2012](#)), which inverts for the east and north component of the velocity field at the corners of an arbitrary triangular mesh covering the area of interest. This method assumes a constant strain rate within each triangle, see [Wang and Wright \(2012\)](#) and [Walters et al. \(2014\)](#) for more details of this technique.

Removing the smoothed GNSS velocities from the InSAR velocity field (Figure 5.5b) should theoretically remove all long wavelength variations leaving only small wavelength noise and local tectonic signals (Figure 5.5c). It is clear that atmospheric noise dominates the residual signal. However, it is still possible to see the sharp offsets in residual velocity across the fault at the Isetpasa and Izmit sections of the NAF.

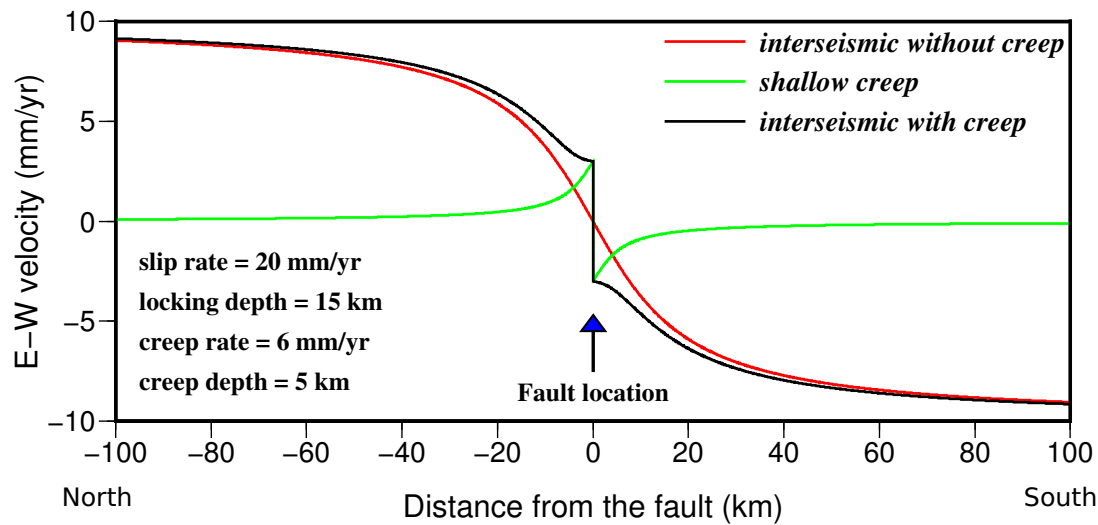


Figure 5.4: A forward calculation of shallow fault creep and interseismic displacement rates illustrating the different wavelengths of deformation from each process. Fault creep has a small wavelength deformation signal compared to the broad signal from interseismic deformation.

The removal of long wavelength signals obviously depends on the choice of smoothing strength when creating the GNSS velocity field. In this case I have used Laplacian smoothing with a smoothing factor (κ^2) equal to $10^{-1.8}$. This value represents a compromise between the solution roughness and the misfit with the observed GNSS.

A truly automatic system would need to be able to differentiate sharp changes in residual velocities that are due to atmospheric signals and those due to tectonic deformation. Currently, this is not yet possible, mainly because the atmospheric residuals are large. It is possible that advances in atmospheric correction techniques will help reduce this noise, thus increasing the signal-to-noise ratio of small wavelength tectonic deformation.

5.3.3 Network inversion filters

Another possible method for detecting fault creep is through time-dependent modelling of continuous geospatial datasets, otherwise known as a Network Inversion Filter (NIF). The Network Inversion Filter technique was first developed for GNSS timeseries measurements by [Segall and Matthews \(1997\)](#) who showed that the method can be used to detect temporal variations in fault slip. The underlying principle for a network inversion filter is to detect anomalous departures from steady-state deformation.

[Bekaert et al. \(2016\)](#) adapted the original NIF approach to also include InSAR time series information, and showed that the method can accurately detect transient slow-slip events on subduction zones. In this case the steady-state signal is due to interseismic loading, and any transient slip episodes due to slow-slip events result in a departure from this steady-state, which the NIF can detect automatically.

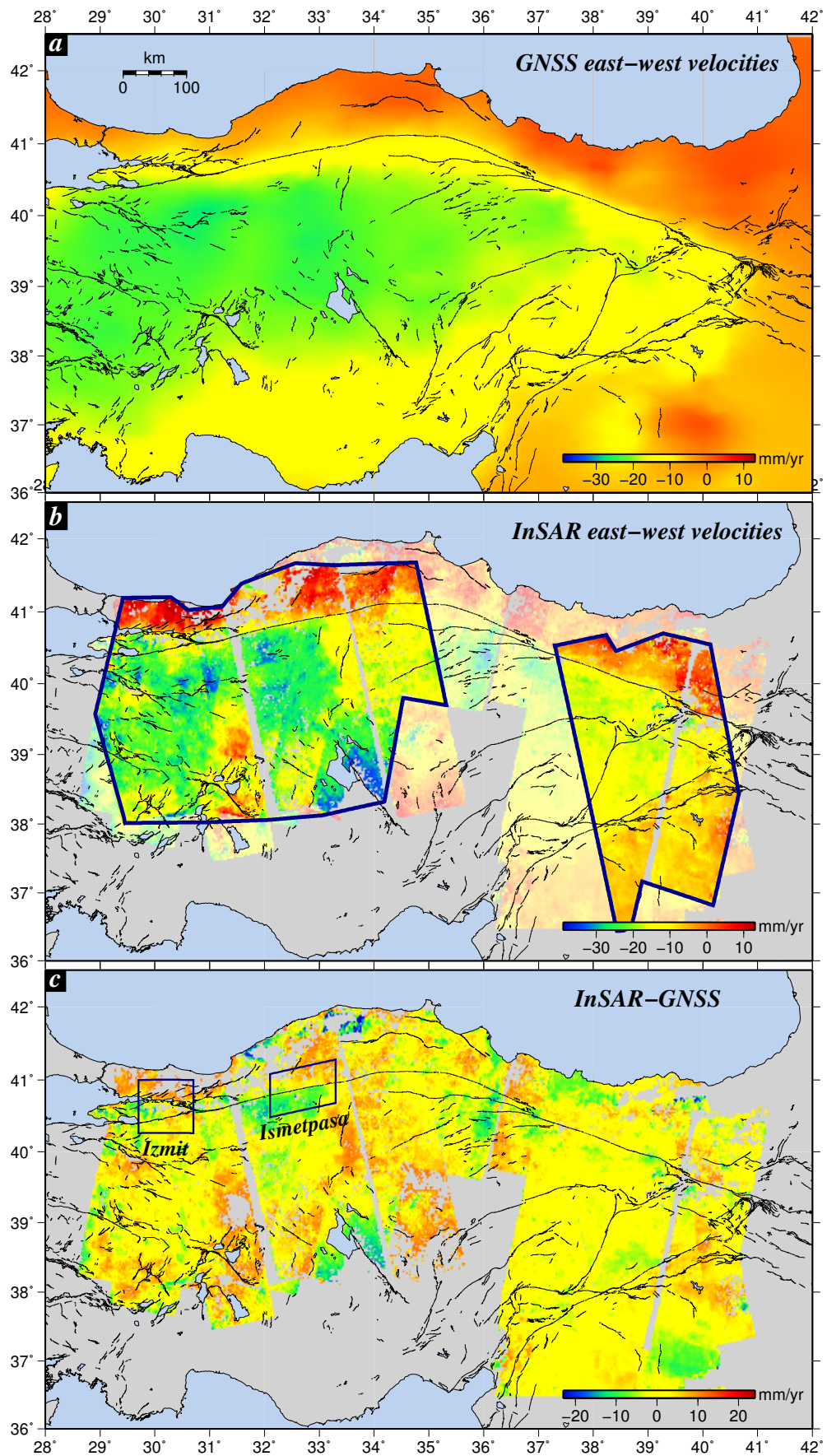


Figure 5.5: (a) The east-west component of the smoothed GNSS velocity field. (b) The east-west component of the InSAR velocity field created in this study (Chapter 4). The polygons indicate regions with both ascending and descending InSAR coverage. (c) The residual velocities after the smoothed GNSS velocity field is removed from the InSAR.

In the case of transient fault creep, the NIF seems like a logical application. In these cases the departure from steady-state due to transient creep episodes could be automatically detected using this approach. However, it would be difficult to investigate long-term fault creep using the traditional NIF, e.g. at the Parkfield segment of the SAF or the Ismetpasa segment of the NAF (e.g. *Jolivet et al., 2015*). This is because long-term fault creep is often at steady state with the interseismic loading (*Bürgmann et al., 2000*). Although it might be possible to use far-field GNSS measurements to constrain the interseismic deformation on the fault plane in the NIF and use near-field measurements to detect departures from this signal that would be due to fault creep.

Therefore, the NIF could be adapted to automatically detect creeping faults using geodetic data and would be worth investigating in the future.

5.3.4 Creepmeter measurements

Original creepmeters consisted of a coil of wire nailed to two posts across a fault. Slow movements along the fault would increase the length of the wire, which could be measured and translated to slip on the fault (e.g. *King et al., 1973*).

Today creepmeters are a little more sophisticated in the sense that the measurements are done electronically. But the principle of measuring the displacement of a wire (or a graphic rod) stretched across a fault remains the same. Creepmeters have been successfully used to show transient slip events and temporal changes in fault creep on the San Andreas Fault in California (e.g. *King et al., 1977, Roeloffs, 2001*).

Creepmeters have recently been installed across the Izmit and Ismetpasa sections of the NAF, in a collaboration between Turkish and US scientists. Preliminary results from a year's data have revealed interesting and varied temporal behaviour in aseismic slip. The Ismetpasa creepmeter shows periods of constantly increasing aseismic slip (i.e. constant creep rate) as well as creep events and periods of no aseismic slip (Figure 5.6).

The double creep events, seen as the two jumps in aseismic slip just before 1/5/15 each occurred over 1 day. It would be impossible to detect such small events with current InSAR measurements.

Installing and managing creepmeters can be a time consuming and expensive task. Nevertheless, creepmeter studies complement information from InSAR. Local studies with creepmeters (along with near-fault GNSS instruments) can be used to examine the detailed temporal evolution of aseismic slip at specific locations along a fault, while InSAR is able to map aseismic creep on a much larger spatial scale.

5.4 Evolution of scale

Figure 5.7 compares the study region of the first interseismic InSAR study by *Wright et al. (2001a)* with that of *Walters et al. (2014)* and this study. It is clear that in-

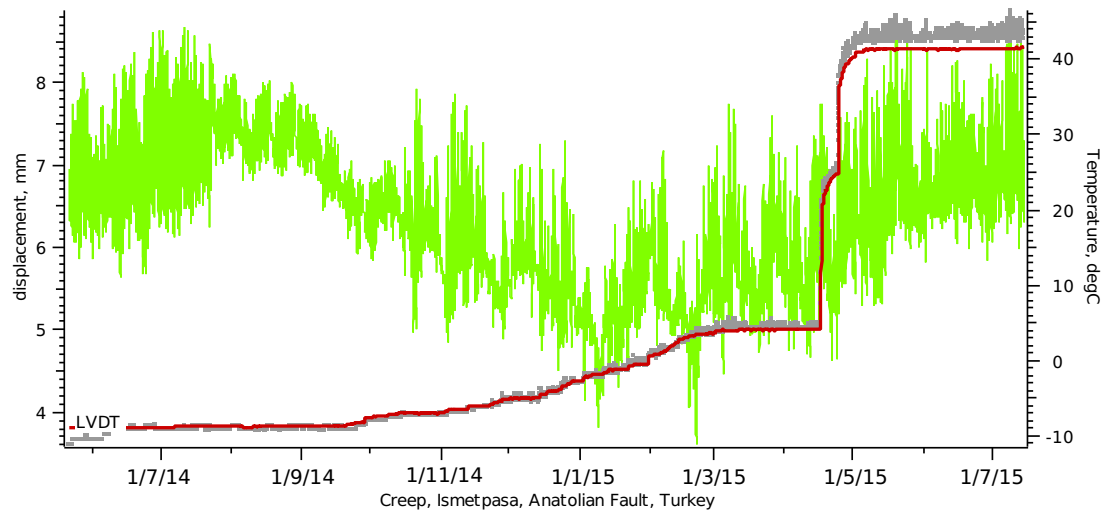


Figure 5.6: Preliminary creepmeter measurements at Ismetpasa between July 2014 and July 2015. The red line shows the displacements of the wire crossing the fault. The green line is the temperature of the instrument, which can also affect the length of the wire. Figure courtesy of Roger Bilham (unpublished).

terseismic deformation studies using InSAR (usually combined with GNSS) have been growing in scale over the last decade and a half. Original studies focused on a small fault or a small section of a large fault (~ 100 km long), while now we are able to do country scale InSAR analysis (~ 1000 km long), an order of magnitude larger than original studies. The next step is to produce InSAR velocity fields on continental scale, and ultimately map continental strain globally with InSAR.

5.5 Towards a global strain map

Earthquake hazard maps such as GSHAP, the Global Seismic Hazard Assessment Program, are commonly based only on seismic catalogues. These maps are used by international agencies, e.g. the World Bank and other UN agencies, to improve disaster risk and a resilience. The insurance industry uses these hazard maps in probabilistic forecasting models to calculate seismic risk and set insurance premiums. However, geodetic measurements are only now slowly starting to be exploited by the insurance industry in their hazard models (*Grossi, 2005*).

The Global Strain Rate Map (GSRM) is a project to ‘determine a globally self-consistent strain rate and velocity field model, consistent with geodetic and geologic field observations’ (*Kreemer et al., 2003, Kreemer et al., 2014*). The model uses GNSS velocity measurements to calculate strain rates across most of the tectonically active regions of the world.

Bird et al. (2015) and *Bird and Kreemer (2015)* showed that earthquake occurrence rate correlates with regions of high strain rates. Therefore, for accurate seismic hazard

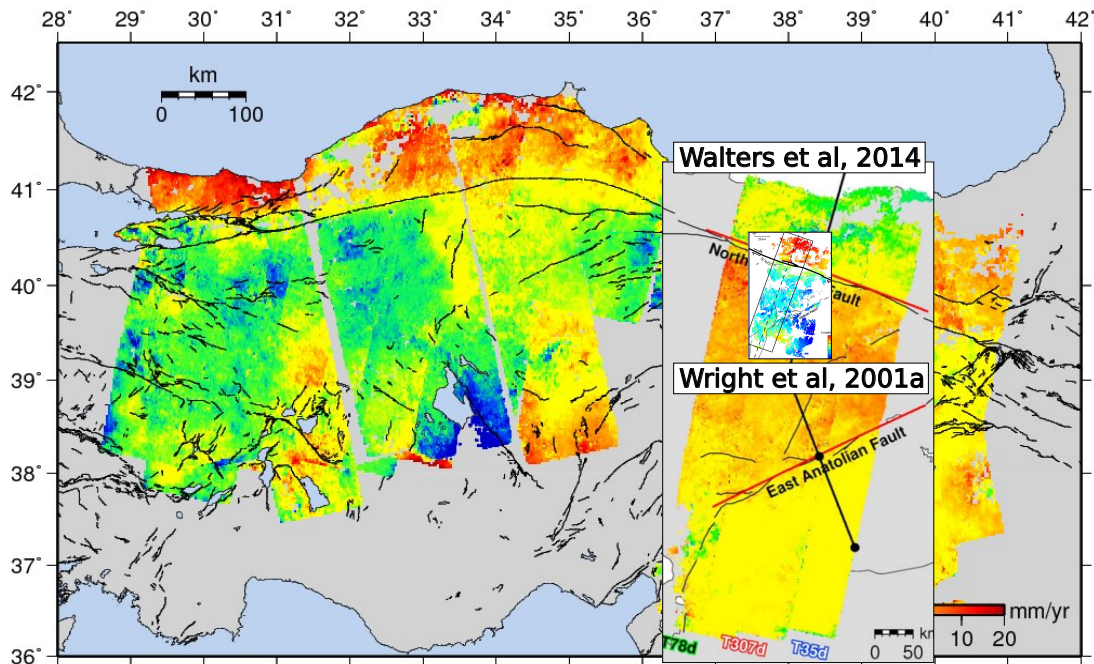


Figure 5.7: The evolution in scale for InSAR studies. The study regions of *Wright et al. (2001a)*, the first interseismic InSAR study, and *Walters et al. (2014)* are shown to scale.

assessment it is important to have accurate maps of strain rates across all major faults. However, the spatial resolution of GNSS measurements globally is extremely variable, from 5-10 km in California to 100s km in Tibet and central Asia. Although this is still useful for large-scale estimates of crustal deformation it is difficult to translate that to strain rates on individual faults. This is particularly important for detecting hidden faults that are currently not yet mapped, but are still accumulating strain to be released in a future earthquake. For example, the faults that caused the Mw 6.5 Bam (Iran) and Mw 7 Darfield (New Zealand) earthquakes could not have been identified before they failed using traditional geological techniques; both occurred on strike slip faults in areas of active sedimentation and did not create any long-term signatures in the landscape.

InSAR velocity maps are complementary to GNSS velocities, because they are at a much higher spatial resolution (~ 30 m for C-band InSAR), and they contain information about vertical motions, which are often not published for GNSS datasets. Therefore, combining global measurements of strain rates from InSAR and GNSS is a logical step forward to a more detailed understanding of seismic hazard globally.

In April 2014 the European Space Agency launched the Sentinel-1a satellite (Figure 5.8), the first of a series of dedicated C-band radar satellites (Sentinel-1b was successfully launched in April 2016). There are 4 key reasons why the Sentinel-1 mission will be a game changer for mapping surface deformation in the tectonically active regions of the world:



Figure 5.8: Artist's impression of the European Space Agency's Sentinel-1 C-band radar satellite. Figure courtesy of ESA.

1. The mission will be a 20 year operational program designed for InSAR, providing a long time series of measurements
2. There will be systematic acquisitions over all active deformation belts around the world
3. The satellites will have a 12 day revisit of most points around the globe, giving 30 images per satellite per year, and a 6 day revisit for many regions with two satellites
4. The satellites will travel in a narrow, well-defined orbital tube, which will reduce baseline related decorrelation errors

Since 1900, 90% of all earthquake-related deaths have occurred in regions that are straining at rates above 12 nanostrains per year. *Wright et al. (2010)* calculated that for a revisit time of 6 days and for a 20 year mission on descending and ascending tracks, Sentinel-1 will be able to measure the strain rate in 99.8% of these straining regions (assuming complete coherence). This effectively means that with a 20 year time series of Sentinel-1 measurements we would be able to accurately map seismic hazard in regions responsible for 90% of all earthquake deaths.

Figure 5.9 shows what is now possible with just 18 months of data from the Sentinel-1a satellite. The east-west velocity field is consistent with the velocities I determined using 8 years of Envisat data over the same region (see Chapter 4).

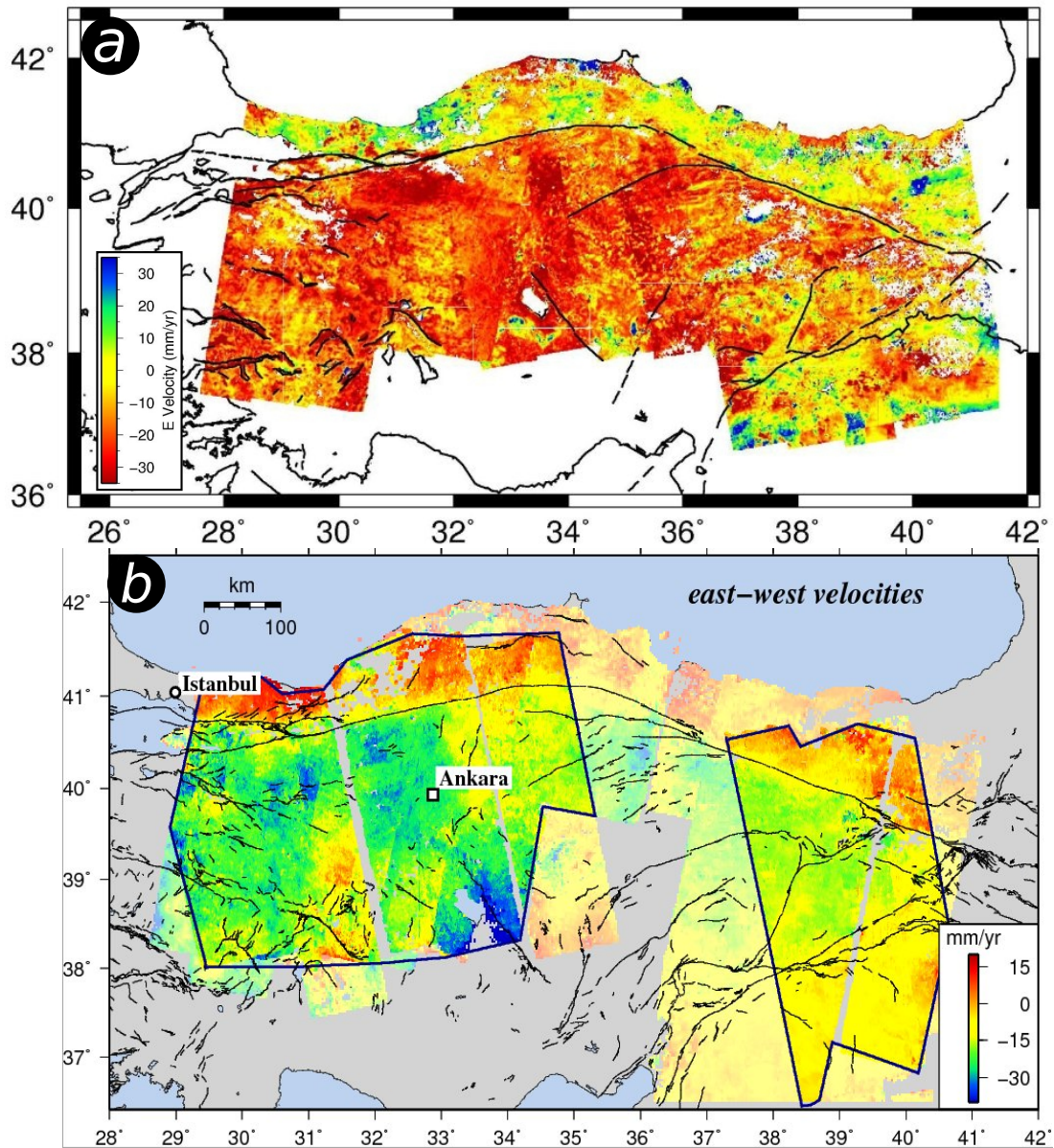


Figure 5.9: (a) The east-west component of the velocity field over Turkey created using 18 months of data from the Sentinel-1a satellite. *Courtesy of Richard Walters.* (b) The east-west velocities created using 8 years of Envisat data (*this study*).

5.6 Future work

5.6.1 Disaster response

It is clear that the Sentinel-1 mission will be extremely important for global InSAR processing. Now that both Sentinel-1a and 1b are in orbit and acquiring data, the maximum amount of time between two radar acquisitions over the same region is 6 days. Most satellite tracks overlap considerably, therefore in reality the time difference between measurements of the the same region is no more than a few days.

Rapid response after natural disasters, such as earthquakes and tropical storms, is important to support rescue, humanitarian, and reconstruction operations in crisis areas. Therefore, rapid damage mapping after a disaster is crucial, i.e., to detect the affected area, including grade and type of damage. *Plank (2014)* showed that analysis of Sentinel-1 data could produce these products in a timely manner and thus, aid in post-disaster recovery.

The key challenge for this is producing systems that are able to handle very large data volumes and process this rapidly and efficiently, produce useful derived products, such as damage maps and displacement maps, and deliver them in a timely manner to the organisations/people in the field after a disaster.

The “Looking inside the Continents from Space (LiCS)” project based at Leeds University and has the ambitious aim of creating a system that is able to process all Sentinel-1 SAR data continuously and produce useful derived products, such as time series measurements, velocity maps and interferograms.

5.6.2 Atmospheric corrections

For the Envisat satellite, the MERIS spectrometer provided the most accurate measurements of the troposphere and because the instrument was located on the same satellite and acquiring data at the same time as the radar data it required no complex interpolations, which often degrades the data quality. Unfortunately the Sentinel-1 satellites do not have onboard spectrometers similar to the MERIS instruments. And in any case, these only worked in cloud-free conditions, while atmospheric errors are often largest during cloudy, turbulent weather conditions, during which spectrometers do not work.

In this thesis I have corrected all interferograms using delay maps derived from the ERA-I weather model. Although these are not as good as the spectrometer estimates (*Bekaert et al., 2015c*) (for my Envisat tracks I achieved about a 6% reduction in noise by applying this correction), the corrections can be applied to all interferograms during all weather conditions.

Other correction methods include a linear correction based on topography (e.g. *Wicks et al., 2002, Elliott et al., 2008*), a power-law correction (*Bekaert et al., 2015a*),

using other spectrometers such as MODIS (e.g. *Li et al., 2009*), and deriving delay maps from other global and local weather models (e.g. *Jolivet et al., 2014*). Despite the many different correction techniques available, the largest source of noise in InSAR interferograms is still the contribution from the atmosphere. *Bekaert et al. (2015c)* showed that different correction techniques work well in different regions. Currently, there is no best “one size fits all” correction method that can be applied globally.

I believe that future work towards producing a robust method for reducing atmospheric noise in radar interferograms would consist of a weighted-correction of a combination, if not all, of these techniques. Each technique could be weighted according to specific weather conditions and/or geographical location. An important step towards this goal would be to accurately assess the effectiveness of each technique on a global dataset. Walters et al. (In prep) have taken the first step and are currently working to produce a global map comparing the effectiveness of the ERA-I weather model correction for InSAR.

5.6.3 Rheology of the crust from fault creep measurements

As discussed in Section 5.3, the new Sentinel-1 mission will enable closer and more detailed studies of surface deformation in the regions close to the fault trace. I believe that closer examinations of large strike-slip faults will reveal more faults with sections partially or fully creeping. Although most post-seismic afterslip decays within a few days to a few years (*Bürgmann et al., 2001, Ergintav et al., 2002*), some persist for decades, e.g. the Ismetpasa section of the North Anatolian Fault, which is thought to have started creeping after the 1944 earthquake (*Cakir et al., 2005*).

An interesting question is: Why do some strike-slip earthquakes result in long-term fault creep while in others the creep decays within a few months? This difference could be due to variations in crustal rheology resulting from spatially variable geology, the presence of fluids or changes in frictional properties on the fault. A detailed study of the displacement time series of afterslip that decays within months after an earthquake compared with that of long term creep as well as its spatial pattern would be a first step towards addressing this question. The displacement time series could be investigated using the Network Inversion Filter approach discussed in Section 5.3, while including measurements from creepmeters and GNSS. Sophisticated visco-elastic modelling and/or rate-and-state friction modelling could then be used to explore how frictional properties vary during these two different slip histories.

5.6.4 Detecting hidden faults

Earthquakes in the continental interiors are generally distributed over large zones hundreds to thousands of kilometres wide. These zones commonly contain many separate faults, each accumulating slip at only a few tenths to a few millimetres per year (*Eng-*

land and Jackson, 2011). It is therefore not surprising that previously unidentified faults rupture regularly, resulting in the loss of life and/or property. The 2003 Bam earthquake (Mw 6.5) in Iran and the Canterbury earthquake (Mw 7) in New Zealand are type examples of such earthquakes.

One of the exciting possibilities from global measurements of surface velocities is the ability to identify regions of localised strain accumulation that do not correlate with previously identified active faults. One of the key challenges with this is the need to differentiate displacements due to tectonic loading on an unknown fault with that due to other processes such as subsurface water level changes or anthropogenic activities.

However once robustly identified, the strain accumulation rate on these faults can be measured and catalogued, which will provide important information for more accurate seismic hazard analysis and forecasting models.

5.7 Concluding remarks

In this thesis I have shown that InSAR is a valuable tool for the large scale analysis of interseismic deformation along continental strike-slip faults. I have demonstrated the importance of using observations from both ascending and descending geometries along with GNSS measurements to create an accurate map of the surface velocity field across a region. Careful analysis of velocities close to the fault trace has enabled a detailed investigation of the creeping behaviour of the NAF near Izmit and Ismetpasa. These techniques are general and can be applied to all strike-slip faults globally. The archived ERS-1/2 and Envisat data remain an extremely valuable resource that can and should be used to extend InSAR time series measurements back to the early 1990s. Together with the new Sentinel-1 data sets, this provides an unprecedented opportunity to explore tectonic deformation over several decades. Atmospheric delays remain the major challenge to exploiting Sentinel-1 data for global strain mapping, the mitigation of these delays are an important goal for the InSAR community.

References

- Aktuğ, B., E. Parmaksız, M. Kurt, O. Lenk, A. Kılıçoğlu, M. A. Gürdal, and S. Özdemir (2013), Deformation of Central Anatolia: GPS implications, *Journal of Geodynamics*, *67*, 78–96. [5.1.3](#)
- Bekaert, D., R. Walters, T. Wright, A. Hooper, and D. Parker (2015c), Statistical comparison of InSAR tropospheric correction techniques, *Remote Sensing of Environment*, *170*, 40–47, doi:[10.1002/2014JB011557](#). [5.6.2](#)
- Bekaert, D., P. Segall, T. Wright, and A. Hooper (2016), A Network Inversion Filter combining GNSS and InSAR for tectonic slip modeling, *Journal of Geophysical Research: Solid Earth*. [5.3.3](#)
- Bekaert, D. P. S., A. Hooper, and T. J. Wright (2015a), A spatially variable power-law tropospheric correction technique for InSAR data, *Journal of Geophysical Research (Solid Earth)*, *120*, 1345–1356, doi:[10.1002/2014JB011558](#). [5.6.2](#)
- Bird, P., and C. Kreemer (2015), Revised tectonic forecast of global shallow seismicity based on version 2.1 of the Global Strain Rate Map, *Bulletin of the Seismological Society of America*, *105*(1), 152–166. [5.5](#)
- Bird, P., D. Jackson, Y. Kagan, C. Kreemer, and R. Stein (2015), GEAR1: A global earthquake activity rate model constructed from geodetic strain rates and smoothed seismicity, *Bulletin of the Seismological Society of America*, *105*(5), 2538–2554. [5.5](#)
- Bürgmann, R., D. Schmidt, R. M. Nadeau, M. d’Alessio, E. Fielding, D. Manaker, T. V. McEvilly, and M. H. Murray (2000), Earthquake potential along the Northern Hayward Fault, California, *Science*, *289*, 1178–1182, doi:[10.1126/science.289.5482.1178](#). [5.3.3](#)
- Bürgmann, R., M. Kogan, V. Levin, C. Scholz, R. King, and G. Steblov (2001), Rapid aseismic moment release following the 5 December, 1997 Kronotsky, Kamchatka, earthquake, *Geophys. Res. Lett.*, *28*(7), 1331–1334. [5.6.3](#)
- Cakir, Z., A. M. Akoglu, S. Belabbes, S. Ergintav, and M. Meghraoui (2005), Creeping along the ismetpasa section of the North Anatolian fault (Western Turkey): Rate and extent from InSAR, *Earth and Planetary Science Letters*, *238*(1), 225–234. [5.6.3](#)
- Cakir, Z., S. Ergintav, H. Ozener, U. Dogan, A. M. Akoglu, M. Meghraoui, and R. Reilinger (2012), Onset of aseismic creep on major strike-slip faults, *Geology*, *40*, 1115–1118, doi:[10.1130/G33522.1](#). [5.1.1](#)
- Cakir, Z., S. Ergintav, A. M. Akoğlu, R. Çakmak, O. Tatar, and M. Meghraoui (2014), InSAR velocity field across the North Anatolian Fault (eastern Turkey): Implications for the loading and release of interseismic strain accumulation, *Journal of Geophysical Research: Solid Earth*, *119*(10), 7934–7943. [5.1.3](#)
- Cetin, E., Z. Cakir, M. Meghraoui, S. Ergintav, and A. M. Akoglu (2014), Extent and distribution of aseismic slip on the Isetpasa segment of the North Anatolian Fault (Turkey) from persistent scatterer InSAR, *Geochemistry, Geophysics, Geosystems*, *15*, 2883–2894, doi:[10.1002/2014GC005307](#). [5.1.2](#), [5.3](#)

- Elliott, J., J. Biggs, B. Parsons, and T. Wright (2008), InSAR slip rate determination on the Altyn Tagh Fault, northern Tibet, in the presence of topographically correlated atmospheric delays, *Geophysical Research Letters*, *35*(12). [5.6.2](#)
- England, P., and J. Jackson (2011), Uncharted seismic risk, *Nature Geoscience*, *4*(6), 348–349. [5.6.4](#)
- Ergintav, S., R. Bürgmann, S. McClusky, R. Cakmak, R. Reilinger, O. Lenk, A. Barka, and H. Özener (2002), Postseismic deformation near the Izmit earthquake (17 August 1999, M 7.5) rupture zone, *Bulletin of the Seismological Society of America*, *92*(1), 194–207. [5.6.3](#)
- Ergintav, S., S. McClusky, E. Hearn, R. Reilinger, R. Cakmak, T. Herring, H. Ozener, O. Lenk, and E. Tari (2009), Seven years of postseismic deformation following the 1999, M = 7.4 and M = 7.2, Izmit-Düzce, Turkey earthquake sequence, *Journal of Geophysical Research (Solid Earth)*, *114*, B07403, doi:[10.1029/2008JB006021](#). [5.1.2](#)
- Grossi, P. (2005), *Catastrophe modeling: A new approach to managing risk*, vol. 25, Springer Science & Business Media. [5.5](#)
- Hussain, E., T. J. Wright, R. J. Walters, D. Bekaert, A. Hooper, and G. A. Houseman (2016), Geodetic observations of postseismic creep in the decade after the 1999 izmit earthquake, turkey: Implications for a shallow slip deficit, *Journal of Geophysical Research: Solid Earth*, *121*(4), 2980–3001. [5.3](#)
- Jolivet, R., C. Lasserre, M.-P. Doin, S. Guillaso, G. Peltzer, R. Dailu, J. Sun, Z.-K. Shen, and X. Xu (2012), Shallow creep on the Haiyuan fault (Gansu, China) revealed by SAR interferometry, *Journal of Geophysical Research: Solid Earth*, *117*(B6). [5.3](#)
- Jolivet, R., P. S. Agram, N. Y. Lin, M. Simons, M.-P. Doin, G. Peltzer, and Z. Li (2014), Improving InSAR geodesy using global atmospheric models, *Journal of Geophysical Research: Solid Earth*, *119*(3), 2324–2341. [5.6.2](#)
- Jolivet, R., M. Simons, P. Agram, Z. Duputel, and Z.-K. Shen (2015), Aseismic slip and seismogenic coupling along the central San Andreas Fault, *Geophysical Research Letters*, *42*(2), 297–306. [5.3.3](#)
- King, C.-Y., R. Nason, and D. Tocher (1973), Kinematics of fault creep, *Philosophical Transactions of the Royal Society of London A: Mathematical, Physical and Engineering Sciences*, *274*(1239), 355–360. [5.3.4](#)
- King, C.-Y., R. D. Nason, and R. O. Burford (1977), Coseismic steps recorded on creep meters along the San Andreas fault, *Journal of Geophysical Research*, *82*(11), 1655–1662. [5.3.4](#)
- Kreemer, C., W. E. Holt, and A. J. Haines (2003), An integrated global model of present-day plate motions and plate boundary deformation, *Geophysical Journal International*, *154*, 8–34, doi:[10.1046/j.1365-246X.2003.01917.x](#). [5.5](#)
- Kreemer, C., G. Blewitt, and E. C. Klein (2014), A geodetic plate motion and global strain rate model, *Geochemistry, Geophysics, Geosystems*, *15*(10), 3849–3889. [5.5](#)
- Li, Z., E. Fielding, P. Cross, and R. Preusker (2009), Advanced InSAR atmospheric correction: MERIS/MODIS combination and stacked water vapour models, *International Journal of Remote Sensing*, *30*(13), 3343–3363. [5.6.2](#)
- McClusky, S., S. Balassanian, A. Barka, C. Demir, M. Hamburger, H. Kahle, K. Kasters, G. Kekelidse, R. King, V. Kotzev, et al. (2000), Gps constraints on crustal movements and deformations for plate dynamics, *J Geophys Res*, *105*, 5695–5720. [5.1.3](#)

- Meade, B. J., Y. Klinger, and E. A. Hetland (2013), Inference of multiple earthquake-cycle relaxation timescales from irregular geodetic sampling of interseismic deformation, *Bulletin of the Seismological Society of America*, *103*(5), 2824–2835. [5.2](#)
- Plank, S. (2014), Rapid damage assessment by means of multi-temporal SARA comprehensive review and outlook to Sentinel-1, *Remote Sensing*, *6*(6), 4870–4906. [5.6.1](#)
- Reilinger, R., S. McClusky, M. Oral, R. King, M. Toksoz, A. Barka, I. Kinik, O. Lenk, and I. Sanli (1997), Global Positioning System measurements of present-day crustal movements in the Arabia-Africa-Eurasia plate collision zone, *Journal of Geophysical Research: Solid Earth*, *102*(B5), 9983–9999. [5.1.3](#)
- Roeloffs, E. A. (2001), Creep rate changes at Parkfield, California 1966–1999: seasonal, precipitation induced, and tectonic, *Journal of Geophysical Research: Solid Earth*, *106*(B8), 16,525–16,547. [5.3.4](#)
- Rousset, B., R. Jolivet, M. Simons, C. Lassarre, B. Riel, P. Milillo, Z. Cakir, and F. Renard (2016), An aseismic slip transient on the North Anatolian Fault, *Geophysical Research Letters*, p. 4, doi:[10.1002/2016GL068250](https://doi.org/10.1002/2016GL068250). [5.3.1](#), [5.3](#)
- Savage, J. (1990), Equivalent strike-slip earthquake cycles in half-space and lithosphere-asthenosphere earth models, *Journal of Geophysical Research: Solid Earth*, *95*(B4), 4873–4879. [5.2](#)
- Savage, J. (2000), Viscoelastic-coupling model for the earthquake cycle, *Journal of Geophysical Research*, *105*. [5.1.3](#), [5.2](#)
- Savage, J., and W. Prescott (1978), Asthenosphere readjustment and the earthquake cycle, *Journal of Geophysical Research: Solid Earth*, *83*(B7), 3369–3376. [5.1.3](#), [5.2](#)
- Savage, J. C., and R. O. Burford (1973), Geodetic determination of relative plate motion in central California, *Journal of Geophysical Research*, *78*, 832–845, doi:[10.1029/JB078i005p00832](https://doi.org/10.1029/JB078i005p00832). [5.2](#)
- Schmidt, D. A., R. Bürgmann, R. M. Nadeau, and M. D’Alessio (2005), Distribution of aseismic slip rate on the Hayward fault inferred from seismic and geodetic data, *Journal of Geophysical Research (Solid Earth)*, *110*, B08406, doi:[10.1029/2004JB003397](https://doi.org/10.1029/2004JB003397). [5.3](#)
- Segall, P., and M. Matthews (1997), Time dependent inversion of geodetic data, *JOURNAL OF GEOPHYSICAL RESEARCH-ALL SERIES-*, *102*, 22–391. [5.3.3](#)
- Thatcher, W. (1983), Nonlinear strain buildup and the earthquake cycle, *Journal of Geophysical Research*, *88*, 5893–5902. [5.1.3](#), [5.2](#)
- Walters, R., B. Parsons, and T. Wright (2014), Constraining crustal velocity fields with InSAR for Eastern Turkey: Limits to the block-like behavior of Eastern Anatolia, *Journal of Geophysical Research: Solid Earth*, *119*(6), 5215–5234. [5.3.2](#), [5.4](#), [5.7](#)
- Wang, H., and T. Wright (2012), Satellite geodetic imaging reveals internal deformation of western Tibet, *Geophysical Research Letters*, *39*(7). [5.3.2](#)
- Wicks, C. W., D. Dzurisin, S. Ingebritsen, W. Thatcher, Z. Lu, and J. Iverson (2002), Magmatic activity beneath the quiescent three sisters volcanic center, central oregon cascade range, usa, *Geophysical Research Letters*, *29*(7). [5.6.2](#)
- Wright, T., B. Parsons, and E. Fielding (2001a), Measurement of interseismic strain accumulation across the North Anatolian Fault by satellite radar interferometry, *Geophysical Research Letters*, *28*(10), 2117–2120. [5.1.3](#), [5.2](#), [5.4](#), [5.7](#)
- Wright, T., M. Garthwaite, H. Jung, and A. Shepherd (2010), How accurately can current, planned and proposed InSAR missions measure slow, long-wavelength tectonic strain?, in *AGU Fall Meeting Abstracts*, vol. 1, p. 06. [5.5](#)

Appendix A

Appendix for the Introduction chapter

Table A.1: Compilation of published slip rate estimates for the North Anatolian Fault

Data/Method used	Slip rate (mm/yr)	Lon. extent along NAF (°E)	Reference	Fault segment
GPS + Euler rot	24 ± 1	26-41	<i>Aktug et al. (2009)</i>	Gulf of Saros
GPS + strain model	25	26.45	<i>Ayhan et al. (2002)</i>	Ganos Fault
GPS + strain model	21	27.02	<i>Ayhan et al. (2002)</i>	Marmara Sea
GPS + strain model	26	27.96	<i>Ayhan et al. (2002)</i>	Gulf of Izmit
GPS + strain model	13	29.32	<i>Ayhan et al. (2002)</i>	near Izmit
GPS + strain model	11	29.77	<i>Ayhan et al. (2002)</i>	Sapanca Lake
GPS + strain model	17	30.3	<i>Ayhan et al. (2002)</i>	Duzce Fault
GPS + strain model	20	31.21	<i>Ayhan et al. (2002)</i>	Bolu-Gerede area
GPS + strain model	17	32	<i>Ayhan et al. (2002)</i>	Marmara region
Seismology	20 ± 2.5	26-31	<i>Ambraseys (2002)</i>	Marmara basin
Seismology	19 ± 2	27.4-30	<i>Ambraseys (2002)</i>	Marmara region
Seismology	20 ± 4	26-31	<i>Ambraseys (2006)</i>	northern branch, W. NAF
Geology	14	26.1-26.5	<i>Armijo et al. (1999)</i>	Marmara region
Geology	17	26-31.5	<i>Armijo et al. (1999)</i>	Marmara region
Geology	38	32.86-37.03	<i>Barka and Hancock (1984)</i>	C. NAF
Geology	5	31.61	<i>Barka (1992)</i>	
Geology	10	39.55	<i>Barka (1992)</i>	
Trench	12-16	32.32	<i>Barka (1992)</i>	
Geology	2-4	26-29	<i>Barka and Reilinger (1997)</i>	Main Marmara Fault
GPS + Euler rot	26 ± 3	26.43-41.08	<i>Barka and Reilinger (1997)</i>	
InSAR	25 ± 1.5	32-34.3	<i>Cetin et al. (2014)</i>	

Trench	6	30.61	<i>Ikeda et al. (1991), Barka (1992)</i>	
GPS	24 ± 4	29–30.5	<i>Ergintav et al. (2009)</i>	W. NAF
GPS	17 ± 5	26.2–27.5	<i>Ergintav et al. (2009)</i>	W. NAF
GPS	25 ± 2	29.5–30.83	<i>Ergintav et al. (2014)</i>	Izmit
GPS	11 ± 2	28.68–29.36	<i>Ergintav et al. (2014)</i>	Princes Island Fault
GPS	~2	27.8–28.83	<i>Ergintav et al. (2014)</i>	Central Marmara Fault
GPS	20 ± 1	26–27.7	<i>Ergintav et al. (2014)</i>	Ganos Fault
GPS	5 ± 2	28.61–29.30	<i>Ergintav et al. (2014)</i>	Southern branch, W. NAF
Seismology	24	26–31	<i>Eyidoğan (1988)</i>	Marmara province
mech model + GPS	24	32.54–41.09	<i>Flerit et al. (2004)</i>	
mech model + GPS	22	32.54–33.99	<i>Flerit et al. (2004)</i>	
Geomechanical model	15.8	29.5	<i>Hergert et al. (2011b)</i>	northern branch, W. NAF
Geomechanical model	17.8	27.25–27.5	<i>Hergert et al. (2011b)</i>	Ganos fault
Geomechanical model	12.8	28.8–29.2	<i>Hergert et al. (2011b)</i>	Prince's Island fault
Geomechanical model	3.2	29.5	<i>Hergert et al. (2011b)</i>	southern branch, W. NAF
Geomechanical model	16	27.5–28.8	<i>Hergert et al. (2011b)</i>	Main Marmara Fault
GPS	24	26–31	<i>Hubert-Ferrari et al. (2000)</i>	northern branch, W. NAF
GPS	6	26–31	<i>Hubert-Ferrari et al. (2000)</i>	southern branch, W. NAF
Offset features	18.5 ± 3.5	33.65–33.87	<i>Hubert-Ferrari et al. (2002)</i>	
Offset features	18 ± 5	33.96	<i>Hubert-Ferrari et al. (2002)</i>	
Seismology	31	28.76–32.32	<i>Jackson and McKenzie (1984)</i>	
Seismology	31	36.25–39.55	<i>Jackson and McKenzie (1984)</i>	
InSAR + friction model	21–25	31.5–34.5	<i>Kaneko et al. (2013)</i>	
Seismology	16	30–36	<i>Kıratzi (1993)</i>	C. NAF
Seismology	27	36–41.5	<i>Kıratzi (1993)</i>	E. NAF

Seismology	16.5	36.4–41.6	<i>Kiratzi and Papazachos (1995)</i>	E. NAF
Seismology	12.1	27–29.1	<i>Kiratzi and Papazachos (1995)</i>	Marmara region
Trench	17	40.82	<i>Kondo et al. (2010)</i>	
Offset features	20.5 ± 5.5	33.85	<i>Kozaci et al. (2007)</i>	C. NAF
Offset features	18.6 + 3.4/ – 3.3	35.17	<i>Kozaci et al. (2009)</i>	
Paleo + geomor	6.4 + 2/ – 1.3	27.09–27.81	<i>Kürçer et al. (2008)</i>	Yenice-Gonen segment
GPS + SLR + Euler rot	25–30	27–40	<i>Le Pichon et al. (1995)</i>	
GPS + offsets	23	27.5–30	<i>Le Pichon et al. (2003)</i>	Main Marmara Fault
GPS + Euler rot	24 ± 1	26–41	<i>McClusky et al. (2000)</i>	
GPS + blocks	24.3 ± 1.6	26–31	<i>Meade et al. (2002)</i>	northern branch, W. NAF
GPS + blocks	6.6 ± 3	26–31	<i>Meade et al. (2002)</i>	southern branch, W. NAF
Trench	17 ± 5	27.32	<i>Meghraoui et al. (2012)</i>	Ganos segment
GPS+InSAR+	20–27	26.82–27.34	<i>Motagh et al. (2007)</i>	Ganos Fault
GPS + SLR + Euler rot	22.9	31.27–34.81	<i>Noomen et al. (1996)</i>	
GPS - directly	25 ± 9	28.87–35.44	<i>Oral et al. (1993)</i>	
Seismology	20	28–30	<i>Papazachos and Kiratzi (1996)</i>	
Seismology	6	26.3–28	<i>Papazachos and Kiratzi (1996)</i>	
Seismology	13	39.5–40	<i>Pinar et al. (1994)</i>	
Seismology	3.5	30.75	<i>Pinar et al. (1996)</i>	
Trench	10 ± 1.5	29.41–29.42	<i>Polonia et al. (2004)</i>	
Offset features	15 ± 3.2	31.12–31.20	<i>Pucci et al. (2008)</i>	Duzce fault
GPS - Euler rot	30 ± 2	26.43–41.08	<i>Reilinger et al. (1997)</i>	
GPS - blocks	24 ± 1	28.8–30.9	<i>Reilinger et al. (2006)</i>	
Trench	15.9 + 10/ – 4.5	26.88	<i>Rockwell et al. (2009)</i>	
GPS - directly	24	26–31	<i>Straub and Kahle (1994)</i>	

GPS - directly	18 – 16 ± 4	26–31	<i>Straub and Kahle (1995)</i>	
GPS - directly	22 ± 3	26–31	<i>Straub et al. (1997)</i>	
GPS	24 ± 2.9	36.5–37.5	<i>Tatar et al. (2012)</i>	
GPS	16.3 ± 2.3	37.5–38.5	<i>Tatar et al. (2012)</i>	
GPS	18.5 ± 2.2	38.5–39.7	<i>Tatar et al. (2012)</i>	
InSAR	20–26	37.75–39.65	<i>Walters et al. (2011)</i>	E. NAF
InSAR	20 ± 3	38.25–38.25	<i>Walters et al. (2014)</i>	E. NAF
Seismology	15 ± 2	35.96–38.27	<i>Westaway (1994)</i>	
InSAR	17–32	38.2–39.55	<i>Wright et al. (2001a)</i>	E. NAF

Table A.2: Compilation of published locking depth estimates for the North Anatolian Fault

Data/Method used	Locking depth (km)	Lon. extent along NAF (°E)	Reference	Fault segment
InSAR	14	31.95–32.79	Cakir et al. (2005)	Central NAF
GPS	3 ± 1.5	29–30.5	Ergintav et al. (2009)	Marmara
GPS	14 ± 7	26.2–27.5	Ergintav et al. (2009)	Marmara
GPS	5 ± 1	29.5–30.83	Ergintav et al. (2014)	Izmit
GPS	9 ± 2	26–27.7	Ergintav et al. (2014)	Ganos
GPS	10	28.68–29.36	Ergintav et al. (2014)	Princes Island fault
GPS + mech model	12	30.89–39.74	Flerit et al. (2004)	Fixed
GPS	15	26–31	Hubert-Ferrari et al. (2000)	Western NAF
GPS + blocks	17	26–31	Meade et al. (2002)	Regional locking depth
GPS + blocks	6.5 ± 1.1	27.3–29.3	Meade et al. (2002)	Marmara local locking depth
GPS+InSAR	8–17	26.82–27.34	Motagh et al. (2007)	Ganos Falt
GPS	21	28.8–30.9	Reiinger et al. (2006)	Izmit
GPS	12.8 ± 3.9	36.5–37.5	Tatar et al. (2012)	
GPS	8.1 ± 3.3	37.5–38.5	Tatar et al. (2012)	
GPS	9.4 ± 3.5	38.5–39.7	Tatar et al. (2012)	
InSAR	13.5–25	37.75–39.65	Walters et al. (2011)	Eastern NAF
InSAR	18 ± 9	38.25–38.25	Walters et al. (2014)	Eastern NAF
InSAR	5–33	38.2–39.55	Wright et al. (2001a)	Eastern NAF
InSAR + GPS	18 ± 6	38.2–39.55	Wright et al. (2001a)	Eastern NAF

References

- Aktug, B., J. Nocquet, A. Cingöz, B. Parsons, Y. Erkan, P. England, O. Lenk, M. Gürdal, A. Kilicoglu, H. Akdeniz, et al. (2009), Deformation of western Turkey from a combination of permanent and campaign GPS data: Limits to block-like behavior, *Journal of Geophysical Research: Solid Earth (1978–2012)*, 114(B10). [A.1](#)
- Ambraseys, N. (2002), The seismic activity of the Marmara Sea region over the last 2000 years, *Bulletin of the Seismological Society of America*, 92(1), 1–18. [A.1](#)
- Ambraseys, N. (2006), Comparison of frequency of occurrence of earthquakes with slip rates from long-term seismicity data: the cases of Gulf of Corinth, Sea of Marmara and Dead Sea Fault Zone, *Geophysical Journal International*, 165(2), 516–526. [A.1](#)
- Armijo, R., B. Meyer, A. Hubert, and A. Barka (1999), Westward propagation of the North Anatolian fault into the northern Aegean: Timing and kinematics, *Geology*, 27(3), 267–270. [A.1](#)
- Ayhan, M. E., C. Demir, O. Lenk, A. Kiliçoglu, Y. Altiner, A. A. Barka, S. Ergintav, and H. Özener (2002), Interseismic strain accumulation in the Marmara Sea region, *Bulletin of the Seismological Society of America*, 92(1), 216–229. [A.1](#)
- Barka, A. (1992), The north Anatolian fault zone, in *Annales tectonicae*, vol. 6, pp. 164–195. [A.1](#)
- Barka, A., and R. Reilinger (1997), Active tectonics of the Eastern Mediterranean region: deduced from GPS, neotectonic and seismicity data, *Annals of Geophysics*, 40(3). [A.1](#)
- Barka, A. A., and P. L. Hancock (1984), Neotectonic deformation patterns in the convex-northwards arc of the North Anatolian fault zone, *Geological Society, London, Special Publications*, 17(1), 763–774. [A.1](#)
- Cakir, Z., A. M. Akoglu, S. Belabbes, S. Ergintav, and M. Meghraoui (2005), Creeping along the ismetpasa section of the North Anatolian fault (Western Turkey): Rate and extent from InSAR, *Earth and Planetary Science Letters*, 238(1), 225–234. [A.2](#)
- Cetin, E., Z. Cakir, M. Meghraoui, S. Ergintav, and A. M. Akoglu (2014), Extent and distribution of aseismic slip on the Isetmpasa segment of the North Anatolian Fault (Turkey) from persistent scatterer InSAR, *Geochemistry, Geophysics, Geosystems*, 15, 2883–2894, doi:10.1002/2014GC005307. [A.1](#)
- Ergintav, S., S. McClusky, E. Hearn, R. Reilinger, R. Çakmak, T. Herring, H. Ozener, O. Lenk, and E. Tari (2009), Seven years of postseismic deformation following the 1999, M = 7.4 and M = 7.2, Izmit-Düzce, Turkey earthquake sequence, *Journal of Geophysical Research (Solid Earth)*, 114, B07403, doi:10.1029/2008JB006021. [A.1](#), [A.2](#)
- Ergintav, S., R. Reilinger, R. Çakmak, M. Floyd, Z. Cakir, U. Doğan, R. King, S. McClusky, and H. Özener (2014), Istanbul’s earthquake hot spots: Geodetic constraints on strain accumulation along faults in the Marmara seismic gap, *Geophysical Research Letters*, 41(16), 5783–5788. [A.1](#), [A.2](#)

- Eyidogan, H. (1988), Rates of crustal deformation in western Turkey as deduced from major earthquakes, *Tectonophysics*, *148*(1), 83–92. [A.1](#)
- Flerit, F., R. Armijo, G. King, and B. Meyer (2004), The mechanical interaction between the propagating North Anatolian Fault and the back-arc extension in the Aegean, *Earth and Planetary Science Letters*, *224*(3), 347–362. [A.1](#), [A.2](#)
- Hergert, T., O. Heidbach, A. Bécel, and M. Laigle (2011b), Geomechanical model of the Marmara Sea regionI. 3-D contemporary kinematics, *Geophysical Journal International*, *185*(3), 1073–1089. [A.1](#)
- Hubert-Ferrari, A., A. Barka, E. Jacques, S. S. Nalbant, B. Meyer, R. Armijo, P. Tapponnier, and G. C. P. King (2000), Seismic hazard in the Marmara Sea region following the 17 August 1999 Izmit earthquake, *Nature*, *404*, 269–273. [A.1](#), [A.2](#)
- Hubert-Ferrari, A., R. Armijo, G. King, B. Meyer, and A. Barka (2002), Morphology, displacement, and slip rates along the North Anatolian Fault, Turkey, *Journal of Geophysical Research: Solid Earth (1978–2012)*, *107*(B10), ETG–9. [A.1](#)
- Ikeda, Y., Y. Suzuki, E. Herece, F. Şarolu, A. M. Isikara, and Y. Honkura (1991), Geological evidence for the last two faulting events on the North Anatolian fault zone in the Mudurnu Valley, western Turkey, *Tectonophysics*, *193*(4), 335–345. [A.1](#)
- Jackson, J., and D. McKenzie (1984), Active tectonics of the Alpine/Himalayan belt between western Turkey and Pakistan, *Geophysical Journal*, *77*, 185–264, doi:[10.1111/j.1365-246X.1984.tb01931.x](https://doi.org/10.1111/j.1365-246X.1984.tb01931.x). [A.1](#)
- Kaneko, Y., Y. Fialko, D. T. Sandwell, X. Tong, and M. Furuya (2013), Interseismic deformation and creep along the central section of the North Anatolian Fault (Turkey): InSAR observations and implications for rate-and-state friction properties, *Journal of Geophysical Research (Solid Earth)*, *118*, 316–331, doi:[10.1029/2012JB009661](https://doi.org/10.1029/2012JB009661). [A.1](#)
- Kiratzi, A. A. (1993), A study on the active crustal deformation of the North and East Anatolian Fault Zones, *Tectonophysics*, *225*(3), 191–203. [A.1](#)
- Kiratzi, A. A., and C. B. Papazachos (1995), Active crustal deformation from the Azores triple junction to the Middle East, *Tectonophysics*, *243*(1), 1–24. [A.1](#)
- Kondo, H., V. Özaksoy, and C. Yildirim (2010), Slip history of the 1944 Bolu-Gerede earthquake rupture along the North Anatolian fault system: Implications for recurrence behavior of multisegment earthquakes, *Journal of Geophysical Research: Solid Earth*, *115*(B4). [A.1](#)
- Kozacı, Ö., J. Dolan, R. Finkel, and R. Hartleb (2007), Late Holocene slip rate for the North Anatolian Fault, Turkey, from cosmogenic ³⁶Cl geochronology: Implications for the constancy of fault loading and strain release rates, *Geology*, *35*(10), 867–870. [A.1](#)
- Kozacı, Ö., J. F. Dolan, and R. C. Finkel (2009), A late Holocene slip rate for the central North Anatolian fault, at Tahtaköprü, Turkey, from cosmogenic ¹⁰Be geochronology: Implications for fault loading and strain release rates, *Journal of Geophysical Research: Solid Earth (1978–2012)*, *114*(B1). [A.1](#)
- Kürçer, A., A. Chatzipetros, S. Z. Tutkun, S. Pavlides, Ö. Ateş, and S. Valkaniotis (2008), The Yenice–Gönen active fault (NW Turkey): Active tectonics and palaeoseismology, *Tectonophysics*, *453*(1), 263–275. [A.1](#)
- Le Pichon, X., N. Chamot-Rooke, S. Lallemand, R. Noomen, and G. Veis (1995), Geodetic determination of the kinematics of central Greece with respect to Europe: Implications for eastern Mediterranean tectonics, *Journal of Geophysical Research: Solid Earth*, *100*(B7), 12,675–12,690. [A.1](#)

- Le Pichon, X., N. Chamot-Rooke, C. Rangin, and A. Sengör (2003), The North Anatolian fault in the Sea of Marmara, *Journal of Geophysical Research: Solid Earth* (1978–2012), 108(B4). [A.1](#)
- McClusky, S., S. Balassanian, A. Barka, C. Demir, M. Hamburger, H. Kahle, K. Kastors, G. Kekelidse, R. King, V. Kotzev, et al. (2000), Gps constraints on crustal movements and deformations for plate dynamics, *J Geophys Res*, 105, 5695–5720. [A.1](#)
- Meade, B. J., B. H. Hager, S. C. McClusky, R. E. Reilinger, S. Ergintav, O. Lenk, A. Barka, and H. Özener (2002), Estimates of seismic potential in the Marmara Sea region from block models of secular deformation constrained by global positioning system measurements, *The Bulletin of the Seismological Society of America*, 92, 208–215, doi:10.1785/0120000837. [A.1](#), [A.2](#)
- Meghraoui, M., M. E. Aksoy, H. S. Akyüz, M. Ferry, A. Dikbaş, and E. Altunel (2012), Paleoseismology of the North Anatolian fault at Güzelköy (Ganos segment, Turkey): Size and recurrence time of earthquake ruptures west of the Sea of Marmara, *Geochemistry, Geophysics, Geosystems*, 13(4). [A.1](#)
- Motagh, M., J. Hoffmann, B. Kampes, M. Baes, and J. Zschau (2007), Strain accumulation across the Gazikoy–Saros segment of the North Anatolian Fault inferred from Persistent Scatterer Interferometry and GPS measurements, *Earth and Planetary Science Letters*, 255(3), 432–444. [A.1](#), [A.2](#)
- Noomen, R., T. Springer, B. Ambrosius, K. Herzberger, D. Kuijper, G.-J. Mets, B. Overgaauw, and K. Wakker (1996), Crustal deformations in the Mediterranean area computed from SLR and GPS observations, *Journal of geodynamics*, 21(1), 73–96. [A.1](#)
- Oral, M. B., R. E. Reilinger, M. N. Toksöz, A. A. Barka, and I. Kinik (1993), Preliminary results of 1988 and 1990 GPS measurements in western Turkey and their tectonic implications, *Contributions of Space Geodesy to Geodynamics: Crustal Dynamics*, pp. 407–416. [A.1](#)
- Papazachos, C. B., and A. A. Kiratzi (1996), A detailed study of the active crustal deformation in the Aegean and surrounding area, *Tectonophysics*, 253(1), 129–153. [A.1](#)
- Pinar, A., Y. Honkura, and M. Kikuchi (1994), Rupture process of the 1992 Erzincan earthquake and its implication for seismotectonics in eastern Turkey, *Geophysical research letters*, 21(18), 1971–1974. [A.1](#)
- Pinar, A., Y. Honkura, and M. Kikuchi (1996), A rupture model for the 1967 Mudurnu Valley, Turkey earthquake and its implication for seismotectonics in the western part of the North Anatolian Fault Zone, *Geophysical research letters*, 23(1), 29–32. [A.1](#)
- Polonia, A., L. Gasperini, A. Amorosi, E. Bonatti, G. Bortoluzzi, N. Cagatay, L. Capotondi, M.-H. Cormier, N. Gorur, C. McHugh, et al. (2004), Holocene slip rate of the North Anatolian Fault beneath the Sea of Marmara, *Earth and Planetary Science Letters*, 227(3), 411–426. [A.1](#)
- Pucci, S., P. De Martini, and D. Pantosti (2008), Preliminary slip rate estimates for the Düzce segment of the North Anatolian Fault Zone from offset geomorphic markers, *Geomorphology*, 97(3), 538–554. [A.1](#)
- Reilinger, R., S. McClusky, M. Oral, R. King, M. Toksoz, A. Barka, I. Kinik, O. Lenk, and I. Sanli (1997), Global Positioning System measurements of present-day crustal movements in the Arabia-Africa-Eurasia plate collision zone, *Journal of Geophysical Research: Solid Earth*, 102(B5), 9983–9999. [A.1](#)

- Reilinger, R., S. McClusky, P. Vernant, S. Lawrence, S. Ergintav, R. Cakmak, H. Ozener, F. Kadirov, I. Guliev, R. Stepanyan, M. Nadariya, G. Hahubia, S. Mahmoud, K. Sakr, A. ArRajehi, D. Paradissis, A. Al-Aydrus, M. Prilepin, T. Guseva, E. Evren, A. Dmitrotsa, S. V. Filikov, F. Gomez, R. Al-Ghazzi, and G. Karam (2006), GPS constraints on continental deformation in the Africa-Arabia-Eurasia continental collision zone and implications for the dynamics of plate interactions, *Journal of Geophysical Research: Solid Earth*, 111(B5), doi:10.1029/2005JB004051. [A.1](#), [A.2](#)
- Rockwell, T., D. Ragona, G. Seitz, R. Langridge, M. E. Aksoy, G. Ucar, M. Ferry, A. J. Meltzner, Y. Klinger, M. Meghraoui, et al. (2009), Palaeoseismology of the North Anatolian fault near the Marmara Sea: Implications for fault segmentation and seismic hazard, *Geological Society, London, Special Publications*, 316(1), 31–54. [A.1](#)
- Straub, C., and H.-G. Kahle (1994), Global Positioning System (GPS) estimates of crustal deformation in the Marmara Sea region, Northwestern Anatolia, *Earth and planetary science letters*, 121(3-4), 495–502. [A.1](#)
- Straub, C., and H.-G. Kahle (1995), Active crustal deformation in the Marmara Sea region, NW Anatolia, inferred from GPS measurements, *Geophysical research letters*, 22(18), 2533–2536. [A.1](#)
- Straub, C., H.-G. Kahle, and C. Schindler (1997), GPS and geologic estimates of the tectonic activity in the Marmara Sea region, NW Anatolia, *Journal of Geophysical Research: Solid Earth (1978–2012)*, 102(B12), 27,587–27,601. [A.1](#)
- Tatar, O., F. Poyraz, H. Gürsoy, Z. Cakir, S. Ergintav, Z. Akpınar, F. Koçbulut, F. Sezen, T. Türk, K. Ö. Hastaoğlu, et al. (2012), Crustal deformation and kinematics of the eastern part of the North Anatolian Fault Zone (Turkey) from GPS measurements, *Tectonophysics*, 518, 55–62. [A.1](#), [A.2](#)
- Walters, R., R. Holley, B. Parsons, and T. Wright (2011), Interseismic strain accumulation across the North Anatolian Fault from Envisat InSAR measurements, *Geophysical research letters*, 38(5). [A.1](#), [A.2](#)
- Walters, R., B. Parsons, and T. Wright (2014), Constraining crustal velocity fields with InSAR for Eastern Turkey: Limits to the block-like behavior of Eastern Anatolia, *Journal of Geophysical Research: Solid Earth*, 119(6), 5215–5234. [A.1](#), [A.2](#)
- Westaway, R. (1994), Evidence for dynamic coupling of surface processes with isostatic compensation in the lower crust during active extension of western Turkey, *Journal of Geophysical Research: Solid Earth*, 99(B10), 20,203–20,223. [A.1](#)
- Wright, T., B. Parsons, and E. Fielding (2001a), Measurement of interseismic strain accumulation across the North Anatolian Fault by satellite radar interferometry, *Geophysical Research Letters*, 28(10), 2117–2120. [A.1](#), [A.2](#)

Appendix B

Supplementary material for Chapter [2](#)

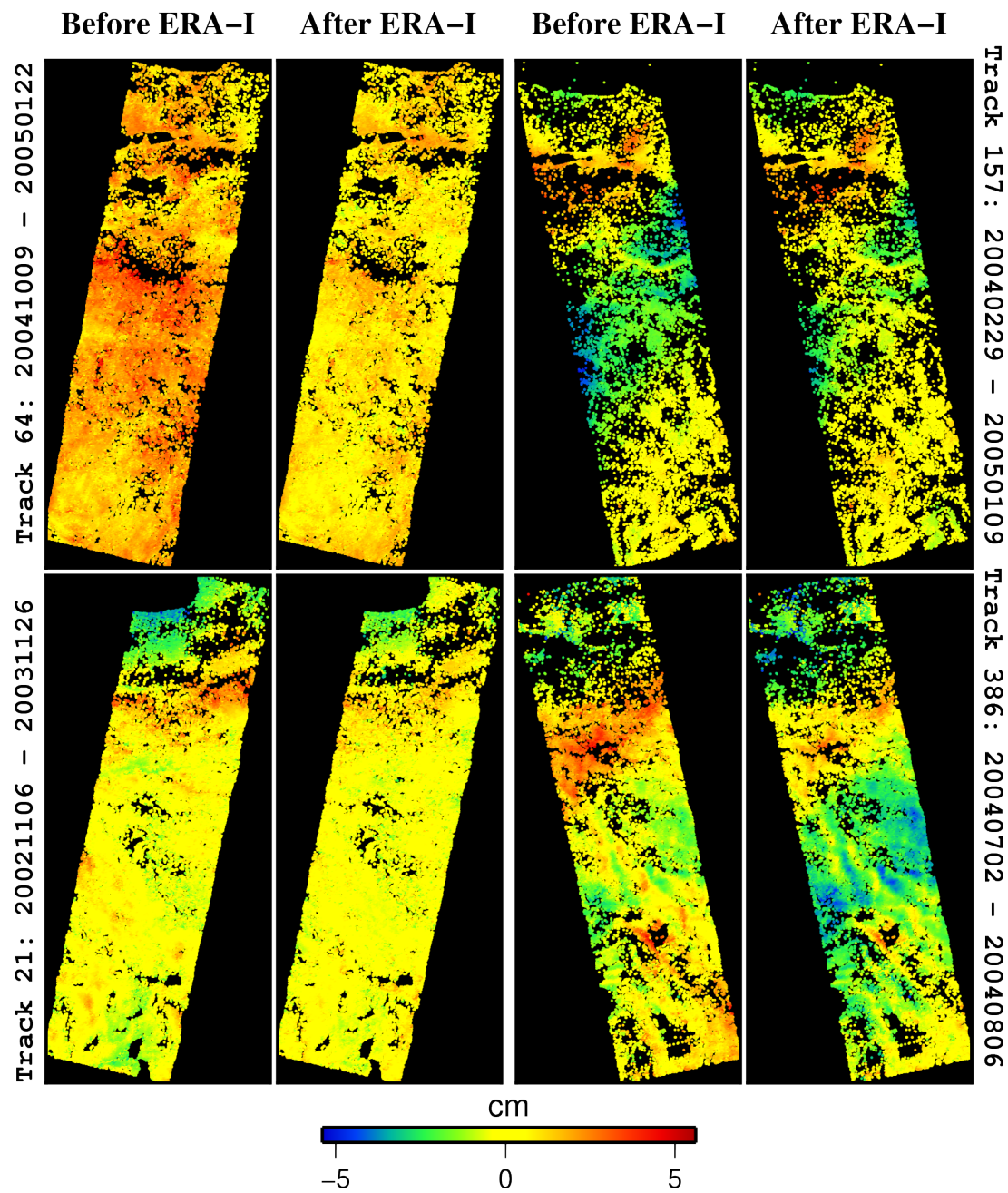


Figure B.1: Four examples of interferograms before any atmospheric corrections and after the ERA-I correction has been applied. The source of each interferogram (track and date span) is shown in vertical on the side. From a visual inspection it is clear that the application of a ERA-I weather model correction for the troposphere results in a decrease in variance across each interferogram. See Figure S2 for a details of the improvements for every interferogram.

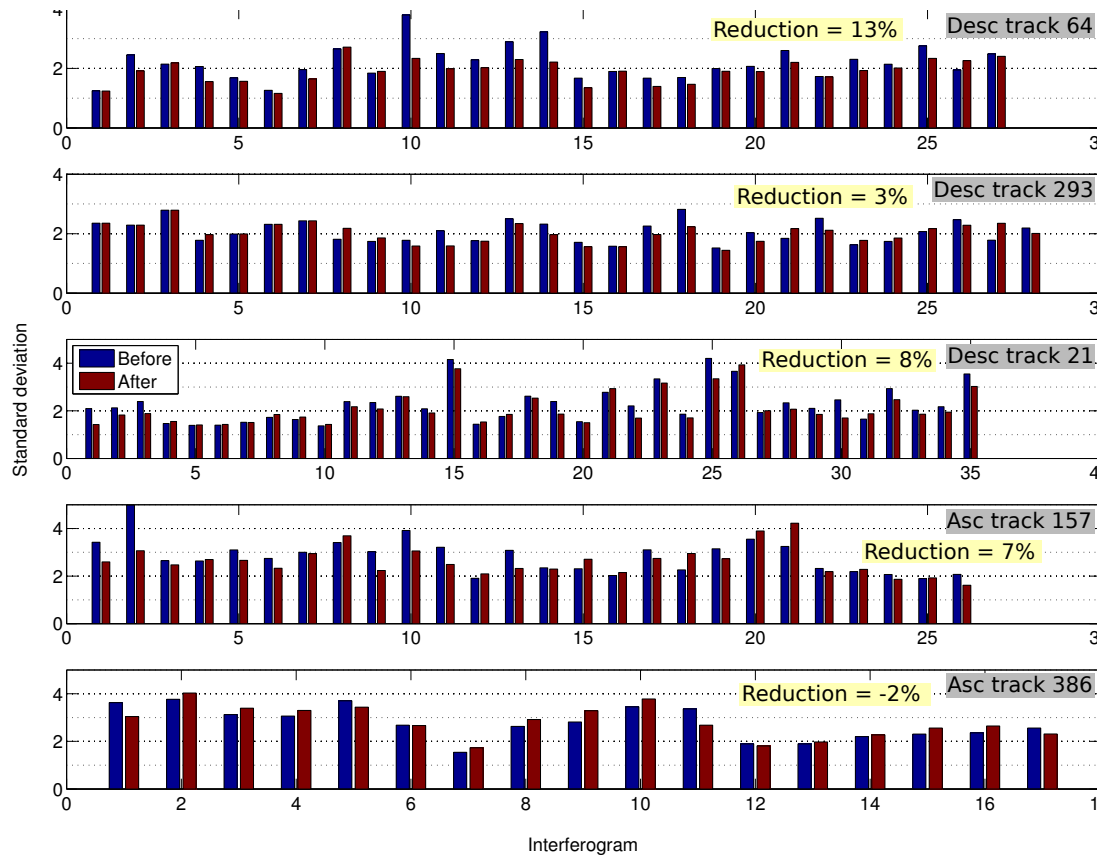


Figure B.2: The reduction in variance after applying the ERA-I weather model correction for atmospheric delays (see Section 2.1 in the paper). For each track used in this study, the red bars indicate the standard deviation of the unwrapped small baseline InSAR displacements (with an orbital ramp removed) for each interferogram without any atmospheric corrections. The blue bars indicate standard deviations after the ERA-I weather model correction. In all cases, other than for track 386, there is a reduction in average variance for each track.

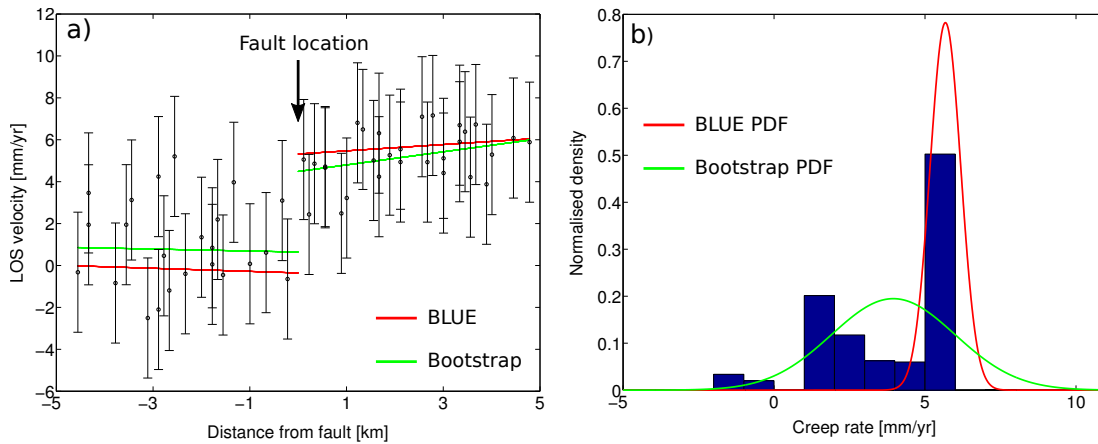


Figure B.3: (a) An example of a short 10 km profile (5 km either side of the fault) of line-of-sight velocities from track 293 projecting velocities within 2.5 km perpendicular distance from the profile. The red line is the Best Linear Unbiased Estimator (BLUE) and the green the mean result from bootstrap resampling. (b) Normalised Probability Density Functions (PDFs) comparing both BLUE and bootstrap techniques. It is clear that in this case, the BLUE method underestimates the uncertainty.

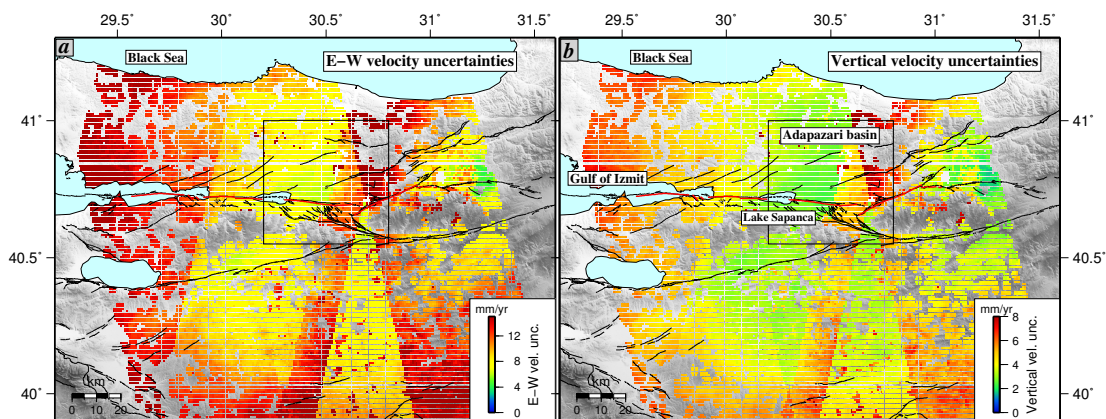


Figure B.4: Uncertainty maps for the E-W velocity (a) and the vertical velocity (b) components decomposed from the InSAR LOS velocities in a Eurasia-fixed reference frame.

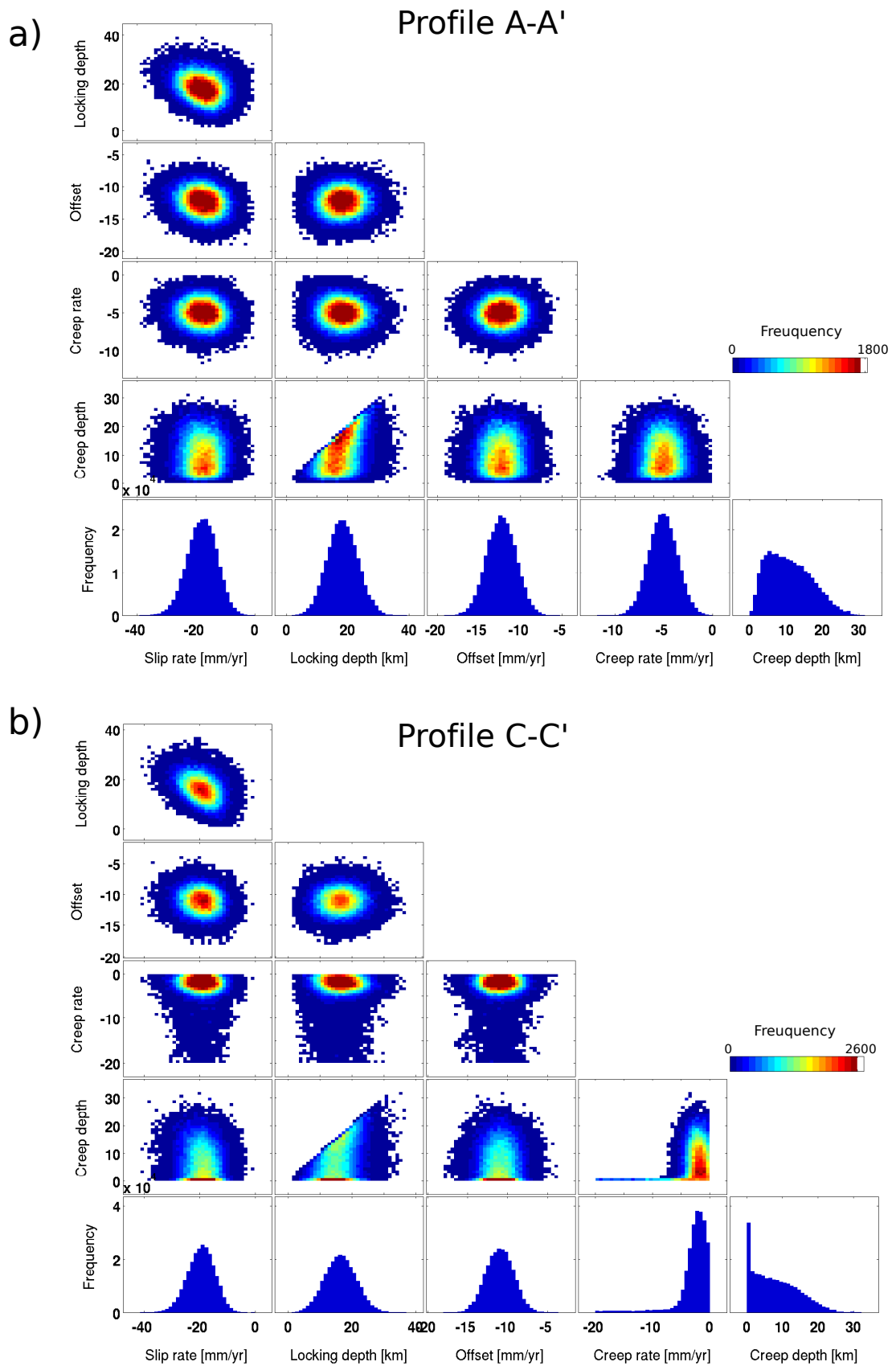


Figure B.5: The sampled marginal probability distributions of the model parameters for profiles A-A' and C-C'. The maximum a posteriori probability solution is highlighted by the red marker and line.

Appendix C

Supplementary material for Chapter 3

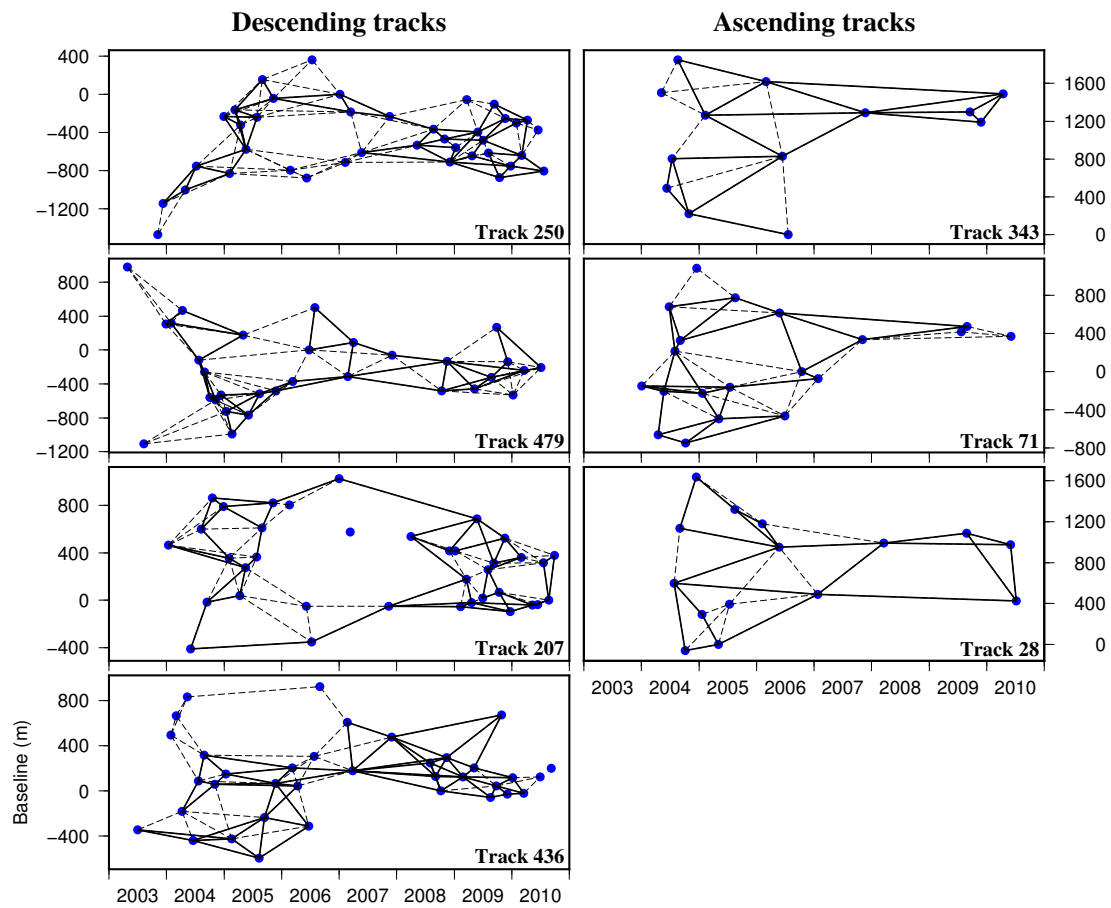


Figure C.1: Baseline vs time plots for each of the tracks used in our study. The combination of dashed and solid lines represent all the interferograms created. The solid black lines are the interferograms used to estimate the average line-of-sight velocity over the time period.

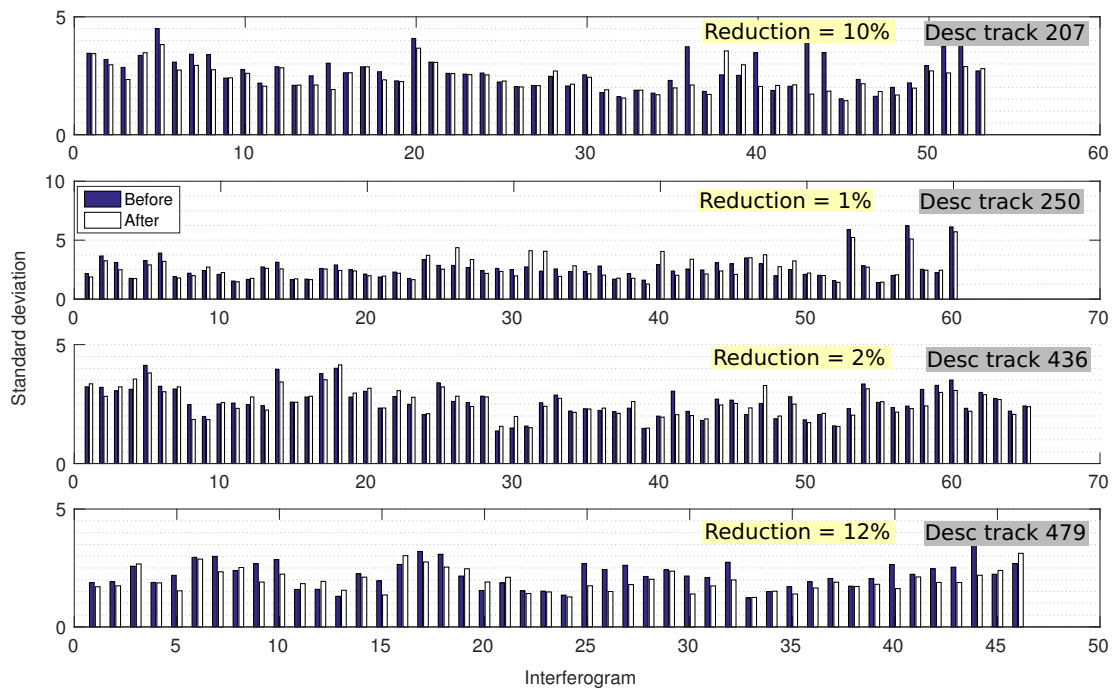


Figure C.2: The reduction in standard deviation for our descending tracks after applying the ERA-I weather model correction for atmospheric delays (see Section 2 in the paper). For each track used in this study, the red bars indicate the standard deviation (calculated after the removal of a long-wavelength ramp) of the unwrapped small baseline InSAR displacements for each interferogram without any atmospheric correction applied. The blue bars indicate standard deviations after the ERA-I weather model correction. In all cases, there is a reduction in average standard deviation for each track.

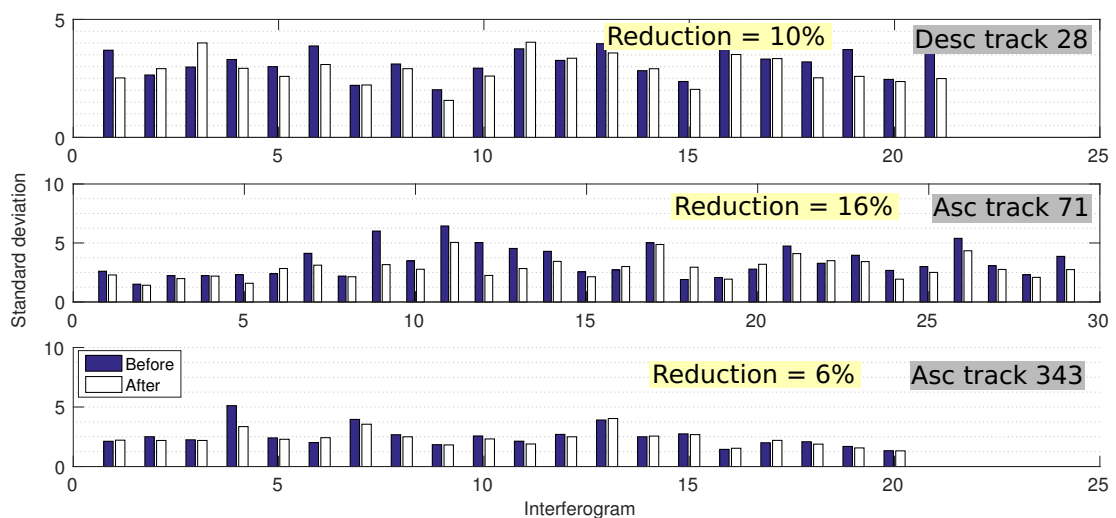


Figure C.3: The reduction in standard deviation for our ascending tracks after applying the ERA-I weather model correction.

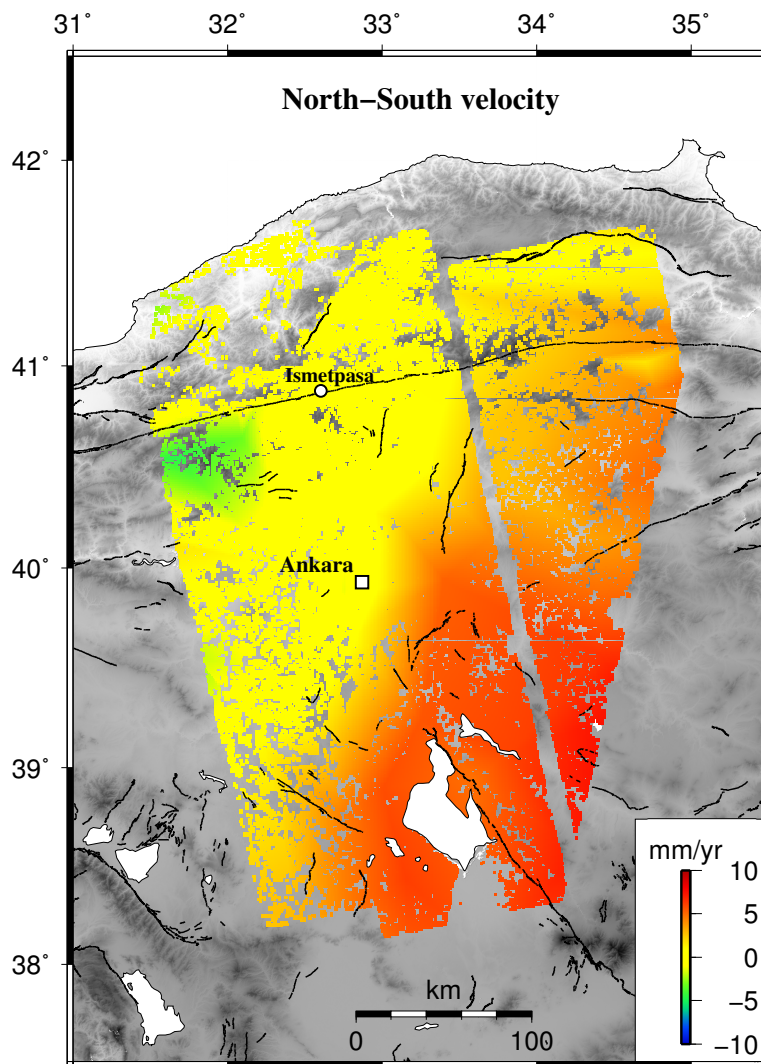


Figure C.4: The north component of the GNSS velocities interpolated to every InSAR grid location.

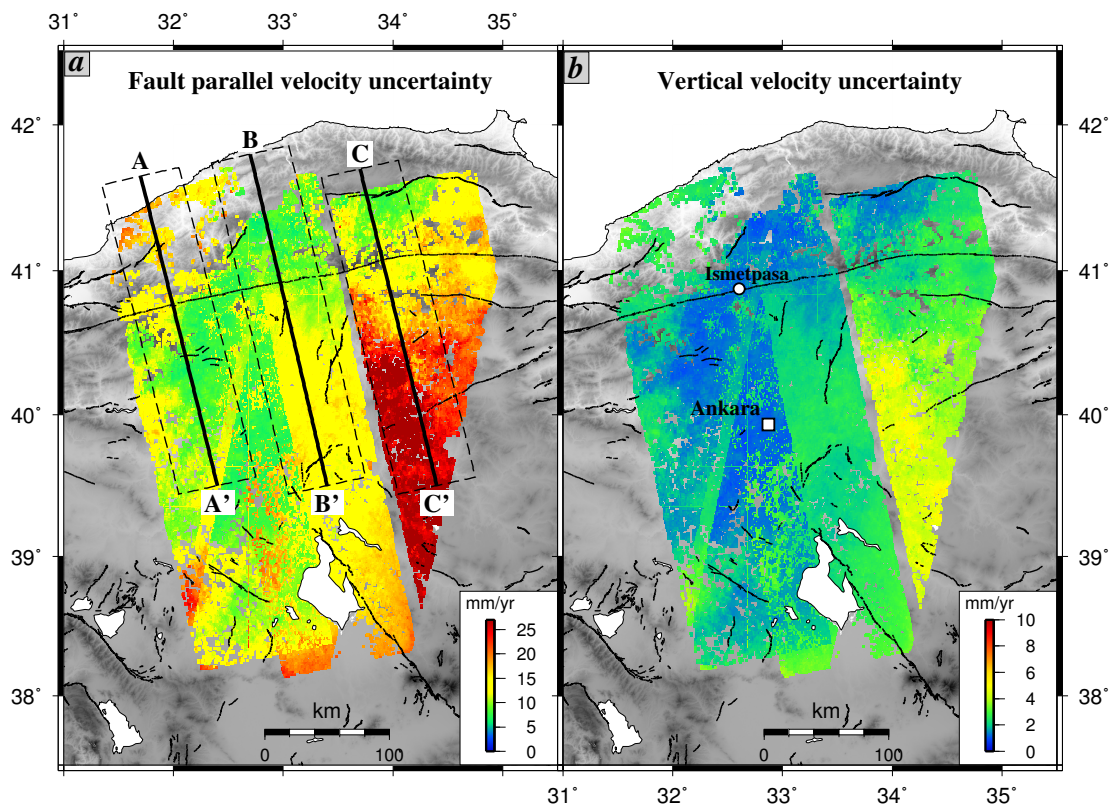


Figure C.5: Fault parallel (a) and vertical (b) velocity uncertainties.

Appendix D

Supplementary material for Chapter [4](#)

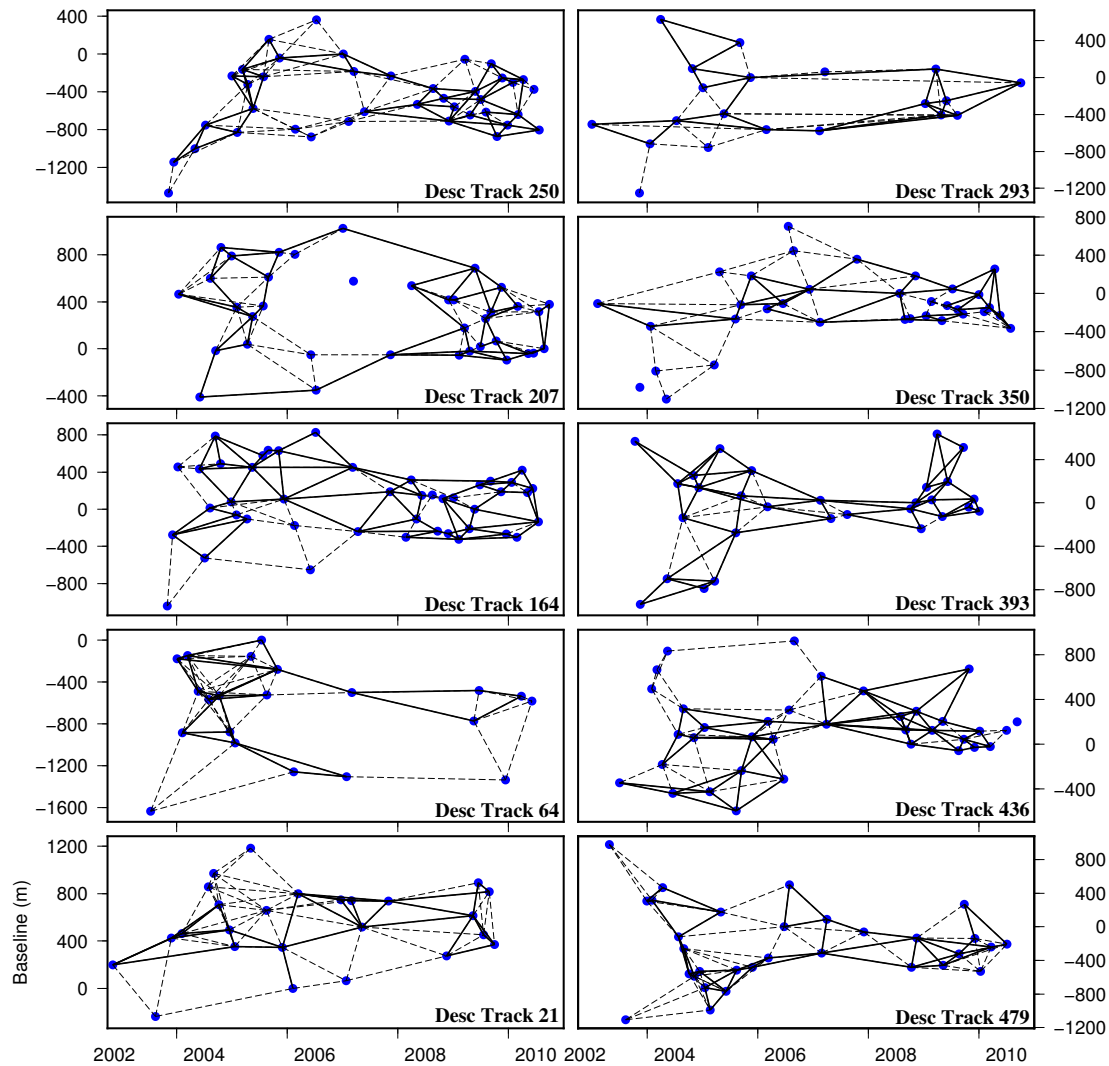


Figure D1: Baseline vs time plots for each of the descending tracks processed in this study. The combination of dashed and solid lines represent all the interferograms created. The solid black lines are the interferograms used to estimate the average line-of-sight velocity over the time period.

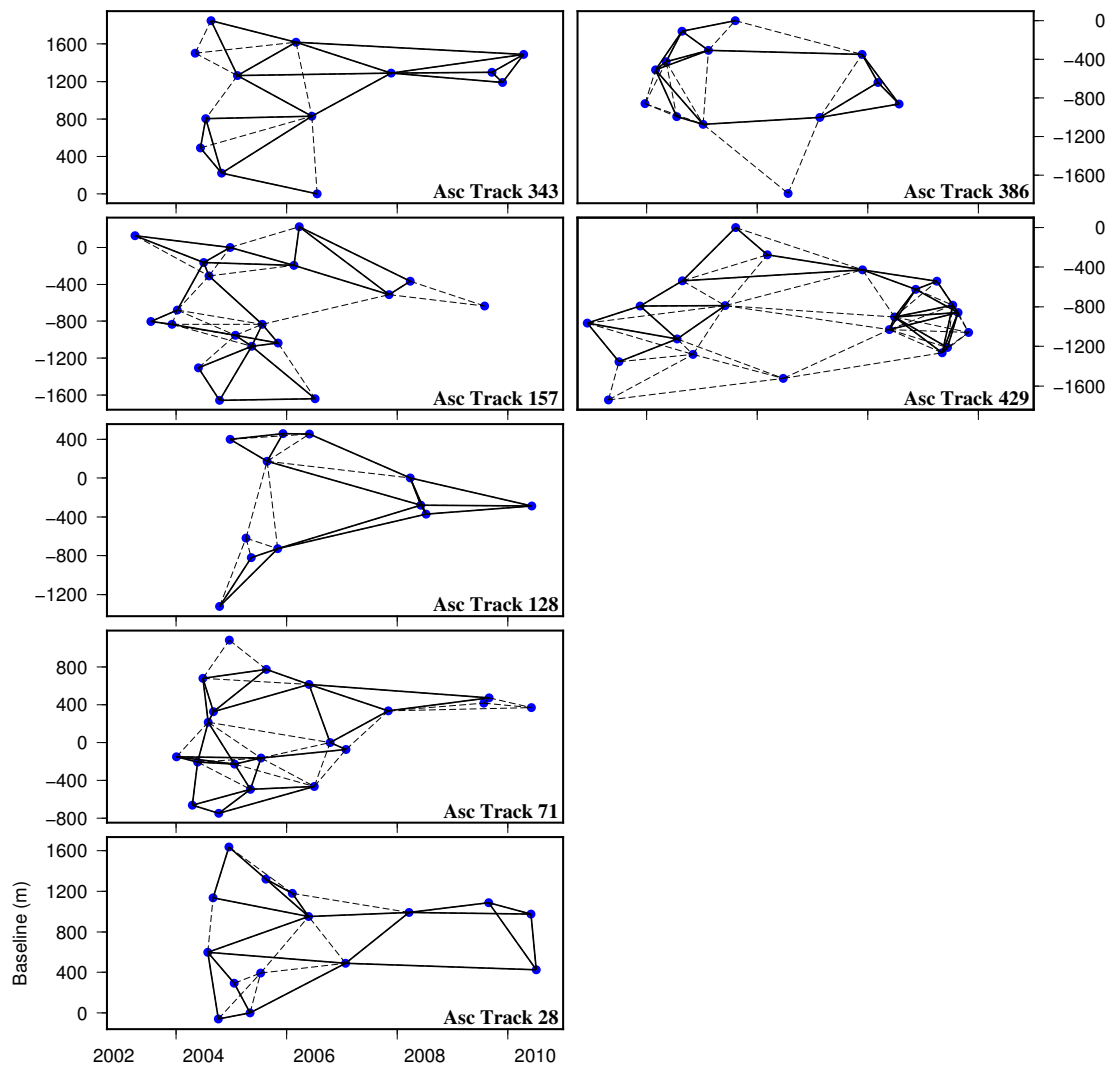


Figure D2: Baseline vs time plots for each of the ascending tracks processed in this study.

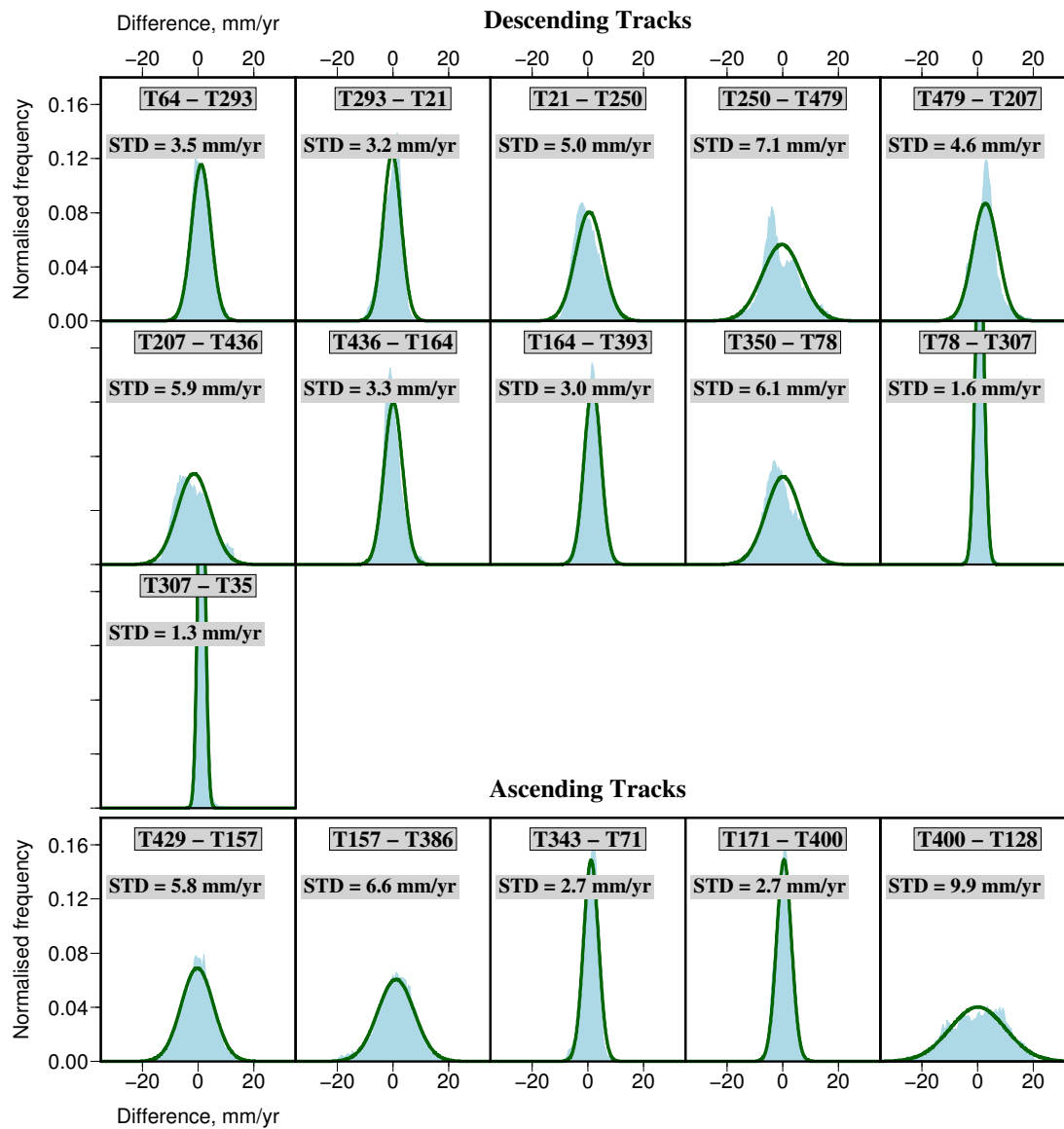


Figure D3: Normalised histograms of the horizontal velocity differences between overlapping InSAR tracks. The green line on each histogram is the best fitting Gaussian, and the number above is the standard deviation of this Gaussian

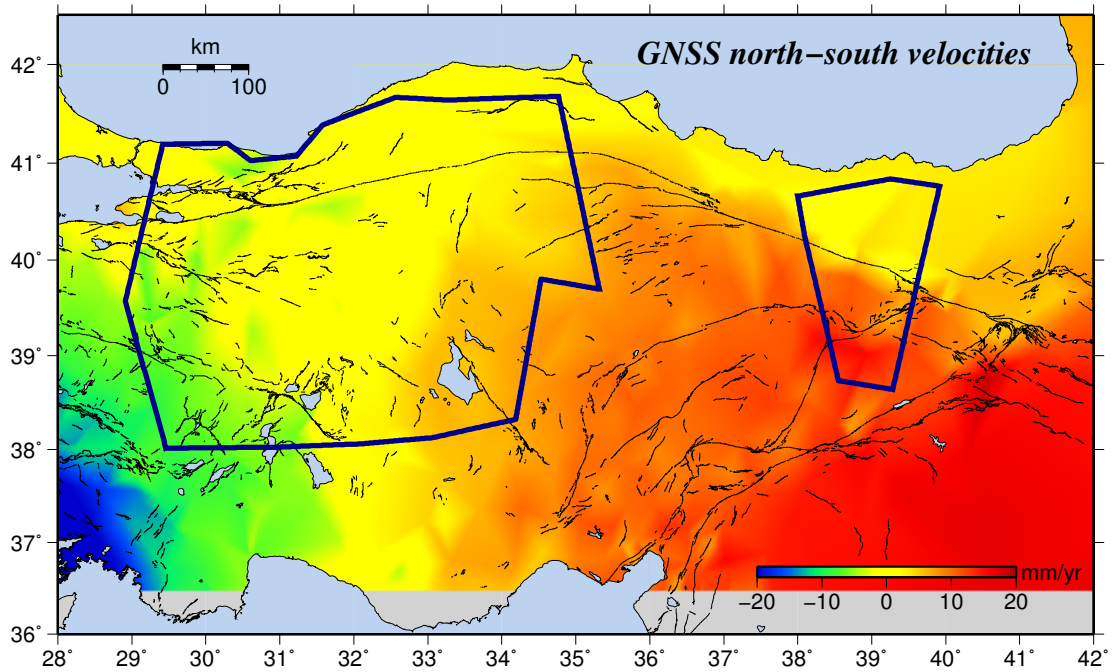


Figure D4: Interpolated GNSS north component velocities. Positive velocities indicate motion to the south while negative velocities implies motion to the south.

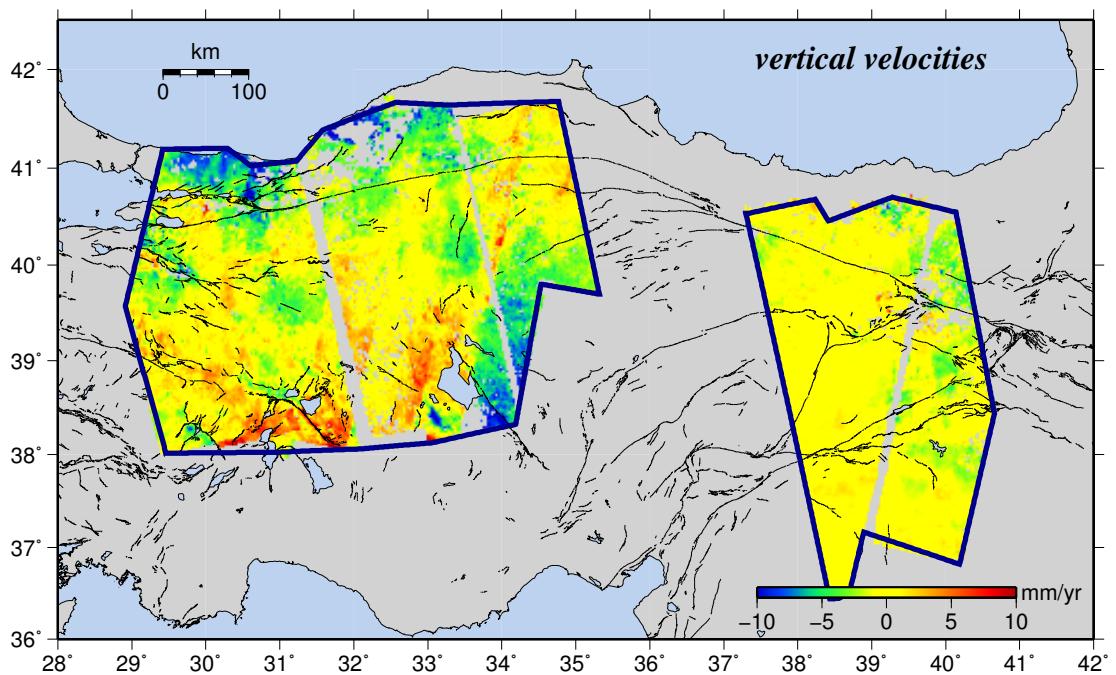


Figure D5: The decomposed vertical component of the InSAR LOS velocities. The blue polygons indicate regions where both ascending and descending LOS InSAR velocities are available. For these regions we solve for the east-west and vertical components of motion while constraining the north-south motion by the GNSS north velocities (Figure S4). Negative vertical motions reflect subsidence.

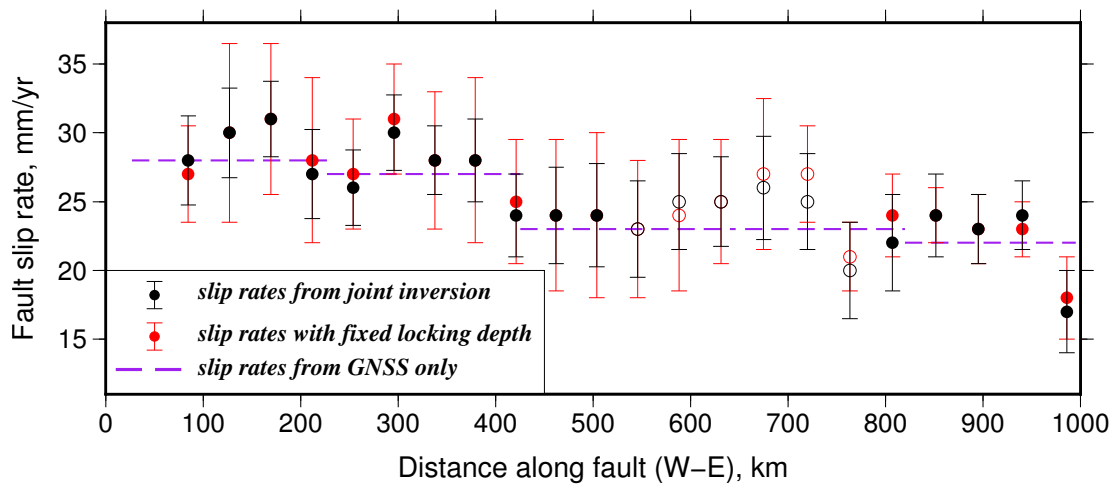


Figure D6: We run a separate set of inversions where we fix the locking depth for all profiles to a constant value of 16 ± 4 km, shown by the red line in Figure 3c in the paper. The corresponding slip rates are indicated by the red circles, while the joint inversion results are shown in black.

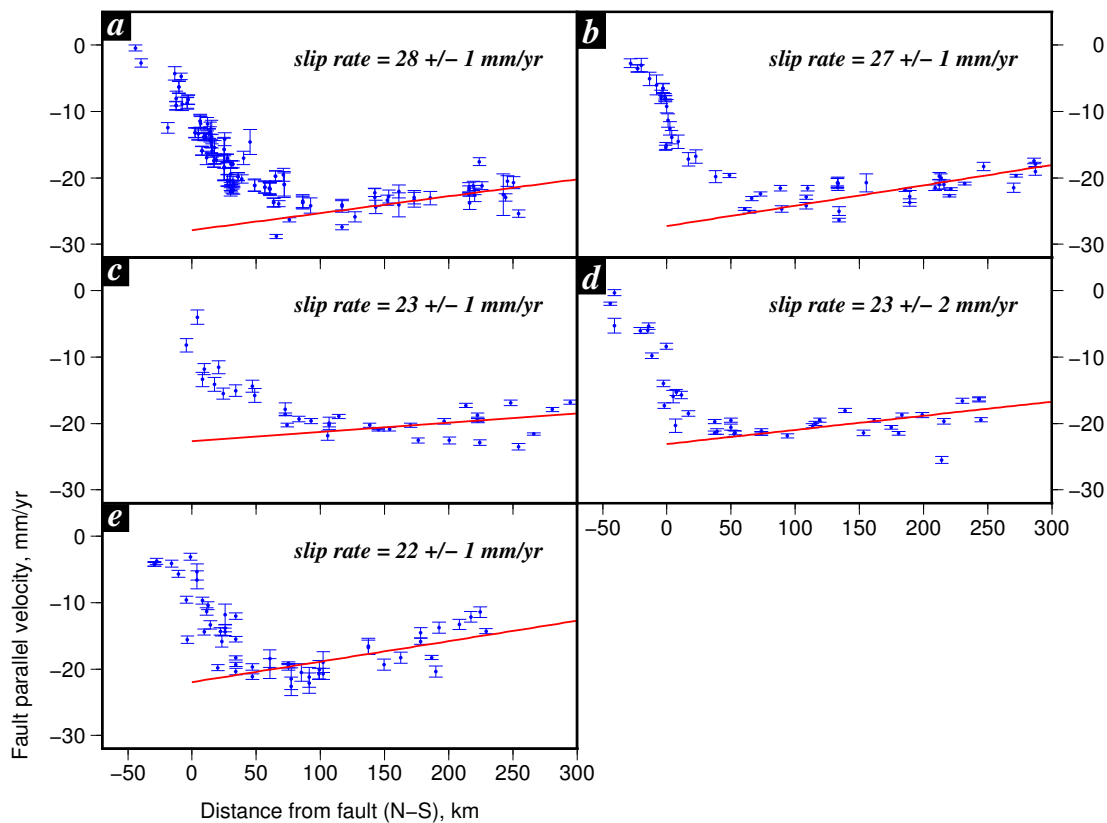


Figure D7: Profiles of GNSS fault parallel velocities at the projection locations shown in purple in Figure 3b in the paper. The red line is the least squares fit through the far-field velocities away from the fault, here defined as beyond 75 km south of the fault. The slip rate is the intersection of this line projected to the fault location.

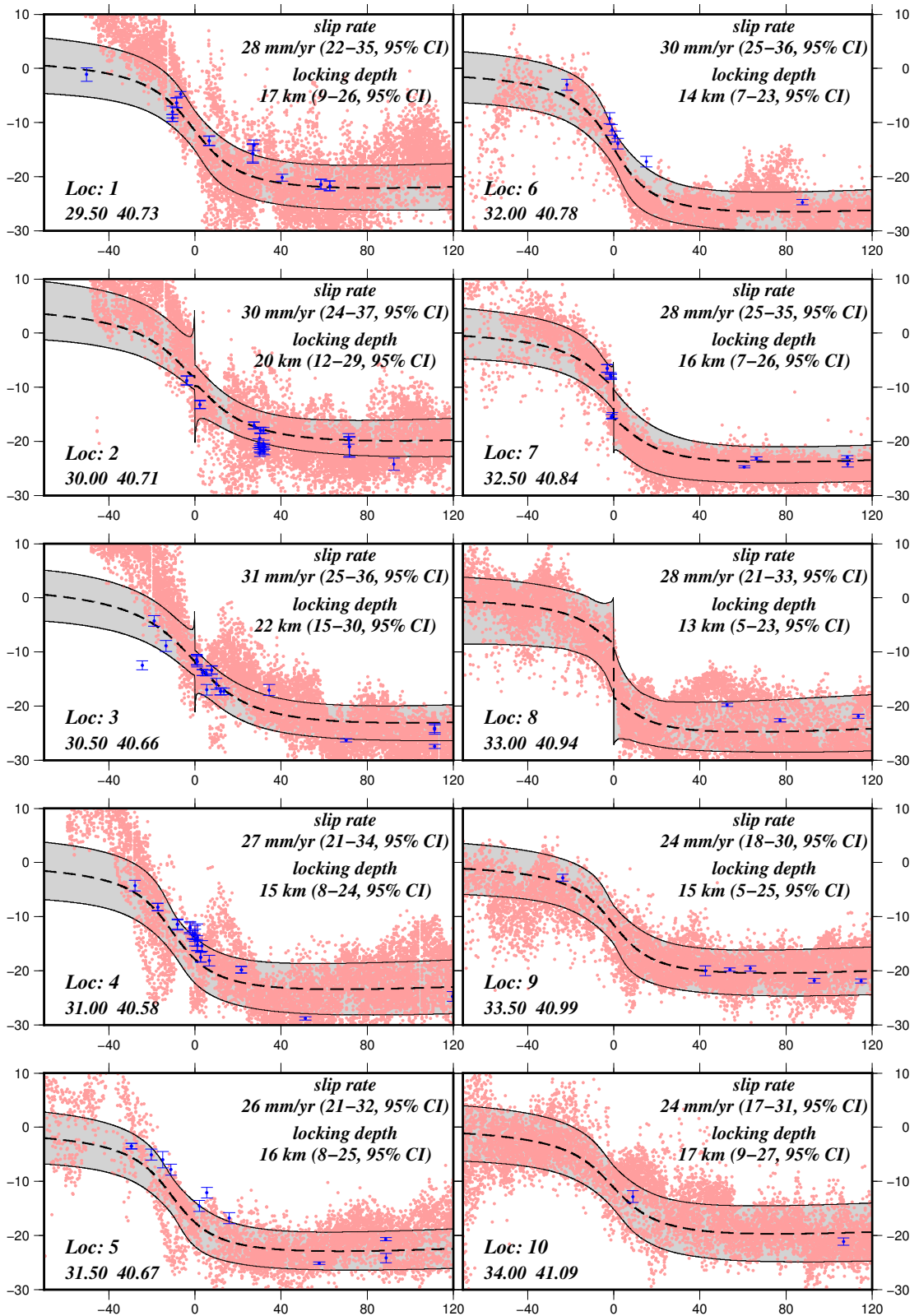


Figure D8: Fault parallel velocity profiles with our MAP model solution. x-axis is distance from fault (km) and y-axis the fault parallel velocity (mm/yr). Locations are the indicated by open circles in Figure 6b in the paper with location 1 corresponding to the western most point.

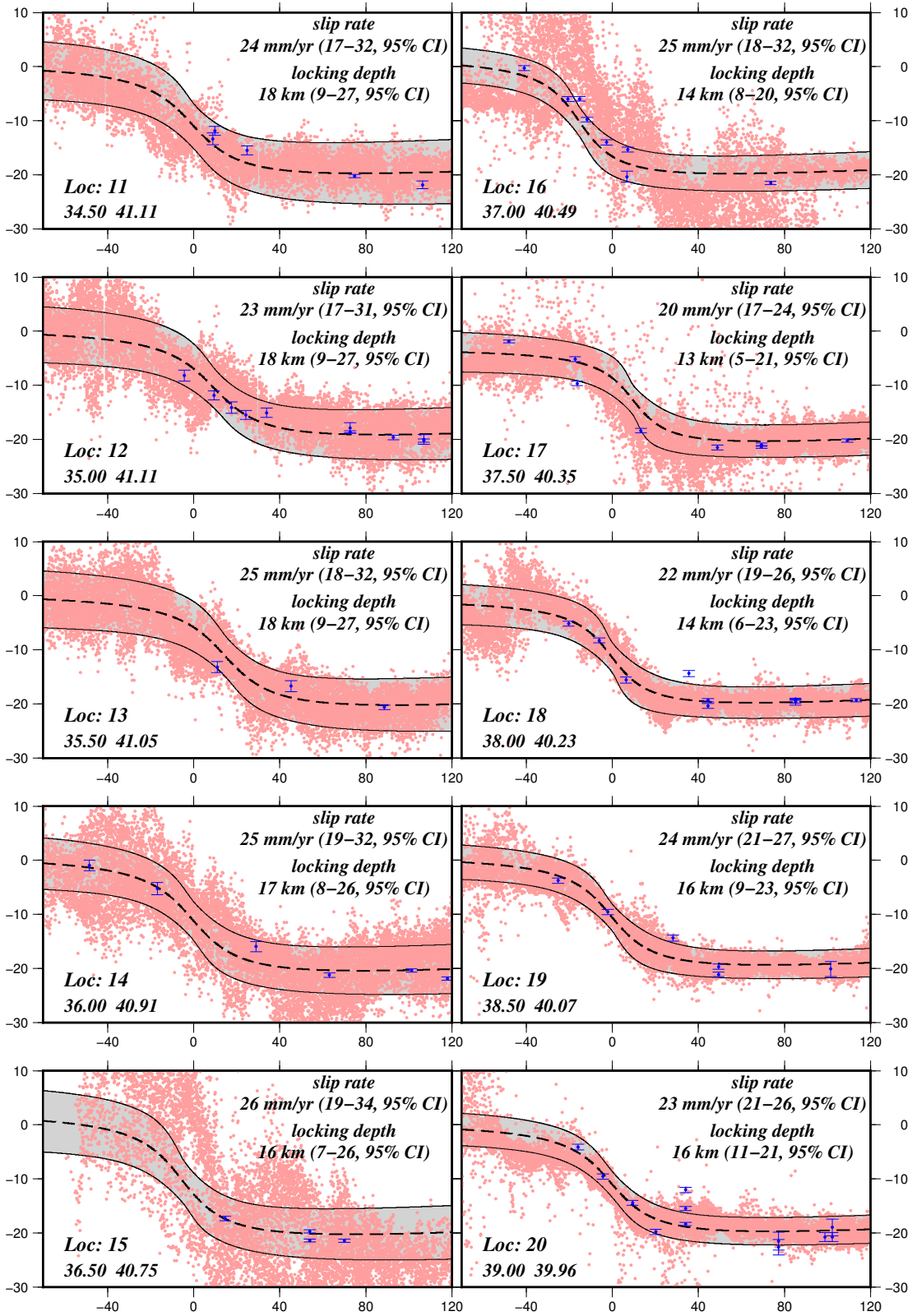


Figure D8: continued.

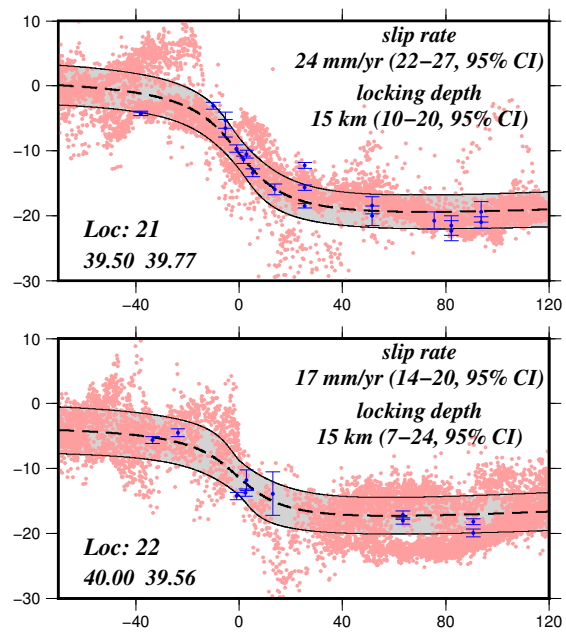


Figure D8: continued.

Appendix E

Appendix of the backmaterial

Table E.1: Compilation of slip rate and locking depth estimates for large strike-slip faults with the time since the last large earthquake ($M_w > 6$)

Fault name	Lon. (°E)	Lat. (°N)	Data source	Locking depth (km)	slip rate (mm/yr)	Reference	Time since last earthquake (yrs)
1 Altn Tagh	90	38.6	GPS94-98	8–36	9 ± 5	<i>Bendick et al. (2000)</i>	677 ± 108
2 Altn Tagh	90	38.6	GPS94-02	20	9 ± 4	<i>Wallace et al. (2004)</i>	681 ± 108
3 Altn Tagh	90	38.6	GPS98-04	15	11.9 ± 3.3	<i>Zhang et al. (2007)</i>	683 ± 108
4 Altn Tagh	96	40	GPS98-04	15	3.9 ± 2.3	<i>Zhang et al. (2007)</i>	53
5 Haiyuan	104	37	InSAR93-98	0–4.2	6.1 ± 1.9	<i>Cavalié et al. (2008)</i>	71
6 Xianshuihe	101.2	31	GPS-07	9.2 ± 3.7	11.4 ± 1.5	<i>Meng et al. (2008)</i>	26
7 Xianshuihe	101.8	30.3	GPS-07	1.0 ± 0.6	8.4 ± 0.8	<i>Meng et al. (2008)</i>	114
8 Xianshuihe	100.5	31.5	GPS98-04	3–6	8.5 ± 1.5	<i>Wang et al. (2009)</i>	81
9 Bolnay	98	49.5	GPS94-02	35	2.6 ± 1	<i>Calais et al. (2003)</i>	97
10 Gobi Altai	98	45.5	GPS94-02	35	1.2 ± 1.2	<i>Calais et al. (2003)</i>	45
11 Chalderan Fault	44	39	GPS99-09		8	<i>Djamour et al. (2011)</i>	330
12 North Tabriz Fault	45	39	GPS99-09	6–26	7–10.3	<i>Djamour et al. (2011)</i>	289
13 North Tabriz Fault	47	37.5	GPS99-09	15.5	8 ± 2	<i>Djamour et al. (2011)</i>	230
14 Kazerun	52	29	GPS97-03		6 ± 2	<i>Walpersdorf et al. (2006)</i>	13
15 Ganos Fault	27	40.7	GPS92-12	9 ± 2	20 ± 1	<i>Ergintav et al. (2014)</i>	97
16 Ganos Fault	27.5	40.8	InSAR92-03	9–17	20–27	<i>Motagh et al. (2007)</i>	91
17 Marmara Fault	28	40.8	GPS88-97	10.5		<i>Le Pichon et al. (2003)</i>	654
18 Marmara Fault	28.5	40.8	GPS92-12		2	<i>Ergintav et al. (2014)</i>	669
19 Princes Island Fault	29.2	40.8	GPS92-12	10	11 ± 3	<i>Ergintav et al. (2014)</i>	236
20 NAF (S. Branch)	30	40.5	GPS92-12		5 ± 2	<i>Ergintav et al. (2014)</i>	1891
21 NAF	29.8	40.6	GPS88-99	21	27.2 ± 0.3	<i>Reilinger et al. (2006)</i>	245

22	NAF	30	40.6	GPS92-12	5 ± 1	25 ± 2	<i>Ergintav et al. (2014)</i>	13
23	NAF	38.8	39.9	InSAR92-99	5–33	17–32	<i>Wright et al. (2001a)</i>	60
24	NAF	32.5	40.8	InSAR92-01	14		<i>Cakir et al. (2005)</i>	57
25	EAF	38.8	38	InSAR03-10	15 ± 5	11 ± 3	<i>Walters et al. (2014)</i>	46
26	S. DSF (WAF)	36	29.531.5	GPS96-01	15 ± 5	4.9 ± 0.4	<i>Al Tarazi et al. (2011)</i>	543
27	S. DSF (JVF)	36	31.533.5	GPS96-01	8 ± 5	4.7 ± 0.4	<i>Al Tarazi et al. (2011)</i>	969
28	C. Alpine	170	43.5	GPS94-98	22 ± 1	36 ± 3.1	<i>Beavan et al. (1999)</i>	283 ± 5
29	C. Alpine	170	43.5	GPS01-10	13–18	27.5 ± 2.5	<i>Beavan et al. (2010)</i>	295 ± 5
30	S. Alpine	169	44	GPS95-98	10 ± 2	23 ± 2	<i>Pearson et al. (2000)</i>	283 ± 5
31	Fairweather	221	59.7	GPS92-02	9.0 ± 0.8	45.6 ± 2	<i>Fletcher and Freymueller (2003)</i>	44
32	Wasatch	248	40	GPS96-08	7 ± 3	3.2 ± 0.2	<i>Velasco et al. (2010)</i>	1235 ± 62
33	Imperial	244.5	32.8	GPS99-00	10	35 ± 5	<i>Lyons et al. (2002)</i>	21
34	Imperial	244.5	32.7	GPS	5.9 ± 3	37.5 ± 5.5	<i>Smith-Konter et al. (2011)</i>	26
35	SAF	244.2	33.5	InSAR92-00	17 ± 4	25 ± 3	<i>Fialko (2006)</i>	250
36	Borrogo	244	33.2	GPS	6.4 ± 1.4	15	<i>Smith-Konter et al. (2011)</i>	37
37	Coyote Creek	243.7	33.2	GPS	6.3 ± 2	15	<i>Smith-Konter et al. (2011)</i>	37
38	Anza	243.5	33.5	GPS	13.7 ± 3.2	15	<i>Smith-Konter et al. (2011)</i>	263
39	Palm Springs	243.5	34	GPS	16.4 ± 8	23	<i>Smith-Konter et al. (2011)</i>	37
40	SJV	243	34.8	GPS	21.5 ± 6.3	12	<i>Smith-Konter et al. (2011)</i>	86
41	OV	242	36	GPS	7.3 ± 4.0	3.1 ± 0.6	<i>Hill and Blewitt (2006)</i>	132
42	Mojave	242	34.5	GPS	15		<i>Johnson et al. (2007)</i>	148
43	Mojave	242	34.5	GPS	18–24		<i>Johnson et al. (2007)</i>	148
44	Mojave	242	34.5	GPS	16.8 ± 0.4	33	<i>Smith-Konter et al. (2011)</i>	148
45	Carrizo	240.5	35	GPS	18.7 ± 2	36	<i>Smith-Konter et al. (2011)</i>	148
46	SAF	240	35	GPS	10.2 ± 3.8	30.6 ± 0.4	<i>Hill and Blewitt (2006)</i>	148

47	Sumatran	100	1	GPS89-93	15	30	<i>Prawirodirdjo et al. (1997)</i>	43
48	Sagaing	96	26	GPS05-08	7.7	21.2	<i>Maurin et al. (2010)</i>	77
49	Sagaing	96	24	GPS05-08	6.3	20.1	<i>Maurin et al. (2010)</i>	17
50	Sagaing	96	22	GPS05-08	20.3	22.4	<i>Maurin et al. (2010)</i>	51
51	El Pilar	296.5	10.5	GPS94-00	14 ± 2	20.5 ± 2	<i>Pérez et al. (2001)</i>	3
52	Septentrional	288	20	GPS86-95	15	8 ± 3	<i>Dixon et al. (1998)</i>	865 ± 95
53	Septentrional	288	20	GPS94-01	15	12.8 ± 2.5	<i>Calais et al. (2002)</i>	865 ± 95
54	Enriquillo	287	18.5	GPS86-95	15	8 ± 4	<i>Dixon et al. (1998)</i>	225
55	Enriquillo	287	18.5	GPS94-01	15	9 ± 9	<i>Calais et al. (2002)</i>	231
56	NH	288	20.4	GPS86-95	15	4 ± 3	<i>Dixon et al. (1998)</i>	49
57	NH	288	20.4	GPS94-01	15	5.2 ± 2	<i>Calais et al. (2002)</i>	55
58	Polochic-Motagua	270.5	15	GPS99-03	21	20	<i>Lyon-Caen et al. (2006)</i>	27
59	Polochic-Motagua	270.5	15	GPS99-06	20	18 ± 2	<i>Franco et al. (2012)</i>	30

DSF: Dead Sea Fault; JVF: Jordan Valley Fault; NAF: North Anatolian Fault; NH: North Hispaniola; OV: Owens Valley; SAF: San Andreas Fault; SJV: San Jacinto Valley; WAF: Wadi Araba Fault

References

- Al Tarazi, E., J. Abu Rajab, F. Gomez, W. Cochran, R. Jaafar, and M. Ferry (2011), GPS measurements of near-field deformation along the southern Dead Sea Fault System, *Geochemistry, Geophysics, Geosystems*, 12(12). [E.1](#)
- Beavan, J., M. Moore, C. Pearson, M. Henderson, B. Parsons, S. Bourne, P. England, D. Walcott, G. Blick, D. Darby, et al. (1999), Crustal deformation during 1994–1998 due to oblique continental collision in the central Southern Alps, New Zealand, and implications for seismic potential of the Alpine fault, *Journal of Geophysical Research: Solid Earth*, 104(B11), 25,233–25,255. [E.1](#)
- Beavan, J., P. Denys, M. Denham, B. Hager, T. Herring, and P. Molnar (2010), Distribution of present-day vertical deformation across the Southern Alps, New Zealand, from 10 years of GPS data, *Geophysical Research Letters*, 37(16). [E.1](#)
- Bendick, R., R. Bilham, J. Freymueller, K. Larson, and G. Yin (2000), Geodetic evidence for a low slip rate in the Altyn Tagh fault system, *Nature*, 404(6773), 69–72. [E.1](#)
- Cakir, Z., A. M. Akoglu, S. Belabbes, S. Ergintav, and M. Meghraoui (2005), Creeping along the ismetpasa section of the North Anatolian fault (Western Turkey): Rate and extent from InSAR, *Earth and Planetary Science Letters*, 238(1), 225–234. [E.1](#)
- Calais, E., Y. Mazabraud, B. Mercier de Lépinay, P. Mann, G. Mattioli, and P. Jansma (2002), Strain partitioning and fault slip rates in the northeastern Caribbean from GPS measurements, *Geophysical Research Letters*, 29(18). [E.1](#)
- Calais, E., M. Vergnolle, V. San’Kov, A. Lukhnev, A. Miroshnitchenko, S. Amarjargal, and J. Déverchère (2003), GPS measurements of crustal deformation in the Baikal-Mongolia area (1994–2002): Implications for current kinematics of Asia, *Journal of Geophysical Research: Solid Earth*, 108(B10). [E.1](#)
- Cavalié, O., C. Lasserre, M.-P. Doin, G. Peltzer, J. Sun, X. Xu, and Z.-K. Shen (2008), Measurement of interseismic strain across the Haiyuan fault (Gansu, China), by InSAR, *Earth and Planetary Science Letters*, 275(3), 246–257. [E.1](#)
- Dixon, T. H., F. Farina, C. DeMets, P. Jansma, P. Mann, and E. Calais (1998), Relative motion between the Caribbean and North American plates and related boundary zone deformation from a decade of GPS observations, *Journal of Geophysical Research: Solid Earth*, 103(B7), 15,157–15,182. [E.1](#)
- Djamour, Y., P. Vernant, H. R. Nankali, and F. Tavakoli (2011), NW Iran-eastern Turkey present-day kinematics: Results from the Iranian permanent GPS network, *Earth and Planetary Science Letters*, 307(1), 27–34. [E.1](#)
- Ergintav, S., R. Reilinger, R. Çakmak, M. Floyd, Z. Cakir, U. Doğan, R. King, S. McClusky, and H. Özener (2014), Istanbul’s earthquake hot spots: Geodetic constraints on strain accumulation along faults in the Marmara seismic gap, *Geophysical Research Letters*, 41(16), 5783–5788. [E.1](#)

- Fialko, Y. (2006), Interseismic strain accumulation and the earthquake potential on the southern San Andreas fault system, *Nature*, *441*(7096), 968–971. [E.1](#)
- Fletcher, H. J., and J. T. Freymueller (2003), New constraints on the motion of the Fairweather fault, Alaska, from GPS observations, *Geophysical Research Letters*, *30*(3). [E.1](#)
- Franco, A., C. Lasserre, H. Lyon-Caen, V. Kostoglodov, E. Molina, M. Guzman-Speziale, D. Monterosso, V. Robles, C. Figueroa, W. Amaya, et al. (2012), Fault kinematics in northern Central America and coupling along the subduction interface of the Cocos Plate, from GPS data in Chiapas (Mexico), Guatemala and El Salvador, *Geophysical Journal International*, *189*(3), 1223–1236. [E.1](#)
- Hill, E. M., and G. Blewitt (2006), Testing for fault activity at Yucca Mountain, Nevada, using independent GPS results from the BARGEN network, *Geophysical Research Letters*, *33*(14). [E.1](#)
- Johnson, K. M., G. E. Hilley, and R. Bürgmann (2007), Influence of lithosphere viscosity structure on estimates of fault slip rate in the Mojave region of the San Andreas fault system, *Journal of Geophysical Research: Solid Earth*, *112*(B7). [E.1](#)
- Le Pichon, X., N. Chamot-Rooke, C. Rangin, and A. Sengör (2003), The North Anatolian fault in the Sea of Marmara, *Journal of Geophysical Research: Solid Earth (1978–2012)*, *108*(B4). [E.1](#)
- Lyon-Caen, H., E. Barrier, C. Lasserre, A. Franco, I. Arzu, L. Chiquin, M. Chiquin, T. Duquesnoy, O. Flores, O. Galicia, et al. (2006), Kinematics of the North American–Caribbean–Cocos plates in Central America from new GPS measurements across the Polochic–Motagua fault system, *Geophysical Research Letters*, *33*(19). [E.1](#)
- Lyons, S. N., Y. Bock, and D. T. Sandwell (2002), Creep along the Imperial Fault, southern California, from GPS measurements, *Journal of Geophysical Research: Solid Earth*, *107*(B10). [E.1](#)
- Maurin, T., F. Masson, C. Rangin, U. T. Min, and P. Collard (2010), First global positioning system results in northern Myanmar: Constant and localized slip rate along the Sagaing fault, *Geology*, *38*(7), 591–594. [E.1](#)
- Meng, G.-j., J.-w. Ren, M. Wang, W.-j. Gan, Q. Wang, X.-j. Qiao, and Y.-l. Yang (2008), Crustal deformation in western Sichuan region and implications for 12 May 2008 Ms 8.0 earthquake, *Geochemistry, Geophysics, Geosystems*, *9*(11). [E.1](#)
- Motagh, M., J. Hoffmann, B. Kampes, M. Baes, and J. Zschau (2007), Strain accumulation across the Gazikoy–Saros segment of the North Anatolian Fault inferred from Persistent Scatterer Interferometry and GPS measurements, *Earth and Planetary Science Letters*, *255*(3), 432–444. [E.1](#)
- Pearson, C., P. Denys, and K. Hodgkinson (2000), Geodetic constraints on the kinematics of the Alpine Fault in the southern South Island of New Zealand, using results from the Hawea–Haast GPS Transect, *Geophysical Research Letters*, *27*(9), 1319–1322. [E.1](#)
- Pérez, O. J., R. Bilham, R. Bendick, J. R. Velandia, N. Hernández, C. Moncayo, M. Hoyer, and M. Kozuch (2001), Velocity field across the southern Caribbean plate boundary and estimates of Caribbean/South-American plate motion using GPS geodesy 1994–2000, *Geophysical Research Letters*, *28*(15), 2987–2990. [E.1](#)
- Prawirodirdjo, L., Y. Bocl, R. McCaffrey, J. Genrich, E. Calais, C. Stevens, S. Puntodewo, C. Subarya, J. Rais, P. Zwick, et al. (1997), Geodetic observations of interseismic strain segmentation at the Sumatra subduction zone, *Geophysical Research Letters*, *24*(21), 2601–2604. [E.1](#)

- Reilinger, R., S. McClusky, P. Vernant, S. Lawrence, S. Ergintav, R. Cakmak, H. Ozener, F. Kadirov, I. Guliev, R. Stepanyan, M. Nadariya, G. Hahubia, S. Mahmoud, K. Sakr, A. ArRajehi, D. Paradissis, A. Al-Aydrus, M. Prilepin, T. Guseva, E. Evren, A. Dmitrotsa, S. V. Filikov, F. Gomez, R. Al-Ghazzi, and G. Karam (2006), GPS constraints on continental deformation in the Africa-Arabia-Eurasia continental collision zone and implications for the dynamics of plate interactions, *Journal of Geophysical Research: Solid Earth*, *111*(B5), doi:10.1029/2005JB004051. [E.1](#)
- Smith-Konter, B. R., D. T. Sandwell, and P. Shearer (2011), Locking depths estimated from geodesy and seismology along the San Andreas Fault System: Implications for seismic moment release, *Journal of Geophysical Research: Solid Earth*, *116*(B6). [E.1](#)
- Velasco, M. S., R. A. Bennett, R. A. Johnson, and S. Hreinsdóttir (2010), Subsurface fault geometries and crustal extension in the eastern Basin and Range Province, western US, *Tectonophysics*, *488*(1), 131–142. [E.1](#)
- Wallace, K., G. Yin, and R. Bilham (2004), Inescapable slow slip on the Altyn Tagh fault, *Geophysical Research Letters*, *31*(9). [E.1](#)
- Walpersdorf, A., D. Hatzfeld, H. Nankali, F. Tavakoli, F. Nilforoushan, M. Tatar, P. Vernant, J. Chéry, and F. Masson (2006), Difference in the GPS deformation pattern of North and Central Zagros (Iran), *Geophysical Journal International*, *167*(3), 1077–1088. [E.1](#)
- Walters, R., B. Parsons, and T. Wright (2014), Constraining crustal velocity fields with InSAR for Eastern Turkey: Limits to the block-like behavior of Eastern Anatolia, *Journal of Geophysical Research: Solid Earth*, *119*(6), 5215–5234. [E.1](#)
- Wang, H., T. Wright, and J. Biggs (2009), Interseismic slip rate of the northwestern Xianshuihe fault from InSAR data, *Geophysical Research Letters*, *36*(3). [E.1](#)
- Wright, T., B. Parsons, and E. Fielding (2001a), Measurement of interseismic strain accumulation across the North Anatolian Fault by satellite radar interferometry, *Geophysical Research Letters*, *28*(10), 2117–2120. [E.1](#)
- Zhang, P.-Z., P. Molnar, and X. Xu (2007), Late Quaternary and present-day rates of slip along the Altyn Tagh Fault, northern margin of the Tibetan Plateau, *Tectonics*, *26*(5). [E.1](#)

